SOLAR IRRADIANCE MODELING AND FORECASTING USING NOVEL STATISTICAL TECHNIQUES

YANG DAZHI

(*B.Eng.*(*Hons.*), *M.Sc.*, *NUS*)

A THISIS SUBMITTED
FOR THE DEGREE OF DOCTOR OF PHILOSOPHY
DEPARTMENT OF ELECTRICAL AND COMPUTER ENGINEERING
NATIONAL UNIVERSITY OF SINGAPORE

2014

I would like to dedicate this thesis to my father YANG Yun and my mother WU Lili.

Declaration

I hereby declare that the thesis is my original work and it has been written by me in its entirety. I have duly acknowledged all the sources of information which have been used in this thesis.

This thesis has also not been submitted for any degree in any university previously.

楊大智

YANG Dazhi

2014

Acknowledgements

My sincere thanks go to Prof. Armin G. Aberle for offering me the opportunity to study in the university and facilitating all administrative matters.

I would like to thank my friends in the labs, Dong Zibo, Dr. Ye Zhen, Gu Chaojun, André M. Nobre and Quan Hao for their companies; and Assist. Prof. Chen Nan and Assoc. Prof. Dipti Srinivasan for their enlightenments on specific domains.

Summary

Electricity grid operations require information on load and generation on a variety of timescales and areas. The advent of significant generation contributions by time variable solar energy sources means that modeling and forecasting methods are becoming increasingly important. I explore and develop a series of methods for solar irradiance modeling and forecasting.

The most fundamental models in solar irradiance modeling and forecasting are the clear sky models. Clear sky models describe the expected total irradiance reaching the Earth's surface during a cloud–free situation. Their unique properties allow us to remove the daily trends in irradiance time series, which is essential for forecasting. I develop a semi–empirical clear sky model for the equatorial region.

Univariate forecasting using the autoregressive integrated moving average model is explored next. To enhance the performance of this classic model in a solar engineering context, knowledge–based decompositions are used to describe the variabilities in irradiance time series.

Although the univariate models could provide adequate forecasting accuracy, solar irradiance is in fact a spatio–temporal quantity, spatio–temporal models are therefore desired. This thesis focuses on space–time kriging using data collected by a ground–based sensor network. Kriging allows prediction at unobserved locations; this is a distinct advantage over other spatio–temporal forecasting methods. To satisfy various model assumptions, some transformations and constraints are considered and described.

One of the assumptions of spatio–temporal models used in this thesis is stationarity.

Therefore, only irradiance data on a horizontal plane should be used in spatio–temporal models. However, such horizontal data can be scarce. Two inverse transposition models are proposed to convert irradiance on a tilted plane to horizontal irradiance. The motivation is to utilize the existing photovoltaic installations (often tilted) as irradiance sensors, and thus forecast irradiance using the above mentioned forecasting models.

To increase the number of monitoring stations in a sensor network and thus allow better forecasting, network expansion strategies are discussed. The information content in a spatio–temporal dataset can be described using entropy. An entropy–based network redesign procedure is described.

As increasing volumes of information become available, partly due to potential implementations of the inverse transposition models and network expansion, we need to consider the effectiveness and interpretability of the data. Threshold distance is developed to describe the spatial information boundaries for forecasting. Parameter selection and shrinkage models can reduce the number of parameters in a spatio–temporal model thus achieve efficient and accurate forecasts.

List of publications

Journal

1. **Dazhi Yang**, Zhen Ye, Lihong Idris Lim and Zibo Dong. 2015. Very short term irradiance forecasting using the lasso. *Solar Energy*, accepted, (Impact factor: 3.541). doi: http://dx.doi.org/10.1016/j.solener.2015.01.016.

2. Lihong Idris Lim, Zhen Ye, Jiaying Ye, **Dazhi Yang** and Hui Du. 2015. A linear identification of diode models from single I–V characteristics of PV panels. *Industrial Electronics, IEEE Transactions on*, in press, (Impact factor: 6.5). doi: http://dx.doi.org/10.1109/TIE.2015.2390193.

3. **Dazhi Yang**, Vishal Sharma, Zhen Ye, Lihong Idris Lim, Lu Zhao and Aloysius W. Aryaputera. 2015. Forecasting of global horizontal irradiance by exponential smoothing, using decompositions. *Energy*, in press, (Impact factor: 4.159). doi: http://dx.doi.org/10.1016/j.energy.2014.11.082.

4. **Dazhi Yang** and Thomas Reindl. 2015. Optimal solar irradiance sampling design using the variance quadtree algorithm. *Renewables: Wind, Water, and Solar*, 2(1):1–8, (Impact factor: TBD). doi: http://dx.doi.org/10.1186/s40807-014-0001-x.

5. Lihong Idris Lim, Zhen Ye, Jiaying Ye, **Dazhi Yang** and Hui Du. 2015. A linear method to extract diode model parameters of solar panels from a single I–V curve. *Renewable Energy*, 76(0):135-142, (Impact factor: 3.361). doi: http://dx.doi.org/10.1016/j.renene.2014.11.018.

6. **Dazhi Yang**, Zhen Ye, André M. Nobre, Hui Du, Wilfred M. Walsh, Lihong Idris Lim and Thomas Reindl. 2014. Bidirectional irradiance transposition based on the Perez model. *Solar Energy*, 110(0):768–780, (Impact factor: 3.541). doi: http://dx.doi.org/10.1016/j.solener.2014.10.006.

7. Haohui Liu, André Nobre, **Dazhi Yang**, Jiaying Ye, Fernando R. Martins, Richardo Rüther, Thomas Reindl, Armin G. Aberle and Ian Marius Peters. 2014. The impact of haze on performance ratio and short–circuit current of PV systems in Singapore, *Photovoltaics, IEEE Journal of*, 4(6):1585–1592, (Impact factor: 3.0). doi: http://dx.doi.org/10.1109/JPHOTOV.2014.2346429.

8. Chaojun Gu, **Dazhi Yang**, Panida Jirutitijaroen, Wilfred M. Walsh and Thomas Reindl. 2014. Spatial load forecasting with communication failure using time–forward kriging, *Power Systems, IEEE Transactions on*, 29(6):2875–2882, (Impact factor: 3.53). doi: http://dx.doi.org/10.1109/TPWRS.2014.2308537.

9. **Dazhi Yang**, Wilfred M. Walsh and Panida Jirutitijaroen. 2014. Estimation and applications of clear sky global horizontal irradiance at the Equator. *Journal of Solar Energy Engineering*. 136(3), (Impact factor: 1.132). doi: http://dx.doi.org/10.1115/1.4027263.

10. **Dazhi Yang**, Zibo Dong, Thomas Reindl, Panida Jirutitijaroen and Wilfred M. Walsh. 2014. Solar irradiance forecasting using spatio–temporal empirical kriging and vector autoregressive models with parameter shrinkage. *Solar Energy*, 103(0):550–562, (Impact factor: 3.541). doi: http://dx.doi.org/10.1016/j.solener.2014.01.024.

11. Yong Sheng Khoo, André Nobre, Raghav Malhotra, **Dazhi Yang**, Richardo Rüther, Thomas Reindl and Armin Aberle. 2014. Optimal orientation and tilt angle for maximizing in–plane solar irradiance for PV applications in Singapore. *Photovoltaics, IEEE Journal of*, 4(2):647–653, (Impact factor: 3.0). doi: http://dx.doi.org/10.1109/JPHOTOV.2013.2292743.

12. Zibo Dong, **Dazhi Yang**, Thomas Reindl and Wilfred M. Walsh. 2014. Satellite image analysis and a hybrid ESSS/ANN model to forecast solar irradiance in the tropics. *Energy Conversion and Management*, 79(0):66–73, (Impact factor: 3.59). doi: http://dx.doi.org/10.1016/j.enconman.2013.11.043.

13. **Dazhi Yang**, Zibo Dong, André Nobre, Yong Sheng Khoo, Panida Jirutitijaroen and Wilfred M. Walsh. 2013. Evaluation of transposition and decomposition models for converting global solar irradiance from tilted surface to horizontal in tropical regions. *Solar Energy*, 97(0):369–387, (Impact factor: 3.541). doi: http://dx.doi.org/10.1016/j.solener.2013.08.033.

14. **Dazhi Yang**, Chaojun Gu, Zibo Dong, Panida Jirutitijaroen, Nan Chen and Wilfred M. Walsh. 2013. Solar irradiance forecasting using spatial–temporal covariance structures and time–forward kriging. *Renewable Energy*, 60(0):235–245, (Impact factor: 3.361). doi: http://dx.doi.org/10.1016/j.renene.2013.05.030.

15. Zibo Dong, **Dazhi Yang**, Thomas Reindl and Wilfred M. Walsh. 2013. Short–term solar irradiance forecasting using exponential smoothing state space model. *Energy*, 55(0):1104–1113, (Impact factor: 4.159). doi: http://dx.doi.org/10.1016/j.energy.2013.04.027.

16. **Dazhi Yang**, Panida Jirutitijaroen and Wilfred M. Walsh. 2012. Hourly solar irradiance time series forecasting using cloud cover index. *Solar Energy*, 86(12):3531–3543, (Impact factor: 3.541). doi: http://dx.doi.org/10.1016/j.solener.2012.07.029.

Conference

1. **Dazhi Yang**, Wilfred M. Walsh, Zibo Dong, Panida Jirutitijaroen and Thomas Reindl. 2013. Block matching algorithms: Their applications and limitations in solar irradiance forecasting. *Energy Procedia*, 33(0):335–342. doi: http://dx.doi.org/10.1016/j.egypro.2013.05.074.

2. **Dazhi Yang**, Panida Jirutitijaroen and Wilfred M. Walsh. 2012. The estimation of clear sky global horizontal irradiance at the Equator. *Energy Procedia*, 25(0):141–148. doi: http://dx.doi.org/10.1016/j.egypro.2012.07.019.

Magazine

1. **Dazhi Yang**, André Nobre, Rupesh Baker and Thomas Reindl. 2014. Large–area solar irradiance mapping. *Photovoltaics International*, 24(0):91–98.

Contents

List of Tables

List of Figures

Nomenclature

Roman Symbols

d_{ij}^2	spatial dispersion between stations i and j
D_n	Kolmogorov–Smirnov test statistic
d_n	day number
E_0	eccentricity correction factor of earth
F_1	circumsolar brightening coefficient
F_2	horizon brightening coefficient
F_{ij}	Perez model coefficients, $i = \{1, 2\}$, $j = \{1, 2, 3\}$
F_{ij}^*	adjusted Perez model coefficients, $i = \{1, 2\}$, $j = \{1, 2, 3\}$
$\boldsymbol{h}$	$\in \mathbb{R}^d$, a d–dimensional translation in space
H	entropy (information theory) [dimensionless]
h_{ij}	dispersion plane distance between stations i and j
$\boldsymbol{I}$	indicator function
I_{beam}	horizontal beam solar irradiance [W/m^2]
I_{cs}	clear sky global horizontal solar irradiance [W/m^2]
I_{csdir}	clear sky direct normal solar irradiance [W/m^2]
I_{dif}	diffuse horizontal solar irradiance [W/m^2]
I_{dir}	direct normal solar irradiance [W/m^2]
I_{glo}	global horizontal solar irradiance [W/m^2]
I_{o}	extraterrestrial direct normal irradiance [W/m^2]
I_{oh}	horizontal extraterrestrial irradiance [W/m^2]
I_{sc}	solar constant = 1362 [W/m^2]
I_{t}	global solar irradiance on a tilted plane [W/m^2]

$I_{\mathrm{t,dif}}$	diffuse solar irradiance on a tilted plane [W/m^2]
$I_{\mathrm{t,dir}}$	direct solar irradiance on a tilted plane [W/m^2]
$I_{\mathrm{t,refl}}$	reflected solar irradiance on a tilted plane [W/m^2]
K_{d}	diffuse horizontal transmittance
K_{n}	direct normal transmittance
K_{nc}	clear sky direct normal transmittance
K_{t}	effective global horizontal transmittance
L_{refl}	reflection loss of reference cell
L_{spec}	spectral loss of reference cell
m_a	relative air mass with altitude correction
m_r	relative optical air mass
(p, d, q)	process orders of an ARIMA model
R_{b}	beam irradiance transposition factor
R_{d}	diffuse transposition factor
R_{r}	transposition factor for ground reflection
s	tilt angle of PV array/sensors
τ	$\in \mathbb{R}^1$, a 1–dimensional translation in time
$z(\boldsymbol{s}; t)$	$\in \mathbb{R}^d \times \mathbb{R}^1$, spatio–temporal process at location $\boldsymbol{s}$ and time t
$z_t(\boldsymbol{s})$	$\in \mathbb{R}^1$, time series of spatial process at location $\boldsymbol{s}$ and time t

Greek Symbols

α	azimuth angle of the Sun
β	azimuth angle of the PV
$\boldsymbol{\Delta}$	proximity matrix
δ	monotone function used in multidimensional scaling
Δ'	sky's brightness
Γ	day angle
γ	variogram
κ	constant $= 1.041$, used in sky's brightness calculation
λ	penalty size

μ	mean, unless otherwise specified
$\boldsymbol{\mu}$	mean vector
∇^d	dth order difference operator
$\phi(\mathcal{B})$	autoregressive operator
ρ	correlation function
$\widehat{\rho}$	empirical correlation function
ρ'	foreground's albedo
$\boldsymbol{\Sigma}$	covariance matrix of a multivariate normal distribution
σ	standard deviation, unless otherwise specified
$\theta(\mathcal{B})$	moving average operator
θ_i	incidence angle
ϑ_z	zenith angle in radians
θ_z	zenith angle in degrees
ε'	sky's clearness

Other Symbols

$\mathcal{B}$	back shift operator
$\mathbb{C}$	covariance function
$\widehat{\mathbb{C}}$	empirical covariance function
$\mathtt{Corr}$	correlation
$\mathtt{Cov}$	covariance
$\widehat{\mathtt{Cov}}$	empirical covariance
$\mathbb{E}$	expectation
$\mathbb{R}^d$	d dimensional space
$\mathcal{S}$	stress function used in multidimensional scaling
$\mathbb{V}$	variance/covariance operator

Acronyms / Abbreviations

AI	Artificial Intelligence
AIC	Akaike Information Criterion
ANN	Artificial Neural Network

ARIMA	AutoRegressive Integrated Moving Average
CC	Cloud Cover
ETS	ExponenTial Smoothing
FZEHS	First Zero Energy House in Singapore
DHI	Diffuse Horizontal solar Irradiance
DNI	Direct Normal solar Irradiance
GHI	Global Horizontal solar Irradiance
KPSS	Kwiatkowski–Phillips–Schmidt–Shin
K–S	Kolmogorov–Smirnov
LOESS	locally weighted smoothing (LOcal regrESSion)
MBE	Mean Bias Error
MDS	MultiDimensional Scaling
MLP	MultiLayer Perceptron
NWP	Numerical Weather Prediction
PV	PhotoVoltaic
RMSE	Root Mean Square Error
cRMSE	centered Root Mean Square Error
nRMSE	normalized Root Mean Square Error
RR	Ramp Rates
SERIS	Solar Energy Research Institute of Singapore
SPA	Solar Position Algorithm
TMY3	Typical Meteorological Year 3
TPS	Thin Plate Spline
TSI	Total Sky Imager

Chapter 1

Introduction

Fossil fuels dominate the world's energy market today. The non–renewable fossil fuels however will eventually be depleted. This inevitable depletion and other negative impacts of fossil fuels usage such as global warming have been the motivation of renewable energy development. Today, solar energy alongside other forms of renewable energy receives attention from environmentalists, social scientists, economists, politicians, operators of electricity supply systems and many other groups promoting sustainable development.

Since the creation of the first modern solar cell in 1954 by Chapin et al. (1954), the technology has advanced tremendously through the years. The efficiency of the silicon solar cell has tripled and its cost has reduced a hundred times. These motivations lead to constant growth of photovoltaic (PV) market. At the end of 2013, world solar PV power capacity increased to 136,697 MW with about 37,007 MW (35% increase from the end of 2012) installed in the year 2013 alone (Shahan, 2014). With the increasing penetration of distributed solar power into the electricity grids, the inherently introduced variability potentially poses challenges for the power system operations.

A power system can be described as consisting of generation, transmission & distribution and load. The main task of a power system is therefore to ensure the delivery of quality electricity to all loads in the system in response to the time–varying electricity demand. A state–of–the–art energy management system consists of many operations to balance the generation and load including network monitoring (e.g. state estimation), generation scheduling (e.g., unit commitment, load forecasting), generation control (e.g. economic dispatch, frequency control) and network analysis & security control (e.g., optimal power flow, short circuit analysis). These operations are well developed for fossil fuels–based power systems. However, solar energy is highly weather–dependent; sudden power ramps and drops when clouds move over a PV installation are still seen as a threat by many grid operators. Fig. 1.1 shows the variation of global horizontal irradiance (GHI) during a typical day in Singapore. These large fluctuations have to be managed for reliable power gird operations.

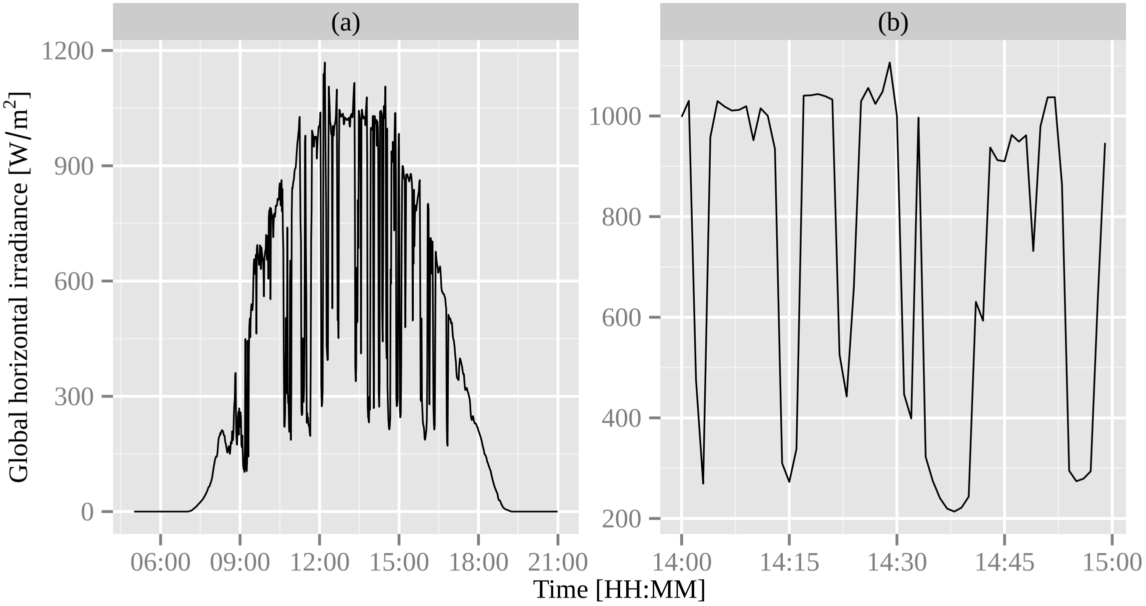

Fig. 1.1 (a) Time series plot for global horizontal irradiance measured on 2012 January 4 at the Solar Energy Research Institute of Singapore. (b) A zoomed view for 2:00–3:00 pm.

The conventional approaches of increasing the spinning reserves in the power system and/or using battery–based energy storage can help manage the variability of solar power. However, these options are costly. Complementary to these, forecasting of the solar power output on different timescales is a powerful tool, which brings solar PV one step closer to being “dispatchable”, and thereby making it more compatible with the current power grid operation. Many desired outcomes of performing forecasting, such as improved power quality and reduced operational costs, have been the driving motivation for the solar energy forecasters.

At this stage, I note that other than irradiance, many other factors have effects on PV performance. One of those factors is temperature. Solar cell performance drops with increasing temperature owing to the drop in open circuit voltage. Nevertheless, as the change in temperature is more gradual than the change in irradiance, short term module temperature forecasting is straightforward. For grid integration purposes, irradiance forecasting contributes most to the overall PV output forecasting uncertainty. This thesis therefore focuses mostly on irradiance forecasting; PV power forecasting is briefly discussed.

1.1 Problem statement

The primary aim of this thesis is to develop spatio–temporal statistical forecasting methods for solar irradiance using data collected by ground–based sensor networks. Several secondary tasks including irradiance modeling, data transformations, monitoring network design are also investigated.

1.2 An overview of motivations and contributions

As the problem statement suggests, various statistical predictive methods will be considered, developed, modified, used and validated in chapters 4, 5 and 9 of the thesis. Statistical forecasting methods are used in a wide range of applications including economic and econometric forecasting, marketing forecasting, financial forecasting, production and technological forecasting, crime forecasting, climate forecasting, demographic forecasting, energy forecasting and many others. What distinguishes solar irradiance forecasting from the others is the domain knowledge. Chapters 3, 4, 6, 7 and 8 therefore address and study the domain knowledge (irradiance modeling) in details.

1.2.1 Chapter 3: the clear sky model

The most fundamental model in solar irradiance modeling and forecasting is the clear sky model. Fig. 1.1 (a) shows a typical diurnal transient of the GHI time series. Apart from the fluctuations which are primarily caused by the moving clouds, the curve has a bell–shaped trend. The bell–shaped curve is a result of Earth's self rotation. In solar engineering, the bell–shaped curve can be modeled using a clear sky model. I develop a semi–empirical clear sky model for Singapore in chapter 3 based on the atmospheric transfer model. The materials presented in chapter 3 are based on (Yang et al., 2012a, 2014c).

1.2.2 Chapter 4: univariate forecasting using decompositions

A commonly used heuristic in forecasting is time series decomposition. Instead of directly applying the forecasting methods to the time series, the series is first decomposed into several sub–series. After the forecast of each sub–series is obtained, the final forecast is obtained by recombining the individual forecasts. This general framework of "decomposition → forecasting → recombination" is depicted in Fig. 1.2. Time series decompositions often improve forecast accuracy because decompositions help in strengthening or attenuating the signals of different time series components (Kourentzes et al., 2014). Decompositions based on wavelet theory have been proposed to elaborate on such effects (e.g. Michis, 2014; Sudheer and Suseelatha, 2015).

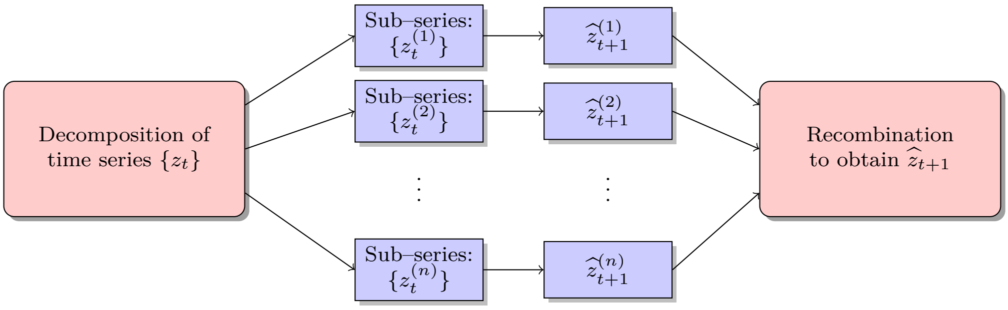

Fig. 1.2 An illustration of forecasting heuristics based on time series decompositions. Let $\{z_t\}$ be the time series of the quantity needs forecast, $\{z_t^{(1)}\} \cdots \{z_t^{(n)}\}$ are n decomposed sub–series. The symbol $\widehat{}$ denotes a forecast.

Following such motivations, three heuristics are proposed in chapter 4 based on knowledge of solar irradiance. Instead of using a general time series decomposition method, such as wavelet or Fourier decompositions, knowledge–based decompositions are considered. Knowledge–based methods have been previously applied in load forecasting (Ho et al., 1990; Rahman and Hazim, 1993). In a book chapter written by Webby et al. (2001), time series forecasting using domain knowledge is discussed from a general perspective. For the specific task of irradiance forecasting, I choose three exogenous parameters for the analyses, namely, direct normal irradiance (DNI), diffuse horizontal irradiance (DHI) and cloud cover index; they are used to decompose the GHI time series. A fundamental univariate forecasting model, namely, the ARIMA (autoregressive integrated moving average) model is used to perform the one–step–ahead predictions. The materials presented in chapter 4 are based on (Yang et al., 2012b, 2015a).

1.2.3 Chapter 5: spatio–temporal kriging

Making generalizations is fundamental to mathematics; forecasting is no exception. Two types of generalizations are discussed in this thesis: (1) generalization of univariate forecasting models to multivariate models and (2) generalization of purely spatial predictive methods to spatio–temporal methods. Chapter 5 considers the later while the former is briefly discussed in chapter 9.

Kriging is a geostatistical interpolation method named after Danie G. Krige who used the method for mineral resources evaluation (Krige, 1951). It is later formalized by Matheron (1963). Most kriging applications are purely spatial, however, kriging formulation can be easily generalized to handle spatio–temporal applications (Cressie and Wikle, 2011). Although there is a rich literature on spatio–temporal kriging in statistics, prior to my publications (Yang et al., 2013b, 2014a), only one conference paper (Inoue et al., 2012) considered spatio–temporal kriging for solar irradiance forecasting. This lack of application is due to three main reasons: (1) some irradiance forecasting methods, such as the satellite–based and sky camera–based methods, are spatio–temporal in nature, (2) the irradiance sensor networks are often spatially sparse and/or have only few sensors; the correlations among the stations are therefore not observed and (3) the field of irradiance forecasting is relatively new, multivariate and spatio–temporal statistics are yet to be exposed and appreciated. Therefore, the kriging framework presented in chapters 5 and 9 is unique to the field of solar engineering[1]. Furthermore, it overcomes several disadvantages of the satellite–based and sky camera–based methods. The materials presented in chapter 5 are based on (Yang et al., 2013b).

1.2.4 Chapters 6 and 7: adding more sensors into the network

Spatio–temporal methods often rely on sensor networks. The sparsity of the network has to be addressed by adding in new stations into the network. This is a network redesign (expansion) problem; I present an entropy–based approach in chapter 8. Beside building new monitoring stations, it is also possible to utilize the existing PV systems as sensors for irradiance and PV output forecasting. This idea is demonstrated by Lonij et al. (2013), where data from 80 rooftop PV systems over a 50×50 km area are used.

PV panels are often installed at inclined surfaces to maximize the energy output of the systems. In order to integrate the PV power output data with horizontal radiometric data, transposition models are essential. A transposition model converts solar irradiance from a horizontal plane to any fixed inclined surface. The schematic diagram of the conversion is shown in Fig. 1.3.

There are several accepted terms describing irradiance components (measured in W/m^2). Global horizontal irradiance (GHI, I_{glo}) refers to irradiance measured on a horizontal surface. It can be decomposed additively into two components: the horizontal beam irradiance (HBI, I_{beam}) and the diffuse horizontal irradiance (DHI, I_{dif}). Sometime, direct normal

---

[1] Shortly after I wrote the Renewable Energy paper with Gu Chaojun, we wrote another paper on load forecasting using kriging. The paper is subsequently published in IEEE Transactions on Power Systems (Gu et al., 2014), showing the wide applicability of kriging.

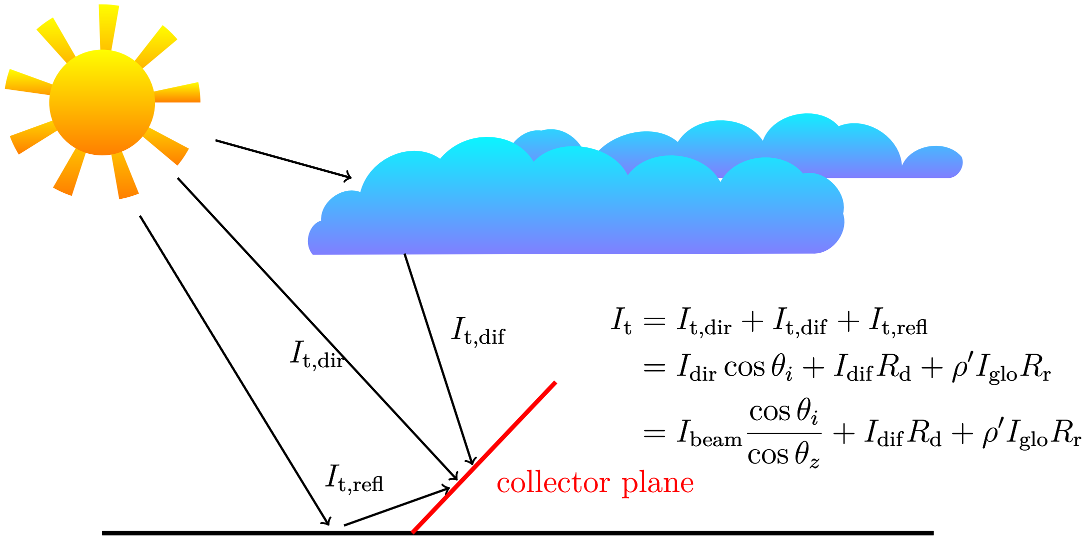

Fig. 1.3 Schematic diagram of various irradiance components received on a collector plane.

irradiance (DNI, I_{dir}) is used instead of HBI. On a tilted surface, tilted global irradiance (I_{t}) can be decomposed additively into the tilted beam irradiance ($I_{\mathrm{t,dir}}$), the tilted diffuse irradiance ($I_{\mathrm{t,dif}}$) and the reflected irradiance ($I_{\mathrm{t,refl}}$). The relationships among the irradiance components are shown in Fig. 1.3. For the time being, R_{d}, R_{r}, ρ', θ_i and θ_z can be treated as known quantities.

Chapter 6 reviews the transposition models. Theoretically, if any two (out of seven) types of irradiance listed above are known, the others can be deterministically calculated through transposition models (Yang et al., 2014d). However, the literature focuses on the horizontal to tilt conversion; there is no reference on the inverse transposition (from tilt to horizontal) beside the pair of papers by Faiman et al. (1987, 1993). In chapter 7, I will show that the assumptions in (Faiman et al., 1987, 1993) are strong, the conversion accuracies are consequently suboptimal.

The materials presented in chapters 6 and 7 are based on (Yang et al., 2013a, 2014d); they are highly original. I summarize the contributions as follows:

- Inverse transposition model using a single reference cell is proposed.
- Ten transposition models and five decomposition models are validated using tropical

irradiance data.

- Anisotropic inverse transposition model using two or more reference cells is proposed.
- Re–parameterization of the Perez model in a tropical environment.

These contributions are more described in the respective chapters.

1.2.5 Chapter 8: network redesign using entropy

The publications on irradiance monitoring network design are surprisingly few. To my knowledge, only five recent journal papers discuss this research problem. Zagouras et al. (2013) uses principle component analysis to reduce the features of a satellite image sequence, the optimal station placement is then found through the k–means clustering algorithm. This method is later extended to similar applications with smaller geographical scales (Zagouras et al., 2014a,b). Yang and Reindl (2015) proposed an alternative clustering–based design using the variance quadtree algorithm. Despite that the methodology adopted in these works is logical, the clustering approach does not support network redesign, i.e., adding stations to the existing networks. There is only one reference which considers the irradiance monitoring network redesign problem. In the recent publication by Davy and Troccoli (2014), a network maintained by the Australian Bureau of Meteorology is redesigned based on uncertainty modeling. Unlike (Davy and Troccoli, 2014) where satellite data and genetic algorithm are used for the redesign of a continental scale network, I consider a metropolitan scale redesign using ground–based data and entropy in chapter 8. The research shown in chapter 8 therefore provides insights and introduces a new dimension to the network design in solar engineering, especially for forecasting applications. The materials presented in chapter 8 are based on a manuscript in progress.

1.2.6 Chapter 9: parameter selection

When considering the aggregation of many PV systems distributed over an area, the transient of the overall energy output is expected to be smoother than the one shown in Fig. 1.1. This is called the geographical smoothing effect; it is well documented in the literature (Curtright and Apt, 2008; Hoff and Perez, 2010; Lave and Kleissl, 2010; Marcos et al., 2012). In general, as the station separation distance increases, the correlation between the irradiance time series collected at two stations reduces. Consequently, as the separation goes beyond a so–called “de–correlation distance”, measurements from the pair of stations become uncorrelated.

The studies on de–correlation distance mostly consider only correlations observed in the along–wind direction. When correlations from all directions are involved, de–correlation distance is usually not seen (Murata et al., 2009). I therefore propose a quantity called the threshold distance which is estimated using correlations from all directions. It is argued in chapter 9 that the data collected beyond the threshold distance provide minimal information to forecasting; they therefore should not be included in a spatio–temporal model. To validate this hypothesis, two spatio–temporal models are used, namely, the time–forward kriging and vector autoregressive (VAR) model. VAR is a generalization of the univariate autoregressive model.

The heuristic herein proposed can be considered as a parameter selection method. Instead of using data from all the stations in the sensor network, only the relevant spatio–temporal neighbors are included in the forecasting model building. In fact, the general idea of parameter shrinkage and selection is ubiquitous in regression analyses. The lasso (least absolute shrinkage and selection operator) is one of the most successful inventions in the literature of regression[2]. I use the lasso to benchmark the proposed selection method. The

---

[2] Lasso is described in this thesis with only minimal sufficient details. There is however a more comprehensive paper on irradiance forecasting using the lasso (Yang et al., 2015b). Data from a dense network of 17 radiometers are used to forecast sub–5–min irradiance. As the motivation therein is different from the motivations of this thesis, I do not include the materials here. However, I strongly encourage the readers to read the lasso paper.

materials presented in chapter 9 are based on (Yang et al., 2014a).

1.3 Data

Data is essential to modeling and forecasting. Beside chapter 4 where typical meteorological year 3 data are used, all other chapters use Singapore data. The choices of datasets are explained in this section. I note that the choices of datasets do not constrain the applicabilities of the proposed methods. All methods proposed and discussed in this thesis are general.

1.3.1 Difference between resource assessment and forecasting

Solar irradiance measurements come from two complementary data sources (Vignola et al., 2012): (1) ground–based instruments and (2) remote sensing satellites. Before the popularization of the satellite–based methods (Perez et al., 2002), the ground–based monitoring networks are the primarily sources for solar resource assessment. For example, Fig. 1.4 shows the New Energy and Industrial Technology Development Organization (NEDO) meteorological network http://app7.infoc.nedo.go.jp/. 834 ground–based weather stations are distributed spatially in Japan. Today, ground–based data are still used to adjust the biased irradiance estimates from satellite–based models (Escobar et al., 2014; Nonnenmacher et al., 2014; Polo et al., 2014).

Although the total number of monitoring stations in the NEDO network is generous, those stations are too sparse to fully capture the fast–changing cloud conditions. Some clouds experience creation, propagation and extinction within the spatial resolution. In fact, most of the networks today are sparse. Other examples of low spatial resolution networks include National Solar Radiation Data Base (NSRDB) http://rredc.nrel.gov/solar/old_data/nsrdb/ and the network in Brazil (Martins and Pereira, 2011). Such networks are useful for resource assessment; they are not suitable for irradiance forecasting.

For the above–mentioned reason, a network of 25 stations in Singapore is used chapters 5,

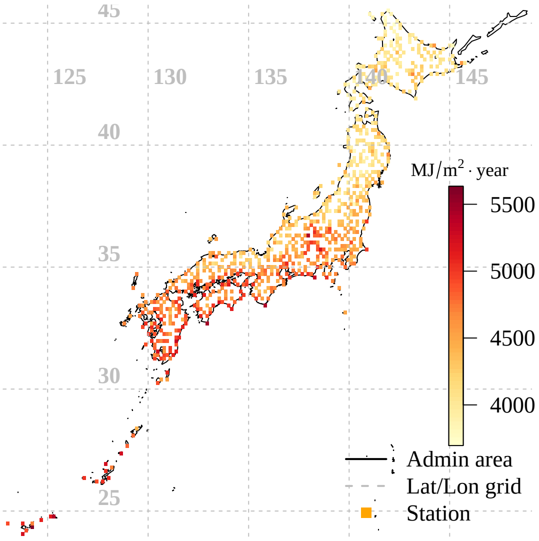

Fig. 1.4 Geographical locations of 834 weather stations in Japan. Each colored pixel denotes a station, with the color indicating the yearly insolation value in MJ/m^2.

8 and 9. Singapore has a total land area of 714.3 km^2; the main island of Singapore measures 50 km in the East–West direction and 26 km in the North–South direction. Fig. 1.5 shows the locations of these 25 stations. The monitoring network was completed in 2013 December. Therefore during the time of publication, not all stations were available[3]. Consequently, partial networks are used in chapters 5 and 9. Nevertheless, chapter 8 demonstrates the full network.

1.3.2 Solar irradiance measuring instruments

The performance of a PV system is determined by two factors, namely, PV system efficiency and weather (Meydbray et al., 2012a). We are therefore interested in two types of measurements: (1) measurement of PV efficiency at reference conditions and (2) solar radiometric measurement.

---

[3] The paper (Yang et al., 2014a) is accepted in 2014 January. As one year worth of data are usually required for publications, only stations built prior to 2013 January are utilized in that study, which is not the full network.

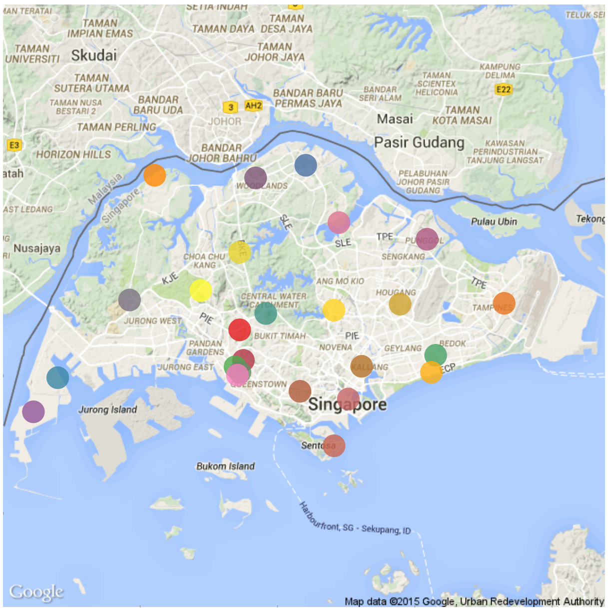

Fig. 1.5 Locations of 25 irradiance monitoring stations in Singapore. Source: Google Maps.

Recall the irradiance components shown in Fig. 1.3, there are three components (I_{dir}, I_{dif} and I_{glo}) on a horizontal surface and four components ($I_{\mathrm{t,dir}}$, $I_{\mathrm{t,dif}}$, $I_{\mathrm{t,refl}}$ and I_{t}) on a tilted surface. These irradiance components can be collected using an instrument called pyranometer (directly or indirectly). Pyranometers are thermopile–based instruments that convert heat to an electrical signal which can then be recorded. A pyranometer is typically used to measure GHI (I_{glo}); if equipped with an additional shadow band to block the direct irradiance, it can also record DHI (I_{dif}); DNI (I_{dir}) can thus be calculated deterministically. Some pyranomters, such as the SPN1 Sunshine Pyranometer, have the capability of measuring GHI and DHI simultaneously. Occasionally for research purposes, pyranometers are used to measure the tilted global irradiance (I_{t}) as well. Instead of measuring the DHI using pyranometers with shadow bands, we can measure DNI using an instrument called pyrheliometer with a solar tracking system that aims the instrument at the sun. Pyranometers and pyrheliometers are used for solar radiometric measurements (Meydbray et al., 2012a,b; Yang et al., 2014b). The price range of industrial-grade pyranometers can reach a few thousand US dollars. Therefore, it is not economic to build sensor networks using such instruments for operational forecasting.

The alternative reference cell is a PV device, which converts a flux of photons directly into an electric current, working similarly to a PV module. Most reference cells are silicon–based; they are less accurate than thermopile–based devices (the major loss mechanisms are discussed in chapter 7. Hundreds of reference cell types are available on the market and are cheaper than pyranometers (about two hundred US dollars). This type of sensor is therefore often used to measure the plane of array irradiance (I_{t}) at a PV site in order to assess the system performance (Meydbray et al., 2012a,b; Yang et al., 2014b); it is also common to install a collection (network) of reference cells within a PV site. To utilize the reference cell data, inverse transposition models (convert irradiance from tilt to horizon) are needed.

Two datasets are used in this thesis to demonstrate the irradiance conversion algorithms. The dataset collected at the first zero energy house in Singapore (FZEHS) is used in chapter 6. It consists of data from one pyranometer and two reference cells. The second dataset comes from the rooftop of SERIS, see chapter 7. It comprises data from two pyranometers and five reference cells. The datasets will be described in details in the respective chapters.

1.4 Error metrics

Error metrics are used to evaluate forecasts and predictions. The International Energy Agency (IEA) developed recommendations for reporting irradiance model accuracy based on three validation metrics: mean bias error (MBE), root mean square error (RMSE) and Kolmogorove–Smirnov integral (KSI)[4] (Beyer et al., 2009; Espinar et al., 2009; IEA, 2012). MBE is given by:

$$\mathrm{MBE} = \frac{1}{N}\sum_{n=1}^{N}\left(\widehat{I}_n - I_n\right) \tag{1.1}$$

---

[4] KSI is used to measure the ability to reproduce the cumulative distributions of measurements.

where $\widehat{I}_n$, $n = 1, 2, \cdots, N$ is the forecast/predicted irradiance (or other quantities being forecast) and I_n is the actual/measured irradiance (quantities). RMSE is given by:

$$\mathrm{RMSE} = \sqrt{\frac{1}{N}\sum_{n=1}^{N}\left(\widehat{I}_n - I_n\right)^2} \tag{1.2}$$

Beside MBE and RMSE, the normalized RMSE (nRMSE) is also frequently used for error display. The nRMSE is in percentage:

$$\mathrm{nRMSE} = \frac{\sqrt{\frac{1}{N}\sum_{n=1}^{N}\left(\widehat{I}_n - I_n\right)^2}}{\frac{1}{N}\sum_{n=1}^{N} I_n} \times 100\% \tag{1.3}$$

For the percentage root mean square error, some authors (e.g. Boyd, 2013) use a centered error metric, i.e.,:

$$\mathrm{cRMSE} = \frac{\sqrt{\frac{1}{N}\sum_{n=1}^{N}\left(\widehat{I}_n - \mathrm{MBE} - I_n\right)^2}}{\frac{1}{N}\sum_{n=1}^{N} I_n} \times 100\% \tag{1.4}$$

When the uncertainty of the forecasts is considered, the expanded uncertainty at 95% confidence interval (U_{95}) is used:

$$U_{95} = k \times \frac{\sqrt{\frac{1}{N}\sum_{n=1}^{N}\left(\widehat{I}_n - I_n\right)^2}}{\frac{1}{N}\sum_{n=1}^{N} I_n} \times 100\% \tag{1.5}$$

where k is a coverage factor, equals to 1.96 for a 95% confidence level. These evaluation indices will be used throughout the thesis, whereby the choices depend on the particular applications.

1.5 Tools used and software sharing policy

All the results shown in this is thesis are computed/simulated using R, a statistical software. Similar to Mathematica and Matlab, R is an integrated suite of software facilities for data manipulation, calculation and graphical display. It has distinct advantages over Mathematica and Matlab in terms of statistical computing and graphics. More information on the software can be found at http://www.r-project.org/.

To address the ability of the scientific community to reproduce and build on research findings reported in this thesis, I would like to share my R code on a case by case basis (such as the code to produce a particular figure or a table). Please contact me at yangdazhi.nus@gmail.com for more information.

1.6 Logic flow and structure of this thesis

The thesis is structured along logical lines of progressive thought. After this introductory chapter presenting the overall motivations and contributions, chapter 2 provides a detailed literature review on the state–of–the–art methods and approaches for solar irradiance forecasting. Chapter 3 is a short chapter describing the most basic irradiance model, namely, the clear sky model. The proposed Singapore local clear sky model will be subsequently used in other chapters. Chapter 4 is devoted to univariate forecasting methods; several decomposition heuristics are proposed to improve forecasts. One of the conclusions from this chapter is that the cloud cover information can improve forecasting accuracy. As clouds are driven primarily by wind, it is logical to consider spatio–temporal forecasting models instead of temporal only (univariate) forecasting models. Time–forward kriging is developed in chapter 5 in a solar engineering context; the spatio–temporal evolution and dependence in solar irradiance random processes are explained through the means of covariance structures. To realize the forecasting algorithm described in chapter 5, data from a sensor network is required. Existing networks are often spatially sparse. A group of two chapters (6 and 7) describe the inverse transposition models which convert irradiance components measured on tilted planes to GHI. Such conversions can potentially increase the number of sensors in a network, and thus improve forecasts. The series continues with chapter 8, where entropy–based network redesign is demonstrated as an alternative approach to improve the network sparsity. Contents presented in chapters 6, 7 and 8 can potentially bring large amounts of data to forecasters. Very often, such information is spread over a large geographical area. However, the spatio–temporal dependence has limits. Chapter 9 develops and verifies two methods defining the threshold distance in an irradiance random field. The temporal threshold is also discussed. The results show that by using parameter selection, the forecast results can be improved.

Chapter 2

Literature review

2.1 Review of solar irradiance forecasting

Before any forecast can be made, data need to be collected. Solar irradiance in nature can be viewed as a random process whose intensity (power per unit area) is a function of both space and time. Any dataset should therefore be considered as a subset of all possible observations that can be made in $\mathbb{R}^d \times \mathbb{R}^1$, where d–dimensions describe space and another dimension describes time. A dataset contains finite samples of irradiance (in one form or another); these samples define the spatio–temporal resolution thus the predictability of the dataset. The links among observational methodologies (e.g., remote sensing, ground instruments, etc), data and forecasts thus become apparent. Forecasting needs at different spatio–temporal scales drive the data collection process thus lead to the development in observational methodologies; observational methodologies determine the available data which then relate to the forecasting skills and choices of forecasting methods.

In the review paper by Inman et al. (2013), the forecasting skills in terms of their applicable time horizontal and spatial resolution based on the current technologies and data are related to the forecasting techniques (see Fig. 2.1). Forecasting techniques can be categorized into 5 classes: 1) forecasting using a wireless sensor network (high spatial proximity); 2) using total sky imagers; 3) using satellite imaging; 4) numerical weather

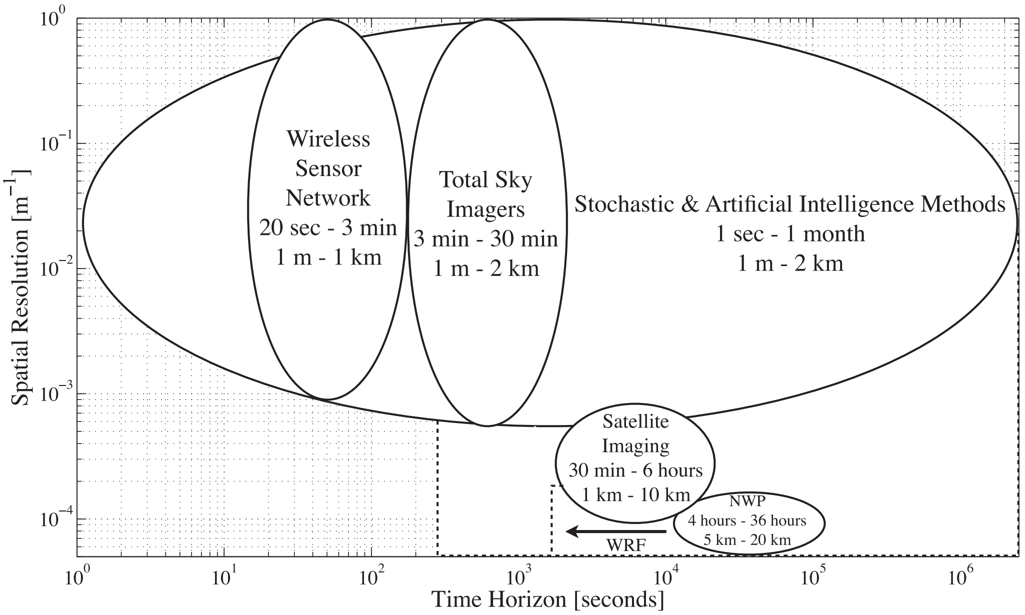

Fig. 2.1 Time horizon and spatial resolution coverages for standard solar irradiance forecasting techniques. Solid lines indicate current limits of techniques while the dashed lines and arrows indicate the future progress of work. Source: Fig. 20 in (Inman et al., 2013). For abbreviations used in the plot, refer to the nomenclature of the thesis.

prediction and 5) using stochastic & artificial intelligence methods (Inman et al., 2013). Other review papers such as (Diagne et al., 2013; Law et al., 2014) categorize forecasting techniques similarly.

2.1.1 Wireless sensor network

A “wireless sensor network” refers to a collection of spatially arranged solar irradiance point sensors. Although the name itself suggests much broader applications, Inman et al. (2013) use the name to describe the irradiance sensing infrastructure for very short–term (a few seconds to 3 minutes) forecasts. Unlike the forecasts with longer horizons where the results are essential for electricity grid operations, the very short–term forecasts find their applications in large photovoltaics (PV) installations. Knowing the potential shading/unshading over a particular section of a PV system in advance may be advantageous to maximum power point tracking algorithms (Hohm and Ropp, 2000). Accurate sub-minute forecasts could also bring possibilities to better control of ramp-absorbing ultracapacitors (Mahamadou et al., 2011; Teleke et al., 2010).

Considering the forecast horizon, the separation of these point sensors needs to be small (a few meters apart). This class of forecasting techniques aims at deriving the information on cloud motion through the sensor networks arranged in designed geometrical configurations. Compared with other forecasting methods, wireless sensor network is new; only a handful of publications are available (see Bosch and Kleissl, 2013; Bosch et al., 2013; Lipperheide et al., 2015; Lorenzo et al., 2014, for examples).

2.1.2 Total sky imager

Beside using data collected by a wireless sensor network, total sky imager (TSI) is also frequently used in very short– and short–term forecasting, mainly due to success of the work by Chow et al. (2011). TSI can be used to forecast both the DNI (Chu et al., 2014; Marquez et al., 2013; Quesada-Ruiz et al., 2014) and GHI (Bernecker et al., 2014; Chow et al., 2011; West et al., 2014). Most research groups use a commercially available TSI such as TSI–800 manufactured by Yankee Environmental Systems (e.g. Chu et al., 2013), while other groups develop their own TSIs (e.g. Yang et al., 2014e).

Sky images are taken sequentially in time; cloud information can be derived from the images through image processing. Template matching algorithms (Li et al., 1994; Sayed, 2009; Wu, 1995) are used to compute the motion vectors describing the cloud movements based on consecutive images. The forecasts can thus be obtained through persisting the motion vectors or more sophistically, by solving the advection–diffusion equation (e.g. Stroud et al., 2010). It is recently reported that forecasting based on deterministic ray tracing method still produces forecasts that are worse than persistence, at 5, 10, 15 min forecast horizons (Chu et al., 2015). In terms of nRMSE, forecast error using TSI varies from 18 to 24% for forecast horizons ranging from 30 s to 15 min (Yang et al., 2014e). Nevertheless, due to its physical–based nature and its potential, TSI–based methods are quickly adopted by many other groups in the past two years not only for irradiance forecasting (e.g. Fu and

Cheng, 2013) but also used for general atmospheric research (e.g. Kazantzidis et al., 2012).

2.1.3 Satellite imaging

The irradiance forecasting methods discussed so far rely on informative local measurements. Such methods have limitations in predicting unobserved locations. The name "local sensing" suggests the need for sampling equipments at every location of interest, which is costly when integrating distributed solar power into electricity grids. Remote sensing provides a solution to the problem (Perez et al., 2007, 2010). Geostationary satellites equipped with radiometers can measure planetary albedo. Ground level irradiance can then be derived (Inman et al., 2013).

Both physical models (e.g. Lacis and Hansen, 1974; Möser and Raschke, 1984) and statistical models (e.g. Justus et al., 1986; Tarpley, 1979) can be used to map the satellite images to irradiance. However, neither approach completes the forecast. To complete the forecast, cloud motion vector algorithms (Cros et al., 2014; Hammer et al., 1999) can be used to obtain the cloud conditions at the next time step (Perez et al., 2002, 2004), mapping is then performed on the forecast images to obtain the future irradiance. An alternative method is to derive the irradiance time series from the satellite images first, stochastic & artificial intelligence methods are then applied on the derived irradiance time series to obtain the forecasts (e.g. Dong et al., 2014). The accuracies of the satellite images–based forecasts can be improved using hybrid systems (e.g. Marquez and Coimbra, 2013).

2.1.4 Numerical weather prediction

Numerical weather prediction (NWP) is another long–lead irradiance forecasting technique. Lorenz et al. (2014) provide a good review on the subject. NWP models consider mechanics and physics (Bjerknes, 1904). The success of a NWP model relies on the knowledge about the initial state of the atmosphere and the physical laws which govern the evolution of the atmosphere (Inman et al., 2013). Well known NWP models include Global Forecast System

(GFS), North American Mesoscale (NAM) model and Weather Research and Forecasting (WRF) model. These models differ from one another in terms of spatial resolution, input parameters and most importantly, the underlying physical models. It is therefore important to choose the forecasting domain, improve data collection and select an NWP system that uses suitable physical models when one attempts to forecast irradiance.

In solar engineering, the physical laws of motion and thermodynamics are rarely scrutinized in detail. As NWP models output hundreds of parameters in each run, irradiance is but one of them, researchers simply run NWP models (Lorenz et al., 2009; Mathiesen et al., 2013; Perez et al., 2013) and study the outputs. As most of the NWP models are not adapted specifically for irradiance forecasting purposes, biased forecasts commonly result. Statistical post–processing such as the application of model output statistics and Kalman filtering are thus used to obtain useful results (e.g. Diagne et al., 2014; Mathiesen and Kleissl, 2011).

2.1.5 Stochastic & artificial intelligence methods

The class of stochastic and artificial intelligence (AI) methods covers the widest ranges in both spatial and temporal domains as shown in Fig. 2.1, owing to the generality of the methods. This class of forecasting methods focuses on input (historical data) and output (forecasts) matching.

Neural networks

The artificial neural network (ANN) is a sub–domain of artificial intelligence (AI). There are many architectures in ANN including multilayer perceptron (MLP), radial basis network, self–organized map, support vector machine and Hopfield networks, and others (Haykin, 2008). These architectures differ from one another greatly. It is however a common perspective that the ANNs are used to perform two types of tasks, namely, regression and pattern recognition. Both of these can be applied in solar irradiance forecasting.

In regression applications, inputs are mapped to outputs in a nonlinear manner. Historical data are used as inputs to an ANN and irradiance of the immediate time steps are the outputs. ANN models therefore take two steps, the training and the forecast. The training phase determines the weights of the artificial neurons and the forecasts are computed based on the trained weights. Similar to regression applications, pattern recognition applications also involve training and testing. Instead of outputting the forecast irradiance, the ANN outputs a natural number representing the classification of objects. For example, we can use ANN to classify the cloud cover index, which is a discrete measure of the opaqueness of the cloud on a scale of 0 (clear) to 10 (opaque).

There is a rich literature on ANN models in solar irradiance forecasting. It is however not the focus of this thesis to discuss the variants in details. Instead, some recent publication patterns in ANN–based forecasts are summarized as follows:

- *Consider exogenous inputs.* It is often recognized that other meteorological and climatological inputs such as temperature and humidity can help improve the irradiance forecasting accuracy. Al-Alawi and Al-Hinai (1998) used climatological variables as inputs to an ANN to predict monthly values of global horizontal irradiance (GHI) over a year. Other examples include (Capizzi et al., 2012; Chow et al., 2012; Sozen et al., 2005).

- *Hybrid ANN with other techniques.* Combining the ANN models with other techniques may improve the forecasting results. Cao and Cao (2006, 2005) combined a recurrent ANN with wavelet analysis for the forecast. Dong et al. (2014) combined self–organized map with exponential smoothing to forecast hourly–ahead irradiance in Singapore. Pedro and Coimbra (2012) combined MLP with evolutionary computing for input selection. Cornaro et al. (2015) combined MLP with model output statistics to improve the forecasts of a NWP model. Other examples include (Cheng et al., 2014; Marquez et al., 2013).

- *Display of new ANN structure in solar irradiance forecasting.* New developments in the evolving field of ANN itself are applied to solar irradiance forecasting. For example, Wu and Chee (2011) applied time delayed neural network; Cao and Lin (2008) applied recurrent wavelet neural network. The dynamic artificial neural network is considered in (Almonacid et al., 2014).

- *Compare various ANN architectures.* Yona et al. (2008) compared MLPs, RNNs, and RBNNs for 24–h–ahead power output forecasting for PV systems. Wu et al. (2014) compared SVM, ANN, and GA for one–hour–ahead PV power forecast. However, these studies can be subjective depending on implementations of the architectures.
- *Regional first report.* Many researchers publish forecasting results with new data from various regions in the world for archive purpose. Azadeh et al. (2009) used MLPs for forecasts for six cities in Iran. Mellit and Pavan (2010) forecast solar irradiance of a grid connected PV plants in Italy. Yap and Karri (2012) forecast global radiation in Australia and compared to a few other techniques.

An evident disadvantage of ANN is its “black–box” nature. The network may determine a desired mapping between input (historical data) and output (forecasts) vectors, but does not provide any information of why a particular input is mapped to a particular output. Despite this criticisms, ANN represents a significant bulk in solar irradiance forecasting. The applications of other AI–based methods such as k–nearest neighbors methods (Paoli et al., 2010), genetic programming (Russo et al., 2014) and fuzzy inference (Huang et al., 2014) are less common than those of the ANN methods.

Statistical models

Another well studied class of irradiance forecasting methods is the class of statistical models, or more specifically, the time series models. Time series considers the so–called “process model”. The process model emphasizes on evolution and dependence. It is described by parameters. Consider equation $z_t = \phi_1 z_{t-1}$ where ϕ_1 is a constant, i.e., the single parameter in this simple model, which can be estimated through fitting. This process is a deterministic process as the value of attribute z at time t is deterministically given by the observation at time $t-1$. However, deterministic processes are rare in environmental data such as solar irradiance time series. Description of the randomness is therefore added into the model, $z_t = \phi_1 z_{t-1} + a_t$ where a_t is the random error of the process at time t. Time series models needs to be built prior to forecasts. Once the model is chosen, parameters can be estimated from historical data, out–of–sample forecasts are then made by "plugging–in" the in–sample values iteratively.

One of the classic statistical forecasting model is the autoregressive integrated moving average (ARIMA) model. It has many variants including autoregressive (AR) model, moving average (MA) model, autoregressive moving average (ARMA) model, ARMA with exogenous variables (ARMAX) model and nonlinear ARMAX model. The ARIMA family is frequently used in solar irradiance forecasting as a benchmark (e.g. Voyant et al., 2011). Reikard (2009) evaluated the performance of ARIMA model at 5, 15, 30, 60 minutes time intervals. Exogenous variables including humidity and cloud cover are also used in that work. Bacher et al. (2009) used AR, ARX and another regressive models.

One of the advantages of the statistical models over the AI–based models is that the statistical models are often intuitive. Consider the ARMA(p, q) model:

$$z_t = \phi_1 z_{t-1} + \cdots + \phi_p z_{t-p} + a_t - \theta_1 a_{t-1} - \cdots - \theta_q a_{t-q} \tag{2.1}$$

where $\phi_1 \cdots \phi_p$ are the autoregressive parameters to be estimated and $\theta_1 \cdots \theta_q$ are the moving average parameters to be estimated. This model has process order (p, q), which indicates that the forecast is a linear combination of observations from p previous steps and the errors from q previous steps. Given the data, the process order can be determined by examining the autocorrelation function and partial autocorrelation function. It is also possible to automate the model building for online forecasting applications through calculating the information criterions.

The exponential smoothing (ETS) family of models is another frequently encountered time series technique (Gardner, 1985, 2006; Roberts, 1982). ETS considers the time series to be a combination of three components, namely, the error (E), trend (T) and seasonal (S) components. It has been shown that many exponential smoothing methods are special cases of the ARIMA model (Abraham and Ledolter, 1983; Box et al., 1994). Although substantial research had been done on the exponential smoothing method, the method was considered as an ad hoc forecasting approach since there was no appropriate underlying stochastic formulation until Hyndman et al. (2002) proposed the state space framework for exponential smoothing. Exponential smoothing received attention in recent years and brought success to forecast in many areas including call centers, energy, financial markets and inventory control (e.g. Taylor, 2004, 2006, 2007, 2008, 2010, 2012a,b; Taylor and Snyder, 2012; Taylor and McSharry, 2007). However, there is only a handful of publications on irradiance forecasting using ETS model (e.g. Dong et al., 2013; Yang et al., 2015a).

Both ARIMA and ETS models are univariate time series models. Forecasts can be obtained using the measurements from a single irradiance monitoring station. This property however reveals the limitation of such models; univariate statistical models only characterize the statistical dependence in time. It is logical to extend such characterization to space. If a univariate time series forecast considers the temporal neighbors as model inputs, spatio–temporal forecasts consider the spatial neighbors as well. This thesis focuses on the applications of spatio–temporal statistical models to the solar irradiance forecasting problem.

2.2 Spatio–temporal statistics: a *very* brief introduction

Before I review the spatio–temporal statistics, some statistical definitions are presented in purely temporal, purely spatial, as well as spatio–temporal frameworks. Appendix A reviews the statistical preliminaries for this thesis.

A **spatio–temporal process** $\{z(\boldsymbol{s};t) : \boldsymbol{s} \in D_s \subset \mathbb{R}^d, t \in D_t \subset \mathbb{R}^1\}$ defines a phenomenon such as solar irradiance which evolves through the spatio–temporal index set $D_s \times D_t$. Both the spatial and the temporal indices can be either continuous or discrete, which give rises to four kinds of spatio–temporal formulations, namely, the continuous space continuous time, continuous space discrete time (time series of **geostatistical processes**), discrete space continuous time and discrete space discrete time (time series of **lattice processes**) formulations.

When D_t is defined as $D_t = \{0, 1, 2, \cdots\}$ instead of $D_t = [0, \infty)$, we have a **time series of spatial processes** $\{z_t(\boldsymbol{x}) : \boldsymbol{x} \in D_s, t = 0, 1, \cdots\}$. At this point, one may immediately link the definition to satellite images, i.e., a geostatistical process sampled at a regular interval. Although such statistical formulations present unique insight to the problem of spatio–temporal prediction, to the author's knowledge, there is no literature on such models in the field of solar energy. Even in the field of statistics, only a handful of researchers explored such models (e.g. Wikle and Cressie, 1999).

On the other hand, when $D_s = \{\boldsymbol{s}_1, \cdots, \boldsymbol{s}_n\}$ and $t = 0, 1, \cdots, T$, we have a n–variate time series $\{\boldsymbol{z}\}$ where $\boldsymbol{z} = \{\boldsymbol{z}_0, \cdots, \boldsymbol{z}_T\}$. In this way, the ARMA$(p, q)$ described in Eqn. 2.1 can be extended into the so–called space–time autoregressive moving average (STARMA) model:

$$\boldsymbol{z}_t = \sum_{k=1}^{p} \boldsymbol{\phi}_k \boldsymbol{z}_{t-k} + \sum_{l=0}^{q} \boldsymbol{\theta}_l \boldsymbol{a}_{t-l} \tag{2.2}$$

where every parameter in Eqn. 2.1 has become a vector or a matrix. The STARMA model and its variant STARIMA model were proposed, described and verified statistically by Deutsch and Pfeifer (1981); Pfeifer and Bodily (1990); Pfeifer and Deutsch (1980a,b,c). STARMA was also applied to solar irradiance forecasting (Glasbey and Allcroft, 2008). In this thesis, one of the variants of the STARMA model, the vector autoregressive (VAR) model, is explored and improved (through means of parameter shrinkage) in chapter 9 in a solar forecasting context.

The STARMA models allow one to forecast solar irradiance at a set of spatial indices simultaneously, i.e., the monitoring stations or the PV systems. However, the model shown in Eqn. (2.2) does not allow prediction on an $(n+1)$th location $\boldsymbol{s}_0$. Consequently, the STARMA family of models cannot handle the problem of off–site predictions. The off–site prediction is important in solar engineering as (occasionally) some of the PV systems do not possess irradiance measurement instruments; predictions at these locations are required for grid integration as well. Other predictive spatio–temporal models are desired. Space–time kriging (also known as spatio–temporal kriging or time–forward kriging) is the suitable tool for predictions at unobserved locations. The principle of space–time kriging lies within the space–time covariance functions.

In the literature of statistics, covariance functions are used to explain space–time coupling. Sherman (2010) reviewed the models for spatio–temporal covariance functions. However, most of the studies on covariance functions are strictly theoretical (De Cesare et al., 2001; Ma, 2003, 2005; Porcu et al., 2006, 2008). To explain the environmental processes, most authors (e.g. Cressie and Huang, 1999; De Iaco et al., 2002; Genton, 2007; Gneiting, 2002; Kyriakidis and Journel, 1999; Stein, 2005) consider the separable and symmetrical approximations as these covariance structures are convenient to model. Non–separable and non–stationary covariance structures were only studied by a few researchers (e.g. Cressie et al., 2010). In this thesis, only the stationary covariance structures are considered; empirical examples of these covariance functions are found in chapters 5 and 9.

The reason for employing the space–time covariance functions is to obtain the covariance at arbitrary settings. In other words, once the distance and time lag between a station pair is known (regardless whether the station is physically present or not), covariance can be read from the fitted covariance function. As covariance structures characterize variations in space and time, it can be used for predictive applications. This class of predictive applications is known as “kriging”.

2.2.1 Space–time kriging

Kriging is briefly introduced in chapter 1. In the kriging method, the variance of the interpolation error is minimized. Kriging was first developed for spatial statistics; it is still recognized as the most promising method for spatial interpolation (e.g. Thiart and Stein, 2013). In solar engineering, various forms of kriging, including simple kriging, ordinary kriging and universal kriging, are often used to interpolate the irradiance conditions at unobserved locations (Alsamamra et al., 2009; Bland and Clayton, 1994; Chen et al., 1994; McKenney et al., 2008; Merino et al., 2001; Moreno et al., 2011; Rehman and Ghori, 2000).

Kriging can be extended to the spatio–temporal case, where the simple kriging predictor $\hat{z}(\boldsymbol{s}_0;t_0)$, the estimate of irradiance z at unobserved location $\boldsymbol{s}_0$ and time t_0, is expressed as a linear combination of historical observed locations:

$$\hat{z}(\boldsymbol{s}_0;t_0) = \sum_{i=1}^{n}\sum_{j=1}^{T_i} w_{ij} z(\boldsymbol{s}_i;t_{ij}) + c = \boldsymbol{W}^\top \boldsymbol{z} + c \tag{2.3}$$

where $\boldsymbol{z} = \left((\boldsymbol{z}^{(1)})^\top, (\boldsymbol{z}^{(2)})^\top, \cdots, (\boldsymbol{z}^{(n)})^\top\right)^\top$ and $\boldsymbol{z}^{(i)} = (z(\boldsymbol{s}_i;t_{ij}) \; : \; j = 1, \cdots, T_i)^\top$ for $i = 1, \cdots, n$ are irradiance data from n locations and T_i previous time steps. $\boldsymbol{W}$ and c can be optimized by minimize the mean squared prediction error. The simple kriging assumes that the mean of the process across space and time:

$$\mu(\boldsymbol{s};t) = \mathbb{E}(z(\boldsymbol{s};t)), \quad \boldsymbol{s} \in D_s, \; t \in D_t$$

is known. Otherwise, ordinary kriging (assuming unknown but constant mean) and universal kriging (assuming the unknown mean is a known function of co–variates, e.g., latitude, longitude) can be used.

Unlike the STARIMA family of models, prior to this thesis, application of space–time kriging in solar irradiance is not found in the literature, except a conference publication by Inoue et al. (2012). However, the space–time kriging method is applied frequently in other fields including agriculture (e.g. Cressie and Majure, 1997), environmental research (e.g. Hartfield and Gunst, 2003; Lophaven et al., 2004), geology (e.g. Bilonick, 1985), geostatistics (e.g. Rouhani and Hall, 1989), and others. Many works were also published in top statistics journals such as Journal of the American Statistical Association (JASA) (e.g. Augustin et al., 2009; Haas, 1995) and Environmetrics (e.g. Haas, 2002; Huang and Hsu, 2004). Its unique ability to forecast unobserved locations give solutions to many previously unsolved problems (Gu et al., 2014). The importance of space–time kriging therefore should not be neglected in the field of solar energy forecasting, especially when good–quality data is lacking.

Chapter 3

Estimation and applications of a Singapore local clear sky model

In this chapter, I analyze Singapore global horizontal irradiance (GHI) measurements and propose an empirical clear sky GHI model for equatorial regions. The empirical formulation simplifies the atmosphere radiative transfer to a single exponential term. The results are benchmarked using locally collected data.

3.1 Introduction to clear sky models

Clear sky is referred to situations where the atmosphere is cloudless. Knowledge of clear sky GHI reaching ground level is a key parameter in the field of solar radiation modeling and evaluation (Ineichen, 2008). There are two approaches to model a clear sky situation, namely, the empirical approach (e.g. Daneshyar, 1978; Haurwitz, 1945, 1946; Ianetz and Kudish, 2008; Kasten and Czeplak, 1980; Paltridge and Proctor, 1976; Robledo and Soler, 2000) and the physical approach (e.g. Gueymard, 1989; Ineichen and Perez, 2002; Yang et al., 2001). When local measurements are made and the relative performance of these models is assessed (e.g. Badescu, 1998; Ianetz et al., 2007; Ineichen, 2006), it transpires that different approaches are optimal in different geographical locations.

Empirical models are bell–shaped functions of time in a day, with model parameters fitted using local clear sky measurements. These models are thus location dependent. Physical models have the advantage of generality and accuracy (Lefevre et al., 2013), but they require more input parameters such as column ozone, column precipitable water and aerosol optical depth which are only measured infrequently and at few locations. For instance, Aerosol Robotic Network (AERONET, http://aeronet.gsfc.nasa.gov) only provides temporal irregular aerosol data for Singapore, which makes the implementation of the physical models unreliable. This chapter therefore aims to develop an empirical clear sky model for the equatorial region. One of key applications of the developed clear sky model is irradiance forecasting. In time series analysis, many models such as autoregressive moving average model (ARMA) require the model inputs to be stationary. Clear sky models are commonly used in irradiance time series detrending. I note that for detrending purpose, the requirement on model accuracy can be slightly relaxed.

Irradiance measurements from two sites, namely, the first zero energy house in Singapore (FZEHS, 1.3094°N, 103.9160°E) and the Solar Energy Research Institute of Singapore (SERIS, 1.3007°N, 103.7718°E) are used. All irradiance measuring devices used in this chapter have an uncertainty of ±5%. Data with time resolution of 5 min are used throughout this chapter.

3.2 Estimation of clear sky irradiance

The goal is to develop the simplest clear sky irradiance model with adequate accuracy.

3.2.1 Model selection

In the literature, many curves or partial curves (e.g. trigonometric functions) are used to model the clear sky irradiance observations. One example of such modeling is given by the Adnot et al. (1979) model:

$$I_{\text{cs}} = a'''(\cos\theta_z)^{b'''} \tag{3.1}$$

where a''' and b''' are regression parameters; θ_z is the zenith angle; I_{cs} is the clear sky GHI. The parameters a''' and b''' control the magnitude and width of the fitting curve respectively. Such models can be improved by including an additional exponential term, as seen in the Robledo and Soler (2000) model:

$$I_{\mathrm{cs}} = a''(\cos\theta_z)^{b''}e^{c''(90-\theta_z)} \tag{3.2}$$

Parameters a'', b'' and c'' are obtained by stepwise regression of $(90-\theta_z)$, $\cos\theta_z$, $\ln(90-\theta_z)$, $\ln(\cos\theta_z)$ and powers of $(90-\theta_z)$ up to fifth degree.

The parameters a''' and a'' can be further decomposed into the product of a deterministic component (extraterrestrial irradiance and solar constant) and a regressive component (fitted by local data), as seen in the Janjai et al. (2011) model:

$$I_{\mathrm{cs}} = a'E_0 I_{\mathrm{sc}}(\cos\theta_z)^{b'}e^{c'\,m_a} \tag{3.3}$$

where

$$\begin{aligned} E_0 =& 1.00011 + 0.034221\cos\Gamma + 0.00128\sin\Gamma \\ &+ 0.000719\cos 2\Gamma + 0.000077\sin 2\Gamma; && (3.4) \\ \Gamma =& 2\pi(d_n-1)/365; && (3.5) \\ m_a =& m_r e^{-0.0001184h}. && (3.6) \end{aligned}$$

$I_{\mathrm{sc}} = 1362\ \mathrm{W/m^2}$ is the solar constant; E_0 is the eccentricity correction factor of the Earth (a dimensionless quantity); Γ is day angle in radians; d_n is day number; h is the altitude in m; m_r is the relative optical air mass (first described by Kasten (1965)) and m_a is the relative air mass with the correction for the effect of the altitude. The term $e^{c'\,m_a}$ is a simple empirical representation of complex physics of radiative transfer. It is similar to a quantity called pseudo–optical depth, which is described by Gueymard and Thevenard (2009). With the above, I propose a modified clear sky model for the equatorial region:

$$I_{\text{cs}} = aE_0 I_{\text{sc}}(\cos\theta_z)^b e^{c(90-\theta_z)} \tag{3.7}$$

3.2.2 Model parameter estimation

A clear sky situation can be identified by using a sky camera (Gueymard, 2012). In situations when a sky camera is not available, a clear sky condition can be selected based on two indices, the **sky's clearness** ε' and the **sky's brightness** Δ', proposed and defined by Perez et al. (1990):

$$\begin{aligned} \varepsilon' &= [(I_{\text{dif}} + I_{\text{dir}})/I_{\text{dif}} + \kappa\vartheta_z^3]/[1+\kappa\vartheta_z^3] && (3.8) \\ \Delta' &= (I_{\text{dif}} m_r)/(E_0 I_{\text{sc}}) && (3.9) \end{aligned}$$

where I_{dif} is diffuse horizontal irradiance (DHI) and I_{dir} is direct normal irradiance (DNI). κ is a constant equal to 1.041 when zenith angle ϑ_z is in radians .

Robledo and Soler (2000) consider the sky to be clear if $\varepsilon' > 5.0$ and sky's brightness $\Delta' < 0.12$. Pattanasethanon et al. (2007) use the condition $\varepsilon' \geq 4.5$ and reference Perez et al. (1993) use $\varepsilon' > 6.0$ to identify clear sky situations. Singapore is very humid throughout the year; a lower GHI is expected in Singapore compared to locations with lower precipitable water vapor. Therefore, a smaller value of ε' is needed to define a clear sky situation in Singapore. I assume that a clear sky situation prevails in Singapore if $\varepsilon' > 3.5$.

One year of 5 min GHI and DHI measurements from the FZEHS from 2011 are used to select possible clear sky time periods using the above criterion; data from SERIS are used for validation. Nonlinear regression is used to fit the parameters in Eqn. (3.7). The fitted parameters are 0.8298, 1.3585 and −0.00135 for a, b and c, respectively, and the modified model for Singapore is given by:

$$I_{\text{cs}} = 0.8298 E_0 I_{\text{sc}}(\cos\theta_z)^{1.3585} e^{-0.00135\times(90-\theta_z)} \tag{3.10}$$

3.2.3 Results

The developed clear sky model is validated using the GHI measured at the SERIS during the year 2012. Fig. 3.1 shows a scatter plot of the measured versus the predicted clear sky GHI. Following Eqn. (1.3), a normalized root mean square error of 5.6% is found. It is observed that some modeled points in Fig. 3.1 deviate far from the measured values. These deviations are due to the misidentifications of the clear sky situations.

A visually straightforward method to validate the clear sky model is superimposing the model with manually identified daily time series with smooth irradiance transients. Fig. 3.2 shows the model performance by comparing it with the SERIS measurements of 11 days selected from years 2011 to 2013. The dotted line gives the maximum value of modeled clear sky GHI. These 11 days are selected manually based on the smoothness of the daily irradiance transients. The model provides an excellent fit to the data.

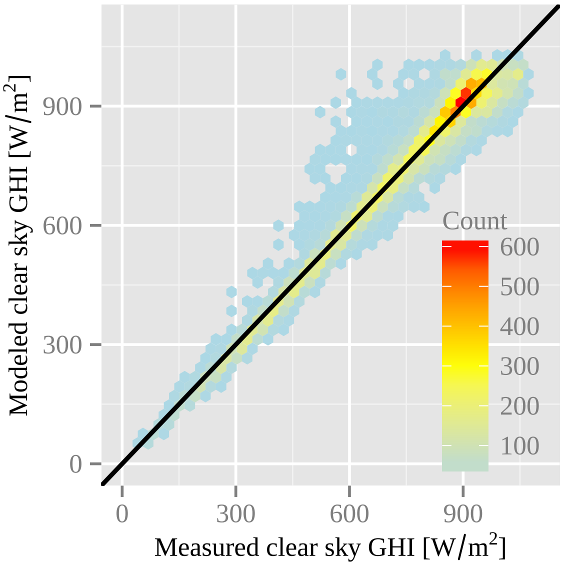

Fig. 3.1 Performance of the modified clear sky model for all clear sky situations at SERIS during year 2012. The hexagon binning algorithm (Carr et al., 2013) is used for visualization.

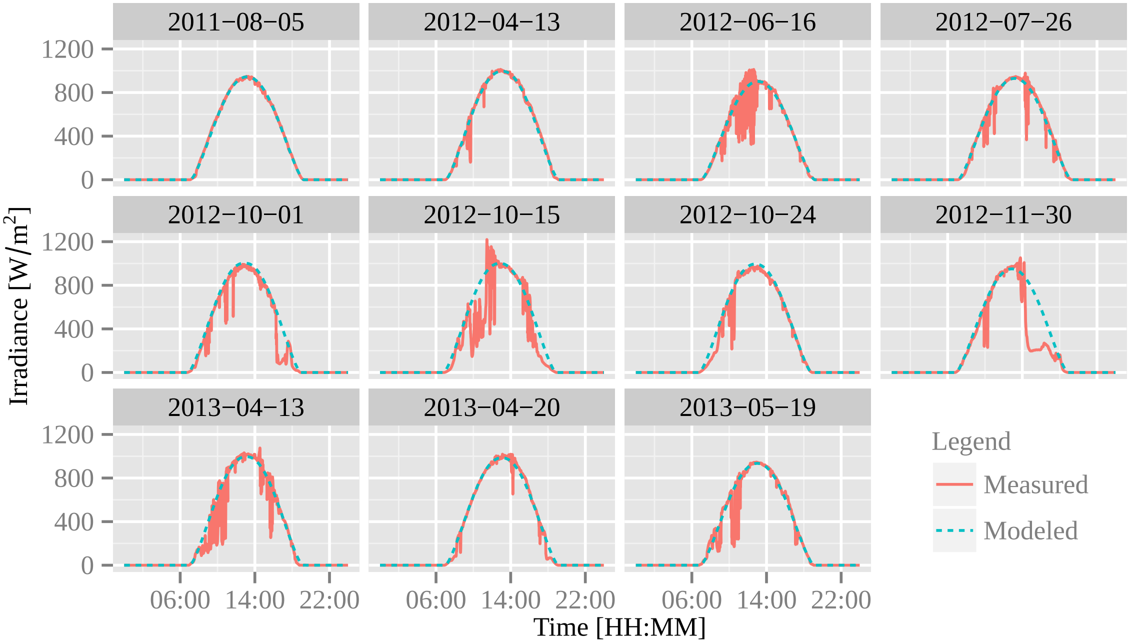

Fig. 3.2 Performance of the modified clear sky model on 11 best clear sky days during the years 2011 to 2013 benchmarked with 5 min SERIS data.

3.3 Chapter conclusion

Singapore local GHI data are used to derive a simple empirical model for clear sky GHI for Singapore. The developed clear sky model approximates the radiative transfer mechanisms with three parameters, namely, a, b and c, which are determined using nonlinear regression with local GHI measurements. The model is simplistic yet provides sufficient accuracy. In my publication (Yang et al., 2014c), two applications of the clear sky model, namely, the missing data handling and detrending, are briefly discussed; I do not reiterate here.

Chapter 4

Time series forecasting using ARIMA and cloud cover index

Clear sky models can be used to detrend the irradiance time series prior to forecast. There are however more general statistical detrending procedures. In this chapter, a seasonal-trend decomposition procedure based on LOESS[1] (abbreviated as STL) is used to decompose the irradiance time series into seasonal, trend and irregular components. A univariate time series analysis technique, the autoregressive integrated moving average (ARIMA) model[2], is explored using the typical meteorological year 3 (TMY3) data (Wilcox and Marion, 2008). Three forecasting methods are proposed using different types of meteorological data as input parameters, namely, global horizontal irradiance (GHI), diffuse horizontal irradiance (DHI), direct normal irradiance (DNI) and cloud cover. The first method applies ARIMA on the STL decomposed GHI time series. The second method forecasts DHI and DNI separately, and then combines the two forecasts to predict GHI. In the third method, an ARIMA model is used to predict discretized cloud cover. GHI at different zenith angles and under different cloud cover conditions is constructed using nonlinear regression, i.e., a look–up table of GHI

---

[1] LOESS is the abbreviation of locally weighted smoothing (or LOcal regrESSion).

[2] In this chapter, the choice of model used for one–step–ahead prediction follows (Yang et al., 2012b). However, other univariate forecasting models can be used. For example, I replace the ARIMA model with exponential smoothing in another paper (Yang et al., 2015a).

regression models is created for different cloud cover conditions. It is found that forecasts using cloud cover information can improve the forecast accuracy.

4.1 Preliminaries

Irradiance forecasting techniques are reviewed in section 2.1. As compared to other methods, the data requirements in stochastic & artificial intelligence methods are more relaxed, which facilitate economic and rapid computation. The majority of methods from this class use ground point sensors such as pyranometers and reference cells.

In the competition between time series models and artificial intelligence models, two models are commonly adopted, namely, the ARIMA model (Martin et al., 2010; Moreno et al., 2011; Reikard, 2009) and the artificial neural networks (ANN) multilayer perceptron model (Martin et al., 2010; Mellit et al., 2010; Paoli et al., 2010). As the forecast abilities of the models arguably depend on implementations, persistence is commonly used to benchmark various forecasting methods. Nevertheless, at 60 min resolution, Reikard (2009) has shown that an ARIMA model dominates all other time series forecasting methods in four out of six test stations used in that study. This chapter thus only explores the ARIMA method.

What distinguishes irradiance forecasting from other forecasting applications is the physical knowledge about the atmosphere. Weather patterns and their accompanying clouds are the most significant atmospheric phenomena affecting solar irradiance at the Earth's surface (Brinsfield et al., 1984), so these must be considered by any irradiance forecasting system.

Many previous studies have developed empirical relationships to relate cloud cover conditions and solar irradiance. Brinsfield et al. (1984); Yaramoglu et al. (1985) studied the impact of scattered clouds on irradiance on an otherwise cloudless day. In these works, large numbers of meteorological data types, such as various irradiance and solar altitude angle, are used to formulate the relationship between cloud cover and solar irradiance. The computation is complex and missing data jeopardize the calculation.

Ehnberg and Bollen (2005) relate the solar elevation angle to insolation under different cloud cover conditions. A total of nine regression lines are constructed to form a look–up table according to nine levels of cloud cover on the standard Oktas scale. The results are tested against stochastically–generated cloud simulations. Luo et al. (2010); Topcu and Oney (1994); Younes and Muneer (2006) relate solar irradiance to cloud cover and zenith angle through regression, while Ododo et al. (1996) develops a relationship between solar irradiance, cloud cover and relative sunshine duration. However, these works do not consider forecasting techniques. Hence in this chapter, methods to forecast hourly solar irradiance including cloud cover effects are proposed.

4.2 Time series analysis

A **time series** is a sequence of observations taken sequentially in time. If the observations are random variables (such as solar irradiance), it is called a **stochastic process**.

4.2.1 The ARIMA model

Recall the ARMA(p, q) model shown in Eqn. (2.1) describing a time series $\{z_t\}$. Define a **backshift operator** $\mathcal{B}$ so that $\mathcal{B}z_t = z_{t-1}$ and more generally $\mathcal{B}^j z_t = z_{t-j}$, Eqn. (2.1) can be then written as:

$$(1 - \phi_1\mathcal{B} - \cdots - \phi_p\mathcal{B}^p)z_t = (1 - \theta_1\mathcal{B} - \cdots - \theta_q\mathcal{B}^q)a_t \tag{4.1}$$

This may be abbreviated even further by writing:

$$\phi(\mathcal{B})z_t = \theta(\mathcal{B})a_t \tag{4.2}$$

where

$$\phi(\mathcal{B}) = 1 - \phi_1\mathcal{B} - \phi_2\mathcal{B}^2 - \cdots - \phi_p\mathcal{B}^p \tag{4.3}$$

$$\theta(\mathcal{B}) = 1 - \theta_1\mathcal{B} - \theta_2\mathcal{B}^2 - \cdots - \theta_q\mathcal{B}^q \tag{4.4}$$

To extend the stationary ARMA model to the ARIMA model which can handle non–stationary time series, the **difference operator** $\nabla = 1 - \mathcal{B}$ is defined or, more generally, $\nabla^d = (1 - \mathcal{B})^d$. Consider the first differences of the series, i.e., $y_t = z_t - z_{t-1}$. This can be re–written as:

$$y_t = (1 - \mathcal{B})z_t = \nabla z_t \tag{4.5}$$

If an ARMA model is constructed using the differenced time series y_t, i.e, $\phi(\mathcal{B})y_t = \theta(\mathcal{B})a_t$, it is equivalent to the ARIMA$(p, 1, q)$ model constructed using the original time series z_t, i.e., $\phi(\mathcal{B})\nabla z_t = \theta(\mathcal{B})a_t$. Generalization of the equation gives the ARIMA(p, d, q) model:

$$\phi(\mathcal{B})\nabla^d z_t = \theta(\mathcal{B})a_t \tag{4.6}$$

where p, d and q are **process orders**.

The order of an ARIMA model can be determined by examining the autocorrelation and partial autocorrelation functions (Box et al., 1994). However, such a model selection process is not suitable for automated forecasting systems. The alternative is to use information criterions for model selection. One particular example of information criterion is called the Akaike information criterion (AIC) (Ricci, 2005). AIC can be computed based on the maximum likelihood estimate of the innovations[3] variance, the length of the time series and the total number of parameters to be fitted. The best ARIMA model will thus be chosen based on the AIC. I implement my models using the forecast package (Hyndman et al., 2014) in R (R Core Team, 2014) and later in this chapter the polynom package (Venables

---

[3] The **innovations** are the differences between the observed values of z_t and the optimal forecasts of those values.

et al., 2009) is also used.

4.2.2 Input parameters and model selection

At the beginning of this chapter, four input parameters for our time series analysis are introduced. GHI is used for our first model. DNI and DHI are used for the second model and cloud cover is used for the third model.

Solar irradiance inputs

Prior to the forecasts, time series decomposition is considered for trend removal. Fig. 4.1 shows an example of the diurnal cycle of the GHI during 2004 December. By using the STL (Cleveland et al., 1990), a time series can be decomposed into seasonal, trend and irregular components. STL is a seasonal-trend decomposition procedure based on LOESS (the locally–weighted regression); it is an iterative filtering procedure. The seasonal component is found by smoothing the seasonal sub–series (e.g. the series of all solar noon values). In each iteration of the STL, the moving average smoothing and LOESS smoothing (Cleveland et al., 1988) are used multiple times. I do not repeat the detailed procedures here; interested readers can refer to the original publications. The decomposition of solar irradiance time series is additive instead of multiplicative. The data used in this chapter are hourly, giving a seasonal component with a period of 24. After the time series is decomposed, the seasonal (diurnal) cycle is subtracted from the original solar irradiance time series, so that the residual is the sum of trend and irregular components. ARIMA is then applied on the residual time series to create a forecast.

Cloud cover inputs

As cloud cover does not have a diurnal pattern, the ARIMA model can be directly applied to the cloud cover index time series. Continuous data are used during the model building to preserve the temporal behavior of cloud transients. However, when I develop the regression

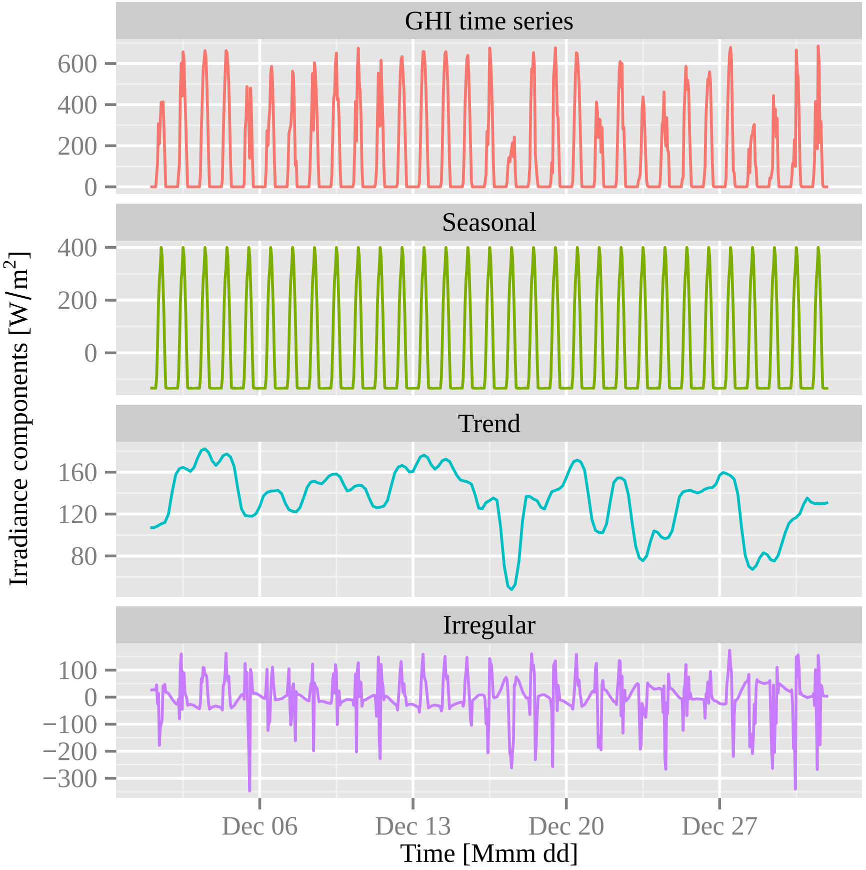

Fig. 4.1 The decomposition of GHI for Miami 2004 December, with irradiance in W/m^2 on the ordinate and day of the month on the abscissa. The top plot is the observed irradiance. The remaining plots show the seasonal, trend and irregular components respectively.

lines for irradiance using cloud cover and zenith angles (details in section 4.3), only daytime values of cloud cover data are used, as night time irradiance is known to be zero. Due to the uncertainties in cloud formation and movement, the time series process orders should be dynamic. Similar to the earlier forecasting models, an ARIMA model is selected and built prior to each point forecast.

4.3 Forecasting models

TMY3 data from http://rredc.nrel.gov/solar/old_data/nsrdb/ are used. The TMY3 data provide an annual dataset that holds hourly meteorological values that typify conditions at a specific location over a longer period of time, such as 30 years. The dataset provides a large variety of hourly meteorological parameters such as solar irradiance components (GHI, DNI and DHI), cloud cover, temperature, humidity, etc. Linear regression analyses were carried out to test for statistical significance of the seven co–variants in relation to GHI.

The backward elimination method (Faraway, 2002) is used to select the most relevant parameters by examining the p–values. In regression, the p-value for each term tests the null hypothesis that the coefficient is equal to zero. The parameter (predictor) with highest p–value greater than 0.001 is removed. The elimination process stops when all the parameters are statistically significant. Table 4.1 shows the p–values of selected seven meteorological parameters throughout the selection process. The raw data sets used in these regression models are Orlando 2005 October, and Miami 2004 December. Three meteorological parameters show high relevancy to global horizontal irradiance: DNI, DHI and cloud cover.

Table 4.1 p–values for linear regression models for Orlando 2005 October, and Miami 2004 December using backward elimination. Eliminated parameters are represented by —.

		Meteorological parameters						
	Step	Diffuse irradiance	Direct irradiance	Cloud cover	Dry-bulb temperature	Pressure	Wind speed	Relative humidity
Orlando	1	$< 2 \times 10^{-16}$	$< 2 \times 10^{-16}$	5.13×10^{-8}	0.083	0.128	0.040	0.311
	2	$< 2 \times 10^{-16}$	$< 2 \times 10^{-16}$	7.00×10^{-8}	0.070	0.044	0.052	—
	3	$< 2 \times 10^{-16}$	$< 2 \times 10^{-16}$	3.69×10^{-8}	—	0.010	0.109	—
	4	$< 2 \times 10^{-16}$	$< 2 \times 10^{-16}$	6.21×10^{-8}	—	0.007	—	—
	5	$< 2 \times 10^{-16}$	$< 2 \times 10^{-16}$	5.32×10^{-7}	—	—	—	—
Miami	1	$< 2 \times 10^{-16}$	$< 2 \times 10^{-16}$	2.69×10^{-6}	0.584	0.712	0.731	0.948
	2	$< 2 \times 10^{-16}$	$< 2 \times 10^{-16}$	1.03×10^{-6}	0.583	0.705	0.734	—
	3	$< 2 \times 10^{-16}$	$< 2 \times 10^{-16}$	1.04×10^{-6}	0.592	0.754	—	—
	4	$< 2 \times 10^{-16}$	$< 2 \times 10^{-16}$	1.05×10^{-6}	0.657	—	—	—
	5	$< 2 \times 10^{-16}$	$< 2 \times 10^{-16}$	5.49×10^{-7}	—	—	—	—

Global horizontal irradiance I_{glo} is represented by the sum of the vertical component of DNI and DHI; the equation is called the **closure equation**:

$$I_{\mathrm{glo}} = I_{\mathrm{dir}} \cos \theta_z + I_{\mathrm{dif}} \tag{4.7}$$

where I_{dir} is DNI, I_{dif} is DHI and θ_z is the zenith angle. The $I_{\mathrm{dir}} \cos \theta_z$ term gives the vertical

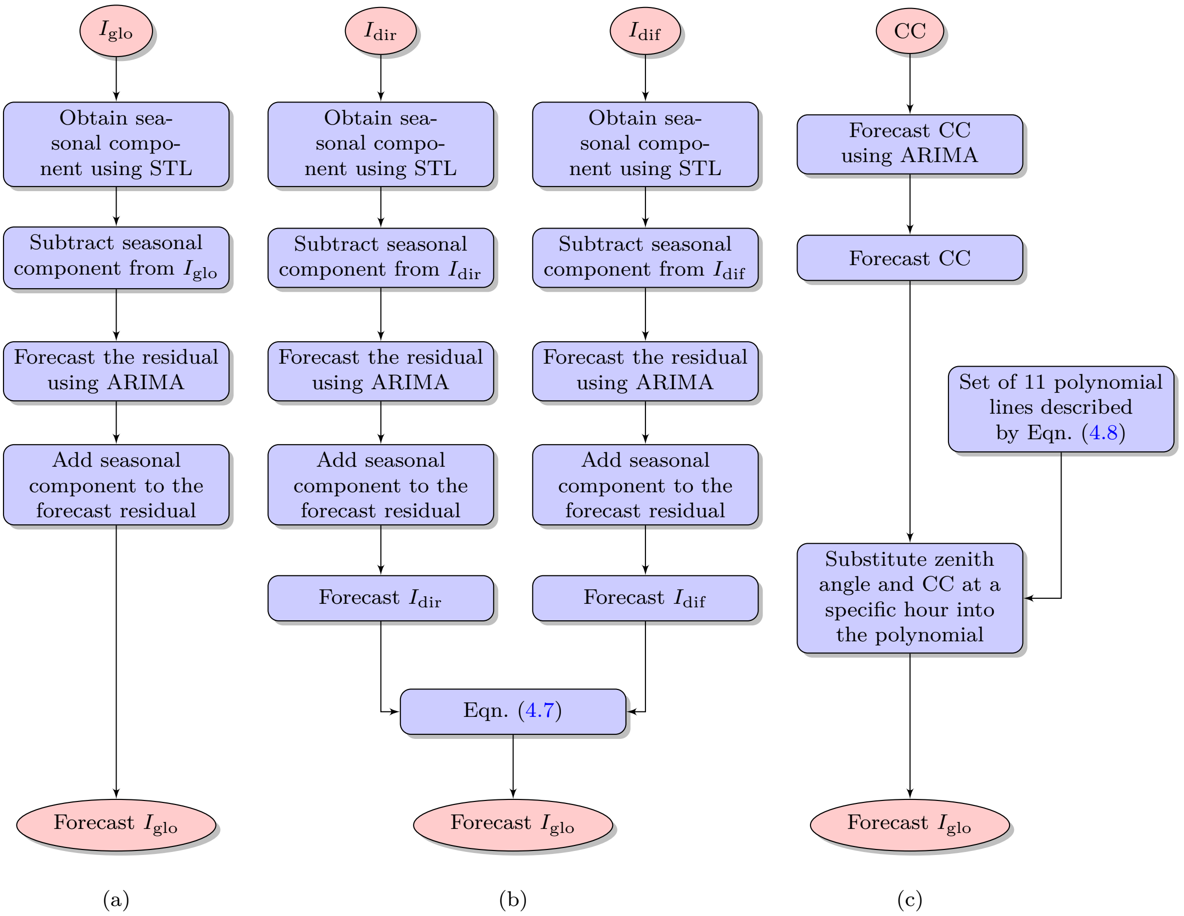

Fig. 4.2 Flow chart of forecasting methods: (a) use irradiance to forecast next hour solar irradiance through decomposition and ARIMA; (b) forecast DNI and DHI separately using decomposition and ARIMA model, the forecasts are then combined using Eqn. (4.7) for forecast GHI; (c) use ARIMA to predict the cloud cover; retrieve the forecast GHI using forecast cloud cover and zenith angle using Eqn. (4.8).

component of DNI. When separate forecasts are made on DNI and DHI, the results can be used to reconstruct GHI.

Since the four meteorological parameters can be related by considering the TMY3 data set, three forecast models are proposed. Fig. 4.2 shows the flow chart of the three proposed models.

Model 1

In this model, I follow the standard detrend → forecast → reconstruct procedure for solar irradiance forecasting. GHI time series is first decomposed into three additive components, namely, the seasonal, trend and irregular components. The seasonal component (diurnal irradiance pattern) is then subtracted from the measured GHI. The residual of this subtraction (trend component plus irregular component) is used as inputs to forecast for the next hour's residual through ARIMA. The final step is to add back the seasonal component to the forecast residual time series to obtain the forecast GHI.

Model 2

In the second model, two separate decompositions are carried out for DNI and DHI time series respectively. The two residual time series are then used as inputs for ARIMA models. The forecast DNI and DHI are then recombined through the closure equation shown in Eqn. (4.7) to obtain the GHI forecast.

Model 3

The third proposed model considers cloud cover. Regression analysis is adopted to analyze the relationships between cloud cover and GHI. Cloud cover data quantify the amount of sky covered by clouds at each time step. Fig. 4.3 shows a scatter plot of I_{glo} versus cosine of zenith angle at each discretized cloud cover condition for our TMY data. Note that the opaque cloud cover used in the plot axis is the amount of sky dome covered by clouds or obscuring phenomena that prevent observing the sky or higher cloud layers at the time indicated (Wilcox and Marion, 2008). It is hypothesized that under different cloud cover conditions, GHI follows higher order polynomials of cosine of zenith angle at a specific time. By inspecting the GHI transient with zenith angle, a quadratic polynomial may not be sufficient to describe the cloud–zenith relationship, while polynomial of order four and above may overfit the data. Therefore I use a polynomial of order three.

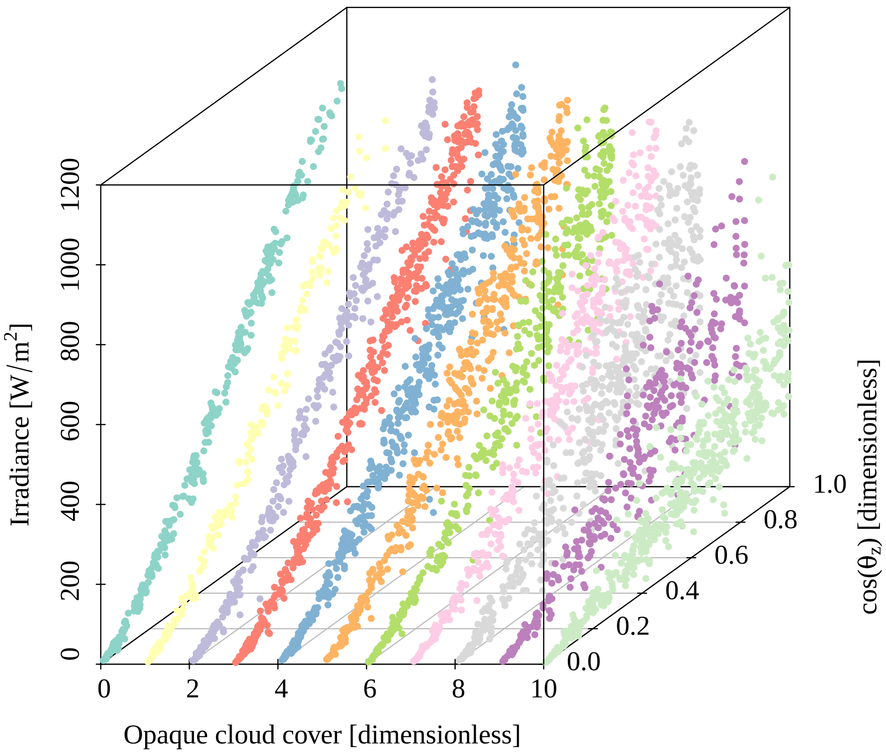

Fig. 4.3 Scatter plot of I_{glo} versus cosine of zenith angle at each cloud cover condition.

To confirm the hypothesis, linear regression of $\cos\theta_z$ up to fifth degree is performed. Table 4.2 reports the p–values of the linear regression models. Polynomials of order four and five yield insignificant parameters. Although several insignificant parameters are reported for third order polynomials, they shall be used to preserve regression models' consistency for all cloud cover conditions. The polynomial selected to correlate GHI and the zenith angle is therefore given by:

$$I_{\mathrm{glo}} = \alpha_0 + \alpha_1 \times \cos\theta_z + \alpha_2 \times \cos^2\theta_z + \alpha_3 \times \cos^3\theta_z \tag{4.8}$$

where α_0, α_1, α_2 and α_3 are regression parameters. Following Eqn. (4.8), a set of 11 regression lines are constructed. These 11 regression lines correspond to 11 cloud cover

Table 4.2 p–values of linear regression models of higher order polynomials using the TMY3 Miami data set.

	Parameters of polynomial of order 3: $I_{\text{glo}} = \alpha_0 + \alpha_1 \times \cos\theta_z + \alpha_2 \times \cos^2\theta_z + \alpha_3 \times \cos^3\theta_z$			
Cloud cover	α_0	α_1	α_2	α_3
0	0·223	$5{\cdot}85\times10^{-15}$	$< 2{\cdot}0\times10^{-16}$	$< 2{\cdot}0\times10^{-16}$
1	0·985	$1{\cdot}66\times10^{-4}$	$< 2{\cdot}0\times10^{-16}$	$< 2{\cdot}0\times10^{-16}$
2	0·075	$5{\cdot}11\times10^{-10}$	$3{\cdot}42\times10^{-14}$	$1{\cdot}32\times10^{-10}$
3	0·079	$1{\cdot}09\times10^{-10}$	$4{\cdot}34\times10^{-9}$	$1{\cdot}63\times10^{-6}$
4	0·235	$9{\cdot}17\times10^{-6}$	$1{\cdot}51\times10^{-4}$	$3{\cdot}94\times10^{-3}$
5	0·593	$3{\cdot}40\times10^{-3}$	$1{\cdot}45\times10^{-4}$	$1{\cdot}38\times10^{-3}$
6	0·657	0·327*	$1{\cdot}02\times10^{-4}$	$1{\cdot}00\times10^{-3}$
7	0·684	0·024	0·028	0·105*
8	0·881	0·392*	$3{\cdot}4 \times 10^{-3}$	$3{\cdot}27\times10^{-3}$
9	0·791	0·209*	0·068*	0·038
10	0·347	$3{\cdot}21\times10^{-4}$	0·545*	0·399*

	Parameters of polynomial of order 4 $I_{\text{glo}} = \alpha_0 + \alpha_1 \times \cos\theta_z + \alpha_2 \times \cos^2\theta_z + \alpha_3 \times \cos^3\theta_z + \alpha_4 \times \cos^4\theta_z$				
Cloud cover	α_0	α_1	α_2	α_3	α_4
0	0·191	$1{\cdot}03\times10^{-5}$	0·012	0·559*	0·561*
1	0·334	$1{\cdot}37\times10^{-3}$	0·061*	0·852*	0·124*
2	0·990	0·194*	$8{\cdot}91\times10^{-5}$	0·008	0·057*
3	0·550	0·040*	$9{\cdot}17\times10^{-3}$	0·104*	0·284*
4	0·713	0·165*	0·069*	0·250*	0·417*
5	0·749	0·203*	0·250*	0·617*	0·904*
6	0·857	0·227*	0·765*	0·670*	0·403*
7	0·820	0·754*	0·160*	0·301*	0·394*
8	0·711	0·301*	0·928*	0·710*	0·471*
9	0·565	0·668*	0·107*	0·162*	0·246*
10	0·978	0·454*	0·376*	0·326*	0·275*

	Parameters of polynomial of order 5 $I_{\text{Glo}} = \alpha_0 + \alpha_1 \times \cos Z + \alpha_2 \times \cos^2 Z + \alpha_3 \times \cos^3 Z + \alpha_4 \times \cos^4 Z + \alpha_5 \times \cos^5 Z$					
Cloud cover	α_0	α_1	α_2	α_3	α_4	α_5
0	0·618	0·077*	0·083*	0·334*	0·428*	0·392*

Note: $*$ denotes parameter is statistically insignificant at a level of 0.05.

possibilities (on the 0 to 10 scale), and thus a look–up table is created.

With the help of this look–up table, once the next hour cloud cover is determined using ARIMA model, the next hour's GHI forecast can be obtained by substituting the zenith angle at the forecast hour into the corresponding regression line.

4.4 Empirical study and discussion

To test the veracity of the three models proposed, two case studies are made. Data from Miami (25°47′16″ N, 80°13′27″ W) and Orlando (28°32′37″ N, 81°22′22″ W) are used in this section. All the forecast values are true out–of–sample forecasts with a one–week moving window as fitting data. The TMY3 data set consists of twelve months from different years, thus, each month is taken as an individual data set for forecasting purposes.

Forecast using model 1

Using the techniques introduced earlier, GHI is used as model input to perform the forecast. Forecasting for the entire TMY data set is carried out. The model is trained using the first week of each month to obtain the decomposed series. Residuals are then obtained by subtracting the fitted seasonal trend from the remaining data from that month. After that, ARIMA process orders and parameters are selected and trained using the first week's residual time series based on AIC. The trained model will produce a single point forecast. For the next time step, model is rebuilt with the "new" measurement which just became available. This procedure is repeated for the entire month. The final step is to add the diurnal pattern to the forecast residual series to obtain the forecast irradiance.

Forecast using model 2

The iterative procedures of DNI and DHI forecast is identical to the forecast for GHI. However, in this model, DNI and DHI are used individually as model inputs.

Forecast using model 3

Look–up tables are developed according to method described in section 4.3. The empirically determined coefficients using the complete TMY3 data set for Miami is shown in Table 4.3. Similarly, the regression coefficients for Orlando can be fitted.

In Fig. 4.4, GHI is represented as a function of the zenith angle for all 11 possible values of cloud coverage. The topmost regression line shows a situation when cloud cover is zero; whereas the bottommost regression line shows a situation when cloud cover is 10. Regression lines representing cloud cover indices 1–9 fall inbetween the two lines.

After constructing this look–up table, ARIMA forecast is applied on cloud cover time series. After obtaining the cloud cover forecast, by searching the table using the forecast

Table 4.3 Regression coefficients for Miami. α_0 to α_3 are the regression coefficients.

Cloud cover	α_0	α_1	α_2	α_3
0	−6·963	441·948	1462·358	−868·380
1	0·106	237·797	1882·965	−1215·547
2	−11·997	413·974	1213·413	−667·429
3	−13·465	477·583	1021·191	−544·869
4	−13·692	457·286	898·256	−440·671
5	−7·689	365·900	1066·004	−566·029
6	8·198	154·058*	1355·005	−712·482
7	−7·615	359·399	778·865	−361·263*
8	3·365	166·766*	1279·514	−810·311
9	−6·369	258·566	840·045*	−601·780*
10	−12·134	406·799	−155·162*	139·128*

Note: $*$ denotes parameter is statistically insignificant at a level of 0.05.

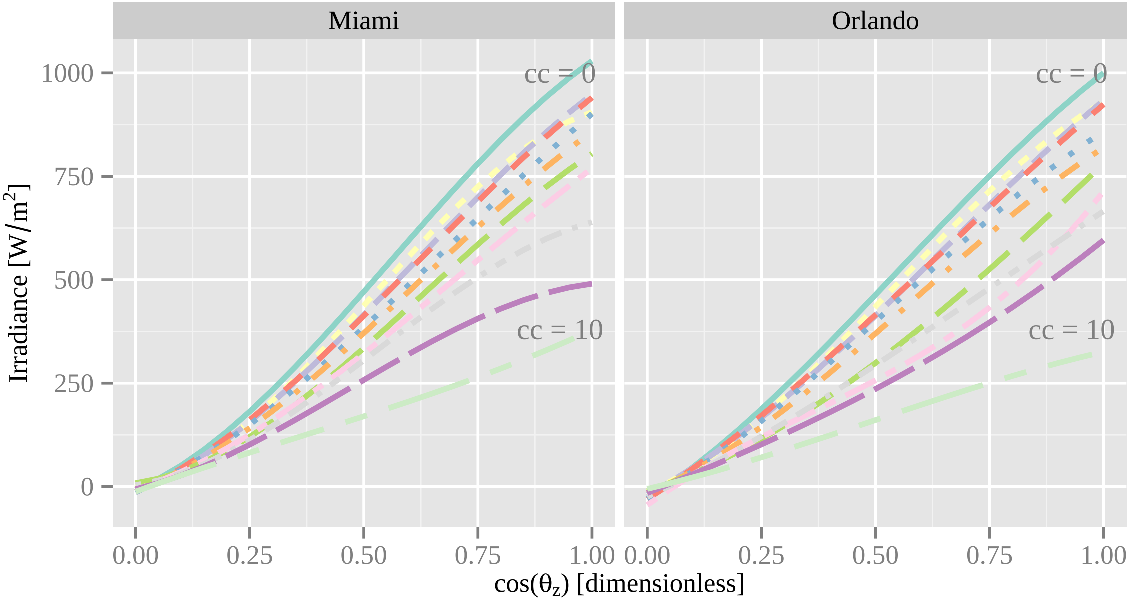

Fig. 4.4 The relationship between irradiance and the zenith angle at different cloud coverage (cc) following Eqn. (4.8).

cloud cover and the respective zenith angle, we can obtain the GHI forecast.

4.4.1 Discussion

The error metric used to evaluate the forecast is the normalized root mean square error following Eqn. (1.3). Table 4.4 shows the nRMSE for all three models using Miami and Orlando data. Overall values recorded in the last row of each table are obtained using the sum of the products of the number of forecast days in a month and the monthly mean values. The total is then divided by total forecast days, which is 281 days in this case.

Table 4.4 Forecast nRMSE (in %) for hourly TMY3 data at selected sites

	Mean observed I_{glo}	nRMSE for Miami			
Fcst Period	(W/m^2)	Model 1 (%)	Model 2 (%)	Model 3 (%)	Persist. (%)
1995 January 8-31	329.67	24.98	22.36	**17.88**	41.00
1981 February 8-28	354.93	23.90	22.19	**21.36**	40.93
1988 March 8-31	414.93	27.44	26.79	**21.47**	40.04
2001 April 8-30	455.80	29.66	29.92	**27.84**	41.72
1990 May 8-31	392.78	28.54	25.23	**20.92**	38.50
1978 June 8-30	382.57	32.40	**31.17**	33.29	42.13
1990 July 8-31	404.75	22.89	23.42	**21.86**	37.62
1994 August 8-31	421.61	25.91	24.95	**23.82**	38.50
1978 September 8-30	387.54	33.03	31.32	**28.09**	43.96
1994 October 8-31	359.95	28.49	27.88	**25.92**	44.58
1977 November 8-30	287.14	28.63	28.57	**26.54**	46.24
2004 December 8-31	296.22	36.60	36.85	**34.45**	52.03
overall	374	28.43	27.45	**25.29**	42.27
	Mean observed I_{glo}	nRMSE for Orlando			
Fcst Period	(W/m^2)	Model 1 (%)	Model 2 (%)	Model 3 (%)	Persist. (%)
1995 January 8-31	281.99	31.78	28.63	**23.07**	44.63
1991 February 8-28	328.05	33.03	30.67	**26.01**	45.77
2001 March 8-31	380.46	35.76	**33.49**	38.83	46.47
1998 April 8-30	485.73	21.99	**22.20**	23.02	33.48
1994 May 8-31	447.92	22.42	21.64	**20.74**	36.44
1996 June 8-30	352.85	37.22	33.46	**32.73**	45.44
1991 July 8-31	370.62	30.02	29.43	**29.11**	42.98
2003 August 8-31	387.51	42.88	**42.27**	42.39	52.87
1999 September 8-30	361.19	39.03	36.95	**36.85**	49.62
2005 October 8-31	344.16	36.42	34.97	**28.95**	49.62
2001 November 8-30	340.65	27.77	**25.84**	30.31	41.80
1996 December 8-31	263.35	34.33	32.92	**27.44**	49.56
overall	362	32.27	30.71	**29.95**	44.36

Persistence is used as a benchmark to our proposed models. A persistence model is simply the assumption that the value for the next time step is the same as the present value. The nRMSE of the persistence model is shown in the last column of Table 4.4. It is found from the table that all three proposed models have significantly lower nRMSE than the persistence model. Among the three models, model 3 has the lowest nRMSE, followed by model 2.

As the nRMSE only shows the overall performance of the models for each month, some daily error analyses can help understand the strengths and weaknesses of each model. It was shown that the accuracy of model 3 depends on the cloud cover data quality (Yang et al., 2015a). It is therefore important to consider the cloud cover data acquisition in terms of accuracy and frequency. Further error analyses can be found in (Yang et al., 2012b) as well.

4.5 Chapter conclusion

Univariate time series model ARIMA is explored in this chapter. Knowledge–based decompositions are considered to further improve the performance of the ARIMA model in the field of solar energy. Three forecasting models are proposed based on GHI decompositions using the STL, closure equation and cloud cover information. All three models show that knowledge based decompositions improve the forecasting accuracies from persistence models. It is worth noting that the forecasts made using model 3 are more accurate in general than models 1 and 2. From a physical point of view, this is expected as the exogenous input (cloud cover index) is considered. As mentioned earlier, cloud coverage is the most important cause of fluctuation in solar irradiance. Due to the continuous nature of the cloud cover time series (even during the night), model 3 is able to preserve the temporal behavior of cloud transients, thus it leads to better forecasts. The merit of the third method is that it only requires low–resolution cloud cover data to improve forecasting.

Chapter 5

Spatio–temporal covariance structures and time–forward kriging

In the previous chapter, the univariate model ARIMA is studied and expanded for solar irradiance forecasting. It was shown that incorporating cloud cover information into the forecasting system can improve the forecast. In fact, as the clouds propagate through space driven primarily by wind, correlative events will occur at neighboring stations. In other words, nearby stations can contribute to the forecasts at the current station. In view of this fact, I consider the spatio–temporal forecast in this chapter.

Statisticians consider properties such as stationarity, full symmetry and separability when modeling spatio–temporal datasets. None of these properties obtain in meteorological data such as wind velocity fields and solar irradiance distributions. In this chapter, a statistical forecast system is constructed to mitigate this problem. Temporal stationarity is first achieved by detrending solar irradiance time series at individual monitoring stations. Spatial stationarity is then approximated through deformations of the geographical space. Various spatio–temporal covariance structures are formed to explore full symmetry and separability (see Appendix A for definitions). Finally, time–forward kriging is used to forecast the hourly spatio–temporal solar irradiance data from 10 Singapore stations. The proposed system is also able to forecast irradiance at arbitrary spatial locations within a monitored area, as mentioned in chapter 1.

5.1 Chapter introduction

Univariate time series models can give acceptable forecasting accuracy; however, they do not provide spatial information. For grid integration, point sensors are required at each PV system site to produce forecasts for these systems. A large number of monitoring stations is therefore required over the area of a power grid. The number of sensors is generally limited and their distribution is irregular. Thus, spatio–temporal estimation for solar irradiance is an important step towards the forecast required by future renewable energy driven cities.

Spatial and temporal behaviors of solar irradiance are related through complex atmospheric mechanisms. Recent advances in space–time statistics (e.g. Cressie and Wikle, 2011; Finkenstadt et al., 2006; Le and Zidek, 2006) allow us to analyze such environmental processes not only in separate temporal and spatial domains, but as a whole. Along this track, little work has been done in the field of solar engineering. Most studies employ separate modeling despite aiming to study solar irradiance across time as well as space (e.g. Glasbey et al., 2001). There are works which provide explanations to spatio–temporal variability in global radiation (Gueymard and Wilcox, 2011), however a long–term (inter–annual) study does not contribute to forecasting applications. This chapter thus aims to develop statistics that describe the spatio–temporal process.

5.1.1 Anisotropy and time–forward kriging

The statistical properties introduced in appendix A indicate that using statistical prediction methods requires careful analytical description and analysis of a dataset. For example, in geostatistics, 2D linear least squares estimation is often performed using kriging algorithms to construct 2D contour images, such as irradiance maps. Rehman and Ghori (2000) plot monthly irradiance contours for Saudi Arabia; Righini et al. (2005) develop contours for Argentina; Bland and Clayton (1994) for Wisconsin and Bechini et al. (2000) for northern

Italy. These authors first identify a variogram model for the region and then apply weighted spatial smoothing kriging techniques to perform the spatial prediction.

Spatial resolution, an important consideration in all spatio–temporal irradiance studies, is often limited by data sparsity. In the context of solar irradiance, it has been shown that the spatial correlation between two locations cuts off at the de–correlation distance (Perez et al., 2012). The dependence metrics used in kriging, such as dispersion or correlation, must be carefully selected. Previous studies have applied kriging techniques to data from stations with large geographical separations. As a result, overestimates of the threshold distance occur, leading to information loss. Furthermore, many authors ignore the anisotropic nature of atmospheric processes by fitting isotropic variogram models. The large fitting errors typical in the literature imply uncertainties in their analyses that render them too inaccurate for practical applications. It is likely that no isotropic variogram model can represent the anisotropic nature of the spatial variability of solar irradiance (Sampson and Guttorp, 1992). I therefore take anisotropy into consideration in this thesis.

5.1.2 Data

Fig. 5.1 shows the geographical locations of 10 irradiance monitoring stations in Singapore. These stations are part of a bigger monitoring network designed for grid integration applications. Silicon sensors are employed at each station, with some also having pyranometers that measure diffuse and global irradiance. The silicon sensors are regularly calibrated by the Fraunhofer Institute for Solar Energy Systems in Germany to achieve an uncertainty of under 5%. The data used in this chapter is hourly data from 2012 November.

5.2 Temporal stationarity

Temporal stationarity for a spatio–temporal process is defined in Eqn. (A.19). Irradiance time series in Singapore is non–stationary as tested by Wu and Chee (2011). My aim at this stage is to obtain a stationary time series at each individual station without assuming

Fig. 5.1 Geographic locations of the 10 stations used in this study. Source: Google Maps.

spatio–temporal separability. Thus, detrend methods similar to those adopted in time series analyses are considered.

Appendix B shows several existing detrend methods. A common practice in these methods is that the authors use bell shape curves to remove the diurnal trend in irradiance time series. In chapter 4, STL is used for detrend. Although such techniques can provide location–specific stationary time series by finding the least squared fitted parameters. Data collected at different irradiance monitoring stations do not necessarily share the same model parameters.

Since Singapore is located near the equator, I only consider the diurnal trend in solar irradiance time series. In the review paper by (Inman et al., 2013), two commonly accepted models for detrending irradiance time series are described, namely, the clear sky model and the extraterrestrial irradiance model. For a given GHI value, the **clear sky index** is defined by the ratio between GHI and its clear sky dual; similarly, the **clearness index** is defined by dividing GHI by the extraterrestrial irradiance. In this chapter, the clearness index[1] method

---

[1] Due to the diffuse irradiance component, clear sky index typically ranges from 0 to 1.3, whereas the clearness index is strictly between 0 and 1.

is used. The horizontal extraterrestrial irradiance is a deterministic parameter given by:

$$I_{\mathrm{oh}} = E_0 I_{\mathrm{sc}} \cos\theta_z \tag{5.1}$$

where E_0 is the eccentricity, I_{sc} is the solar constant, and θ_z is the zenith angle.

Trend removal via the clearness index is commonly used, however, it does not guarantee a stationary detrended series. Therefore we perform the Kwiatkowski–Phillips–Schmidt–Shin (KPSS) test (Kwiatkowski et al., 1992) to assess stationarity in our detrended series. The KPSS test has a null hypothesis, H_0, to imply stationarity, and an alternative hypothesis H_1 to imply a unit root, i.e., non–stationary. The hypothesis testing is based on searching for a unit root in the time series autocorrelation model. In other words, if the observation at time t strongly depends on the observation at time $t-1$ with coefficient larger than 1 ($z_t = \mu + \phi_1 z_{t-1}$, $\phi_1 > 1$), the series is defined to be explosive. The p–value is a measure of the evidence against H_0: the smaller the p–value, the stronger evidence against H_0. The monthly time series at each station has a p–value greater than 0.1, which indicates strong evidence in favor of the null hypothesis. As all hypothesis tests suffer from the problem of probability of false declaration, when the number of test points increases, the probability of falsely declaring significance is likely to increase. However, this issue can be disregarded here, since I only utilize several weeks' data in the stationarity analyses.

5.3 Spatial stationarity

Covariance estimation of spatial processes is fundamental for many problems of spatial interpolation and design of monitoring networks (Sampson and Guttorp, 1992). However, most environmental spatio–temporal processes (e.g. De Luna and Genton, 2005; Gneiting, 2002) cannot be assumed to be stationary nor isotropic. For instance, it is known that no isotropic variogram can accurately model irradiance data (Rehman and Ghori, 2000; Sampson and Guttorp, 1992). Anisotropy is also discovered in the famous Irish wind data

(Haslett and Raftery, 1989). Therefore, a forecasting method using a covariance structure needs to be rigorously examined, avoiding to falsely make the isotropic assumption.

To understand non–stationarity and anisotropy, we need to consider variability measures. Statistical measures on variability include correlation, covariance, and dispersion, etc. Correlation and covariance are similarity measures, while dispersion is a dissimilarity measure. In this chapter, dispersion is used. **Spatial dispersion** (a measure of variability) is defined as (Sampson and Guttorp, 1992):

$$d_{ij}^2 = \mathbb{V}\{z_t(\boldsymbol{s}_i) - z_t(\boldsymbol{s}_j)\} \tag{5.2}$$

where $z_t(\boldsymbol{s}_i)$ and $z_t(\boldsymbol{s}_j)$ denote two temporal processes at location $\boldsymbol{s}_i$ and $\boldsymbol{s}_j$, respectively.

Consider a one–dimensional example, see Fig. 5.2. A measurement station a is located at the origin of a line. There is a second station b to the left of the origin with a certain distance. Similarly, a third station c is located at the right of the origin with the same distance. Suppose a dimensionless dispersion of 3 is set between a and b and 2 is set between a and c. The contradiction is obvious, as in a stationary and isotropic environment, the dispersion between a, b and a, c should be the same. This example illustrates both non–stationarity and anisotropy. In a physical world, the non–stationarity and anisotropy is frequently observed. In addition, asymmetry is also observed, i.e., $d_{ij}^2 \neq d_{ji}^2$.

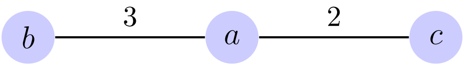

Fig. 5.2 A one–dimensional example. a, b and c are measurement stations with the numbers indicating their dispersions.

Eqns. (A.20) and (A.21) reveal the solution to the above problem. Suppose the variability in the random process, in this case the dispersion, is only a function of the stations' separation distance, the covariance in that space is both stationary and isotropic. Sampson and Guttorp (1992) proposed a two–step method to estimate such covariance structures using a non–parametric approach. The first step is called multidimensional scaling (MDS) and the second step is called thin plate spline (TPS) mapping.

5.3.1 G plane and D plane

In both of the above steps, two planes are considered, namely, the geographic (physical) space, where stationarity and isotropy of the random process are not assumed, and a new space where stationarity and isotropy are assumed. Sampson and Guttorp refer to the geographic space as the G plane and the dispersion space (the transformed space) as the D plane.

The desired properties in the D plane are stationarity and isotropy. In other words, the distance in the D plane needs to vary monotonically with dispersion. Using Eqn. (5.2), the pairwise dispersion can be computed. These calculated dispersions are used to retrieve the D plane distance. For every station in the G plane, there will be a corresponding station in the D plane.

5.3.2 Monotonicity and computation for the D plane representations

The locations of stations in the D plane should be set following the dispersion, i.e, station pair with a small dispersion should be close to each other in D plane, and vice versa. In particular, the D plane distance h_{ij} should increase monotonically with dispersion. MDS is used to determine the monotone function. Appendix C shows the details of the computation. I briefly repeat some key steps here.

The input to MDS is a proximity matrix. In this application, the square root of dispersion $\{d_{ij}\}$ give the elements in the proximity matrix. A monotone function is found to transform the proximities to the D plane distances.

$$\delta(d_{ij}) \approx h_{ij} \tag{5.3}$$

Multidimensional scaling provides a “principle components” representation of the pattern of proximities or dissimilarities (i.e., spatial dispersion) among a set of objects. There are two types of MDS, namely, classical MDS and non–metric MDS. Classical MDS takes a matrix of dissimilarities as input, and outputs an object map in lower dimensions. The method to solve for the coordinates of projection is eigendecomposition. While the classical MDS provides an initialization to the non–metric MDS, iterative monotonic regression is carried out to minimize the stress function $\mathcal{S}$:

$$\mathcal{S} = \sqrt{\frac{\sum\limits_{i<j}(h_{ij} - \delta(d_{ij}))^2}{\sum\limits_{i<j} h_{ij}^2}}, \quad i \in \{1, 2, \cdots, n-1\},\ j \in \{2, 3, \cdots, n\} \tag{5.4}$$

The minimization uses the method of steepest descent, see appendix C for details. Through non–metric MDS, $\mathcal{S}$ is minimized and the converged configuration gives the locations of stations in the D plane. We note that in the G plane, coordinates are given using latitudes and longitudes. The output of the MDS can be transformed back to such coordinates using rigid motions (such as rotation, translation and reflection) and uniform stretching.

5.3.3 Thin plate spline mapping between the G and D planes

Once the stations’ coordinates in the G plane and the D plane have been established, a $\mathbb{R}^2 \to \mathbb{R}^2$ mapping between these two planes is needed. Let the station coordinates in the G plane be denoted by (x_i, y_i) and those in the D plane by (x_i^*, y_i^*); a bivariate function $f : \mathbb{R}^2 \to \mathbb{R}^2$ that maps the coordinates from the G plane to the D plane is desired:

$$\begin{pmatrix} x_i^* \\ y_i^* \end{pmatrix} = f \begin{pmatrix} x_i \\ y_i \end{pmatrix} \tag{5.5}$$

The algorithm determines such a function by minimizing a certain roughness/smoothness criterion. For example, in one dimensional cubic spline interpolation:

$$J_f = \int [f''(x)]^2 dx \tag{5.6}$$

is minimized, subject to first and second order derivative constraints at the knots and at the boundaries. A cubic spline is a spline constructed of piecewise third–order polynomials which pass through a set of n control points (knots). The minimization constraint first considers the continuity at the knots by equating the gradients (first order derivatives) of two polynomials at each knot. The second order derivative is then minimized using the sum of the square of the derivative of the gradient (see Eqn. (5.6)) to ensure the fitted spline is the smoothest.

If the cubic spline described above performs a $\mathbb{R}^1 \rightarrow \mathbb{R}^1$ mapping, the method can be extended to a $\mathbb{R}^2 \rightarrow \mathbb{R}^1$ mapping which applies to the present problem. Bookstein (1989) states the generalization of this mapping:

$$J_f = \iint_{\mathbb{R}^2} \left[\left(\frac{\partial^2 f}{\partial x^2} \right)^2 + 2 \left(\frac{\partial^2 f}{\partial x \partial y} \right)^2 + \left(\frac{\partial^2 f}{\partial y^2} \right)^2 \right] dxdy \tag{5.7}$$

J_f is the measure of roughness/smoothness which is proportional to the bending energy of an idealized thin plate of infinite extent (Sampson and Guttorp, 1992). The interpolators minimizing the bending energy are linear combinations of a basis function $U(\cdot)$ centered at those n observed locations. Thin plate spline is used to perform this interpolation. TPS is frequently used in morphometrics Bookstein (1989, 1997a). The method to determine the function f is shown in appendix D.

This method maps an anisotropic random process to an isotropic random process. For examples of applying such deformation techniques to environmental data, one can refer to (e.g. Capizzi et al., 2012; Guttorp et al., 1994; Le and Zidek, 2006; Meiring et al., 1998; Schmidt and O'Hagan, 2003). The following section describes the covariance functions. I further explore the other two properties, namely, separability, full symmetry in the next sections.

5.4 Covariance and Kriging

After trend removal (section 5.2) and space deformation (section 5.3), stationary spatio–temporal data can be obtained. Some stationary spatio–temporal covariance functions are introduced here; they will be used later to forecast the clearness index.

5.4.1 Separable model

Recall Eqn. (A.23), the covariance function is separable if it can be written as the product of a purely spatial and a purely temporal covariance functions. Since use of covariance or correlation will lead to the same kriging results, here I follow the approach of Gneiting et al. (2007) and fit a purely temporal correlation function of the Cauchy type:

$$\rho_T(\tau) = (1 + a|\tau|^{2\alpha})^{-1} \tag{5.8}$$

where ρ stands for correlation and a, α are model parameters. For the spatial correlation function I choose an exponential model with a nugget effect (a term derived from from mining geostatistics):

$$\rho_S(\boldsymbol{h}) = (1 - \nu)\text{exp}(-c \cdot \|\boldsymbol{h}\|) + \nu \boldsymbol{I}_{\boldsymbol{h}=\boldsymbol{0}} \tag{5.9}$$

where ν and c are parameters to be fitted. $\boldsymbol{I}$ is a binary indicator function, equals to 1 if $\boldsymbol{h} = \boldsymbol{0}$, 0 otherwise. Therefore the separable covariance function is given by:

$$\mathbb{C}_{SEP}(\boldsymbol{h}; \tau) = \rho_T(\tau) \cdot \rho_S(\boldsymbol{h}) \cdot \sigma^2 \tag{5.10}$$

where σ^2 is the variance of the spatio–temporal process.

5.4.2 Fully symmetric model

We can construct the fully symmetric but generally non–separable correlation function using the separable model described earlier. Gneiting et al. (2006) states the theorem:

Theorem. *Suppose that $\varphi(r)$, $r \geq 0$, is a completely monotone function, and that $\psi(r)$, $r \geq 0$, is a positive function with a completely monotone derivative. Then*

$$\mathbb{C}(\boldsymbol{h};\tau) = \frac{\sigma^2}{\psi(|\tau|^2)^{d/2}}\varphi\left(\frac{\|\boldsymbol{h}\|^2}{\psi(|\tau|^2)}\right), \quad (\boldsymbol{h};\tau) \in \mathbb{R}^d \times \mathbb{R}^1 \tag{5.11}$$

is a stationary covariance function on $\mathbb{R}^d \times \mathbb{R}^1$.

There are several choices (Gneiting, 2002) in selecting $\varphi(r)$ and $\psi(r)$, for example:

$$\varphi_1(r) = \exp(-cr^{\gamma}), \quad c > 0,\ 0 < \gamma \leq 1 \tag{5.12}$$

$$\varphi_2(r) = (1 + cr^{\gamma})^{-\nu}, \quad c > 0,\ 0 < \gamma \leq 1,\ \nu > 0 \tag{5.13}$$

$$\varphi_3(r) = 2^{\nu}[\exp(cr^{1/2}) + \exp(-cr^{1/2})]^{-\nu}, \quad c > 0,\ \nu > 0 \tag{5.14}$$

$$\psi_1(r) = (ar^{\alpha} + 1)^{\beta}, \quad a > 0,\ 0 < \alpha \leq 1,\ 0 \leq \beta \leq 1 \tag{5.15}$$

$$\psi_2(r) = \ln(ar^{\alpha} + b)/\ln(b), \quad a > 0,\ b > 1,\ 0 \leq \alpha \leq 1 \tag{5.16}$$

$$\psi_3(r) = (ar^{\alpha} + b)/[b(ar^{\alpha} + 1)], \quad a > 0,\ 0 < b \leq 1,\ 0 \leq \alpha \leq 1 \tag{5.17}$$

Gneiting (1997) and the references therein prove the complete monotonicity of the above functions. If we select $\psi_1(r)$ and $\varphi_1(r)$ and substitute them into Eqn. (5.11), and consider only the two dimensional space case, we have:

$$\mathbb{C}(\boldsymbol{h};\tau) = \frac{\sigma^2}{(1 + a|\tau|^{2\alpha})^{\beta}}\left[\exp\left(-\frac{c \cdot \|\boldsymbol{h}\|^{2\gamma}}{(1 + a|\tau|^{2\alpha})^{\beta\gamma}}\right)\right], \quad (\boldsymbol{h};\tau) \in \mathbb{R}^2 \times \mathbb{R} \tag{5.18}$$

If we let $\gamma = 1/2$ and include a nugget effect, the above equation becomes:

$$\mathbb{C}(\boldsymbol{h};\tau) = \frac{\sigma^2 \cdot (1 - \nu)}{(1 + a|\tau|^{2\alpha})^{\beta}}\left[\exp\left(-\frac{c \cdot \|\boldsymbol{h}\|}{(1 + a|\tau|^{2\alpha})^{\beta/2}}\right) + \frac{\nu}{1 - \nu}\boldsymbol{I}_{\boldsymbol{h}=\boldsymbol{0}}\right] \tag{5.19}$$

Furthermore, Gneiting (2002) considered a reparameterization of Eqn. (5.19), namely, multiplying another purely temporal covariance function $(1+a|\tau|^{2\alpha})^{-\zeta}$ to it:

$$\mathbb{C}_{FS}(\boldsymbol{h};\tau)=\frac{\sigma^2\cdot(1-\nu)}{(1+a|\tau|^{2\alpha})^{\beta^*}}\left[\exp\left(-\frac{c\cdot\|\boldsymbol{h}\|}{(1+a|\tau|^{2\alpha})^{\beta/2}}\right)+\frac{\nu}{1-\nu}\boldsymbol{I}_{\boldsymbol{h}=\boldsymbol{0}}\right] \tag{5.20}$$

where $\beta^*=\beta+\zeta$. Eqn. (5.20) reveals an immediate link between Eqns. (5.8) and (5.9). β can be considered as a space–time interaction parameter, and $0\leq\beta\leq 1$. If $\beta=0$, Eqn. (5.20) is reduced to the separable model shown in Eqn. (5.10).

5.4.3 Time–forward kriging

Time–forward kriging is used here to assess the predictive performance of the spatio–temporal structures just developed. Consider a spatio–temporal process $\{z(\boldsymbol{s};t):\boldsymbol{s}\in D_s\subset\mathbb{R}^d, t\in D_t\subset\mathbb{R}^1\}$ evolves through the spatio–temporal index set $D_s\times D_t$. Given observations:

$$\boldsymbol{Z}\equiv\begin{pmatrix}z(\boldsymbol{s}_1;t_1) & z(\boldsymbol{s}_2;t_2) & \cdots & z(\boldsymbol{s}_p;t_p)\end{pmatrix}^\top \tag{5.21}$$

at p space–time coordinates, predictions at unobserved coordinates $(\boldsymbol{s}_0;t_0)$ can be obtained using the **simple kriging predictor**:

$$\widehat{z}(\boldsymbol{s}_0;t_0)=\mu(\boldsymbol{s}_0;t_0)+\boldsymbol{c}(\boldsymbol{s}_0;t_0)^\top\boldsymbol{C}^{-1}(\boldsymbol{z}-\boldsymbol{\mu}) \tag{5.22}$$

where $\boldsymbol{C}\equiv\texttt{Cov}(\boldsymbol{Z})$, $\boldsymbol{c}(\boldsymbol{s}_0;t_0)\equiv\texttt{Cov}(z(\boldsymbol{s}_0;t_0),\boldsymbol{Z})$ and $\boldsymbol{\mu}\equiv\mathbb{E}(\boldsymbol{Z})$ (Cressie and Huang, 1999). When the number of temporal indices at each station is identical, $\boldsymbol{Z}$ can be decomposed, such that:

$$\boldsymbol{Z}=\begin{pmatrix}\boldsymbol{z}^{(1)\top} & \boldsymbol{z}^{(2)\top} & \cdots & \boldsymbol{z}^{(m)\top}\end{pmatrix}^\top \tag{5.23}$$

and

$$\boldsymbol{z}^{(k)}=\begin{pmatrix}z(\boldsymbol{s}_1;t_k) & z(\boldsymbol{s}_2;t_k) & \cdots & z(\boldsymbol{s}_n;t_k)\end{pmatrix}^\top,\quad k=1,\cdots,m \tag{5.24}$$

where n and m are numbers of spatial and temporal indices, $nm = p$. Subsequently, the $\boldsymbol{C}$ in Eqn. (5.22) is:

$$\boldsymbol{C} = \begin{pmatrix} \boldsymbol{C}_0 & \boldsymbol{C}_1^\top & \cdots & \boldsymbol{C}_{m-1}^\top \\ \boldsymbol{C}_1 & \boldsymbol{C}_0 & \cdots & \boldsymbol{C}_{m-2}^\top \\ \vdots & \vdots & \ddots & \vdots \\ \boldsymbol{C}_{m-1} & \boldsymbol{C}_{m-2} & \cdots & \boldsymbol{C}_0 \end{pmatrix}, \quad \in \mathbb{R}^{nm \times nm} \tag{5.25}$$

and

$$\boldsymbol{C}_\tau = \begin{pmatrix} C_{11,\tau} & C_{12,\tau} & \cdots & C_{1n,\tau} \\ C_{21,\tau} & C_{22,\tau} & \cdots & C_{2n,\tau} \\ \vdots & \vdots & \ddots & \vdots \\ C_{N1,\tau} & C_{N2,\tau} & \cdots & C_{nn,\tau} \end{pmatrix}, \quad \in \mathbb{R}^{n \times n} \tag{5.26}$$

where $\tau = 0, \cdots, m-1$ and

$$\begin{aligned} C_{ij,\tau} &= C_{ij,k-l} \\ &= \mathtt{Cov}(z(\boldsymbol{s}_i; t_k), z(\boldsymbol{s}_j; t_l)) \\ &= \mathtt{Cov}(z(\boldsymbol{s}_i; t_k), z(\boldsymbol{s}_j; t_k - \tau)), \quad \forall k > l \end{aligned} \tag{5.27}$$

If $C_{ij,\tau}$ is estimated empirically using $\widehat{\mathtt{Cov}}\{z(\boldsymbol{s}_i; t), z(\boldsymbol{s}_j; t-\tau)\}$, $i, j \in \{1, \cdots, n\}$; the method is then called **empirical kriging**. It can also be estimated from the empirical covariance function $\widehat{\mathbb{C}}(\boldsymbol{h}; \tau)$ as seen in Eqns. (5.10) and (5.20). Similar to $\boldsymbol{C}$, for one time step ahead prediction, the $\boldsymbol{c}$ in Eqn. (5.22) can be expanded as:

$$\boldsymbol{c} = \begin{pmatrix} \boldsymbol{c}_m^\top & \cdots & \boldsymbol{c}_2^\top & \boldsymbol{c}_1^\top \end{pmatrix}^\top, \quad \in \mathbb{R}^{nm \times 1} \tag{5.28}$$

and

$$\boldsymbol{c}_\tau = \begin{pmatrix} c_{01,\tau} & c_{02,\tau} & \cdots & c_{0n,\tau} \end{pmatrix}^\top, \quad \in \mathbb{R}^{n \times 1} \tag{5.29}$$

where $\tau = m, \cdots, 1$ and

$$c_{0j,\tau} = \texttt{Cov}(z(\boldsymbol{s}_0; t_k), z(\boldsymbol{s}_j; t_k - \tau)) \tag{5.30}$$

Vector $\boldsymbol{c}$ can be constricted using the covariance functions, which only require distance and time lags. Unlike forecasting using time series of spatial processes, time–forward kriging is able to forecast $(n+1)$th point in space.

5.5 Singapore case study

After the data detrend process, temporal stationary clearness index data are obtained. I now demonstrate the deformation of geographical coordinates to obtain spatial stationarity. Two weeks of hourly data from 2012 November 1–14 are used for model fitting.

5.5.1 Spatial stationarity

Fig. 5.3 shows the G plane spatial dispersion versus geographical inter–station distances. The inter–station distances are calculated by pairwise great circle distance (longitude and latitude are used as input while the output is in kilometers). Therefore, 45 pairs ($= n \times (n-1)/2$, when $n = 10$) with their respective spatial dispersions are plotted. It is clear from Fig. 5.3 that no isotropic variogram model could accurately reflect the data.

MDS is performed using the spatial dispersions as the inputs. Fig. 5.4 shows the relationship between spatial correlation in D plane distance. It can be observed that the spread of the correlation becomes significantly narrower than the previous anisotropic case (Fig. 5.3). This decrease is quantified using the residual sum–of–square. After fitting the exponential correlation functions to Fig. 5.3 and Fig. 5.4, the residual sum–of–square values are 0.01938 and 0.01081 respectively. I thus conclude that MDS effectively reduces anisotropy.

Thin plate spline mapping is performed after the station coordinates in the D plane are derived. Fig. 5.5 shows the thin plate spline transformation grids from the G to the D plane.

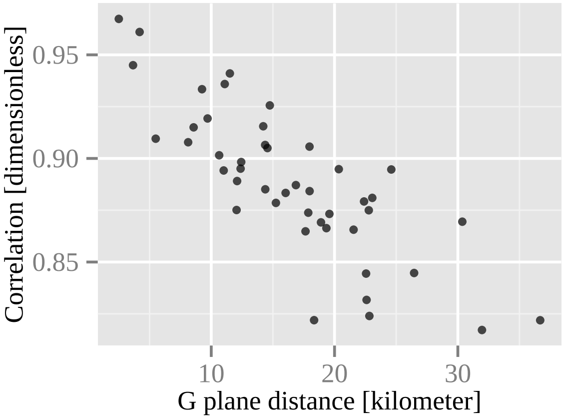

Fig. 5.3 Spatial correlation on geographical plane shows anisotropy.

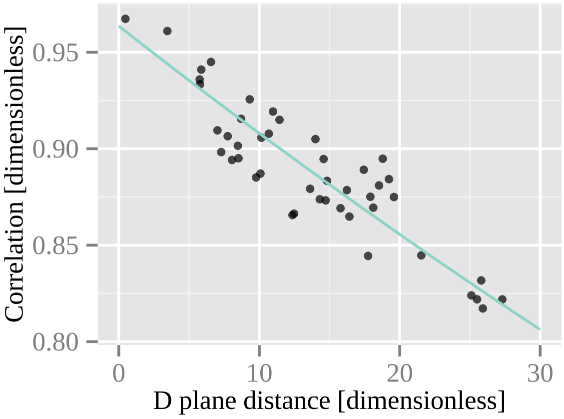

Fig. 5.4 Spatial correlation on dispersion plane shows improved isotropy.

I note that rotation, reflection and enlargement are used to transform the MDS results so that the final D plane coordinates follow the original G plane latitudes and longitudes.

5.5.2 Model fitting

The exponential correlation function expressed in Eqn. (5.9) is fitted using the results shown in Fig. 5.4. The fitted parameters are $\widehat{\nu} = 0.036381$ and $\widehat{c} = 0.005943$. For the purely temporal correlation function in Eqn. (5.8), the fitted parameters are $\widehat{a} = 0.2044$ and $\widehat{\alpha} = 0.7871$. Note that a and α are obtained with $|\tau| \leq 3$, i.e. $M = 3$. For hourly solar irradiance, the order of the autoregressive parameter is usually within this range. Fig. 5.6 shows the

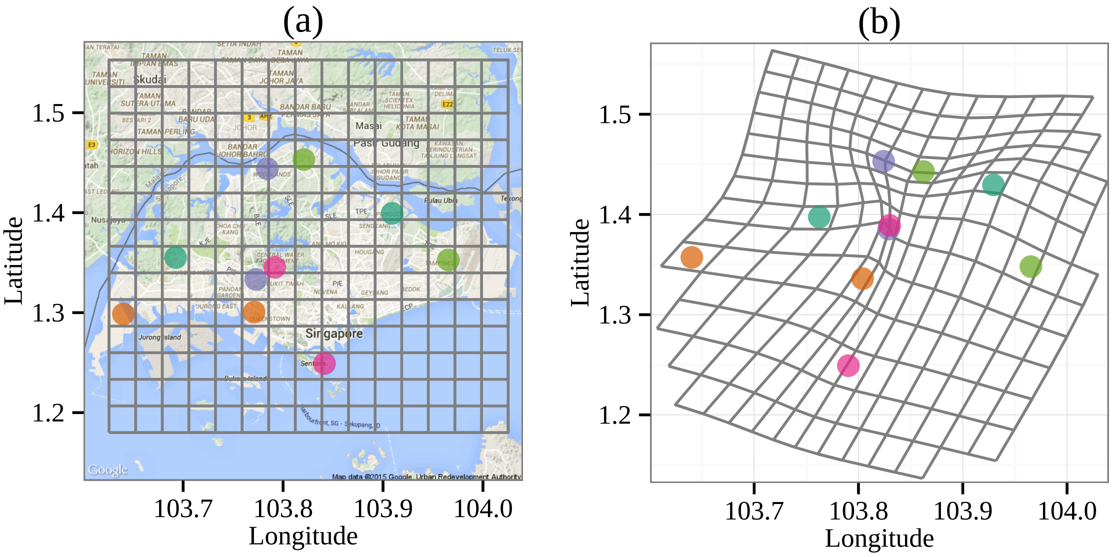

Fig. 5.5 Thin plate spline transformation grids from G plane to D plane. Plot (a) shows the original G plane locations with rectangular grid; (b) shows the D plane locations after MDS with bended grid.

fit. The fitted parameter for the fully symmetric model is $\widehat{\beta} = 0.8923$.

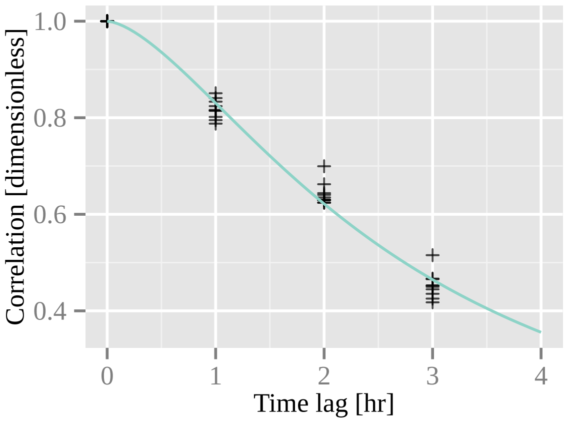

Fig. 5.6 Temporal correlation fitted using first two week's data from 2012 November. Nonlinear least square is used to obtain the fitted line.

Table 5.1 Forecast RMSE for hourly Singapore clearness index data at the 10 stations for 2012 November 15–30.

	RMSE for clearness index			
Station	Persistence	Separable covariance	Fully symmetric covariance	Empirical kriging
S301	0.196	0.156	0.154	0.145
S500	0.200	0.145	0.142	0.153
S104	0.195	0.150	0.148	0.152
S304	0.187	0.134	0.131	0.169
S305	0.194	0.152	0.149	0.146
S116	0.196	0.142	0.139	0.153
S106	0.201	0.143	0.139	0.154
S102	0.192	0.142	0.139	0.156
S108	0.193	0.152	0.149	0.155
S105	0.181	0.142	0.141	0.134
overall	0.193	0.146	0.144	0.152

5.5.3 Forecast

The hourly ahead forecasts is evaluated using one month clearness index data in this section. Eqn. (1.2) is used to compute the RMSE (see Table 5.1) of the forecast clearness index. Two weeks of hourly data from 2012 November 1–14 are used to perform the model fitting, thus the forecasts show the results from the remaining 16 days of data, namely, 2012 November 15–30. The persistence model is used to benchmark the data.

The rightmost column of Table 5.1 shows results of empirical kriging. Recall that empirical kriging does not depend any covariance function fitting. The covariance matrix $\boldsymbol{C}$ and covariance vector $\boldsymbol{c_0}$ are computed based on sample covariance $\widehat{\texttt{Cov}}(\cdot)$.

5.6 Discussion and conclusion

Isotropy describes rotational invariance. In other words, the spatial covariance is only a function of distance $\|\boldsymbol{h}\|$. We have seen in Fig. 5.4 that MDS can effectively improve anisotropy by reducing the scattering of points in the correlation versus distance plot. However, the result is not perfect. To examine the goodness of fit of MDS, the Shepard plot is employed. The Shepard plot is a plot of D plane distance h_{ij} against the square root of dispersion d_{ij} together with an monotonic regression (the solid line) of the h_{ij} on the d_{ij}. Perfect MDS results would indicate that h_{ij} strictly increases with d_{ij}. Fig. 5.7 shows the Shepard plot for clearness index data from 10 Singapore stations.

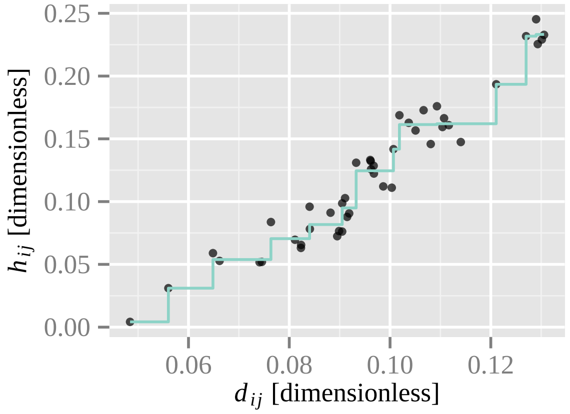

Fig. 5.7 Shepard plot for Singapore *clearness index* data. D-plane distance h_{ij} is plotted against dissimilarity d_{ij}. An isotonic regression of h_{ij} on d_{ij} is shown by the solid line.

The origin of the fitting errors is explained in appendix C, which is summarized to be the degeneracy in the proximity matrix. Fig. 5.8 shows the spatial dispersions between the pairwise stations. The red dots in the plot show the spatial dispersion only involving stations S106, S104 and S304; the green triangles show the spatial dispersion only involving stations S301, S305 and S116. It is obvious that no isotropic variogram model can be fitted to these data without sacrificing some data points. An ad hoc solution to the problem is to remove either groups of stations from the MDS step. Data from S301, S305 and S116 are removed for illustration. Fig. 5.9 shows the new Shepard plot which indicates a perfect fit.

Several questions arise from the above observation:

1. Why the isotropy improves after removing some boundary stations (see Fig. 5.1)?
2. If irradiance is modeled as spatio–temporal random processes, is there any threshold distance describing the spatial boundary of the process?
3. How can we define and determine the threshold distance?
4. After the threshold distance is set, how the model parameters change?
5. Will the threshold distance improve the kriging accuracies?

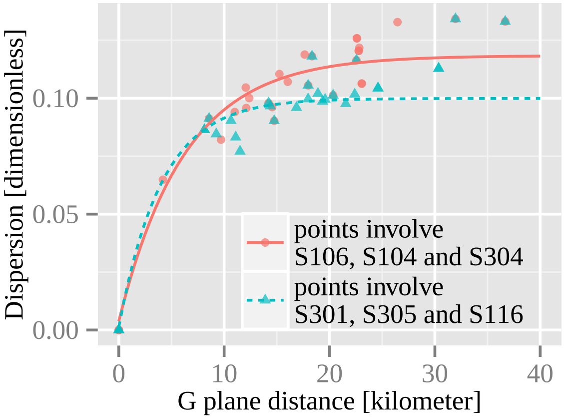

Fig. 5.8 Spatial dispersion indicate two variogram models are involved in the data.

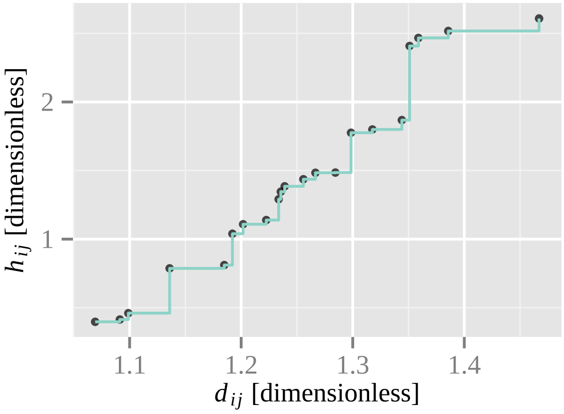

Fig. 5.9 Shepard diagram after removing stations S301 S305 and S116.

6. Does the threshold distance apply to other forecasting models?

These questions will be answered in chapter 9, which presents a correlation–based study on the threshold distance in the solar irradiance random process. By properly defining a threshold distance, the time–forward kriging parameters can be reduced without loss of forecast accuracies. The vector autoregressive model is also explored; the results are found to be consistent with those from kriging. Before we look at the parameter shrinkage in spatio–temporal irradiance forecasting, transposition models are discussed in chapters 6 and 7.

Chapter 6

Inverse transposition using a single reference cell

In the previous chapter, space–time kriging is used to forecast the hourly clearness index in Singapore. The developed methodology outperforms the persistence model. The foundations of the method are built on top of two transformations of the data: (1) temporal stationarity is achieved by detrending the data and (2) a space deformation technique is applied to approximate, if not obtain, the spatial stationarity. The aim of chapter 5 is to devise a methodology to forecast solar irradiance over a wide area, using time series from a network of monitoring stations as input. However, the costs of developing and maintaining such solar irradiance sensor networks are high, especially when pyranometers are used to collect the global horizontal irradiance (GHI) data.

The alternative to a pyranometer is a reference cell. Reference cells (silicon sensors) are usually installed with PV systems for performance evaluation (Meydbray et al., 2012a; Yang et al., 2014b). As many PV systems are tilted towards the equator to maximize the yearly energy yield, the reference cells are therefore installed at the plane of array (POA) tilts. Utilizing the data collected by the reference cells can facilitate irradiance forecasting. However the tilted irradiance data cannot be used directly, one is therefore often compelled to convert the irradiance received at an arbitrary tilt to GHI.

In this chapter, as well as in chapter 7, methods for reconstructing GHI using tilted irradiance measurements are discussed. The existing literature however focuses on using transposition and decomposition models to predict the solar irradiance on tilted surface from the solar irradiance data on a horizontal plane. My developments here are therefore novel.

6.1 Literature review on transposition and decomposition models

Many transposition models have been proposed in the literature to convert solar irradiance on the horizontal plane to that on a tilted plane. The global irradiance, I_t, on a tilted plane of s degrees from the horizontal, can be evaluated from the equation:

$$I_\mathrm{t} = I_\mathrm{dir}\cos\theta_i + I_\mathrm{dif}R_\mathrm{d} + \rho' I_\mathrm{glo}R_\mathrm{r} \tag{6.1}$$

where I_dir is the direct normal solar irradiance (DNI), I_dif is the diffuse horizontal irradiance (DHI), I_glo is the GHI, θ_i is the angle of incidence of the sun rays on the tilted plane, R_d is the diffuse transposition factor, ρ' is the foreground's albedo, and R_r is the transposition factor for ground reflection.

It should be noted that the incidence angle θ_i of the sun's rays on a surface with an arbitrary tilt angle s and azimuth is purely geometric; its formulation can be found in standard texts (e.g. Duffie and Beckman, 2006). Ground reflection is considered as an isotropic process by most studies, and is characterized by R_r, which is a function of tilt angle s (Gueymard, 2009). The formulations for the diffuse transposition factor R_d can be classified as isotropic (e.g. Badescu, 2002; Koronakis, 1986; Liu and Jordan, 1962; Tian et al., 2001) and anisotropic (e.g. Hay, 1979; Klucher, 1979; Perez et al., 1990; Reindl et al., 1990b; Skartveit and Olseth, 1986; Temps and Coulson, 1977). Details and mathematical formulations for R_d are summarized by Evseev and Kudish (2009); Noorian et al. (2008) for both types. The recent paper by David et al. (2013) evaluates the performance of various anisotropic transposition models in a tropical environment.

In order to compute the irradiance on a tilted surface, we need to know all three irradiance components on a horizontal surface, namely, GHI, DNI and DHI. The closure equation describes a well–known relationship among the three components:

$$I_{\mathrm{glo}} = I_{\mathrm{dir}} \cos\theta_z + I_{\mathrm{dif}} \tag{6.2}$$

where θ_z is the zenith angle. This relationship implies that we should have at least two irradiance measurements in order to accurately predict the global solar irradiance on a tilted plane.

Multi–sensor approaches (e.g. Faiman et al., 1993) are often used to resolve this issue. When two irradiance sensors are installed at two different tilts, we can accurately solve for I_{dir} and I_{dif} using simultaneous equations (use Eqn. (6.1) twice, by having two sets of parameters obtained from two tilts). Otherwise, decomposition models are used to estimate I_{dir} and I_{dif} from a single I_{glo} measurement.

To separate the direct and diffuse components from I_{glo}, many empirical relationships have been proposed. Instead of relating the irradiance components directly, most papers in the literature use the concept of transmittance. Transmittance is a representation of fraction of extraterrestrial irradiance reaching the ground (see section 6.2 for details). Most approaches aim to represent diffuse horizontal transmittance K_{d} or direct normal transmittance K_{n} as a function of the effective global horizontal transmittance K_{t} (K_{t} is also known as the clearness index) and other predictors. Gueymard (2009) suggests that the direct and diffuse separation be made dependent on zenith angle, ambient temperature and relative humidity. Garrison (1985); Garrison and Sahami (1995) suggest the separation should consider solar elevation, surface albedo, atmospheric precipitable water and snow cover. These multivariate models are complex and the input measurements are not always available.

I seek simple empirical models to separate direct and diffuse components from global solar irradiance. Erbs et al. (1982); Orgill and Hollands (1977) use univariate approaches, namely, GHI as the only input. Maxwell (1987) considers a bivariate model using GHI and zenith angle as inputs. Reindl et al. (1990a) proposed versions of his model as both univariate and bivariate models. Zhang (2006) used GHI and elevation angle (equals to $90° - \theta_z$) as inputs, the decomposition model is then constructed using the Gompertz function. These models are developed from the measurements taken at some specific locations; therefore their accuracy must be carefully evaluated if they are applied to places different from the ones included in the databases used for their development (Padovan and Col, 2010).

While the methods for converting solar irradiance from horizontal to tilted planes are well described, the reverse process, i.e. converting from tilted to horizontal, is lacking in the literature. For reasons described in the beginning of this chapter, an algorithm which converts solar irradiance on a tilted plane to horizontal irradiance using a single set of tilted measurements is proposed in this chapter.

The rest of this chapter is organized as follows. Section 6.2 evaluates the performance of various transposition and decomposition models in tropical regions. The performance of ten transposition models (four isotropic models and six anisotropic models) is first examined using the tropical data set in section 6.2.2. Measurements of both GHI and DHI are used as inputs for these transposition models. The converted results are compared to tilted measurements. Five decomposition models are then selected and verified in section 6.2.3. The predicted DHI is compared to the measured DHI. The transposition models and decomposition models are combined and evaluated in section 6.2.4. In other words, only GHI is used to convert irradiance from horizontal to tilt; the results are again compared to the tilted measurements. Section 6.3 describes the process of converting solar irradiance from tilt to horizontal. Results and analyses of the proposed algorithm are shown in section 6.4. Section 6.5 concludes the findings of this chapter.

6.2 Horizontal to tilt: an evaluation

6.2.1 Background

Define two types of transmittance:

$$I_{\mathrm{glo}} = K_{\mathrm{t}} I_{\mathrm{oh}}; \tag{6.3}$$

$$I_{\mathrm{dir}} = K_{\mathrm{n}} I_{\mathrm{o}} \tag{6.4}$$

K_{t} and K_{n} are **effective global horizontal transmittance** and **direct normal transmittance** respectively, while I_{oh} is horizontal extraterrestrial irradiance and I_{o} is extraterrestrial direct normal irradiance. The extraterrestrial irradiance is the function of zenith angle θ_z and eccentricity correction factor E_0 as shown below:

$$I_{\mathrm{oh}} = E_0 I_{\mathrm{sc}} \cos\theta_z; \tag{6.5}$$

$$I_{\mathrm{o}} = E_0 I_{\mathrm{sc}} \tag{6.6}$$

E_0 is also know as the reciprocal of the square of the Earth radius factor (e.g. see Maxwell, 1987); and is given by Eqn. (3.4). Recall that E_0 also depends on Γ which is defined as the eccentric anomaly of the Earth in the orbit around the Sun (Maxwell, 1987) or day angle (Janjai et al., 2011) as seen in Eqn. (3.5). I_{sc} is the solar constant, equal to 1362 $\mathrm{W/m^2}$. Note that Eqn. (6.5) is identical to Eqn. (5.1), its purpose here is to distinguish from I_{o}.

As Singapore has a latitude of 1.3°N, the “rule–of–thumb” installation angle for fixed panels should be 1.3°. However, in practice, the installation angle in Singapore is usually chosen to be between 5° to 20° to enhance panels’ output by promoting self cleaning by rain. A highly tilted plane introduces anisotropic features into derived the R_{r} values (Gueymard, 2009), but this effect is not significant for slopes less than 20°. As a result, I use an isotropic approximation for R_{r}:

$$R_{\mathrm{r}} = (1 - \cos s)/2, \tag{6.7}$$

in this section, where s is the tilt angle for the plane of incidence. An anisotropic formulation is however adopted in chapter 7 wherein data from larger tilt angles are used.

Both isotropic and anisotropic R_d models are discussed extensively in the literature. Ten models are compared in the following section. Among the ten models, four are isotropic models (see Badescu, 2002; Koronakis, 1986; Liu and Jordan, 1962; Tian et al., 2001) and six are anisotropic models (see Hay, 1979; Klucher, 1979; Perez et al., 1990; Reindl et al., 1990b; Skartveit and Olseth, 1986; Temps and Coulson, 1977). These ten models are provided in appendix E.

By combining Eqns. (6.3) to (6.7), Eqn. (6.1) is written using the K–indices:

$$I_\mathrm{t} = K_\mathrm{n} I_\mathrm{o} \cos\theta_i + (K_\mathrm{t} - K_\mathrm{n}) I_\mathrm{oh} R_\mathrm{d} + \rho' K_\mathrm{t} I_\mathrm{oh}[(1-\cos s)/2] \tag{6.8}$$

I call Eqn. (6.8) the target function. In order to find I_t, the tilted global solar irradiance, we need to know all the parameters on the right side of Eqn. (6.8). Among these parameters, θ_i is purely geometric and can be easily calculated. I select a fixed value of 0.2 for ρ' as suggested by Gueymard (2009) owing to the total absence of snow and ice in Singapore. As such, the only unknowns in the target function are K_t, K_n and R_d.

When all the horizontal irradiance components are known, I_t can be evaluated directly through Eqn. (6.1). When only the GHI is known, decomposition models are needed to predict DNI and DHI. I choose five models which are considered as “universal” models to formulate the relationship between K_t and K_n, including the Erbs et al. (1982) model, Orgill and Hollands (1977) model, Maxwell (1987) model, Reindl et al. (1990a) univariate model and Reindl et al. (1990a) bivariate model. These models are summarized in appendix F. Using a combination of transposition models and decomposition models, I_t values can be obtained using Eqn. (6.8).

6.2.2 Evaluation of 10 transposition models

The irradiance data used in this section were obtained from the first zero energy house in Singapore (FZEHS), which is shown in Fig. 6.1. The building has two PV arrays mounted on the metal roof. The azimuths of the PV arrays are 66° NE and 246° SW on the east and west roofs, respectively. The inclination angles of the east roof is 18.3° and 6.1° for the west roof.

Fig. 6.1 The first zero energy house in Singapore.

Three irradiance measurement devices are installed, namely, two calibrated silicon sensors installed in the plane of array of each roof and a pyranometer installed horizontally on the roof, which is nameed S111. The silicon sensor facing east is named S111a and the west facing one is named S111b. The measurements from S111 are used as inputs to the transposition models, as this particular device (a Delta–T Sunshine SPN1 Pyranometer) measures GHI and DHI simultaneously. The model output is compared to the measurements from S111a and S111b. Various transposition models are examined using 5 min data from these three stations over a period of one year, namely, 2011. For zenith angle and incidence angle calculation, solar position algorithm (SPA) (Reda and Andreas, 2004, 2008) from the National Renewable Energy Laboratory is used.

Mean bias error (MBE) shown in Eqn. (1.1), centered root mean square error (cRMSE) in Eqn. (1.4) and the expanded uncertainty at 95% confidence interval (U_{95}) in Eqn. (1.5) are used as error metrics following (Boyd, 2013). Table 6.1 shows the MBE, cRMSE and U_{95} for tilted solar irradiance prediction using ten transposition models. The results are calculated based on measurements from S111a and S111b.

Table 6.1 Performance of ten transposition models (converting from horizontal to tilted) over a period of one year, 2011.

	S111a	$s = 18.3°$	66° NE	S111b	$s = 6.1°$	246° SW
Model	MBE [W/m^2]	cRMSE [%]	U_{95} [%]	MBE [W/m^2]	cRMSE [%]	U_{95} [%]
All sky, N=44495						
Isotropic						
Liu and Jordan	2.99	10.28	20.19	6.69	8.14	16.34
Badescu	-2.08	10.13	19.88	6.13	8.13	16.26
Tian	-13.15	10.02	20.68	0.46	8.11	15.89
Koronakis	4.78	10.34	20.40	6.88	8.14	16.37
Anisotropic						
Hay	6.78	8.55	17.09	5.47	8.17	16.27
Reindl	7.09	8.56	17.13	5.49	8.17	16.27
Temps and Coulson	25.56	10.22	23.64	26.12	9.74	23.39
Klucher	14.36	10.00	20.84	15.88	9.38	20.21
Perez	2.45	8.64	16.99	5.67	8.03	16.03
Skartveit and Olseth	6.27	8.58	17.09	5.41	8.13	16.28
Mean observed [W/m^2]			398.59			369.62
Clear sky, N=757						
Isotropic						
Liu and Jordan	-5.07	5.40	10.48	8.94	2.11	4.81
Badescu	-7.75	5.27	10.52	8.62	2.11	4.76
Tian	-13.59	5.20	10.77	5.48	2.11	4.40
Koronakis	-4.13	5.32	10.44	9.04	2.11	4.82
Anisotropic						
Hay	1.24	3.34	6.53	5.85	2.37	4.91
Reindl	1.35	3.33	6.54	5.86	2.37	4.91
Temps and Coulson	6.86	4.54	9.07	17.97	2.16	6.48
Klucher	6.54	4.56	9.10	17.75	2.16	6.43
Perez	5.54	4.12	8.21	9.45	2.11	5.04
Skartveit and Olseth	1.24	3.33	6.53	5.85	2.37	4.91
Mean observed [W/m^2]			766.17			717.75

The results shown in Table 6.1 are separated into all sky condition and clear sky conditions to further elaborate on the errors. The selection of clear sky situation is similar to the method used in chapter 3 considering the sky's clearness ε' and the sky's brightness Δ'. Table 6.1 shows that all transposition models perform better under clear sky conditions due to a relatively isotropic sky and small diffuse components. Some strong biases are observed for Klutcher model and Temps and Coulson model for both sky conditions. In the original paper, the scatter plots of the modeling errors are displayed; they show consistency with Table 6.1. Interested readers can refer to (Yang et al., 2013a).

6.2.3 Evaluation of 5 decomposition models

DNI and DHI can be predicted from GHI using the decomposition models in situations when the DNI or DHI measurements are unavailable. Table 6.2 shows the performance of five decomposition models over a period of one year, 2011. GHI measurements from the SPN1 pyranometer are used as inputs to the decomposition models to predict DHI and DNI; the output (predicted DHI) is compared with DHI measurements from the SPN1.

Table 6.2 Performance of five decomposition models (predicting DHI from GHI in a tropical region) over a period of one year, 2011.

Model	MBE [W/m^2]	cRMSE [%]	U_{95} [%]
All-sky, N=44495			
Erbs	-13.32	32.02	71.81
Orgill	-12.85	34.50	68.80
Reindl (univariate)	-13.74	34.71	69.37
Maxwell	-13.27	34.94	69.73
Reindl (bivariate)	0.43	31.76	62.26
Mean observed [W/m^2]			195.49
Clear-sky, N=757			
Erbs	66.59	24.50	126.57
Orgill	76.26	25.89	143.37
Reindl (univariate)	85.97	22.00	157.21
Maxwell	97.36	43.29	191.07
Reindl (bivariate)	117.46	23.83	211.76
Mean observed [W/m^2]			111.46

The large cRMSE values obtained in Table 6.2 are consistent with the results from the many studies of the literature. The errors originate from the one–to–many mapping from GHI to DHI. Recall that GHI and DHI may also be represented using transmittance K_t and K_d. Fig. 6.2 shows the scatter plot for K_t, K_d pairs during 2011 January under different zenith angle ranges. It is observed that the possible range of K_d varies from 0.1 to 0.5 for K_t values greater than 0.1. The range of K_d is weakly dependent on zenith angle. As all the decomposition models describe a one–to–one mapping between K_t and K_d, a large cRMSE is expected. The details of the one–to–many mapping could be found in the study by Ridley et al. (2010).

More elaborate separation methods (e.g. Maxwell and Reindl bivariate models) do not out–perform the simpler ones (e.g. the Erbs, Orgill and Reindl univariate models). This

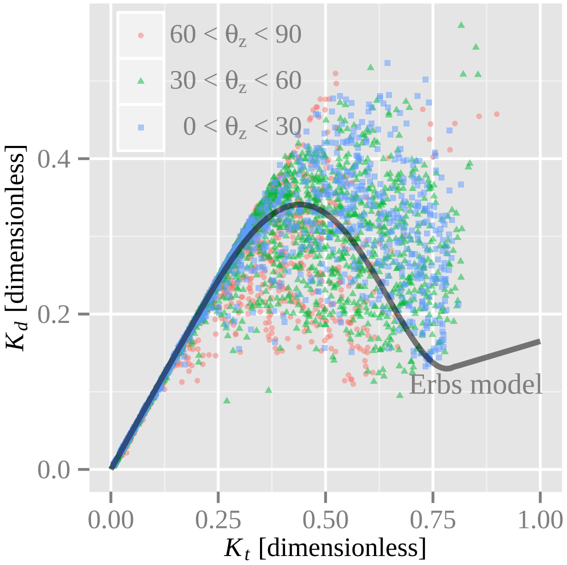

Fig. 6.2 Scatter plot for K_{t}, K_{d} pairs during 2011 January under different zenith angle ranges. Erbs model is plotted to demonstrate the non–injective mapping from K_{t} to K_{d}.

conclusion is also observed by Gueymard (2009) in his comparison of models with mid–latitude data. It is interesting to note that the decomposition models perform worse in clear sky conditions as compared to all sky conditions. Large positive MBEs are observed for all models showing strong over–prediction. This is expected as: with the same K_{t} value, K_{d} is much smaller during a clear sky condition than cloudy conditions, i.e., clear sky conditions are very likely to be the points below the curve in Fig. 6.2.

6.2.4 Combination of decomposition models and transposition models

Decomposition models alone introduce large errors for DHI prediction. The effect of these errors on irradiance conversion by assuming unavailable DHI measurements is examined in this section. In other words, GHI is used as the only input for conversion from horizontal to tilt.

The four isotropic models used in section 6.2.2 show similar accuracy for I_{t} prediction. The classic Liu and Jordan model is thus selected to represent all isotropic models. As the Klucher model and the Temps and Coulson model do not perform well, as shown in Table 6.1, these models are not considered in this analyses. The Hay model is not included as it can be represented using the Skartveit and Olseth model when $\Omega = 0$ (see appendix E). Therefore, only three anisotropic models, namely, those of Perez, Reindl and Skartveit and Olseth, are selected.

Table 6.3 shows the error metrics for various combinations of transposition models and decomposition models over a period of one year, 2011. For this exercise, only GHI measurements from S111 are used as inputs to Eqn. (6.8). DHI and DNI components are estimated using decomposition models and the results (converted I_t values) are compared with the measurements from S111a and S111b separately.

Table 6.3 Performance of five decomposition models with four transposition models (converting from horizontal to tilted) over a period of one year, 2011. Only GHI measurements from SPN1 are used as input, DNI and DHI are estimated using various decomposition models, the output (converted global irradiance on tilted plane) is compared with measurements from the reference cells.

	S111a	$s = 18.3°$	66° NE	S111b	$s = 6.1°$	246° SW
Model	MBE [W/m^2]	cRMSE [%]	U_{95} [%]	MBE [W/m^2]	cRMSE [%]	U_{95} [%]
Isotropic						
Liu and Jordan						
+ Erbs	0.86	11.25	22.05	7.18	8.25	16.60
+ Orgill	0.86	11.25	22.06	7.25	8.24	16.61
+ Reindl (univariate)	1.03	11.11	21.79	7.18	8.23	16.57
+ Maxwell	2.17	**10.48**	20.57	6.85	**8.23**	16.53
+ Reindl (bivariate)	1.41	11.30	22.16	7.49	8.25	16.66
Anisotropic						
Perez						
+ Erbs	0.91	10.02	19.65	6.29	8.17	16.36
+ Orgill	0.72	10.01	19.61	6.31	8.16	16.35
+ Reindl (univariate)	0.72	9.89	18.39	6.23	8.15	16.32
+ Maxwell	2.18	9.55	18.76	6.13	8.22	16.44
+ Reindl (bivariate)	0.70	9.93	19.47	6.41	8.16	16.35
Reindl						
+ Erbs	4.81	9.84	19.43	6.11	8.30	16.59
+ Orgill	5.12	9.79	19.36	6.16	8.31	16.61
+ Reindl (univariate)	6.27	**9.43**	18.70	6.97	7.99	16.03
+ Maxwell	8.80	10.05	20.08	6.74	8.12	16.22
+ Reindl (bivariate)	7.92	9.59	19.13	8.03	**7.90**	15.96
Skartveit and Olseth						
+ Erbs	4.02	9.85	19.41	6.04	8.31	16.59
+ Orgill	4.36	9.81	19.34	6.10	8.31	16.61
+ Reindl (univariate)	4.69	9.79	19.32	5.99	8.33	16.63
+ Maxwell	6.19	10.84	21.46	5.38	8.69	17.27
+ Reindl (bivariate)	5.47	10.13	20.03	6.22	8.42	16.83
Mean observed [W/m^2]			398.59			369.62

Table 6.3 shows that the best performance using a combination of transposition models and decomposition models is given by Reindl plus the Reindl univariate model for S111a, Reindl plus the Reindl bivariate model for S111b. It is important to note that, for small inclination angles, for example S111b, the performance of anisotropic models is very similar to those using the isotropic approximation. It should be noted that if decomposition models are used to estimate DHI and DNI, there will be small additional errors to the results from Table 6.1.

6.3 Converting irradiance from tilt to horizontal

Tilt to horizontal irradiance conversion is studied in this section. Although by using an anisotropic R_d formulation can reduce conversion errors, for small collector tilts like those encountered in the tropics, the Liu and Jordan isotropic approximation is used for R_d:

$$R_\mathrm{d} = \frac{1+\cos s}{2} = \cos^2\left(\frac{s}{2}\right) \tag{6.9}$$

through out this section. Tilt to horizontal conversion using an anisotropic model is demonstrated in chapter 7.

6.3.1 Problem formulation

Regardless the choice of decomposition model, the target function is a piecewise nonlinear equation due to the nature of various decomposition models. A numerical method is used to search for the root of the equation.

Most numerical techniques that involve gradient calculation are computationally expensive. I choose a simple search method using the bisection procedure combined with the linear or quadratic inverse interpolation. This method is described by Brent (1973). This method is implemented in both C (Forsythe et al., 2001) and R (R Core Team, 2014). As Brent's method only works for continuous functions, I perform the minimization for each

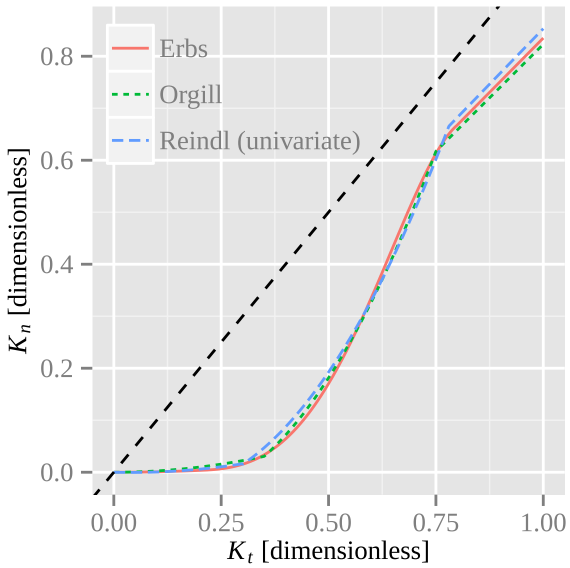

Fig. 6.3 K_n versus K_t for three univariate decomposition models, namely, Erbs, Orgill and Reindl (univariate) models.

intervals for our target function, i.e., for each K_t range described in various decomposition models. Although Brent's method efficiently finds the solutions to the target function, it overlooks certain physical constraints of our application. In fact, the only applied constraint is the non–negativity of all transmittances.

6.3.2 Univariate Models

For all three univariate decomposition models, the constraints are satisfied under all circumstances. Fig. 6.3 shows K_n versus K_t plotted for three univariate decomposition models, namely, the Erbs, Orgill and Reindl (univariate) models. It is clear that K_n is positive for all K_t in these three models. The fact that K_n is smaller for all corresponding K_t (curves are below the 1:1 line) leads to positive K_d values as

$$K_\mathrm{d} = K_\mathrm{t} - K_\mathrm{n} \tag{6.10}$$

6.3.3 Reindl (Bivariate) Model

For the Reindl (bivariate) model, the constraints are given in appendix F. Following the constraints, a valid region for K_{t}, K_{n} pairs under Reindl model assumptions can be drawn. I refer the interested readers to (Yang et al., 2013a).

6.3.4 Maxwell Model

The Maxwell model is another bivariate model which is more elaborate than previously described decomposition models. Several additional parameters are involved in the model to relate K_{d} and K_{t}, namely, K_{nc}, m_r and ΔK_{n}. Three constraints apply to the Maxwell model: 1) $\theta_z \leq 86°$; 2) $\Delta K_{\mathrm{n}} \geq 0$ and 3) $K_{\mathrm{nc}} > \Delta K_{\mathrm{nc}}$.

Clear sky direct normal transmittance K_{nc} represents the maximum proportion of direct normal irradiance reaching the Earth's surface at any instant. Therefore the valid range for K_{nc} is between 0 and 1. As the relationship between K_{nc} and θ_z is empirical, we need to examine the range of zenith angle used to develop Eqn. (6.8). Maxwell (1987) uses relative optical air mass values in the range from 1 to 12 to develop Eqn. (F.10). The air mass range of 1 to 12 corresponds to zenith angle ranged from $0°$ to $85.853°$ ($\approx 86°$) which give rise to the first constraint for the algorithm, $\theta_z \leq 86°$.

The second constraint relates to ΔK_{n}, $\Delta K_{\mathrm{n}} \geq 0$ (see Figs. 3–5 in (Maxwell, 1987) for details). ΔK_{n} is a function of θ_z and K_{t}. Fig. 6.4 plots the variation of ΔK_{n} with K_{t} for various zenith angles. It is clear from Fig. 6.4 that for large zenith angles, ΔK_{n} may take negative values for certain values of K_{t}. Therefore, K_{t} is only valid below a certain threshold. For instance when $\theta_z = 80°$, K_{t} must be smaller than 0.6 for any valid ΔK_{n} estimation.

$K_{\mathrm{nc}} - \Delta K_{\mathrm{n}} > 0$ is the third constraint. This constraint is necessary as the value of direct normal transmittance should not go beyond the clear sky condition. Fig. 6.5 plots the variation of K_{n} ($K_{\mathrm{n}} = K_{\mathrm{nc}} - \Delta K_{\mathrm{n}}$) with K_{t} for various zenith angles. For various zenith angles, the function $K_{\mathrm{n}} = f(K_{\mathrm{t}})$ intersects the x–axis at different positions. These

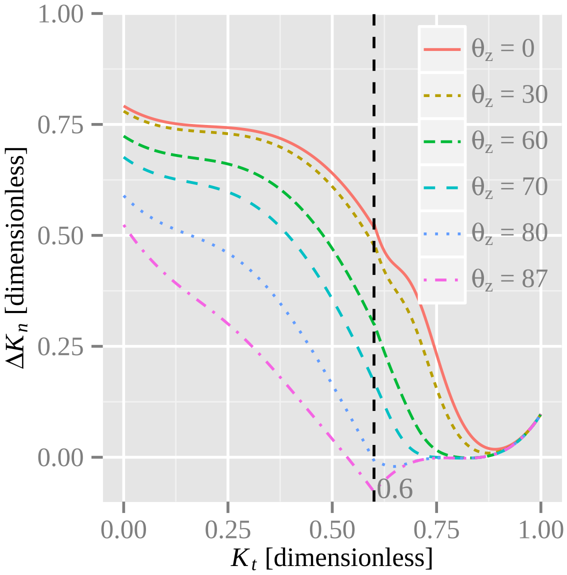

Fig. 6.4 ΔK_n versus K_t for various zenith angles.

x–intercepts act as lower bounds for possible K_t values.

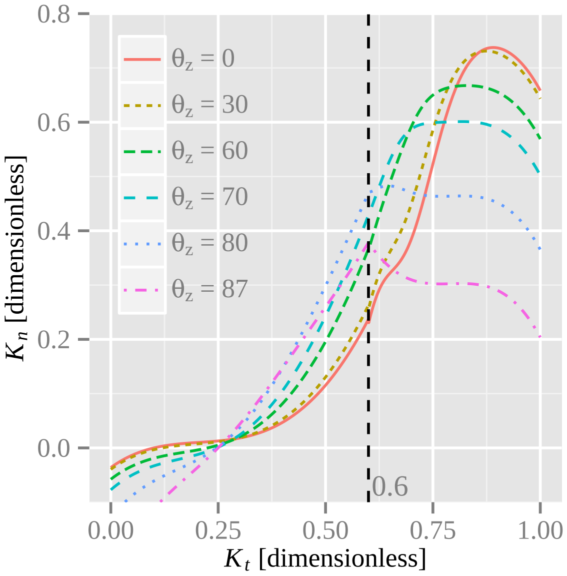

Fig. 6.5 K_n versus K_t for various zenith angles.

As these three constraints describe necessary conditions for the existence of K_t, all must be satisfied for the solutions obtained by Brent's minimization to be valid for Maxwell model.

6.4 Results and discussions

Table 6.4 and 6.5 show the monthly performance of various models converting solar irradiance on tilted planes to GHI. It is observed that the cRMSE for irradiance conversion from tilt to horizontal is slightly larger than those from horizontal to tilt conversions. Recall that all the decomposition models are shown to introduce large errors in K_{d} and K_{n} in section 6.2. These errors will be carried forward into prediction of I_{dif} and I_{dir}.

When irradiance is converted from tilt to horizontal, all three irradiance components on the horizontal plane, namely, GHI, DNI and DHI need to be approximated (related through various decomposition models). The errors from decomposition models will be embedded in all three irradiance components. On the other hand, when we convert irradiance from horizontal to tilt, only DNI and DHI are approximated, while GHI is measured. Therefore, in this case, the errors from decomposition models will be embedded in DNI and DHI components only, thus a smaller cRMSE is expected in Table 6.3 than in Tables 6.4 and 6.5.

6.4.1 Case study of the Maxwell model

Tables 6.4 and 6.5 show the overall performance of our algorithm converting solar irradiance from tilt to horizontal. I focus on the performance of my algorithm over a one–day period in this section. The conversion results from the Maxwell model are used to illustrate the findings.

In the morning, due to a smaller incident angle at S111a than at S111b, a larger DNI component is received at S111a. S111a expects higher irradiance levels than measurements at S111b. Similarly, in the afternoon, measurements at S111a are lower than measurements at S111b. This geometric configuration is illustrated in Fig. 6.6 (a), showing a typical day's measurements at S111a and S111b during 2011 July 5. I apply the algorithm and constraints described in section 6.3 on the one–day data. The tilt to horizontal conversion result on 2011 July 5 is shown Fig. 6.6 (b). A significant reduction in the difference between two

Table 6.4 Performance of five decomposition models (tilted to horizontal), using Liu and Jordan isotropic approximation for R_d, over a period of six months, from 2011 January to June. Global irradiance on tilted plane measurements from silicon sensors are inputs, the output converted GHI is compared to SPN1 GHI measurements.

	S111a	$s = 18.3°$	66° NE	S111b	$s = 6.1°$	246° SW
Model	MBE [W/m^2]	cRMSE [%]	U_{95} [%]	MBE [W/m^2]	cRMSE [%]	U_{95} [%]
2011 January						
Erbs	-6.35	15.21	30.07	-1.87	9.65	18.96
Orgill	-6.56	15.19	30.05	-1.90	9.64	18.94
Reindl (univariate)	-6.48	14.94	29.56	-1.81	9.61	18.88
Maxwell	-8.45	13.91	27.61	-2.02	8.63	16.95
Reindl (bivariate)	-10.40	14.13	28.23	-3.37	8.75	17.24
2011 February						
Erbs	-15.66	12.00	24.40	-11.47	6.28	13.33
Orgill	-16.00	12.13	24.70	-11.43	6.28	13.34
Reindl (univariate)	-15.81	11.94	24.33	-11.31	6.24	13.25
Maxwell	-17.74	11.34	23.30	-11.89	5.84	12.45
Reindl (bivariate)	-17.41	12.35	25.23	-11.84	6.12	13.03
2011 March						
Erbs	-4.30	13.56	26.67	-4.78	9.29	18.39
Orgill	-4.75	13.68	26.93	-4.79	9.27	18.36
Reindl (univariate)	-4.70	13.39	26.56	-4.62	9.21	18.24
Maxwell	-6.21	12.18	24.07	-5.87	8.00	15.95
Reindl (bivariate)	-6.59	13.33	26.32	-6.06	8.87	17.65
2011 April						
Erbs	-9.14	12.80	25.44	-13.78	8.29	17.54
Orgill	-9.08	12.87	25.57	-13.71	8.27	17.52
Reindl (univariate)	-8.99	12.76	25.36	-13.55	8.23	17.42
Maxwell	-10.70	11.72	23.41	-15.37	7.40	15.87
Reindl (bivariate)	-10.62	12.52	24.93	-16.21	7.65	16.56
2011 May						
Erbs	-5.52	12.14	23.93	-12.90	8.10	17.16
Orgill	-5.25	12.21	24.07	-12.85	8.13	17.23
Reindl (univariate)	-5.13	12.15	23.95	-12.74	8.08	17.12
Maxwell	-6.43	11.04	21.83	-14.34	7.39	15.80
Reindl (bivariate)	-5.99	11.86	23.40	-14.93	7.52	16.29
2011 June						
Erbs	-5.18	13.45	26.51	-6.99	9.55	19.10
Orgill	-5.19	13.50	26.61	-7.01	9.57	19.15
Reindl (univariate)	-5.02	13.40	26.41	-6.94	9.55	19.09
Maxwell	-5.48	12.18	24.02	-7.89	8.84	17.72
Reindl (bivariate)	-6.18	12.93	25.51	-9.16	8.98	18.17

stations is evident.

6.5 Chapter conclusion

In this chapter, transposition models and its converse, the inverse transposition models, are studied. Irradiance data collected using reference cells on two tilted planes, namely, a 18.3°

Table 6.5 Continuation of previous table with 2011 July to December data.

Station	S111a	$s = 18.3°$	66° NE	S111b	$s = 6.1°$	246° SW
Model	MBE [W/m^2]	cRMSE [%]	U_{95} [%]	MBE [W/m^2]	cRMSE [%]	U_{95} [%]
2011 July						
Erbs	-20.44	13.32	27.38	-18.65	7.82	17.21
Orgill	-20.44	13.46	27.69	-18.42	7.88	17.32
Reindl (univariate)	-20.03	13.36	27.45	-18.31	7.85	17.25
Maxwell	-20.91	12.35	25.49	-19.76	7.51	16.59
Reindl (bivariate)	-20.88	13.38	27.50	-19.44	7.60	16.90
2011 August						
Erbs	-17.99	11.80	24.58	-14.44	5.99	13.68
Orgill	-17.92	11.86	24.72	-14.44	6.00	13.74
Reindl (univariate)	-17.68	11.74	24.46	-14.38	5.94	13.62
Maxwell	-19.91	10.57	22.35	-16.36	5.33	12.56
Reindl (bivariate)	-20.59	11.35	23.87	-17.21	5.49	13.20
2011 September						
Erbs	-27.13	12.67	27.75	-13.50	6.96	15.11
Orgill	-27.04	12.64	27.77	-13.41	7.00	15.20
Reindl (univariate)	-26.62	12.40	27.25	-13.34	6.95	15.11
Maxwell	-41.26	10.04	23.72	-23.88	4.03	11.00
Reindl (bivariate)	-30.65	12.37	27.58	-15.68	6.66	14.90
2011 October						
Erbs	-14.95	12.82	26.26	-6.85	7.15	14.50
Orgill	-14.94	12.85	26.33	-6.90	7.15	14.52
Reindl (univariate)	-14.87	12.67	25.99	-6.78	7.11	14.42
Maxwell	-17.89	12.13	25.18	-7.58	6.20	12.67
Reindl (bivariate)	-20.10	12.16	25.44	-9.18	6.53	13.52
2011 November						
Erbs	-1.75	11.30	22.18	-1.11	7.50	14.71
Orgill	-2.02	11.51	22.60	-1.16	7.49	14.96
Reindl (univariate)	-2.08	11.38	22.34	-1.01	7.44	14.62
Maxwell	-2.64	10.38	20.39	-0.84	6.22	12.21
Reindl (bivariate)	-3.90	10.79	21.24	-1.94	6.86	13.49
2011 December						
Erbs	12.62	14.76	29.79	23.60	13.99	30.97
Orgill	11.88	14.89	29.97	23.06	14.05	31.00
Reindl (univariate)	12.18	14.96	30.13	23.19	14.01	30.96
Maxwell	11.41	13.73	27.56	24.02	12.09	27.17
Reindl (bivariate)	10.32	14.17	28.30	24.60	13.57	30.10

NE facing plane and a 6.1° SW facing plane, are individually used to reconstruct the GHI measurements made using the horizontally installed SPN1 pyranometer. cRMSE of $\approx 13\%$ and $\approx 6\%$ are found for the two tilts respectively.

Inverse transposition model aims at solving three unknowns (namely, I_{glo}, I_{dir}, I_{dif}) using a set of tilted irradiance measurements I_{t}. Although Eqn. (6.2) provides a link between GHI, DHI and DNI, so that one of the three unknown can be represented using the other two, we still cannot solve two unknowns using one equation. Decomposition models provide representations of DNI (or DHI) using GHI, my method is thus able to reconstruct all horizontal

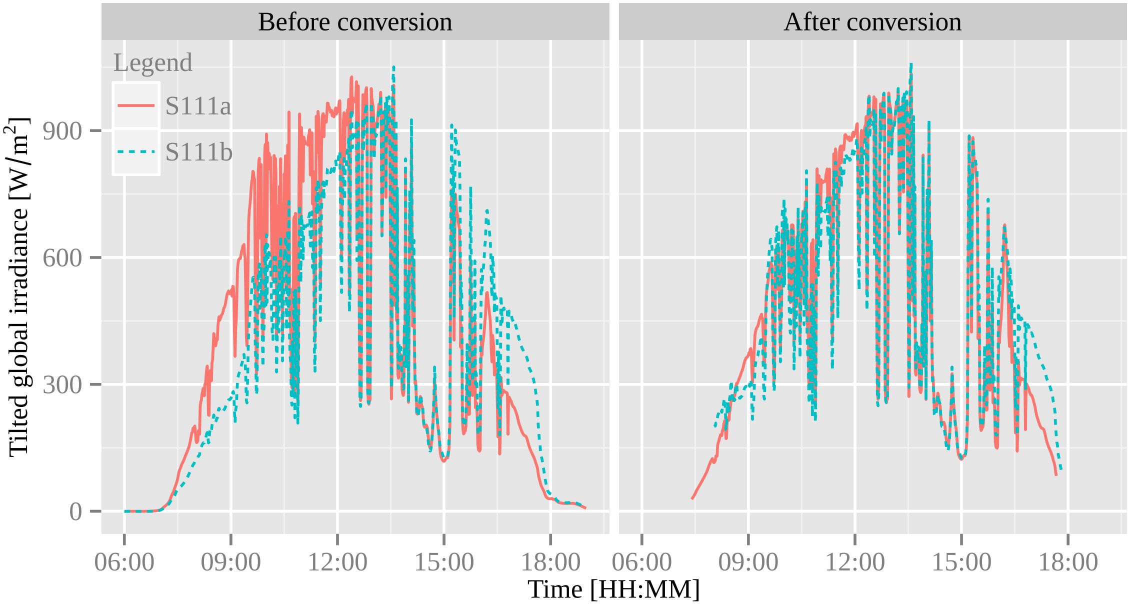

Fig. 6.6 (a) Time series plot for I_{t} measured on 2011 July 5 at stations S111a and S111b. (b) Converted GHI.

irradiance components using Eqn. (6.1). However, the non–injective decomposition models are the main source of errors. To solve the inverse transposition model deterministically, we can utilize two sets of irradiance measurements from two different tilt angles for horizontal data reconstruction. In the next chapter, such inverse decomposition models are described.

As the eventual goal of this chapter is to input these transposed horizontal data into the spatio–temporal forecasting models, their accuracies have to considered. The accuracies of the inverse transposition models depend on the tilt angle of the reference cell. In this chapter, the cRMSE from data using the 6.1° sensor is within the tolerable range for forecasting applications, however the conversion errors using data from the 18.3° sensor is significant. For many PV systems installed in the mid–latitude sites, the array tilts are often in the range of 20° to 40°. The inverse transposition models herein described are not validated with such configurations, nevertheless, the errors are believed to be even larger than those displayed in Tables 6.4 and 6.5. In the next chapter, data from 10°, 20°, 30° and 40° are used for validation of the inverse transposition models using both single– and multiple–

sensors approaches. One can find that by using the multi–reference cells approach, the inverse transposition models errors are significantly reduced.

Chapter 7

Inverse transposition using two or more reference cells

The previous chapter shows how to use the data from a single reference cell on an arbitrary tilted plane to estimate the horizontal irradiance components. In this section, inverse transposition models that use data from multiple–reference cells are proposed with validation.

Both isotropic and anisotropic transposition models have been introduced earlier, their formulations can be found in Appendix E. Although the isotropic transposition models are simplistic, the anisotropic nature of diffuse irradiance has been the largest source of error associated with this assumption (Ma and Iqbal, 1983). Among those anisotropic transposition models seen in the previous chapter, the Perez model is the most universal and most frequently used transposition model. In contrast with chapter 6 where many transposition models are considered and compared, I focus on the Perez model in this chapter. Nevertheless, multi–sensor inverse transposition model using the isotropic assumptions (Faiman et al., 1987, 1993) is used as a benchmark toward the end of this chapter.

Beside switching the inverse transposition model from a single–sensor approach to a multi–sensor approach, several other improvements are made in this chapter: 1) an anisotropic formulation of R_{r} is considered, 2) reflection loss and spectral loss of the reference cell are taken into the account, and most importantly 3) the Perez model coefficients are adjusted using the tropical data.

7.1 An introduction to the Perez model

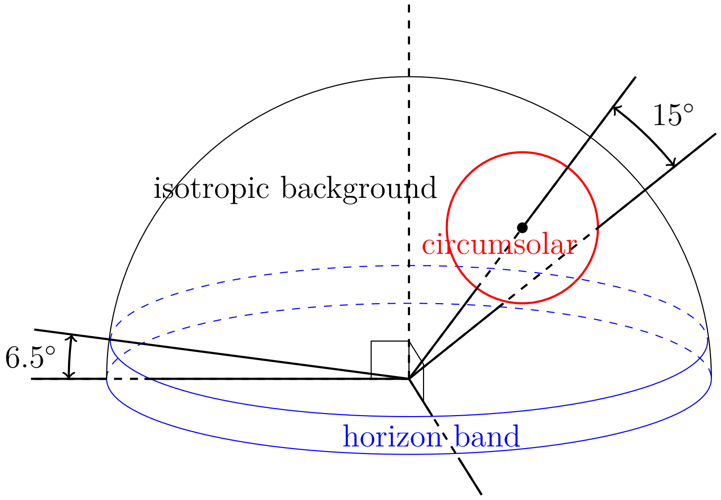

Fig. 7.1 The three–part geometrical framework described by Perez et al. (1986).

The Perez irradiance model offers a practical representation of solar irradiance by considering the sky hemisphere as a three–part geometrical framework, namely, circumsolar disc, horizon band and the isotropic background, as shown in Fig. 7.1. Radiation from each of these zones is modeled differently to account various types of scattering which cause the anisotropy. Perez et al. (1986) proposed the first version of the Perez model. The **simplified Perez diffuse irradiance model** was then proposed (Perez et al., 1987); it is given by:

$$I_{\mathrm{t,dif}} = I_{\mathrm{dif}} \left[(1 - F_1) \frac{1 + \cos s}{2} + F_1 \frac{a}{b} + F_2 \sin s \right], \tag{7.1}$$

where I_{dif} and $I_{\mathrm{t,dif}}$ are diffuse irradiance on horizontal plane and tilted plane, respectively; s is the plane tilt angle;

$$a = \max\{0, \cos\theta_i\}, \tag{7.2}$$

$$b = \max\{\cos 85^\circ, \cos\theta_z\}, \tag{7.3}$$

given by Perez et al. (1988) are a result of the approximation by assuming that all circumsolar energy originates from a point source; θ_i is the solar incidence angle; θ_z is the zenith angle in degrees;

$$F_1 = \max\{0, F_{11}(\varepsilon') + \Delta' F_{12}(\varepsilon') + \vartheta_z F_{13}(\varepsilon')\}, \tag{7.4}$$

$$F_2 = F_{21}(\varepsilon') + \Delta' F_{22}(\varepsilon') + \vartheta_z F_{23}(\varepsilon'), \tag{7.5}$$

are defined as reduced brightness coefficients where Δ' is the sky's brightness; ε' is the sky's clearness, ϑ_z is the zenith angle in radians. The parameters involved in Δ' and ε' calculations have been defined earlier in chapters 3, 5 and 6. The unknown parameters F_{11}, F_{12}, F_{13}, F_{21}, F_{22}, F_{23} can be determined empirically from measurements of the irradiance on tilted surfaces. The set of F_{11}, F_{12}, F_{13}, F_{21}, F_{22}, F_{23} has evolved many times. The most widely accepted set of coefficients is given by Perez et al. (1990) as shown in Appendix E and repeated here in Table 7.1, which is based on data from Albany (USA), Geneva (Switzerland), Los Angeles (USA), Albuquerque (USA), Phoenix (USA), Cape Canaveral (USA), Osage (USA), Trappes (France), and Carpentras (France).

Table 7.1 Perez model coefficients for irradiance as a function of the sky's clearness index ε' (Perez et al., 1990)

ε'	F_{11}	F_{12}	F_{13}	F_{21}	F_{22}	F_{23}
$[1, 1.065)$	−0.0083	0.5877	−0.0621	−0.0596	0.0721	−0.022
$[1.065, 1.23)$	0.1299	0.6826	−0.1514	−0.0189	0.066	−0.0289
$[1.23, 1.5)$	0.3297	0.4869	−0.2211	0.0554	−0.064	−0.0261
$[1.5, 1.95)$	0.5682	0.1875	−0.2951	0.1089	−0.1519	−0.014
$[1.95, 2.8)$	0.873	−0.392	−0.3616	0.2256	−0.462	0.0012
$[2.8, 4.5)$	1.1326	−1.2367	−0.4118	0.2878	−0.823	0.0559
$[4.5, 6.2)$	1.0602	−1.5999	−0.3589	0.2642	−1.1272	0.1311
$[6.2, +\infty)$	0.6777	−0.3273	−0.2504	0.1516	−1.3765	0.2506

Although Table 7.1 is considered to be at an asymptotic level of optimization, the locations (see above) used to fit the original set of coefficients do not include a tropical site. Meteorological differences between the original sites and tropical regions may therefore affect the performance of the transposition model. Singapore is located near the equator with a latitude of 1.3°N and has a tropical climate. It is therefore well–suited for investigating the effect of locally (under a tropical weather condition) adjusted model coefficients. I explicitly express the mathematical derivations here to facilitate further applications in other locations where model coefficients adjustment may apply.

7.2 Model coefficients adjustment

A least square approach is used to adjust the model coefficients F_{11}, F_{12}, F_{13}, F_{21}, F_{22}, F_{23}. Substituting Eqns. (7.4) and (7.5) into Eqn. (7.1) yields

$$\begin{aligned} I_{\mathrm{t,dif}} =& I_{\mathrm{dif}}\frac{1+\cos s}{2} + I_{\mathrm{dif}}\left(\frac{a}{b} - \frac{1+\cos s}{2}\right)(F_{11} + \Delta' F_{12} + \vartheta_z F_{13}) \\ &+ I_{\mathrm{dif}} \sin s (F_{21} + \Delta' F_{22} + \vartheta_z F_{23}). \end{aligned} \tag{7.6}$$

Given n tilted sensors and m samples of I_{dif} (and $I_{\mathrm{t,dif}}$ correspondingly), the equivalent linear algebra of (7.6) is

$$\boldsymbol{A}\boldsymbol{X} = \boldsymbol{Y}, \tag{7.7}$$

where

$$\boldsymbol{X} = \begin{pmatrix} F_{11} & F_{12} & F_{13} & F_{21} & F_{22} & F_{23} \end{pmatrix}^{\top}, \in \mathbb{R}^6 \tag{7.8}$$

and

$$\boldsymbol{A} = \begin{pmatrix} A_1^{1,1} & A_2^{1,1} & A_3^{1,1} & A_4^{1,1} & A_5^{1,1} & A_6^{1,1} \\ \vdots & \vdots & \vdots & \vdots & \vdots & \vdots \\ A_1^{1,m} & A_2^{1,m} & A_3^{1,m} & A_4^{1,m} & A_5^{1,m} & A_6^{1,m} \\ \vdots & \vdots & \vdots & \vdots & \vdots & \vdots \\ A_1^{n,1} & A_2^{n,1} & A_3^{n,1} & A_4^{n,1} & A_5^{n,1} & A_6^{n,1} \\ \vdots & \vdots & \vdots & \vdots & \vdots & \vdots \\ A_1^{n,m} & A_2^{n,m} & A_3^{n,m} & A_4^{n,m} & A_5^{n,m} & A_6^{n,m} \end{pmatrix}, \quad \in \mathbb{R}^{nm\times 6} \tag{7.9}$$

with $A_1^{i,j} = I_{\text{dif}}^j \left[a_{i,j}/b_j - (1+\cos s_i)/2\right]$, $A_2^{i,j} = \Delta_j' A_1^{i,j}$, $A_3^{i,j} = \vartheta_z^j A_1^{i,j}$, $A_4^{i,j} = I_{\text{dif}}^j \sin s_i$, $A_5^{i,j} = \Delta_j' A_4^{i,j}$, $A_6^{i,j} = \vartheta_z^j A_4^{i,j}$, $i = 1, \cdots, n$, $j = 1, \cdots, m$.

$$\boldsymbol{Y} = \begin{pmatrix} Y_{1,1} & \cdots & Y_{1,m} & \cdots, Y_{n,1} & \cdots & Y_{n,m} \end{pmatrix}^\top, \quad \in \mathbb{R}^{nm} \tag{7.10}$$

with $Y_{i,j} = I_{\text{t,dif}}^{i,j} - I_{\text{dif}}^j (1+\cos s_i)/2$, $i = 1, \cdots, n$, $j = 1, \cdots, m$. The least square solution to Eqn. (7.7) is given by

$$\boldsymbol{X} = \left(\boldsymbol{A}^\top \boldsymbol{A}\right)^{-1} \boldsymbol{A}^\top \boldsymbol{Y}. \tag{7.11}$$

This least squares method is described by Perez et al. (1988). To establish an accurate fit, the method requires n sets of measurements of tilted diffuse irradiance and a set of horizontal diffuse irradiance measurements (each set has m samples), i.e., $I_{\text{t,dif}}^{i,j}$ and I_{dif}^j. However in practice, tilted diffuse irradiance measurements are scarce. This is particularly true in developing countries where long term, precisely calibrated irradiance datasets are often not available. Cost–effective silicon sensors can however be used to measure global tilted irradiance, $I_{\text{t}} = I_{\text{t,dif}} + I_{\text{t,dir}}$, where $I_{\text{t,dir}}$ is the in–plane direct irradiance. Such sensors are commonly installed in medium and larger PV systems for system monitoring and it is likely that such data becomes widely available as PV systems proliferate globally. A novel approach that circumvents the need for tilted diffuse component observations is therefore proposed.

Two types of devices are commonly used to perform radiometric measurements, namely, thermopile pyranometers and reference cells. Meydbray et al. (2012a) pointed out three disadvantages of reference cells as compared to a tilted pyranometer: 1) reference cells suffer from spectral loss as they have a narrow wavelength response, 2) reference cells suffer from reflection losses owing to its flat surface design and 3) the linearity of the reference cells' output signals is affected by temperature, this however can be corrected with an on–board temperature sensor. Therefore the spectral and reflection losses need to be accounted for when the reference cell measurements are used. The losses are embedded in the formulations as follows.

7.2.1 Derivation of $I_{\mathrm{t,dif}}$

The irradiance due to ground reflection (extended from Temps and Coulson, 1977), $I_{\mathrm{t,refl}}$, is given by

$$I_{\mathrm{t,refl}} = \frac{1}{2}\rho'(I_{\mathrm{beam}} + I_{\mathrm{dif}})(1 - \cos s)[1 + \sin^2(\theta_z/2)]|\cos(\alpha - \beta)| \tag{7.12}$$

where ρ' is the foreground's albedo, α and β are the azimuth of sun and plane respectively. I_{beam} is the horizontal direct irradiance or horizontal beam irradiance; $I_{\mathrm{beam}} = I_{\mathrm{dir}} \cos\theta_z$. Note that this reflected irradiance component was given earlier as $\rho' I_{\mathrm{glo}} R_{\mathrm{r}}$ in chapter 6 and $R_{\mathrm{r}} = 0.5(1 - \cos s)$ follows an isotropic assumption. This isotropic assumption on the transposition factor for ground reflection is adopted by many recent studies (e.g. Evseev and Kudish, 2009; Gueymard, 2009; Yadav and Chandel, 2013; Yoshida et al., 2013) due to its simplicity, nevertheless an anisotropic model for R_{r} is used in this chapter. Many authors have proposed anisotropic ground reflection models (Gardner and Nadeau, 1988; Gueymard, 1987), but lack of experimental data has hampered their validation. Eqn. (7.12) models R_{r} as $0.5(1 - \cos s)[1 + \sin^2(\theta_z/2)]|\cos(\alpha - \beta)|$. This anisotropic model was first proposed by Temps and Coulson (1977), and is a well–accepted anisotropic model for R_{r} (Elminir et al., 2006).

It is convenient here to add Eqn. (7.12) in the $I_{\mathrm{t,dif}}$ expression so $I_{\mathrm{t,dif}}$ now accounts for both in–plane diffuse and reflected components; at the same time, the reflection loss and spectral loss as L_{refl} and L_{spec} are added into the formulation, then Eqn. (7.6) becomes

$$\begin{aligned} I_{\mathrm{t,dif}} =& 0.5\rho'(I_{\mathrm{bream}} + I_{\mathrm{dif}})(1 - \cos s)\left[1 + \sin^2\left(\frac{\theta_z}{2}\right)\right]|\cos(\alpha - \beta)|(1 - L_{\mathrm{refl}})(1 - L_{\mathrm{spec}}) \\ &+ I_{\mathrm{dif}}\frac{1 + \cos s}{2}(1 - L_{\mathrm{refl}})(1 - L_{\mathrm{spec}}) \\ &+ I_{\mathrm{dif}}\left(\frac{a}{b} - \frac{1 + \cos s}{2}\right)(1 - L_{\mathrm{refl}})(1 - L_{\mathrm{spec}})(F_{11} + \Delta' F_{12} + \vartheta_z F_{13}) \\ &+ I_{\mathrm{dif}} \sin s(1 - L_{\mathrm{refl}})(1 - L_{\mathrm{spec}})(F_{21} + \Delta' F_{22} + \vartheta_z F_{23}). \end{aligned} \tag{7.13}$$

Having obtained the $I_{\mathrm{t,dif}}$ representation, to construct I_{t}, $I_{\mathrm{t,dir}}$ is expressed as follows.

7.2.2 Derivation of $I_{\mathrm{t,dir}}$

$I_{\mathrm{t,dir}}$ can be calculated from I_h deterministically by geometry as:

$$I_{\mathrm{t,dir}} = I_{\mathrm{beam}} \frac{\cos\theta_i}{\cos\theta_z}. \tag{7.14}$$

If considering spectral and reflection losses, Eqn. (7.14) becomes:

$$I_{\mathrm{t,dir}} = I_{\mathrm{beam}} \frac{\cos\theta_i}{\cos\theta_z}(1-y)(1-L_{\mathrm{spec}}). \tag{7.15}$$

Here I use a set of parameter y provided by Fraunhofer ISE, which gives a piecewise linear representation of the reflection loss in $I_{\mathrm{t,dir}}$,

$$y = \begin{cases} 0, & \text{if } \theta_i \in [0, 30^\circ); \\ 0.0006(\theta_i - 30^\circ), & \text{if } \theta_i \in [30^\circ, 40^\circ); \\ 0.006 + 0.0012(\theta_i - 40^\circ), & \text{if } \theta_i \in [40^\circ, 50^\circ); \\ 0.018 + 0.0029(\theta_i - 50^\circ), & \text{if } \theta_i \in [50^\circ, 60^\circ); \\ 0.047 + 0.0068(\theta_i - 60^\circ), & \text{if } \theta_i \in [60^\circ, 65^\circ); \\ 0.081 + 0.0098(\theta_i - 65^\circ), & \text{if } \theta_i \in [65^\circ, 70^\circ); \\ 0.13 + 0.0166(\theta_i - 70^\circ), & \text{if } \theta_i \in [70^\circ, 75^\circ); \\ 0.213 + 0.0276(\theta_i - 75^\circ), & \text{if } \theta_i \in [75^\circ, 80^\circ); \\ 0.351 + 0.047(\theta_i - 80^\circ), & \text{if } \theta_i \in [80^\circ, 85^\circ); \\ 0.586 + 0.0828(\theta_i - 85^\circ), & \text{if } \theta_i \in [85^\circ, 90^\circ), \end{cases} \tag{7.16}$$

to account for the reflection loss of $I_{\mathrm{t,dir}}$ on the glass surface of silicon sensors.

Substituting Eqns. (7.13) and (7.15) into the equation $I_{\mathrm{t}} = I_{\mathrm{t,dir}} + I_{\mathrm{t,dif}}$, and dividing

I_{dif} on both sides yields:

$$\begin{aligned}\frac{I_{\text{t}}}{I_{\text{dif}}} =& \frac{I_{\text{beam}}\cos\theta_i(1-y)(1-L_{\text{spec}})}{I_{\text{dif}}\cos\theta_z} \\ &+ 0.5\rho'\frac{I_{\text{glo}}}{I_{\text{dif}}}(1-\cos s)[1+\sin^2(\theta_z/2)]|\cos(\alpha-\beta)|(1-L_{\text{refl}})(1-L_{\text{spec}}) \\ &+ \frac{1+\cos s}{2}(1-L_{\text{refl}})(1-L_{\text{spec}}) \\ &+ \left(\frac{a}{b}-\frac{1+\cos s}{2}\right)(1-L_{\text{refl}})(1-L_{\text{spec}})(F_{11}+\Delta' F_{12}+\vartheta_z F_{13}) \\ &+ \sin s(1-L_{\text{refl}})(1-L_{\text{spec}})(F_{21}+\Delta' F_{22}+\vartheta_z F_{23}). \end{aligned} \tag{7.17}$$

where $I_{\text{glo}} = I_{\text{dif}} + I_{\text{beam}}$ is the global horizontal irradiance. Write Eqn. (7.17) into linear algebra form:

$$\boldsymbol{A}^*\boldsymbol{X} = \boldsymbol{Y}^*, \tag{7.18}$$

where

$$\boldsymbol{A}^* = \begin{pmatrix} H_1^{1,1} & \Delta_1' H_1^{1,1} & \vartheta_z^1 H_1^{1,1} & H_2^{1,1} & \Delta_1' H_2^{1,1} & \vartheta_z^1 H_2^{1,1} \\ \vdots & \vdots & \vdots & \vdots & \vdots & \vdots \\ H_1^{1,m} & \Delta_m' H_1^{1,m} & \vartheta_z^m H_1^{1,m} & H_2^{1,m} & \Delta_m' H_2^{1,m} & \vartheta_z^m H_2^{1,m} \\ \vdots & \vdots & \vdots & \vdots & \vdots & \vdots \\ H_1^{n,1} & \Delta_1' H_1^{n,1} & \vartheta_z^1 H_1^{n,1} & H_2^{n,1} & \Delta_1' H_2^{n,1} & \vartheta_z^1 H_2^{n,1} \\ \vdots & \vdots & \vdots & \vdots & \vdots & \vdots \\ H_1^{n,m} & \Delta_m' H_1^{n,m} & \vartheta_z^m H_1^{n,m} & H_2^{n,m} & \Delta_m' H_2^{n,m} & \vartheta_z^m H_2^{n,m} \end{pmatrix}, \quad \in \mathbb{R}^{nm\times 6} \tag{7.19}$$

with

$$H_1^{i,j} = \left(\frac{a_{i,j}}{b_j}-\frac{1+\cos s_i}{2}\right)(1-L_{\text{refl}})(1-L_{\text{spec}}), \tag{7.20}$$

$$H_2^{i,j} = \sin s_i(1-L_{\text{refl}})(1-L_{\text{spec}}); \tag{7.21}$$

and

$$\boldsymbol{Y}^* = \begin{pmatrix} Y^*_{1,1} & \cdots & Y^*_{1,m} & \cdots & Y^*_{n,1} & \cdots & Y^*_{n,m} \end{pmatrix}^\top, \quad \in \mathbb{R}^{nm} \tag{7.22}$$

with

$$\begin{aligned} Y^*_{i,j} = & \frac{I^{i,j}_{\mathrm{t}}}{I^j_{\mathrm{dif}}} - (1 - L_{\mathrm{refl}})(1 - L_{\mathrm{spec}}) \\ & \times \left(\frac{1 + \cos s_i}{2} + 0.5\rho' \frac{I^j_{\mathrm{glo}}}{I^j_{\mathrm{dif}}} (1 - \cos s_i)[1 + \sin^2(\theta^j_z/2)] |\cos(\alpha_j - \beta_i)| \right) \\ & - \frac{I^j_{\mathrm{beam}} \cos \theta^{i,j}_i (1 - y_{i,j})(1 - L_{\mathrm{spec}})}{I^j_{\mathrm{dif}} \cos \theta^j_z}. \end{aligned} \tag{7.23}$$

Then, the parameters of F_{11}, F_{12}, F_{13}, F_{21}, F_{22}, F_{23} can be optimized by the least square method as follows:

$$\boldsymbol{X} = \left(\boldsymbol{A}^{*\top} \boldsymbol{A}^* \right)^{-1} \boldsymbol{A}^{*\top} \boldsymbol{Y}^*. \tag{7.24}$$

7.2.3 Derivation of α, θ_i and θ_z

By inspecting each components of (7.24), we need to calculate α, θ_i and θ_z. They are three frequently encountered solar positioning parameters. There are many simplified approximations for these parameters (e.g. Masters, 2004; Michalsky, 1988). To ensure sufficient accuracy, the Solar Position Algorithm (SPA) from National Renewable Energy Laboratory is used to calculate the azimuth of the sun, the incidence angle and the zenith angle. The details of this algorithm can be found in the open source C program by Reda and Andreas (2004, 2008).

7.2.4 Performance

All measurements used in this chapter are taken from the meteorological station at Solar Energy Research Institute of Singapore (SERIS). The horizontal global irradiance, I_{glo}, is measured by three devices: a silicon sensor (±5% uncertainty), a pyranometer (CMP11 from Kipp & Zonen, ±3% uncertainty) and a pyranometer (SPN1 from Delta–T, ±5%

uncertainty); horizontal diffuse irradiance is measured by the same pyranometer (SPN1); in–plane global irradiance is measured by four other silicon sensors with different tilts: 10°, 20°, 30°, 40°, with the same azimuth of 64° NE. All silicon sensors were calibrated at Fraunhofer ISE CalLab with on–board temperature sensors to perform temperature correction. Measurements are sampled with overall historical data availability higher than 99.7%. The sampling rate is 1 second; and the data is logged as 1 min averages. Fig. 7.2 shows a photograph of the irradiance measurement station located on the roof of SERIS.

Fig. 7.2 Photograph of the irradiance measurement station located on the rooftop of Solar Energy Research Institute of Singapore (SERIS).

The Perez model has been used mostly for hourly application despite its initial instantaneous design. To ensure sufficient samples, an hourly averaged data set over the entire year 2013 is used to adjust the Perez model coefficients; data from 2014 January to 2014 May are used for validation. Data points with $\theta_z > 87°$ and $\theta_i > 90°$ are not considered. For horizontal irradiance inputs, the interpolated values are used:

$$I_{\text{dif}} = I_{\text{glo}}^{(\text{CMP11})} \frac{I_{\text{dif}}^{(\text{SPN1})}}{I_{\text{glo}}^{(\text{SPN1})}}, \tag{7.25}$$

$$I_{\text{beam}} = I_{\text{glo}}^{(\text{CMP11})} - I_{\text{dif}}, \tag{7.26}$$

since CMP11 is an industrial standard sensor with higher accuracy than SPN1. The ratio of diffuse/global irradiance is derived from the SPN1 data. $I_{\text{glo}}^{(\text{CMP11})}$, $I_{\text{dif}}^{(\text{SPN1})}$ and $I_{\text{glo}}^{(\text{SPN1})}$ are readings from CMP11 (GHI) and SPN1 (DHI and GHI), respectively.

Following procedures described in sections 7.2.1 to 7.2.3, the adjusted set of F_{11}^*, F_{12}^*, F_{13}^*, F_{21}^*, F_{22}^*, F_{23}^* are calculated, as shown in Table 7.2. The readings from the four tilted silicon sensors (at 10°, 20°, 30° and 40°) are used for fitting the new parameters. The mean bias error (MBE) in W/m^2 and percentage root mean square error (nRMSE) in % are selected as the error metrics for the evaluation. The error calculations are shown in Eqns. (1.1) and (1.3) respectively. Table 7.3 shows the MBE and nRMSE of irradiance conversion results to various tilts using standard Perez model with coefficient sets F and F^* for hourly data.

Table 7.2 Locally fitted Perez model coefficients using one year (2013) of hourly irradiance data from Singapore.

ε'	F_{11}^*	F_{12}^*	F_{13}^*	F_{21}^*	F_{22}^*	F_{23}^*
$[1, 1.065)$	0.0485	0.5018	−0.1070	0.1976	−0.4549	0.0051
$[1.065, 1.23)$	0.3239	0.3845	−0.2828	0.2682	−0.5768	−0.0013
$[1.23, 1.5)$	0.5479	0.3355	−0.4283	0.1301	−0.1287	0.0166
$[1.5, 1.95)$	0.6305	0.8401	−0.5762	0.1082	−0.1478	0.1072
$[1.95, 2.8)$	1.1469	−0.1501	−0.7686	0.0979	−0.5319	0.1802
$[2.8, 4.5)$	1.9053	−2.7319	−0.9979	0.0982	−0.3522	0.2872
$[4.5, 6.2)$	1.0591	0.4510	−0.5650	0.1126	−0.5392	0.2710
$[6.2, +\infty)$	0.0949	−9.0339	−0.4739	0.0742	−0.2914	0.3272

Table 7.3 Error comparison for irradiance conversion from horizontal to tilted planes in Singapore using the Perez model with coefficient sets F (original) and F^* (adjusted).

s	MBE [W/m^2]		nRMSE [%]	
	F	F^*	F	F^*
10°	2.54	4.21	2.31	2.26
20°	-2.39	0.63	2.73	2.13
30°	-0.01	4.02	3.57	3.19
40°	-3.17	1.47	4.60	4.00

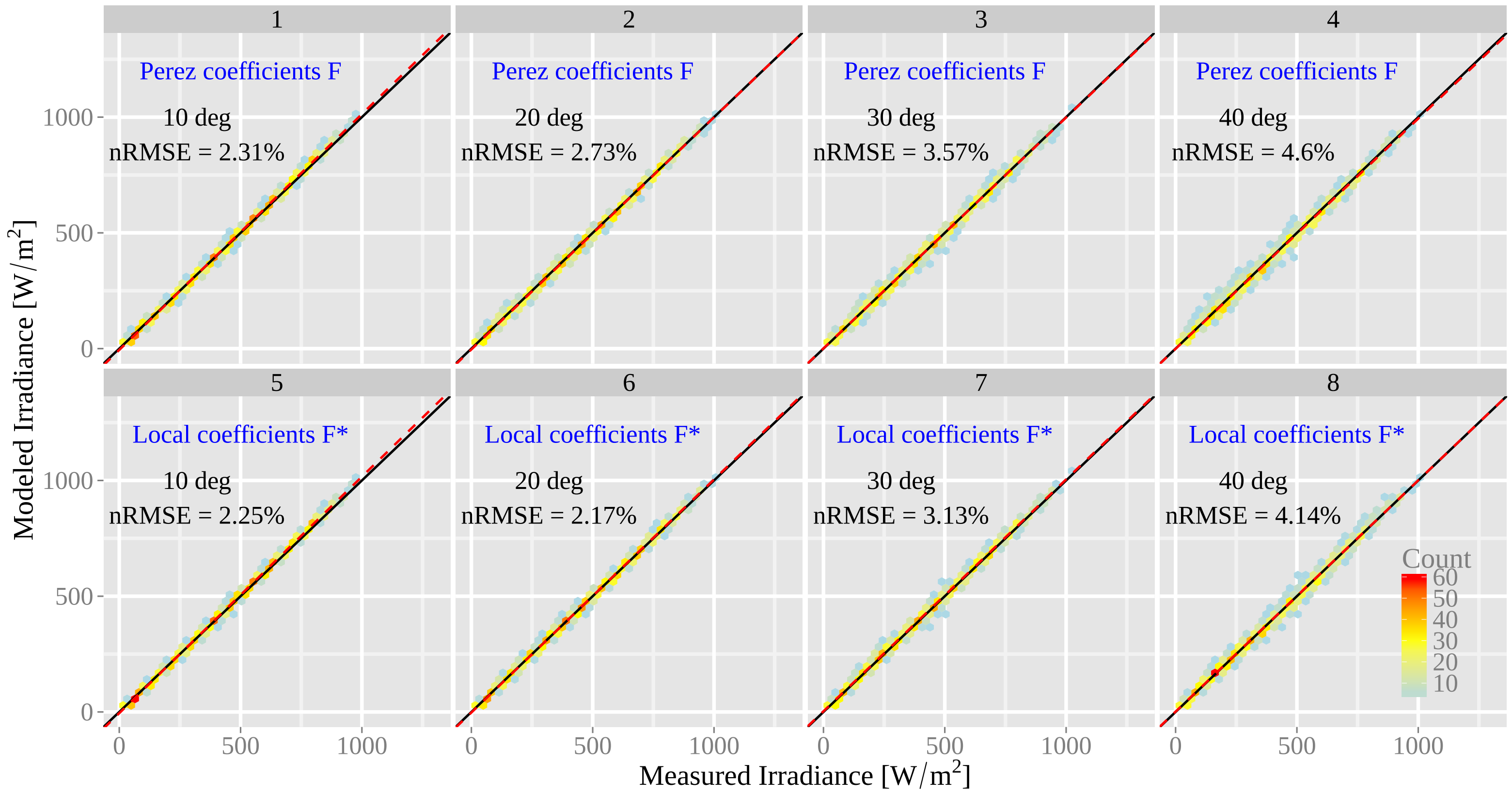

Fig. 7.3 Horizontal to tilt transposition modeling scatters using the (Perez et al., 1990) coefficients F and the locally fitted coefficients F^* on hourly data. The hexagon binning algorithm (Carr et al., 2013) is used for visualization. The black solid lines are the identity lines while the red dashed lines are the linearly fitted lines.

I further describe the errors by showing the scatter plots of the modeled values versus the measurements (see Fig 7.3 for results from hourly data). Minimal deviations from the 45° lines are observed in these plots showing unbiased (small MBE) estimations under both sets of model coefficients. It can be concluded that the coefficients adjusted for the local irradiance conditions in Singapore perform better than the original ones from (Perez et al., 1990) in both hourly and instantaneous applications. Considering that the improvements in nRMSE are marginal, this exercise confirms the broad applicability of the Perez model for irradiance conditions including the tropics. For applications of the Perez model at locations remote from the ones listed in section 7.1, locally fitted model coefficients may be helpful to improve the conversion accuracies. Table 7.3 suggests that the errors are small enough to be compatible with measurement uncertainties (for example ±3% for CMP11 from Kipp & Zonen), the improvements made are however significant given the large sample size.

7.3 Solutions to the inverse transposition problem

In some instances, it is necessary to apply the inverse Perez model, i.e., converting irradiance from tilt to horizontal. For example, one may seek to leverage in–plane irradiance readings from PV systems (typically made at larger PV systems for performance ratio evaluation) for GHI data, which then can be used to create irradiance maps of an area. With increasing penetration levels of variable solar power into electricity grids, such irradiance maps as well as spatio–temporal solar irradiance forecasting techniques become more and more relevant. One such example where GHI data are required is space–time kriging. A novel technique is introduced in this section, namely, irradiance conversion from tilt to horizontal using two or more silicon sensors. The merit of this new technique goes to its cost–effectiveness, as only silicon sensors (measuring tilted global irradiance) are required for this conversion algorithm. Neither tilted diffuse measurements nor pyranometers are needed.

To facilitate the analysis, define $k = I_{\text{beam}}/I_{\text{dif}}$, then Eqn. (7.17) can be re–arranged as:

$$\begin{aligned} I_{\text{t}} =& \frac{k I_{\text{dif}} \cos\theta_i (1-y)(1-L_{\text{spec}})}{\cos\theta_z} + I_{\text{dif}} \frac{1+\cos s}{2}(1-L_{\text{refl}})(1-L_{\text{spec}}) \\ &+ 0.5\rho' I_{\text{dif}}(1+k)(1-\cos s)[1+\sin^2(\theta_z/2)]|\cos(\alpha-\beta)|(1-L_{\text{refl}})(1-L_{\text{spec}}) \\ &+ I_{\text{dif}}\left(\frac{a}{b} - \frac{1+\cos s}{2}\right)(1-L_{\text{refl}})(1-L_{\text{spec}})\left(F_{11} + \frac{I_{\text{dif}}}{I_{\text{o}}\cos\theta_z}F_{12} + \vartheta_z F_{13}\right) \\ &+ I_{\text{dif}} \sin s (1-L_{\text{refl}})(1-L_{\text{spec}})\left(F_{21} + \frac{I_{\text{dif}}}{I_{\text{o}}\cos\theta_z}F_{22} + \vartheta_z F_{23}\right). \end{aligned} \tag{7.27}$$

Note that the invention of parameter k is strictly for mathematical convenience. One could consider k as a form of I_{glo}, since $I_{\text{glo}} = I_{\text{beam}} + I_{\text{dif}}$. By inspecting the equation, two cases are made:

- $S = 0$, i.e., irradiance readings from horizontal silicon sensors are available. (This is a null problem; its inclusion is to maintain mathematical completeness.);
- $S > 0$, i.e., irradiance readings from horizontal silicon sensors are unavailable.

7.3.1 Case of $s = 0$

In this case, $\theta_i = \theta_z$, $a = b$, and Eqn. (7.27) is simplified to

$$k I_{\text{dif}}(1-y)(1-L_{\text{spec}}) + I_{\text{dif}}(1-L_{\text{refl}})(1-L_{\text{spec}}) = I_{\text{t},0}. \tag{7.28}$$

where $I_{\text{t},0}$ is the irradiance received by a zero degree tilted silicon sensor.

- If I_{dif} is known, k can be solved from Eqn. (7.28) as

$$k = \frac{I_{\text{t},0}/I_{\text{dif}} - (1-L_{\text{refl}})(1-L_{\text{spec}})}{(1-y)(1-L_{\text{spec}})}. \tag{7.29}$$

  Thus $I_{\text{beam}} = k I_{\text{dif}}$ and $I_{\text{glo}} = (1+k) I_{\text{dif}}$.

- If k is known, from Eqn. (7.28)

$$I_{\mathrm{dif}} = \frac{I_{\mathrm{t},0}}{k(1-y)(1-L_{\mathrm{spec}}) + (1-L_{\mathrm{refl}})(1-L_{\mathrm{spec}})}. \tag{7.30}$$

  So $I_{\mathrm{beam}} = kI_{\mathrm{dif}}$ and $I_{\mathrm{glo}} = (1+k)I_{\mathrm{dif}}$.

- If both I_{dif} and k are unknown, then with only one equation there exist infinite solutions. There are two ways to deal with the issue. Applying decomposition models to approximate the diffuse irradiance from horizontal irradiance (e.g. Erbs et al., 1982; Maxwell, 1987). However, due to the non–injective nature of the mapping from GHI to DHI, using decomposition models introduces large errors (Ridley et al., 2010). In the other case, irradiance readings from another tilted silicon sensor can assist to find the unique solution by providing the additional equation, which will be discussed in section 7.3.2 as a special case.

In general, when global irradiance measurements from horizontal silicon sensors ($I_{\mathrm{t},0}$) are available, the derivation of I_{dif} and I_{glo} becomes straightforward and the Perez model is not required for reconstruction.

7.3.2 Case of $s > 0$

In this case, Eqn. (7.27) can be re–arranged to:

$$(\mathtt{A}I_{\mathrm{dif}} + \mathtt{B}k + \mathtt{C})I_{\mathrm{dif}} = I_{\mathrm{t}}, \tag{7.31}$$

where

$$\mathtt{A} = \frac{\left[F_{12}\left(\frac{a}{b}-\frac{1+\cos s}{2}\right)+F_{22}\sin s\right](1-L_{\text{refl}})(1-L_{\text{spec}})}{I_{\text{o}}\cos\theta_z}, \tag{7.32}$$

$$\begin{aligned}\mathtt{B} =& \frac{\cos\theta_i(1-y)(1-L_{\text{spec}})}{\cos\theta_z} + (1-L_{\text{refl}})(1-L_{\text{spec}}) \\ & \times 0.5\rho'(1-\cos s)[1+\sin^2(\theta_z/2)]|\cos(\alpha-\beta)|,\end{aligned} \tag{7.33}$$

$$\begin{aligned}\mathtt{C} =& (1-L_{\text{refl}})(1-L_{\text{spec}})\Big\{0.5\rho'(1-\cos s)[1+\sin^2(\theta_z/2)]|\cos(\alpha-\beta)| \\ & + \frac{1+\cos s}{2} + (F_{11}+\vartheta_z F_{13})\left(\frac{a}{b}-\frac{1+\cos s}{2}\right) + (F_{21}+\vartheta_z F_{23})\sin s\Big\}.\end{aligned} \tag{7.34}$$

- If I_{dif} is known, k can be solved from Eqn. (7.31) as

$$k = \frac{I_{\text{t}}/I_{\text{dif}} - \mathtt{A}I_{\text{dif}} - \mathtt{C}}{\mathtt{B}}. \tag{7.35}$$

  Thus $I_{\text{beam}} = kI_{\text{dif}}$ and $I_{\text{glo}} = (1+k)I_{\text{dif}}$.

- If k is known, from Eqn. (7.31)

$$\mathtt{A}I_{\text{dif}}^2 + (\mathtt{B}k+\mathtt{C})I_{\text{dif}} - I_{\text{t}} = 0. \tag{7.36}$$

  If $\mathtt{A} = 0$, the equation has a unique solution:

$$I_{\text{dif}} = \frac{I_{\text{t}}}{\mathtt{B}k+\mathtt{C}}. \tag{7.37}$$

  If $\mathtt{A} \neq 0$ and $(\mathtt{B}k+\mathtt{C})^2 + 4\mathtt{A}I_{\text{t}} \geq 0$, Eqn. (7.31) can be solved as

$$I_{\text{dif}} = \frac{-(\mathtt{B}k+\mathtt{C}) \pm \sqrt{(\mathtt{B}k+\mathtt{C})^2+4\mathtt{A}I_{\text{t}}}}{2\mathtt{A}}. \tag{7.38}$$

  Any negative solution should be ignored as $I_{\text{dif}} \geq 0$.

- If both I_{dif} and k are unknown, as mentioned in section 7.3.1, irradiance values from another silicon sensor with different tilt are necessary to get the unique solution. Suppose the irradiance values from two different tilted silicon sensors are $I_{\mathrm{t},1}$ and $I_{\mathrm{t},2}$, respectively, it follows from Eqn. (7.31) that

$$(\mathtt{A}_1 I_{\mathrm{dif}} + \mathtt{B}_1 k + \mathtt{C}_1) I_{\mathrm{dif}} = I_{\mathrm{t},1}, \tag{7.39}$$

$$(\mathtt{A}_2 I_{\mathrm{dif}} + \mathtt{B}_2 k + \mathtt{C}_2) I_{\mathrm{dif}} = I_{\mathrm{t},2}. \tag{7.40}$$

Mutually dividing Eqns. (7.39) and (7.40) to eliminate I_{dif} yields

$$k = \frac{(\mathtt{A}_2 I_{\mathrm{t},1} - \mathtt{A}_1 I_{\mathrm{t},2}) I_{\mathrm{dif}} + \mathtt{C}_2 I_{\mathrm{t},1} - \mathtt{C}_1 I_{\mathrm{t},1}}{\mathtt{B}_1 I_{\mathrm{t},2} - \mathtt{B}_2 I_{\mathrm{t},1}}. \tag{7.41}$$

Substituting Eqn. (7.41) into Eqn. (7.39) yields

$$\mathtt{A}^* I_{\mathrm{dif}}^2 + \mathtt{B}^* I_{\mathrm{dif}} + \mathtt{C}^* = 0, \tag{7.42}$$

where

$$\mathtt{A}^* = \mathtt{A}_1 + \mathtt{B}_1 \frac{\mathtt{A}_2 I_{\mathrm{t},1} - \mathtt{A}_1 I_{\mathrm{t},2}}{\mathtt{B}_1 I_{\mathrm{t},2} - \mathtt{B}_2 I_{\mathrm{t},1}}, \tag{7.43}$$

$$\mathtt{B}^* = \mathtt{C}_1 + \mathtt{B}_1 \frac{\mathtt{C}_2 I_{\mathrm{t},1} - \mathtt{C}_1 I_{\mathrm{t},2}}{\mathtt{B}_1 I_{\mathrm{t},2} - \mathtt{B}_2 I_{\mathrm{t},1}}, \tag{7.44}$$

$$\mathtt{C}^* = -I_{\mathrm{t},1}. \tag{7.45}$$

If $\mathtt{A}^* = 0$, the group of Eqns. (7.39) and (7.40) has a unique solution:

$$I_{\mathrm{dif}} = -\frac{\mathtt{C}^*}{\mathtt{B}^*}. \tag{7.46}$$

If $\mathtt{A}^* \neq 0$ and $b^{*2} - 4\mathtt{A}^*\mathtt{C}^* \geq 0$, the two solutions to Eqns. (7.39) and (7.40) are

$$I_{\mathrm{dif}} = \frac{-\mathtt{B}^* \pm \sqrt{b^{*2} - 4\mathtt{A}^*\mathtt{C}^*}}{2\mathtt{A}^*}, \tag{7.47}$$

where the negative root should be ignored.

The closed form solutions presented above cover all cases of data availability. Model coefficients F_{11}, F_{12}, F_{13}, F_{21}, F_{22}, F_{23} are selected in the following manner:

- Values of defined coefficients `A`, `B` and `C` are only functions of F_{11}, F_{12}, F_{13}, F_{21}, F_{22}, F_{23}.
- Eight sets of `A`, `B` and `C` can be calculated based on different Perez model coefficients. These values lead to eight diffuse horizontal irradiance (DHI) estimates, thus eight global horizontal irradiance (GHI) estimates.
- Eight ε' values can be then calculated using GHI/DHI estimates.
- If the assumed ε' agrees with the calculated ε', the set is selected as the true estimated GHI. Furthermore, direct normal irradiance (DNI) can be calculated using true estimates of GHI.

7.3.3 Case study

With the reliable data of 5 months (2014 January to May), the inverse problem of Perez transposition is validated using 10 case studies:

1. I_{dif} is known, reconstruct I_{glo} from $I_{\text{t,10}}$ (10° tilted silicon sensor);
2. I_{dif} is known, reconstruct I_{glo} from $I_{\text{t,20}}$ (20° tilted silicon sensor);
3. I_{dif} is known, reconstruct I_{glo} from $I_{\text{t,30}}$ (30° tilted silicon sensor);
4. I_{dif} is known, reconstruct I_{glo} from $I_{\text{t,40}}$ (40° tilted silicon sensor);
5. I_{dif} is unknown, reconstruct I_{glo} from $I_{\text{t,10}}$ and $I_{\text{t,20}}$;
6. I_{dif} is unknown, reconstruct I_{glo} from $I_{\text{t,10}}$ and $I_{\text{t,30}}$;
7. I_{dif} is unknown, reconstruct I_{glo} from $I_{\text{t,10}}$ and $I_{\text{t,40}}$;

8. I_{dif} is unknown, reconstruct I_{glo} from $I_{\mathrm{t},20}$ and $I_{\mathrm{t},30}$;
9. I_{dif} is unknown, reconstruct I_{glo} from $I_{\mathrm{t},20}$ and $I_{\mathrm{t},40}$;
10. I_{dif} is unknown, reconstruct I_{glo} from $I_{\mathrm{t},30}$ and $I_{\mathrm{t},40}$.

These 10 case studies cover all sensor permutations. In addition to these, I define another 8 case studies whose choices are justified in section 7.3.4.

11. I_{dif} is unknown, reconstruct I_{glo} from $I_{\mathrm{t},10}$, $I_{\mathrm{t},20}$ and $I_{\mathrm{t},30}$;
12. I_{dif} is unknown, reconstruct I_{glo} from $I_{\mathrm{t},10}$, $I_{\mathrm{t},30}$ and $I_{\mathrm{t},40}$;
13. I_{dif} is unknown, reconstruct I_{glo} from $I_{\mathrm{t},20}$, $I_{\mathrm{t},30}$ and $I_{\mathrm{t},40}$;
14. I_{dif} is unknown, reconstruct I_{glo} from $I_{\mathrm{t},10}$, $I_{\mathrm{t},20}$, $I_{\mathrm{t},30}$ and $I_{\mathrm{t},40}$;
15. I_{dif} is unknown, reconstruct I_{glo} from $I_{\mathrm{t},10}$ only (with decomposition model);
16. I_{dif} is unknown, reconstruct I_{glo} from $I_{\mathrm{t},20}$ only (with decomposition model);
17. I_{dif} is unknown, reconstruct I_{glo} from $I_{\mathrm{t},30}$ only (with decomposition model);
18. I_{dif} is unknown, reconstruct I_{glo} from $I_{\mathrm{t},40}$ only (with decomposition model).

Table 7.4 shows the error metrics for reconstructions, which follows Eqns. (1.1) and (1.3). The errors are observed to be in the same range as those reported in Table 7.3. By using two silicon sensors on different tilts (case studies (5), (6) and (7)), it is possible to produce better results than deriving the I_{dif} from data of the SPN1 sensor (case studies (3) and (4)). Therefore a pair of carefully modeled silicon sensors is preferred over a suboptimal grade pyranometer due to the lower cost of silicon sensors.

7.3.4 Benchmarking

The studies on inverse transposition is rarely encountered in the literature. Nevertheless, the works by Faiman et al. (1987, 1993) reveal a simplistic approach to the inverse transposition

Table 7.4 Errors from the proposed method to solve the inverse Perez model. Faiman et al. (1987) model and Yang et al. (2013a) model are used to benchmark the results.

Case	Inverse Perez model		Faiman et al. (1987) model		Yang et al. (2013a) model	
	MBE [W/m^2]	RMSE [%]	MBE [W/m^2]	RMSE [%]	MBE [W/m^2]	RMSE [%]
(1)	-4.12	1.87	—		—	
(2)	-0.02	1.69	—		—	
(3)	-3.26	2.64	—		—	
(4)	0.55	3.84	—		—	
(5)	-3.88	2.57	-7.68	5.11	—	
(6)	-4.53	2.43	-5.61	4.63	—	
(7)	-3.86	2.33	-6.42	5.01	—	
(8)	1.30	3.21	1.38	5.45	—	
(9)	0.73	2.70	-0.18	5.04	—	
(10)	3.06	5.66	-6.54	7.32	—	
(11)	—		-5.87	3.61	—	
(12)	—		-6.16	3.71	—	
(13)	—		-0.64	4.08	—	
(14)	—		-5.01	3.49	—	
(15)	—		—		1.11	4.01
(16)	—		—		3.75	7.27
(17)	—		—		-13.68	16.13
(18)	—		—		-26.72	23.00

problem. In both works, a multi–pyranometer approach is used to solve the problem by first assuming isotropy in both diffuse irradiance and irradiance due to ground reflection. I implement the method outlined by Faiman et al. (1987) to benchmark my results.

With isotropic assumptions on the diffuse transposition factor and the transposition factor due to ground reflection, Eqn. (7.13) is simplified to:

$$\begin{aligned} I_{\mathrm{t,dif}} =& 0.5\rho'(I_{\mathrm{beam}} + I_{\mathrm{dif}})(1-\cos s)(1-L_{\mathrm{refl}})(1-L_{\mathrm{spec}}) \\ &+ I_{\mathrm{dif}}\frac{1+\cos s}{2}(1-L_{\mathrm{refl}})(1-L_{\mathrm{spec}}). \end{aligned} \tag{7.48}$$

Together with the in–plane direct irradiance, Eqns. (7.48) and (7.15) are substituted into $I_{\mathrm{t}} = I_{\mathrm{t,dif}} + I_{\mathrm{t,dir}}$ and yield:

$$\begin{aligned} I_{\mathrm{t}} =& 0.5\rho'(I_{\mathrm{beam}} + I_{\mathrm{dif}})(1-\cos s)(1-L_{\mathrm{refl}})(1-L_{\mathrm{spec}}) \\ &+ I_{\mathrm{dif}}\frac{1+\cos s}{2}(1-L_{\mathrm{refl}})(1-L_{\mathrm{spec}}) \\ &+ I_{\mathrm{beam}}\frac{\cos\theta_i}{\cos\theta_z}(1-y)(1-L_{\mathrm{spec}}). \end{aligned} \tag{7.49}$$

By inspecting, Eqn. (7.49) can be conveniently written into:

$$I_{\mathrm{t}} = p' I_{\mathrm{beam}} + q' I_{\mathrm{dif}} \tag{7.50}$$

with

$$p' = \left[\frac{\cos\theta_i}{\cos\theta_z}(1-y) + \rho'\left(\frac{1-\cos s}{2}\right)(1-L_{\mathrm{refl}})\right](1-L_{\mathrm{spec}}), \tag{7.51}$$

$$q' = \left[\frac{(1+\cos s)+\rho'(1-\cos s)}{2}\right](1-L_{\mathrm{refl}})(1-L_{\mathrm{spec}}), \tag{7.52}$$

which can be readily calculated. Given n tilted sensors, this equation can then be written into linear algebra form:

$$\tilde{\mathbf{A}}\tilde{\mathbf{X}} = \tilde{\mathbf{Y}} \tag{7.53}$$

where

$$\tilde{\mathbf{X}} = \begin{pmatrix} I_{\mathrm{beam}} & I_{\mathrm{dif}} \end{pmatrix}^{\top}, \quad \in \mathbb{R}^2 \tag{7.54}$$

$$\tilde{\mathbf{Y}} = \begin{pmatrix} I_{\mathrm{t}}^1 & \cdots & I_{\mathrm{t}}^n \end{pmatrix}^{\top}, \quad \in \mathbb{R}^n \tag{7.55}$$

and

$$\tilde{\mathbf{A}} = \begin{pmatrix} p_1' & q_1' \\ \vdots & \vdots \\ p_n' & q_n' \end{pmatrix}. \quad \in \mathbb{R}^{n\times 2} \tag{7.56}$$

The least square solution to Eqn. (7.53) is given by:

$$\tilde{\mathbf{X}} = (\tilde{\mathbf{A}}^{\top}\tilde{\mathbf{A}})^{-1}\tilde{\mathbf{A}}^{\top}\tilde{\mathbf{Y}}. \tag{7.57}$$

Based on Eqn. (7.57), I_{beam} and I_{dif} can be calculated based on data from any $n \geq 2$ sensors, and thus I_{glo}. The Faiman et al. (1987) model is used in case studies (5) to (14) covering all sensors permutations. Table 7.4 shows the error metrics of the model. It can be seen that the isotropic Faiman et al. (1987) model only performs marginally worse than the proposed inverse Perez model. Further to that, when 3 or more sensors are used (case studies (11) to (14)), the errors are smaller than the errors from the 2 sensors cases of the Faiman et al. (1987) model.

These above comparison between the isotropic and anisotropic approaches to the inverse transposition problem aligns with the results reported in a previous work by Gueymard (2009) which evaluates the horizontal to tilt conversions. The improvements from using isotropic models to using anisotropic models in both works are shown to be certain but marginal. I note that the Perez model depends on ε' binning, the retrieved ε' values might not agree with the expected bin. Thus, when we follow the procedures described in section 7.3.2, the conversion of a small percentage of data points will be unsuccessful. The failure rate of the algorithm is about 2 to 3 percent. This issue however can be addressed by redefining the ε' binning. On the other hand, the isotropic approach has guaranteed solutions. The trade–off between the isotropic and anisotropic approaches can be evaluated based on the applications.

All of the tilt to horizontal conversion algorithms shown in this chapter use at least two sensors in GHI reconstruction. However, more than common, there is only a single sensor available. In this case, the method introduced in chapter 6 is used. Erbs univariate decomposition model (Erbs et al., 1982) is repeated here using the new data for benchmarking. Table 7.4 shows the error metrics for case studies (15) to (18). The RMSE calculated using measurements from the 10° tilt and the 20° tilt sensors improve from the ones reported in chapter 6 as various losses are accounted in this chapter. Since the mapping between GHI and DHI is non–injective owing to different sky conditions, the errors using the Yang et al. (2013a) model are much larger than the ones using multiple sensor approaches. It can thus be concluded that by including another reference cell at an alternative tilt, the accuracy of tilt to horizontal conversion can be improved substantially. I have shown that the uncertainties of the proposed algorithm are within the uncertainties of the measurements. The proposed conversion algorithm is therefore well suited and sophisticated enough to describe the experimental results; a further refinement is not necessary.

7.4 Chapter conclusion

A least squares method is first introduced to optimize the Perez transposition model using the tropical data. The locally fitted set of coefficients outperforms the original set of coefficients. Such regional optimizations of the Perez model coefficients are promoted. This chapter then establishes closed form solutions for two–way conversion among various components received on a horizontal plane and the ones received on tilted planes. At this stage, all of the irradiance components listed in the nomenclature section have been modeled. Such modeling gives convenience to a series of solar engineering problems, including:

- Use I_{glo} (pyranometer) and I_{dif} (another pyranometer with shadow band or shadow pattern) measurements to model I_{t} for PV module performance benchmarking. The second pyranometer can be replaced by a pyrheliometer who measures I_{beam}.
- Use measured $I_{\text{t},1}$ and $I_{\text{t},2}$ (two reference cells) to reconstruct I_{glo} and I_{dif}. The reconstructions are used to generate GHI maps and as inputs to irradiance forecasting algorithms. This can be enhanced with tilted pyranometers, with equipment cost being the trade–off.
- Use I_{glo} (pyranometer) and I_{t} (reference cell) to reconstruct the often desired horizontal component, I_{dif}, for financial saving on equipments.

Of particular importance to the methods introduced in this chapter is that observations need not use costly pyranometers, but can be derived from low–cost reference cells. Since performance monitoring using reference cells is very commonly carried out in larger PV systems, it greatly increases the potential number of sites that can benefit from a locally–optimized Perez model, even in the absence of a research–grade meteorological station.

Chapter 8

Network redesign using entropy

Many existing solar irradiance monitoring networks were built particularly for resource assessment purposes; they are often spatially sparse. In order for the networks to handle other increasingly important tasks, such as irradiance forecasting for grid integration, their spatial sparsity must be addressed by adding in new monitoring stations.

Chapters 6 and 7 present two approaches of converting the tilted irradiance measurements to GHI. These methods allow solar forecasters to utilize the data from the existing PV systems, and thus make better forecasts by considering the additional data. Another direct approach to the network sparsity issue is network expansion.

8.1 Chapter introduction

The network design approaches in solar engineering literature have two other key differences with the one herein described: (1) the approach in (Yang and Reindl, 2015; Zagouras et al., 2013, 2014a,b) uses satellite images as the input data to the design algorithms, (2) their approach designs the network from scratch, i.e., it does not consider the existing irradiance monitoring networks. Building new networks is costly, especially when the networks are expected to be maintained for long period of time. However, there are many available networks which have been operating for decades, e.g., the National Solar Radiation

Data Base (http://rredc.nrel.gov/solar/old_data/nsrdb/1991-2005/tmy3/), the New Energy and Industrial Technology Development Organization (http://app7.infoc.nedo.go.jp/). It is sometimes desired to revamp and expand these networks to better accomplish the needs for resources assessment and other emerging applications such as irradiance forecasting. Utilizing the existing monitoring networks is thus economically justified. An example project is described in a recent publication (Davy and Troccoli, 2014), where the irradiance monitoring network maintained by the Australian Bureau of Meteorology is redesigned based on uncertainty modeling. Furthermore, the network construction projects are often multi–phase. After the first phase of the project, ground data become available, which in turn lead to better decisions and inference on stations' locations in the following phases.

Unlike (Davy and Troccoli, 2014) where satellite data and genetic algorithm are used for the redesign, I consider the ground data and entropy[1]. Although there is no literature on statistical network redesign in solar engineering, rich literature is present in geosciences. Two most adopted approaches are the kriging–based redesign (Ashraf et al., 1997; Zimmerman, 2006) and the entropy–based redesign (Mogheir et al., 2006; Owlia et al., 2011). The two approaches are being compared in (Lee and Ellis, 1997); and I adopt the later in this chapter. For a more detailed discussion on entropy–based redesign, readers are referred to the recent book by Singh (2013). Section 8.3 briefly reviews the entropy–based redesign problems.

Before I reveal the redesign criteria, some practical issues associated with solar irradiance spatio–temporal data have to be considered first. In particular, two issues are constantly being overlooked by solar engineers during problem solving, namely, the statistical distribution of the (transformed) irradiance data and the isotropy of the spatial covariance structure. Many statistical procedures have assumptions on distribution of the inputs data. Violation of such assumptions of distribution may lead to unreliable and non–interpretable results. It is therefore mandatory to perform some preliminary analyses, such as the normality test, prior to modeling. The heterogeneous spatial covariance structure of an irradiance random

---

[1] In information theory, entropy is the average amount of information contained in each message received. See Eqn. (8.10) for definition.

field is another practical issue. In spatial statistics, isotropic variograms or isotropic covariance functions are often used to explain the spatial or spatio–temporal dependency in the data. However, isotropy is rarely observed in environmental processes; many works overlook this by fitting an isotropic model to the anisotropy data. This will result in suboptimal predictive performance at the unobserved locations and at future time. I will address both issues in sections 8.1.2 and 8.2.

8.1.1 Data

The analyses presented in chapter 5 consider data from 10 irradiance monitoring stations in Singapore. As mentioned in chapter 5, those 10 stations belong to a bigger monitoring network. The irradiance monitoring network with 25 stations in Singapore was completed in 2013 December[2]. Fig. 8.1 shows the locations of these stations[3]. As Singapore is located near the equator, there is no significant seasonal variation in the clear sky irradiance it neither has significantly different weather patterns among months. Hourly data from 2014 July are therefore used in this chapter. As the focus here is the methodology, the use of one month data is sufficient.

8.1.2 Normality test

Clear sky model developed in chapter 3 is first used to detrend the irradiance time series. In statistics, normally distributed data are more amenable to standard analyses. However, removing the diurnal trend from the time series does not guarantee a normal distribution (Dong et al., 2013); further hypothesis testing is needed if we want to assume normal in the following analyses. I use the Kolmogorov–Smirnov (K–S) test to test normality.

---

[2] I wrote the Renewable Energy paper (Yang et al., 2013b) in early 2013, consequently, the data used in chapter 5 are from 2012 November and have only 10 stations.

[3] Only data from 24 stations are used in this chapter; one station experienced data loss during the period of analyses.

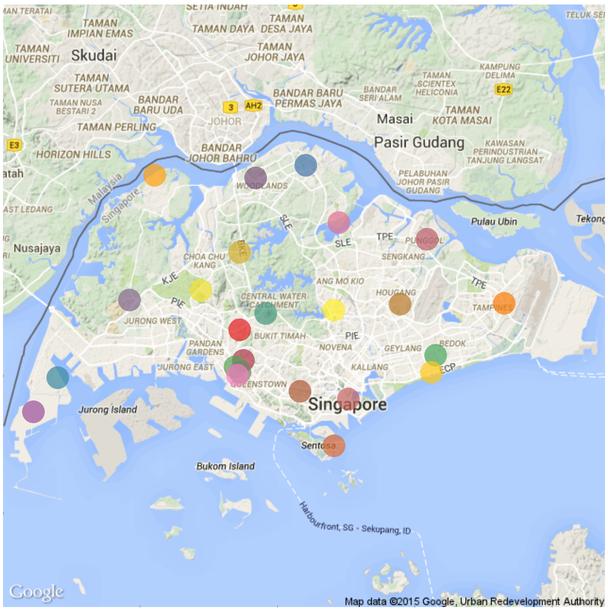

Fig. 8.1 Locations of 24 irradiance monitoring stations used in this chapter. Source: Google Maps.

For data with length n, the **K–S test statistic** is given by

$$D_n = \sup_x |\widehat{F}_n(x) - F(x)| \tag{8.1}$$

where $\widehat{F}_n(x)$ is the **empirical distribution function**:

$$\widehat{F}_n(x) = \frac{1}{n}\sum_{i=1}^{n} \boldsymbol{I}_{(X_i \le x)} \tag{8.2}$$

where $\boldsymbol{I}_{(\cdot)}$ is an indicator function, which equals to 1 if $X_i \le x$, 0 otherwise. The null hypothesis H_0 of the K–S test is the samples follow a specific distribution $F(x)$, in this case the normal distribution; the alternative hypothesis H_1 is the sample do not follow the specific distribution. The null hypothesis is rejected if $D_n > c$, where the critical value c is found from the K–S table. Fig. 8.2 shows the approximately normal distributions of the clear sky index at four selected stations. After running the K–S tests for all 24 stations, only 2 tests reject H_0. Thus there are reasons to assume that this particular set of clear sky index data is normally distributed. The station specific mean and variance will be dealt later.

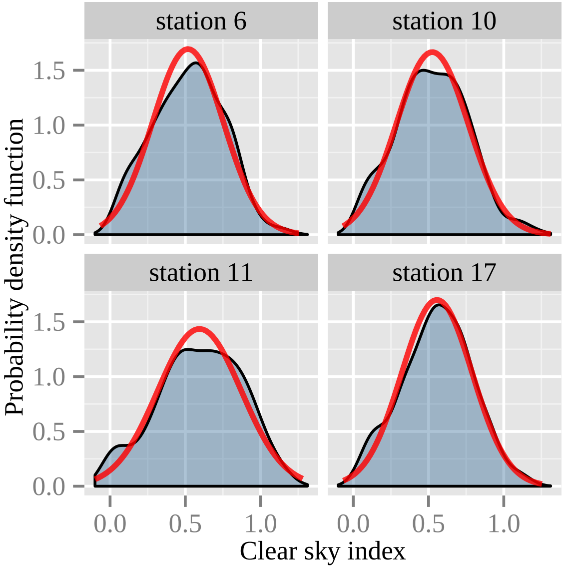

Fig. 8.2 The distributions of the clear sky index at four selected stations. The red curves are normal density functions with station specific mean and variance.

8.2 The S–G method: a revisit

The entropy–based network redesign will be discussed in section 8.3. At this stage, I would like to point out that a particular step in the redesign is to estimate the spatio–temporal covariance structure of the clear sky index process. Therefore, a preliminary analysis on spatial correlation is first carried out. Fig. 8.3 shows the correlation versus geographical distance plot using the hourly clear sky index data from 2014 July; the scatters show strong anisotropy. Therefore the Sampson and Guttorp (1992) method (the S–G method) discussed in chapter 5 is again useful in the present situation. However, the S–G method herein used is slightly different from the one shown in chapter 5. Ever since the invention of the S–G method, many researchers (Bruno et al., 2009; Damian et al., 2001; Guttorp and Sampson, 1994; Meiring et al., 1998; Monestiez et al., 1993) have proposed variants to the method; I take this opportunity to present these variants.

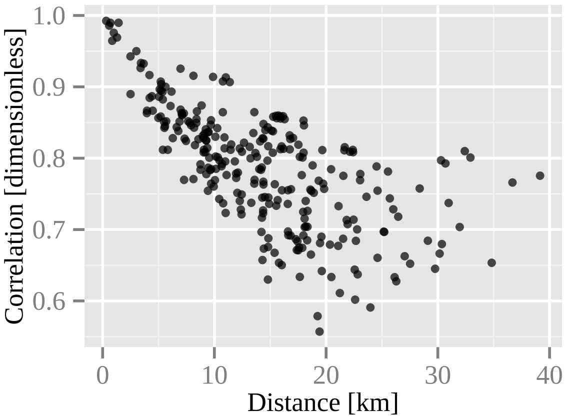

Fig. 8.3 Spatial correlation on geographical plane shows anisotropy.

8.2.1 The D plane representation

Recall that the S–G method considers dispersion as the dissimilarity measure for the time series of spatial process. The algorithm takes two steps, namely, the multidimensional scaling (MDS) step and the thin plate spline (TPS) mapping step. The method considers two planes: the anisotropic geographical plane (G plane) and the approximately isotropic dispersion plane (D plane).

The goal of this section is to retrieve the D plane coordinates using the dispersion. Instead of using the dispersion defined in Eqn. (5.2), the **correlation dispersion** (Guttorp and Sampson, 1994) between two locations $\boldsymbol{s}_i$ and $\boldsymbol{s}_j$ is used:

$$d_{ij} = 2 - 2\texttt{Corr}\Big(z(\boldsymbol{s}_i;t), z(\boldsymbol{s}_j;t)\Big) \tag{8.3}$$

where $\texttt{Corr}(\cdot)$ denotes correlation. In chapter 5, the non–metric multidimensional scaling approach is used to retrieve the stations' location in the D plane. The non–metric MDS aims at minimizing the stress $\mathcal{S}$ (recall the definition given by Eqn. (5.4)) over all monotone functions $\delta(\cdot)$. Once the D plane coordinates are found via the non–metric MDS, a parametric class of correlation function $\rho_S(\boldsymbol{h}, \boldsymbol{\theta})$ (see Eqn. (5.9), where parameter $\boldsymbol{\theta}$ is $\{\nu, c\}$) is fitted so that the correspondence between the D plane distance and the correlation can be established, allowing covariance estimation for unobserved locations.

The above procedure treats the scaling and correlation function fitting separately. However, Monestiez and Switzer (1991) considers the separation to be unnatural and proposes an elegant **alternating algorithm** which fits the variogram and scales the coordinates simultaneously:

- *The A–step*: Move the n points to minimize the least square criterion:

  $$\sum_{i<j} \Big(d_{ij} - \gamma(h_{ij}, \boldsymbol{\theta})\Big)^2 \tag{8.4}$$

  for a fixed $\boldsymbol{\theta}$. $\gamma(h_{ij}, \boldsymbol{\theta})$ is a parametric family of variogram model with parameter $\boldsymbol{\theta}$.

- *The B–step*: Based on the new D plane locations, estimate the value of $\boldsymbol{\theta}$ through the same least square objective function, i.e., Eqn. (8.4).

The algorithm can be initialized by fitting a variogram to the G plane coordinates. As the two steps are iterative, choice on the stopping criterions can be made either reaching a defined tolerance level or reaching a defined maximum iterations.

8.2.2 Thin plate spline bending

After obtaining the set of D plane stations' coordinates, a bivariate mapping function $f : \mathbb{R}^2 \to \mathbb{R}^2$ that maps an arbitrary G plane point to its D plane dual is needed. The bijective mapping procedure is described in appendix D. This procedure performs an exact interpolation from the G plane to the D plane, i.e., the fitted function passes through all points in the D plane. One practical issue of the exact interpolation is overfitting; and it will lead to the thin plane folding. The folding is due to the degeneracy in the dispersion matrix and it cannot be guaranteed that each TPS mapping is bijective (Damian et al., 2001; Monestiez et al., 1993). TPS folding leads to undesired poor extrapolations to unobserved locations.

There are a few ways that can solve the folding problem, for instance, we can choose a high dimensional D plane. However, it is argued that a high dimensional D plane solves the folding but not the overfitting by introducing an even more closely fitted variogram (Monestiez et al., 1993). Another solution is to introduce a penalty term during the thin plane spline mapping. Recall that the choice of function $f(\cdot)$ is made by minimizing the roughness criterion:

$$J_f = \iint_{\mathbb{R}^2} \left[\left(\frac{\partial^2 f}{\partial x^2} \right)^2 + 2 \left(\frac{\partial^2 f}{\partial x \partial y} \right)^2 + \left(\frac{\partial^2 f}{\partial y^2} \right)^2 \right] dxdy \tag{8.5}$$

Wahba and Wendelberger (1980) notes that this roughness criterion is proportional to the bending energy of a thin plate. In consideration of the above, a penalty term is included, so that the function being minimized becomes:

$$\sum_{i=1}^{n} \Big(x_i^* - f_{x^*}(x_i, y_i) \Big)^2 + \sum_{i=1}^{n} \Big(y_i^* - f_{y^*}(x_i, y_i) \Big)^2 + \lambda \Big(J_{f_{x^*}} + J_{f_{y^*}} \Big) \tag{8.6}$$

where λ is the **penalty scale**. By including the penalty term, the spline becomes a smoothing spline. When $\lambda = 0$, the spline is the interpolating spline; when $\lambda \to \infty$, the TPS is affine and has zero bending energy. The last term of expression (8.6) has the sum two integrals. Bookstein (1997b) showed the closed formula for this sum:

$$\frac{1}{8\pi} (\boldsymbol{V}_{x^*} \boldsymbol{L}_n^{-1} \boldsymbol{V}_{x^*}^{\top} + \boldsymbol{V}_{y^*} \boldsymbol{L}_n^{-1} \boldsymbol{V}_{y^*}^{\top}) \tag{8.7}$$

where $\boldsymbol{L}_n^{-1}$ is the $n \times n$ upper left submatrix of $\boldsymbol{L}^{-1}$, see appendix D. At this stage, the only remaining problem is to choose a proper value for λ. Several methods to select lambda were proposed in the literature including simulated annealing Iovleff and Perrin (2004), cross validation Meiring et al. (1997b) and the stopping rule approach Meiring et al. (1997b). Regardless of which procedure, the goal is to find a small λ such that the resulting D plane is smooth without folding. For the application of redesign the monitoring network, a simple trial and error approach is sufficient as the S–G method is only performed once.

8.2.3 Implementation

Before I move on to entropy–based design, I summarize the S–G method with Fig. 8.4. The correlation dispersion in Eqn. (8.3) can be calculated empirically. Alternatively, the correlation matrix can be estimated using the EM algorithm (Le and Zidek, 2006). It is found that the empirical estimates do not differ much from the ones estimated via the EM algorithm. Without loss of generality, an exponential variogram is used for Eqn. (8.4):

$$\gamma(h) = \begin{cases} \tilde{a} + (2 - \tilde{a})[1 - \exp(-\tilde{t}h)] & \text{if } h > 0; \\ 0 & \text{otherwise.} \end{cases} \tag{8.8}$$

Parameters $\tilde{a}$ and $\tilde{t}$ are fitted using the alternating algorithm.

Fig. 8.4 shows the correlation versus the great–circle distance plots on the first column; shows the original and deformed Singapore maps in the second column. The topmost scatter plot is identical to Fig. 8.3, showing anisotropy in space. The S–G method is applied using the correlation dispersion estimates with $\lambda = 0$; and the results are shown in the middle row. It is clear that the anisotropy is significantly reduced. However, the D plane for the $\lambda = 0$ case has slight foldings at the left and bottom of the map. The λ value is therefore gradually increased until the map is folding free, with an increasing anisotropy as the trade–off. Such a case is found with $\lambda = 0.001$. I note that the great–circle distance displayed here is not used as the G plane distance due to its non–Euclidean geometry. The Lambert conformal conic projection is used to flatten the Earth's curvature. After the computation, the coordinates of the D plane objects (including map polygons, grid and station locations) are projected back to longitude and latitude through the inverse Lambert projection for plotting.

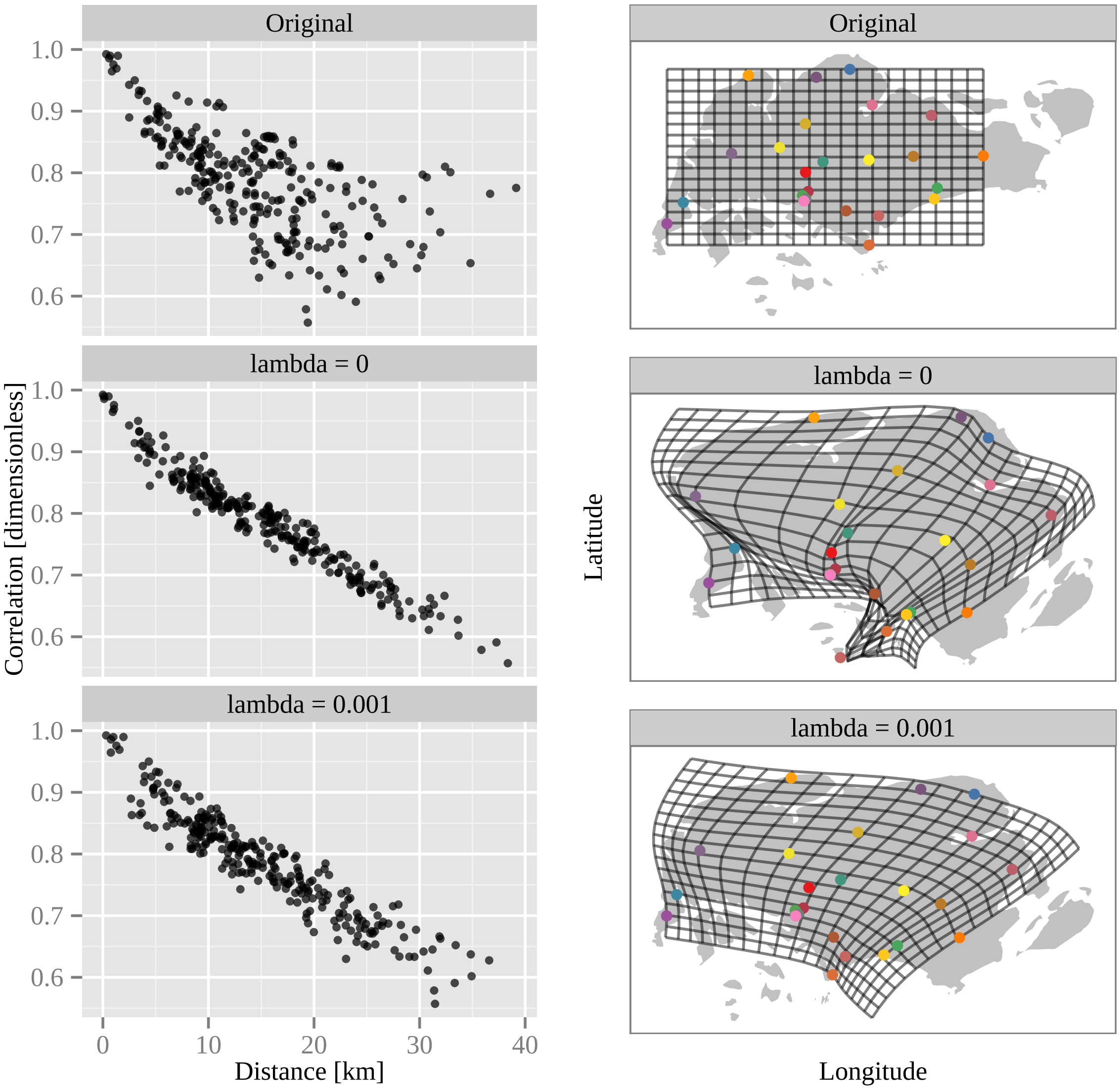

Fig. 8.4 An illustration of the S–G method.

8.3 The entropy–based design

The S–G method discussed in the previous section is a non–parametric way to improve heterogeneous spatial covariance estimation. The estimated covariance structure is used for monitoring network redesign in this section. The entropy concept is considered.

8.3.1 The differential entropy

Consider the **Shannon's entropy** (Shannon, 1948) for a discrete random variable X which takes countably many values $\{x_1, x_2, \cdots\}$:

$$H(p) = -\sum_i p(x_i) \log p(x_i) \tag{8.9}$$

where $p(x_i) = \mathbb{P}(X = x_i)$ is the probability mass function of X; $\mathbb{P}(\cdot)$ denotes probability; the summation is over all possible values of X. The **differential entropy** (Cover and Thomas, 2005) can be defined by analogy, i.e., sums and probabilities are replaced by integrals and density functions:

$$H(f) = -\int_{\mathbb{R}^1} f(x) \log f(x) dx \tag{8.10}$$

where $f(x)$ is the probability density function (pdf) of the continuous random variable X. Following the definition, the entropy for multivariate distributions can be derived (Ahmed and Gokhale, 1989; Zografos and Nadarajah, 2005). For example, consider an n–variate normal distribution with pdf:

$$f(\boldsymbol{x}) = \frac{1}{\sqrt{(2\pi)^n |\boldsymbol{\Sigma}|}} \exp\left(-\frac{1}{2}(\boldsymbol{x}-\boldsymbol{\mu})^\top \boldsymbol{\Sigma}^{-1}(\boldsymbol{x}-\boldsymbol{\mu})\right) \tag{8.11}$$

with mean vector $\boldsymbol{\mu}$ and covariance matrix $\boldsymbol{\Sigma}$. Its entropy is derived as:

$$\begin{aligned}
H(f) =& -\int \cdots \int_{\mathbb{R}^n} f(\boldsymbol{x}) \ln f(\boldsymbol{x}) d\boldsymbol{x} \\
=& \int \cdots \int_{\mathbb{R}^n} f(\boldsymbol{x}) \left\{ \frac{1}{2} \ln\left((2\pi)^n |\boldsymbol{\Sigma}|\right) + \frac{1}{2}(\boldsymbol{x}-\boldsymbol{\mu})^\top \boldsymbol{\Sigma}^{-1}(\boldsymbol{x}-\boldsymbol{\mu}) \right\} d\boldsymbol{x} \\
=& \frac{1}{2} \ln\left((2\pi)^n |\boldsymbol{\Sigma}|\right) + \frac{1}{2}\mathbb{E}\left((\boldsymbol{x}-\boldsymbol{\mu})^\top \boldsymbol{\Sigma}^{-1}(\boldsymbol{x}-\boldsymbol{\mu})\right) \\
=& \frac{1}{2} \ln\left((2\pi)^n |\boldsymbol{\Sigma}|\right) + \frac{n}{2} \\
=& \frac{n}{2} + \frac{n}{2}\ln(2\pi) + \frac{1}{2}\ln|\boldsymbol{\Sigma}|
\end{aligned} \tag{8.12}$$

The expectation in Eqn. (8.12) is n, because:

$$\begin{aligned}\mathbb{E}\Big((\boldsymbol{x}-\boldsymbol{\mu})^\top\boldsymbol{\Sigma}^{-1}(\boldsymbol{x}-\boldsymbol{\mu})\Big) =&\mathbb{E}\left\{\text{trace}\Big(\boldsymbol{\Sigma}^{-1}(\boldsymbol{x}-\boldsymbol{\mu})(\boldsymbol{x}-\boldsymbol{\mu})^\top\Big)\right\}\\ =&\text{trace}\left\{\boldsymbol{\Sigma}^{-1}\mathbb{E}\Big((\boldsymbol{x}-\boldsymbol{\mu})(\boldsymbol{x}-\boldsymbol{\mu})^\top\Big)\right\}\\ =&\text{trace}(\boldsymbol{\Sigma}^{-1}\boldsymbol{\Sigma})=n \qquad (8.13)\end{aligned}$$

By observing Eqn. (8.12), it can be seen that for given n, the entropy depends only on the determinant of the covariance matrix. This result greatly simplifies the later analysis. Before I discuss the network redesign problem, the conditional differential entropy $H(X|Y)$ for given two random variables X and Y with a joint density $f(x,y)$ is first defined:

$$\begin{aligned}H(X|Y)=&-\iint_{\mathbb{R}^2} f(x,y)\log f(x|y)dxdy\\ =&-\iint_{\mathbb{R}^2} f(x,y)\log\frac{f(x,y)}{f(y)}dxdy\\ =&-\iint_{\mathbb{R}^2} f(x,y)\log f(x,y)dxdy+\int_{\mathbb{R}^1}\int_{\mathbb{R}^1} f(x,y)dx\log f(y)dy\\ =&-\iint_{\mathbb{R}^2} f(x,y)\log f(x,y)dxdy+\int_{\mathbb{R}^1} f(y)\log f(y)dy\\ =&H(X,Y)-H(Y) \qquad (8.14)\end{aligned}$$

This also holds for multivariate cases, i.e., $H(\boldsymbol{X}|\boldsymbol{Y})=H(\boldsymbol{X},\boldsymbol{Y})-H(\boldsymbol{Y})$.

8.3.2 The redesign problems

Let $\boldsymbol{z}_t$ be a p–dimensional random vector representing the irradiance random field at p discrete sites and at time t, $t\in\{1,\cdots,T\}$. Among the p sites, g are observed (gauged) and u are unobserved (ungauged); $p=g+u$. We can thus write:

$$\begin{aligned}\boldsymbol{z}_t=&\left(\left(\boldsymbol{z}_t^{(1)}\right)^\top \ \left(\boldsymbol{z}_t^{(2)}\right)^\top\right)^\top\\ =&\left(z_t^{(11)}\ \ \ldots\ \ z_t^{(1u)}\ \ z_t^{(21)}\ \ \ldots\ \ z_t^{(2g)}\right)^\top \qquad (8.15)\end{aligned}$$

where $\boldsymbol{z}_t^{(1)}$ denotes the unobserved data at time t and $\boldsymbol{z}_t^{(2)}$ denotes the monitored data at time t. Together as $\boldsymbol{z}_t$, $t \in \{1, \cdots, T\}$, they represent the information available at the time of design, our primary interest is thus $\boldsymbol{z}_{T+1}$, namely, the random field at a future time. To redesign the monitoring network, we can either select or remove stations from $u \cup g$, so that the prospective random field is:

$$\boldsymbol{z}_{T+1} = \left(\left(\boldsymbol{z}_{T+1}^{(rem)} \right)^\top \quad \left(\boldsymbol{z}_{T+1}^{(sel)} \right)^\top \right)^\top \tag{8.16}$$

The fundamental identity in entropy–based design problem is:

$$\begin{aligned} H_{\text{total}} =& H_{\text{pred}} + H_{\text{meas}} \\ =& H\left(\boldsymbol{z}_{T+1}^{(rem)} \middle| \boldsymbol{z}_{T+1}^{(sel)} \right) + H\left(\boldsymbol{z}_{T+1}^{(sel)} \right) \end{aligned} \tag{8.17}$$

where H_{pred} is minimized, or equivalently H_{meas} is maximized, as the total entropy is assumed constant (Shewry and Wynn, 1987). This design is called the variability absorption design (Lee and Ellis, 1997). The maximum variability absorption design aims at optimizing a configuration (sel) so that the unobserved sites (rem) has least uncertainty.

At this point, 3 types for redesign can be raised: 1) optimal design by selecting a given number of stations among the p locations (e.g. Bueso et al., 1998); 2) reduction design by removing some of the existing network (e.g. Wu and Zidek, 1992) and 3) extension design by adding some stations into the existing network (e.g. Zidek et al., 2000). We are interested in the third design in this work. From Eqn. (8.14), we thus have:

$$H\left(\boldsymbol{z}_{T+1}^{(sel)} \right) = H\left(\boldsymbol{z}_{T+1}^{(g)} \right) + H\left(\boldsymbol{z}_{T+1}^{(add)} \middle| \boldsymbol{z}_{T+1}^{(g)} \right) \tag{8.18}$$

where (add) denotes some additional stations from u. The redesign criterion is therefore:

$$\max \left[H\left(\boldsymbol{z}_{T+1}^{(add)} \middle| \boldsymbol{z}_{T+1}^{(g)} \right) \right] \tag{8.19}$$

The marginal normality of the clear sky index data is shown earlier, the assumption is extended further here. Let $\boldsymbol{z}_{T+1}^{(add)}$ and $\boldsymbol{z}_{T+1}^{(g)}$ be jointly normal with covariance:

$$\boldsymbol{\Sigma} = \begin{pmatrix} \boldsymbol{\Sigma}_{aa} & \boldsymbol{\Sigma}_{ag} \\ \boldsymbol{\Sigma}_{ga} & \boldsymbol{\Sigma}_{gg} \end{pmatrix} \tag{8.20}$$

where $\boldsymbol{\Sigma}_{aa}$, $\boldsymbol{\Sigma}_{ag}$ and $\boldsymbol{\Sigma}_{gg}$ are sub–covariances of the respective subscripts, where a denotes the additional stations and g denotes the existing network, the entropy in Eqn. (8.19) is (Bueso et al., 1998):

$$H\left(\boldsymbol{z}_{T+1}^{(add)} \middle| \boldsymbol{z}_{T+1}^{(g)}\right) = \frac{1}{2} \log \left|\boldsymbol{\Sigma}_{a|g}\right| + \text{const.} \tag{8.21}$$

where const. is the cardinality of (add). In other words, if the number of additional stations is fixed, only the first term in Eqn. (8.21) needs to be considered. $\boldsymbol{\Sigma}_{a|g}$ is the conditional covariance. $\boldsymbol{\Sigma}_{a|g}$ can be easily found via the Bartlett (1933) decomposition:

$$\boldsymbol{\Sigma}_{a|g} = \boldsymbol{\Sigma}_{aa} - \boldsymbol{\Sigma}_{ag}\boldsymbol{\Sigma}_{gg}^{-1}\boldsymbol{\Sigma}_{ga} \tag{8.22}$$

For all possible (add) in the set $\{ADD\}$, we compute the determinant of the conditional covariance, the set maximizes the determinant should be chosen.

The entries of the covariance matrices in Eqn. (8.22) can be found via the variogram shown in Eqn. (8.8):

$$\Sigma_{ij} = \widehat{\sigma}_i^2 \cdot \widehat{\sigma}_j^2 \cdot \Big(2 - \gamma(h_{ij})\Big)/2, \quad i, j \in a \cup g \tag{8.23}$$

where $\widehat{\sigma}_i^2$ and $\widehat{\sigma}_j^2$ are the variance estimates at $\boldsymbol{s}_i^*$ and $\boldsymbol{s}_j^*$ respectively. We note that during the variance estimation at the unobserved locations, the non–homogeneity in the variance field is smoothed using the same thin plate splines.

8.4 Case study: adding 3 stations

Suppose there is budget to set up 3 new irradiance monitoring stations in Singapore, the methods introduced earlier are used to redesign the existing monitoring network by adding these 3 stations at preferred locations. Based on the locations of the existing network, a 10 by 10 grid of potential sites are set, as shown in Fig. 8.5.

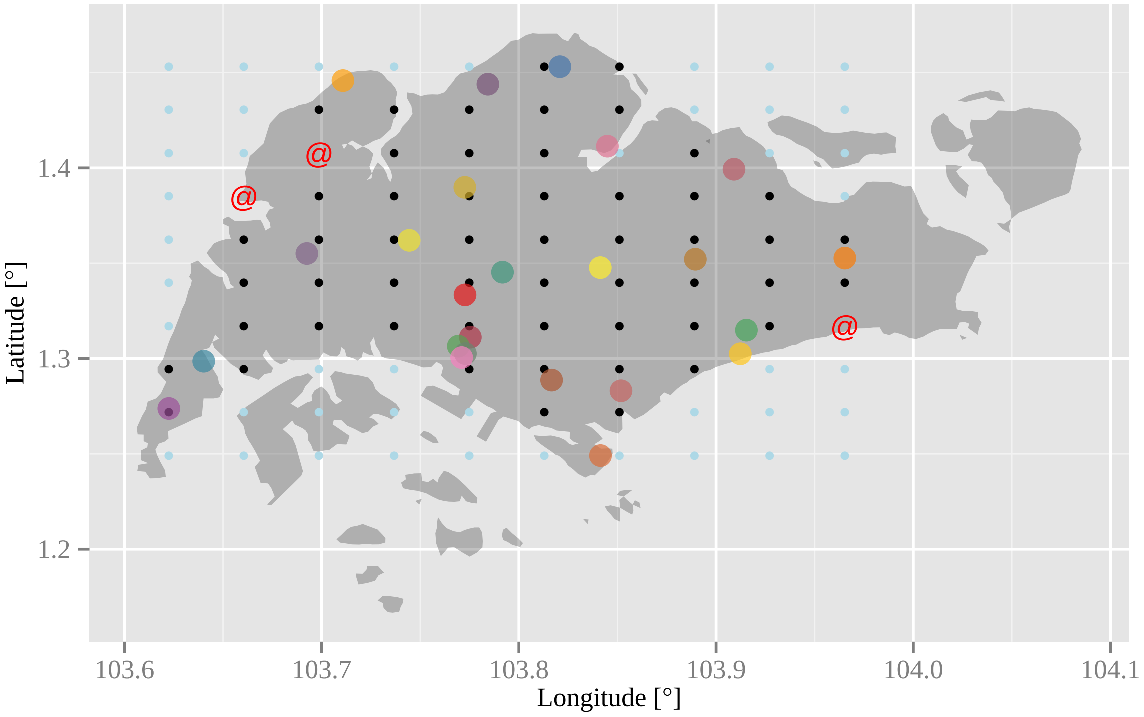

Fig. 8.5 A 10 by 10 grid of potential locations for new monitoring sites. Light blue dots denote stations not on the main island. Colored dots show the existing network. The symbol @ indicates the locations of the 3 new locations following the entropy–based redesign.

I only consider the potential locations on the main island (show as small black dots) as setting up a monitoring station over the ocean is unrealistic. 56 potential locations, as a result, are used in the redesign; the cardinality of set $\{ADD\}$ is $C_3^{56} = 27720$. For each element in $\{ADD\}$, the logarithm of the determinant shown in Eqn. (8.21) is calculated[4]. The run time for the determinant calculation is 4.21 seconds on a late 2013 MacBook Pro computer. The 3 stations maximizing the conditional entropy is represented with symbol

---

[4] The dimensions of $\mathbf{\Sigma}_{aa}$, $\mathbf{\Sigma}_{ag}$ and $\mathbf{\Sigma}_{gg}$ are 3×3, 3×24 and 24×24 respectively.

@ in Fig. 8.5.

The optimal locations of the new stations can be refined by using more potential sites. However, the number of possible combinations increases substantially. For example, if we perform the analysis on a 100 by 100 grid, the cardinality of set $\{ADD\}$ is $C_3^{10000} \approx 1.67 \times 10^{11}$. In this case, evolutionary computing can be used to select the optimal locations; same entropy criterion can be used as the objective function.

8.5 Chapter conclusion

An entropy–based method is introduced to redesign (expand) the existing irradiance monitoring network. Much attention is paid to the non–parametric covariance estimation as the particular criterion of network expansion relies heavily on the estimated covariance. Solar irradiance random fields in nature is “almost surely" anisotropic, the S–G method is therefore necessary in the spatio–temporal covariance related applications. Previously unaddressed issue, the thin plate folding, is discussed in details here. The trade–off between the measure of isotropy and the severeness of the folding is made clear. Several data issues including the stationarity of the clear sky index time series, the marginal and joint normality of the data and non–homogeneity of the variance field are also briefly discussed.

Chapter 9

Space–time forecasting models with parameter shrinkage

Chapters 6 and 7 discuss two distinct approaches to the inverse transposition problem. Such practices would allow us to gather more data into the forecasting system. Furthermore, when it is financially acceptable, additional monitoring stations can be build at strategic locations using the methods presented in chapter 8, to provide data. Recall that in chapter 5, the irradiance spatio–temporal random process is characterized using the covariance structures. However, two problems arise as the spatial sampling points within an area increase: 1) the size of the covariance matrix becomes large thus increases the computation burden and 2) some covariances become degenerate thus make the isotropic transform impossible[1]. Similar problems are found in the time domain, too. A key objective of this chapter is to reduce the number of parameters in the characterization of the process.

Properly designed shrinkage models can improve forecast accuracies from a model that uses irrelevant information. I propose two novel methods to quantify the long-term threshold distance of the spatio–temporal irradiance process, namely, deriving the threshold distance from the distributions of maximum daily cross-correlation and from the isotropic dispersion.

---

[1] Although the penalized TPS mapping can be used to resolve the bending, when the bending is severe, the use of large λ value will result in underfitting, recall section 8.2.2 for more details.

I also apply two spatio–temporal predictive methods, namely, space–time kriging and vector autoregressive (VAR) models. It is found that the forecasting accuracies do not increase by including more stations beyond the threshold distance[2]. This result allows for the design of simplified monitoring networks and improved forecasting techniques.

9.1 Monitoring network, predictability and model parameter shrinkage

An important objective of monitoring networks is to predict values of an attribute of interest at unobserved locations using observed data at known locations. The spatial sparsity and sampling rate of the networks directly determine the predictability of the networks in both space and time. Two extreme examples are given in chapter 2. Bosch and Kleissl (2013); Bosch et al. (2013) use networks with super fine spatial resolution for sub–minute prediction and Perez et al. (2007, 2010) use satellite images for days–ahead prediction. The link between the network and its predictability is immediately seen.

For intra–hour irradiance forecasts, the most suitable network is seen in (Lonij et al., 2013). Electricity output data from a dense network of residential rooftop PV systems (80 systems over a 50 × 50 km area) are used to derive the cloud patterns and movements, thus forecast the solar power. Along–wind and cross–wind directional correlations are considered. This is only possible owing to the observations provided by many station pairs, i.e., a good spatial resolution.

The above mentioned techniques and applications use cloud motion analyses. Unfortunately, most existing irradiance monitoring networks are far more sparse than the network in (Lonij et al., 2013), and suffer from measurement errors and occasional downtime. Alternative forecast techniques are needed.

Spatio–temporal forecasting based on data from sparse sampling in the presence of noise

---

[2] The threshold distance herein developed is likely to be frequency dependent, i.e., varies with data time resolution. Further research may apply.

and missing data represents the paradigmatic problem of spatio–temporal statistics (Cressie and Wikle, 2011). Spatio–temporal statistics is not a new field of study, however, its development lags far behind the spatial statistics (Ma, 2003). Furthermore, the developments in the predictive models are mostly theoretical. In recent years, few researchers have used spatio–temporal statistics to model environmental processes such as wind velocity fields (De Luna and Genton, 2005; Gneiting, 2002; Porcu et al., 2008) and solar irradiance (Inoue et al., 2012; Yang et al., 2013b). These applications use data that can be considered as temporally rich and spatially sparse. De Luna and Genton (2005) point out that if the prediction is only in the time direction, spatial stationarity and isotropy assumptions can be relaxed by means of VAR models. However, considering the spatial dependence in the data, a model building strategy has to be included. This statement reveals the core idea of this chapter: parameter shrinkage in a spatio–temporal predictive model.

In linear regression analyses, parameter shrinkage is directly related to the goodness of fit of a hyperplane. By logically selecting and/or weighting the regression inputs, the predictive performance can be further optimized from the least square solution (Miller, 2002); although the estimators are usually biased (the unbiased estimators are given by the least square solution). A VAR model can be considered as a linear regression model; general parameter shrinkage models for VAR have been developed and well-accepted. Ridge regression, the lasso (Tibshirani, 1996, 2011), least angle regression (LARS) (Efron et al., 2004) and elastic nets regression (Zou and Hastie, 2005) have shown to improve the estimation errors in many multivariate regression problems. However, these methods are not tailored to environmental modeling.

I propose two novel methods for parameter selection and shrinkage in solar irradiance forecasting using spatio–temporal statistical models in this chapter. Both methods identify a threshold distance in irradiance random processes. The **threshold distance** is an important quantity that specifies the maximum separation between locations whose values may be correlated.

The first method uses standard deviations of inter–station correlation distributions to quantify the threshold distance in the irradiance field. This means that the irradiance values sampled at two stations lose correlation beyond a certain distance. Previously, this de–correlation distance was simulated (assuming along–wind and rigid clouds) by Perez et al. (2012) using univariate time series data of various time averaging horizons. Lonij et al. (2013) confirmed the estimation of 15 min along–wind de–correlation distance of ≈10 km using measured data from 80 stations. In this chapter, I use only a sparse network of 13 stations to estimate the 5 min threshold distance. Note that I choose the name "threshold distance" (instead of the de–correlation distance) owing to the fact that the estimation not only considers the along–wind situations but all possible directional correlations.

The second proposed method uses spatial dispersion to quantify the threshold distance. Recall that the irradiance process is almost surely anisotropic. In this case, multidimensional scaling (MDS) (as seen in chapter 5) is appropriate to transform the anisotropic geographical plane to an isotropic dispersion plane. The threshold distance is then estimated on the dispersion plane. The estimated distance thus derived agrees well with that from the first method. While both approaches are empirical in that the magnitude of the result and its error will be limited by the dataset, the methodologies are well–suited to application to irradiance observations.

Once the threshold distance is determined, data from stations beyond the threshold distance will not be considered in model building. Therefore this distance constraint becomes an automatic parameter selection tool for models such as kriging and VAR. The forecasts using partial networks are compared with several other existing methods including the persistence model, full network space–time kriging, VAR with ridge/lasso regression and full network VAR models. The results of the proposed shrinkage models are better than the full network model in general. Furthermore, the threshold distance also provides guidelines in monitoring network design.

9.1.1 Data

The analyses are performed using one year (2013), 5 min GHI data collected at 13 meteorological stations across Singapore whose locations are indicated in Fig. 9.1. Some of these stations have appeared in Fig. 5.1. Only data with zenith angles smaller than 70° are used to avoid the measurement errors due to large zenith angle and possible shading.

Fig. 9.1 Locations of the 13 stations used in this chapter. Source: Google Maps.

9.2 Analysis of spatio–temporal lag distribution

The cross–covariance and the cross–correlation as functions of time lags provide measures of the similarity of two stationary time series (Podobnik et al., 2011).

9.2.1 Lag correlation between a pair of stations

Cloud transients dominate solar irradiance variability, while the movements of clouds are driven primarily by wind. The von Mises (or circular normal) distribution is the most commonly used circular distribution describing the distribution of wind direction (Xu et al., 2010). I hypothesize that the daily temporal lag between two stations is governed by a zero centered, symmetrical distribution. I quantify the daily temporal lag between two stations using the maximum cross–correlation of two GHI time series.

Detrended time series must be used in the calculation of cross–correlations between a pair of stations. This is essential for proper analyses for two reasons: 1) detrending prevents two time series from being correlated if they are uncorrelated, and 2) detrending captures the underlying true correlation between two time series (Horvatic et al., 2011). The clear sky index is therefore used instead of GHI to account for the cross–correlation. The clear sky index is calculated by dividing the GHI series by its corresponding clear sky irradiance. The clear sky model is described in chapter 3.

As an example, Fig. 9.2 shows the cross–correlation between stations S104 and S105 (4.19 km apart) on 2013 June 11. A max correlation of 0.872 is observed at time lag +5 minutes. This indicates that whatever happens at S105 may cause a similar event at S104 five minutes later on that day. The possibility can be described by magnitudes of correlation coefficients: higher correlation indicates a higher possibility.

The daily maximum cross–correlation experiment between S104 and S105 is repeated for the entire year. The distribution (histogram) is shown in Fig. 9.3. The time lag which corresponds to the maximum daily cross–correlation is on the horizontal axis; while the frequency of occurrence (number of days which a particular time lag occurred in the year 2013) is shown on the vertical axis. Note that all the maximum cross–correlation coefficients used in Fig. 9.3 are significant at 95% confidence with all insignificant coefficients being rejected. The $1-\alpha$ confidence interval of the cross–correlation coefficient θ is approximated by Wasserman (2003):

$$(a,b)=\left(\widehat{\theta}-\frac{z_{\alpha/2}}{\sqrt{n-3}},\widehat{\theta}+\frac{z_{\alpha/2}}{\sqrt{n-3}}\right) \tag{9.1}$$

where $\widehat{\theta}$ is the estimate of cross–correlation coefficient θ. $z_{\alpha/2}$ is the value of the $1-\alpha/2$ percentile point of the standard normal distribution. n is the number of data points, 110 in

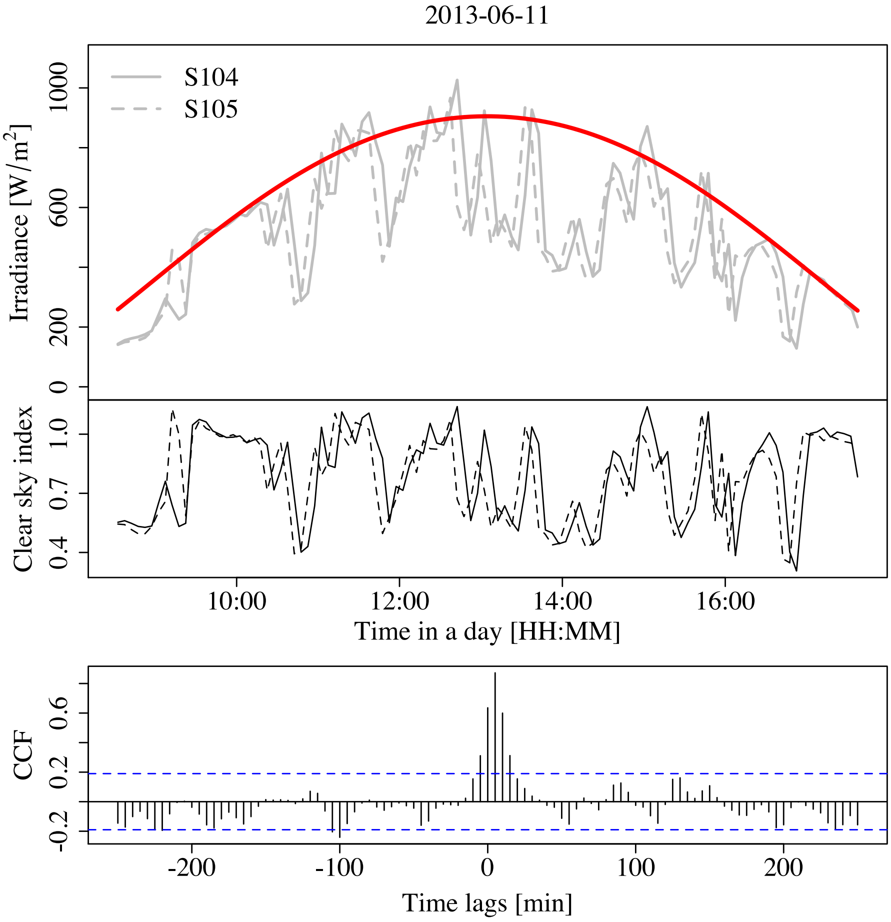

Fig. 9.2 The cross–correlation function (CCF) between stations S104 and S105 (4.19 km apart) on 2013 June 11. The clear sky irradiance and two irradiance time series are shown in the top window while the clear sky index (dimensionless) time series are shown in the middle. A maximum correlation of 0.872 is observed at time lag +5 minutes. The dashed blue lines in the bottom plot indicate the 95% confidence interval for correlation estimates.

this case. For a small correlation coefficient under the null hypothesis of zero correlation, the approximated critical values at the $\alpha = 5\%$ level are $\pm 1.96/\sqrt{n-3} \approx \pm 0.19$ (see dashed blue lines in Fig. 9.2). This confidence interval approximation assumes white noise inputs.

9.2.2 Hovmöller diagram analyses

Hovmöller diagram is an effective way to visualize spatio–temporal data. The axes of the Hovemöller diagram are usually longitude or latitude (on the abscissa) and time (on the ordinate). To visualize the distance–time relationship for temporal lag distribution among

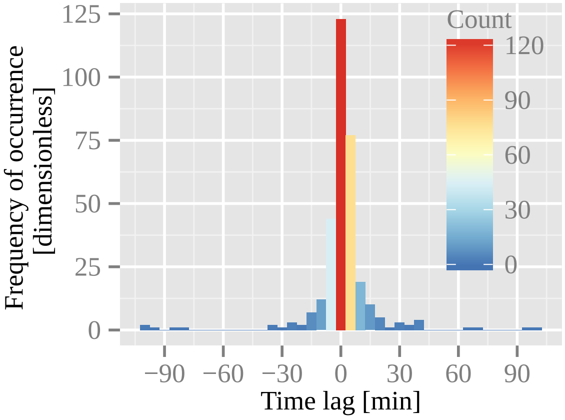

Fig. 9.3 The distribution of the time lag of the daily max cross–correlation between station S104 and S105 (4.19 km apart).

stations, kilometer distance is used on the abscissa. Fig. 9.4 shows the time lag distributions for all possible station pairs. To make the visual contrast, I plot the Hovmöller diagram in Fig. 9.4 in log of frequency.

The Hovmöller diagram herein shown is a combination of histograms seen from the top down. For each column of blocks, the diagram represents the histogram at a specific distance, i.e., the time lag correlation distribution between a particular pair of stations. Since 13 stations are involved, $n(n-1)/2 = 78$ columns are shown in the Hovmöller diagram.

Symmetrical distributions from many columns are seen in Fig. 9.4 where the colors are distributed evenly at both sides of the zero time lag line. The observed symmetry agrees with the earlier hypothesis. As the standard deviation indicates the deviation from the mean, it is an effective statistic to represent the magnitude of possible time lag between two stations. Fig. 9.5 shows the standard deviation of lag distribution against the distances across 78 pairs of stations.

It may be expected that as the separation distance between station pairs increases, the standard deviation in the lag distribution will increase and eventually converge. I seek to quantify this convergence so that threshold distance can be deduced. I use the so–called “L–method” to determine the threshold distance from Fig. 9.5. The application of the L–

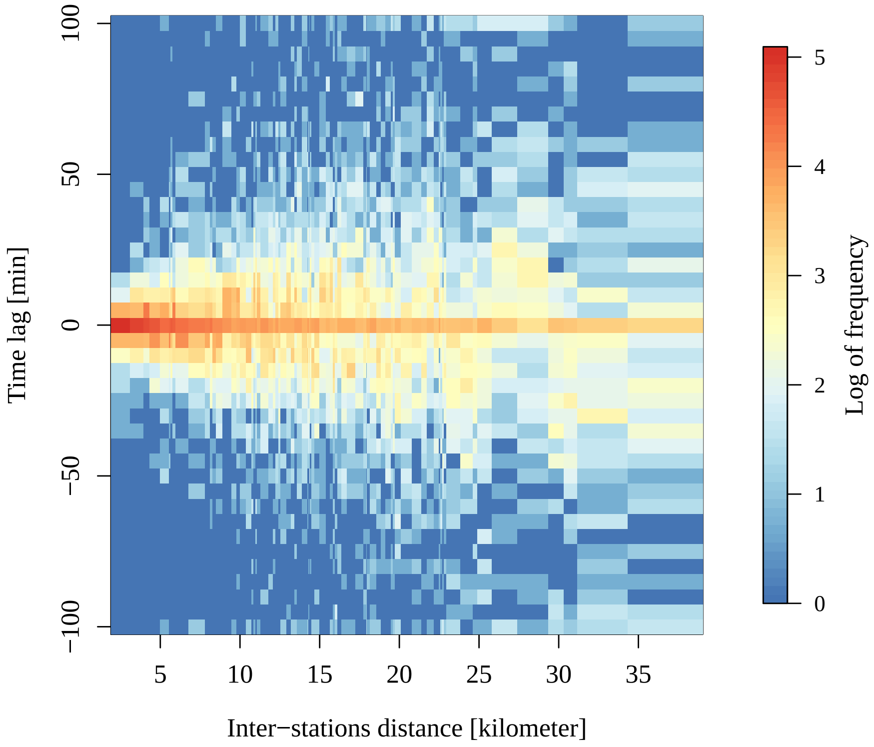

Fig. 9.4 Hovmöller diagram using inter–stations distance on the abscissa. Color bar indicates the log of frequency of occurrence at respective time lags.

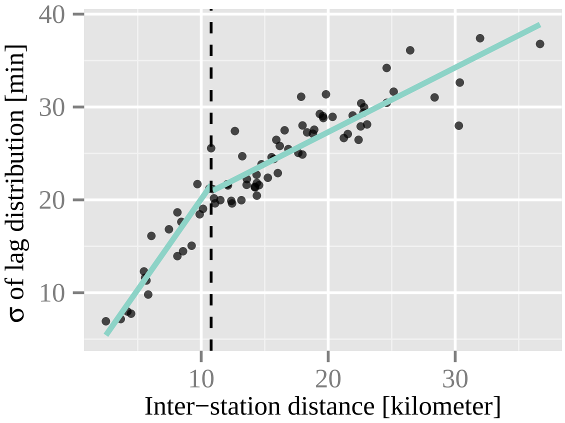

Fig. 9.5 The standard deviations σ of time lag distributions against the distances across 78 pairs of stations. Threshold distance of 10.78 km is estimated using the L–method.

method here is novel. The L–method was originally designed for the detection of anomalies in time series (Salvador and Chan, 2005); its ability to use two separate linear least square regression lines to identify the “knee” suits the present application. The total root mean squared error $RMSE_c$ of the two regression lines is given by:

$$RMSE_c = \frac{c}{b} \times RMSE(L_c) + \frac{b-c}{b} \times RMSE(R_c) \tag{9.2}$$

Given a set of points with indices $i = 1, \cdots, b$ (see Fig. 9.5, $b = 78$ in our case), the L–method first separates them into two sets, namely, the sequence of points L_c with indices $i = 1, \cdots, c$ and the sequence of points R_c with indices $i = c+1, \cdots, b$. Two separate linear regression lines are fitted using these two sets of points; and their fitting root mean square errors are $RMSE(L_c)$ and $RMSE(R_c)$ respectively. $RMSE_c$ can thus be found following the above equation. As c can vary from 2 to $b-2$; a particular value of c would minimize $RMSE_c$. In addition, any $c \in \{2, 3, \cdots, b-2\}$ corresponds to a pair of stations; the distance between this pair of stations can thus be calculated. It is found that a distance of 10.78 km (the $c = 20$ case) minimizes $RMSE_c$ (see the dashed vertical line in Fig. 9.5).

The threshold distance in Singapore has been determined. Although a distribution of temporal lag correlation may exist at a larger distance, correlations beyond the threshold distance is assumed to be non–informative. Perez et al. (2012) estimated the de–correlation distance of 5 min irradiance observations to be 3 km at a mid latitude site. However only correlations in the along–wind directions are considered in that study. If the correlations of all directions are involved, the de–correlation distance is usually not observed (Murata et al., 2009). The aim of threshold distance is shrinking the regression parameters in a spatio–temporal predictive model (a long–term statistical quantity), but not quantifying the absolute (short–term) de–correlation distance.

Daily maximum correlation analysis is used to define the spatio–temporal correlation limits. Although the analysis appears to be short–term (daily), it is in fact a long–term (yearly) analysis since only the standard deviations of daily time lag distributions for an entire year are considered. In the following section, I estimate the correlation threshold distance using another method.

9.3 Analysis of thin plate spline bending

9.3.1 Isotropy transformation

A useful metric in quantifying spatio–temporal dissimilarity is spatial dispersion, defined in Eqn. (5.2). If an irradiance random field is isotropic (invariant of rotation in space), the threshold distance can be estimated using L–method on a dispersion versus distance plot (following a similar fitting procedure as the method described in section 9.2). However, isotropy is rarely observed; the distance in the geographical plane may not provide useful correspondence between dispersion and distance. I therefore use the two–step transformation introduced in chapter 5 to transform the anisotropic G plane to D plane, so that the relationship between the dispersion and distance can be established.

The mathematics for multidimensional scaling and thin plate spline mapping is shown in appendices C and D. Fig. 9.6 shows the transformation. It uses the same data across the same time period as the earlier exercise in section 9.2. On subplot (a), we have the station locations identical to the one shown in Fig. 9.1. Subplot (b) shows the transformed dispersion grid.

The transformed D plane has improved isotropy from the anisotropic G plane. While searching for the threshold distance, a one–to–one correspondence between the distance and the dispersion must be established, i.e., dispersion should be a function of separation distance only. The threshold distance using the L–method on D plane is thus more robust. Fig. 9.7 shows the correspondence between the spatial dispersion and the D plane inter–station distance; a total of 78 points are plotted using data from the 13 stations. Analysis using the L–method identifies a threshold distance of 10.43 km, which agrees well with the previous estimation of 10.78 km using the correlation distribution method.

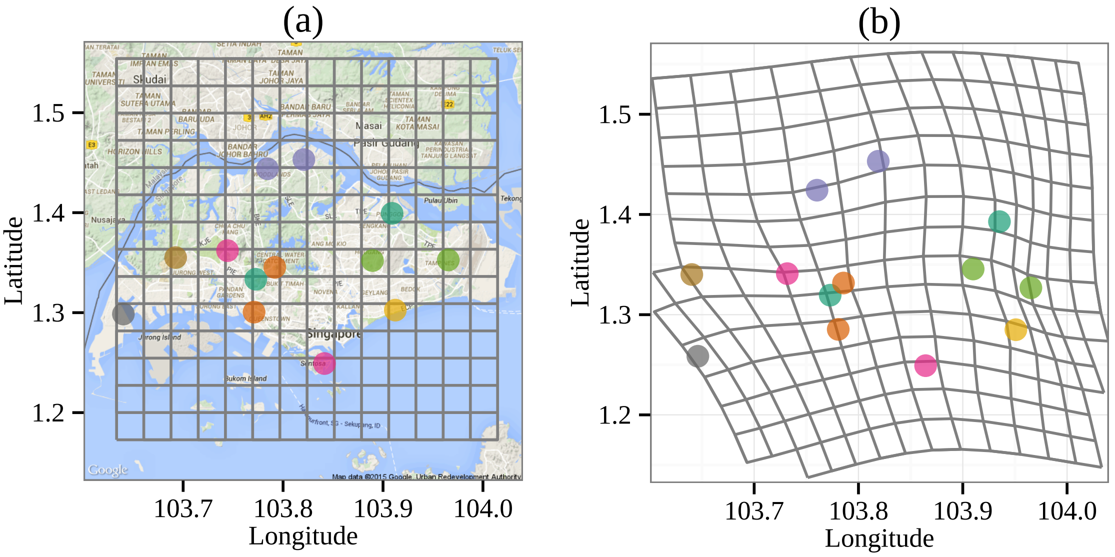

Fig. 9.6 The G plane coordinates are mapped to the D plane through a bijective function. Points in plot (a) show the original G plane locations in the rectangular grid; (b) show the D plane locations after the multidimensional scaling in the deformed grid.

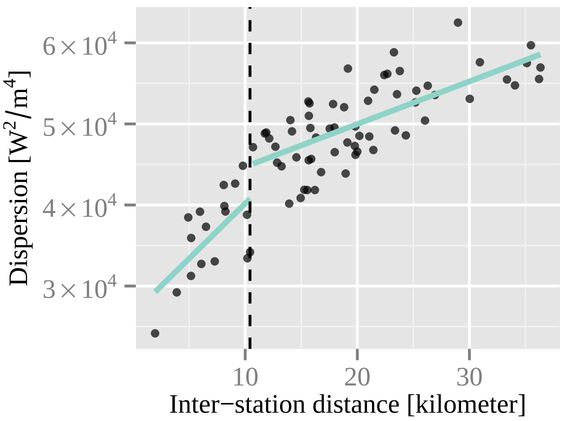

Fig. 9.7 Spatial dispersion versus the D plane inter–station distance for GHI measurements.

9.4 Predictive performance and conclusion

Threshold distance in spatio–temporal irradiance fields in Singapore is estimated using two distinct methods in section 9.2 and section 9.3. In this section, I demonstrate a forecasting application of the estimated threshold distance.

9.4.1 Some spatio–temporal forecasting models

Space–time kriging

Space–time kriging uses proximities such as covariance to forecast the spatio–temporal process $z(\boldsymbol{s}_0; t_0)$ at location $\boldsymbol{s}_0$ and time t_0. The explicit expression of its point estimate, $\widehat{z}(\boldsymbol{s}_0; t_0)$, is given in chapter 5. Recall when data from m previous steps and n locations are used, the spatio–temporal covariance matrix $\boldsymbol{C}$ has dimension $\mathbb{R}^{nm\times nm}$. I will use space–time kriging to validate the shrinkage model in the next section.

Vector autoregressive model

Beside the space–time kriging, VAR is also considered. In the VAR model, we consider a time series of spatial process $\{z_t(\boldsymbol{s}) : \boldsymbol{s} \in D_s, t = 0, 1, \cdots\}$ where $D_s = \{\boldsymbol{s}_1, \cdots, \boldsymbol{s}_n\}$. Recall Eqn. (2.2), if we only consider the autoregressive part and include a constant term $\boldsymbol{\zeta}$, we have a VAR(p) model:

$$\boldsymbol{z}_t = \boldsymbol{\zeta} + \sum_{k=1}^{p} \boldsymbol{\phi}_k \boldsymbol{z}_{t-k} + \boldsymbol{a}_t \quad , \tag{9.3}$$

i.e.,

$$\begin{pmatrix} z_t(\boldsymbol{s}_1) \\ z_t(\boldsymbol{s}_2) \\ \vdots \\ z_t(\boldsymbol{s}_n) \end{pmatrix} = \boldsymbol{\zeta} + \boldsymbol{\phi}_1 \begin{pmatrix} z_{t-1}(\boldsymbol{s}_1) \\ z_{t-1}(\boldsymbol{s}_2) \\ \vdots \\ z_{t-1}(\boldsymbol{s}_n) \end{pmatrix} + \cdots + \boldsymbol{\phi}_p \begin{pmatrix} z_{t-p}(\boldsymbol{s}_1) \\ z_{t-p}(\boldsymbol{s}_2) \\ \vdots \\ z_{t-p}(\boldsymbol{s}_n) \end{pmatrix} + \boldsymbol{a}_t \tag{9.4}$$

where $\boldsymbol{\phi}_k$, $k = 1, \cdots, p$ are $n \times n$ matrices, $\boldsymbol{\zeta}$ and $\boldsymbol{a}_t$ are n dimensional vectors. To solve for matrices $\boldsymbol{\phi}_k$, a n–variate time series $\{\boldsymbol{z}\}$, $\boldsymbol{z} = \{\boldsymbol{z}_0, \cdots, \boldsymbol{z}_T\}$, formed by the $(T+1) \times n$ observations is considered. VAR(p) models can also be written in concise matrix notation:

$$\boldsymbol{Z}^* = \boldsymbol{B}\boldsymbol{X}^* + \boldsymbol{U}^* \tag{9.5}$$

where

$$\boldsymbol{Z}^* = \begin{pmatrix} \boldsymbol{z}_p & \boldsymbol{z}_{p+1} & \cdots & \boldsymbol{z}_T \end{pmatrix} = \begin{pmatrix} z_p(\boldsymbol{s}_1) & z_{p+1}(\boldsymbol{s}_1) & \cdots & z_T(\boldsymbol{s}_1) \\ z_p(\boldsymbol{s}_2) & z_{p+1}(\boldsymbol{s}_2) & \cdots & z_T(\boldsymbol{s}_2) \\ \vdots & \vdots & \ddots & \vdots \\ z_p(\boldsymbol{s}_n) & z_{p+1}(\boldsymbol{s}_n) & \cdots & z_T(\boldsymbol{s}_n) \end{pmatrix} \tag{9.6}$$

$$\boldsymbol{B} = \begin{pmatrix} \boldsymbol{\zeta} & \boldsymbol{\phi}_1 & \boldsymbol{\phi}_2 & \cdots & \boldsymbol{\phi}_p \end{pmatrix} = \begin{pmatrix} \zeta_1 & & & & \\ \vdots & \boldsymbol{\phi}_1 & \boldsymbol{\phi}_2 & \cdots & \boldsymbol{\phi}_p \\ \zeta_n & & & & \end{pmatrix} \tag{9.7}$$

$$\boldsymbol{X}^* = \begin{pmatrix} 1 & 1 & \cdots & 1 \\ \boldsymbol{z}_{p-1} & \boldsymbol{z}_p & \cdots & \boldsymbol{z}_{T-1} \\ \boldsymbol{z}_{p-2} & \boldsymbol{z}_{p-1} & \cdots & \boldsymbol{z}_{T-2} \\ \vdots & \vdots & \ddots & \vdots \\ \boldsymbol{z}_0 & \boldsymbol{z}_1 & \cdots & \boldsymbol{z}_{T-p} \end{pmatrix} = \begin{pmatrix} 1 & 1 & \cdots & 1 \\ z_{p-1}(\boldsymbol{s}_1) & z_p(\boldsymbol{s}_1) & \cdots & z_{T-1}(\boldsymbol{s}_1) \\ z_{p-1}(\boldsymbol{s}_2) & z_p(\boldsymbol{s}_2) & \cdots & z_{T-1}(\boldsymbol{s}_2) \\ \vdots & \vdots & \ddots & \vdots \\ z_{p-1}(\boldsymbol{s}_n) & z_p(\boldsymbol{s}_n) & \cdots & z_{T-1}(\boldsymbol{s}_n) \\ z_{p-2}(\boldsymbol{s}_1) & z_{p-1}(\boldsymbol{s}_1) & \cdots & z_{T-2}(\boldsymbol{s}_1) \\ z_{p-2}(\boldsymbol{s}_2) & z_{p-1}(\boldsymbol{s}_2) & \cdots & z_{T-2}(\boldsymbol{s}_2) \\ \vdots & \vdots & \ddots & \vdots \\ z_{p-2}(\boldsymbol{s}_n) & z_{p-1}(\boldsymbol{s}_n) & \cdots & z_{T-2}(\boldsymbol{s}_n) \\ \vdots & \vdots & \ddots & \vdots \\ z_0(\boldsymbol{s}_1) & z_1(\boldsymbol{s}_1) & \cdots & z_{T-p}(\boldsymbol{s}_1) \\ z_0(\boldsymbol{s}_2) & z_1(\boldsymbol{s}_2) & \cdots & z_{T-p}(\boldsymbol{s}_2) \\ \vdots & \vdots & \ddots & \vdots \\ z_0(\boldsymbol{s}_n) & z_1(\boldsymbol{s}_n) & \cdots & z_{T-p}(\boldsymbol{s}_n) \end{pmatrix} \tag{9.8}$$

$$\boldsymbol{U}^* = \begin{pmatrix} \boldsymbol{a}_p & \boldsymbol{a}_{p+1} & \cdots & \boldsymbol{a}_T \end{pmatrix} = \begin{pmatrix} a_p(\boldsymbol{s}_1) & a_{p+1}(\boldsymbol{s}_1) & \cdots & a_T(\boldsymbol{s}_1) \\ a_p(\boldsymbol{s}_2) & a_{p+1}(\boldsymbol{s}_2) & \cdots & a_T(\boldsymbol{s}_2) \\ \vdots & \vdots & \ddots & \vdots \\ a_p(\boldsymbol{s}_n) & a_{p+1}(\boldsymbol{s}_n) & \cdots & a_T(\boldsymbol{s}_n) \end{pmatrix} \tag{9.9}$$

If we write the residual sum–of–square (RSS) of the model as:

$$\mathrm{RSS}(\boldsymbol{B}) = (\boldsymbol{Z}^* - \boldsymbol{B}\boldsymbol{X}^*)^\top(\boldsymbol{Z}^* - \boldsymbol{B}\boldsymbol{X}^*) \tag{9.10}$$

and set its first order derivative with respect to $\boldsymbol{B}$ to zero, i.e., $(\boldsymbol{Z}^* - \boldsymbol{B}\boldsymbol{X}^*)(\boldsymbol{X}^*)^\top = 0$, the stationary point for this quadratic function can be found. The least square estimator for matrix $\boldsymbol{B}$ is thus given by:

$$\widehat{\boldsymbol{B}} = \boldsymbol{Z}^*(\boldsymbol{X}^*)^\top[\boldsymbol{X}^*(\boldsymbol{X}^*)^\top]^{-1} \tag{9.11}$$

Any VAR model has its equivalent regression representation. Eqn. 9.5 can be re–written to n regression problems, each one being:

$$\boldsymbol{Z} = \boldsymbol{X}\boldsymbol{\beta} + \boldsymbol{U} \tag{9.12}$$

where

$$\boldsymbol{Z} = \begin{pmatrix} z_p(\boldsymbol{s}_k) & z_{p+1}(\boldsymbol{s}_k) & \cdots & z_T(\boldsymbol{s}_k) \end{pmatrix}^\top, \quad k \in \{1, \cdots, n\} \tag{9.13}$$

$$\boldsymbol{X} = (\boldsymbol{X}^*)^\top \tag{9.14}$$

$$\boldsymbol{U} = \begin{pmatrix} a_p(\boldsymbol{s}_k) & a_{p+1}(\boldsymbol{s}_k) & \cdots & a_T(\boldsymbol{s}_k) \end{pmatrix}^\top, \quad k \in \{1, \cdots, n\} \tag{9.15}$$

The least square estimates for $\boldsymbol{\beta}$, a vector with length $p \times n + 1$, is thus given by:

$$\widehat{\boldsymbol{\beta}} = (\boldsymbol{X}^\top\boldsymbol{X})^{-1}\boldsymbol{X}^\top\boldsymbol{Z} \tag{9.16}$$

which minimizes $(\boldsymbol{Z} - \boldsymbol{X}\boldsymbol{\beta})^\top(\boldsymbol{Z} - \boldsymbol{X}\boldsymbol{\beta})$. We can see from the above equations that for each station $\boldsymbol{s}_k$, the prediction is made using a linear combination of its own past values and the past values from all other stations.

Ridge regression

As mentioned earlier in section 9.1, many parameter shrinkage models such as the ridge regression have been proposed to simplify the above VAR model (and other regression problems). The idea behind ridge regression is to penalize the size of the regression parameters. The ridge regression estimator solves the regression problem using ℓ_2 penalized least squares:

$$\widehat{\boldsymbol{\beta}}^{\text{ridge}} = \underset{\boldsymbol{\beta}}{\operatorname{argmin}} \left\{ \|\boldsymbol{Z} - \boldsymbol{X}\boldsymbol{\beta}\|_2^2 + \lambda \|\boldsymbol{\beta}\|_2^2 \right\} \tag{9.17}$$

where $\|\boldsymbol{Z} - \boldsymbol{X}\boldsymbol{\beta}\|_2^2 = (\boldsymbol{Z} - \boldsymbol{X}\boldsymbol{\beta})^\top (\boldsymbol{Z} - \boldsymbol{X}\boldsymbol{\beta})$ is the ℓ_2–norm loss function, i.e., RSS. $\|\boldsymbol{\beta}\|_2^2 = \boldsymbol{\beta}^\top \boldsymbol{\beta}$ is the ℓ_2–norm penalty on $\boldsymbol{\beta}$. λ is a tuning parameter which regulates the strength of the penalty. When $\lambda = 0$, we get the linear regression estimate; when $\lambda = \infty$, $\widehat{\boldsymbol{\beta}}^{\text{ridge}} = 0$. The equivalent minimization problem is:

$$\text{minimize} \quad (\boldsymbol{Z} - \boldsymbol{X}\boldsymbol{\beta})^\top (\boldsymbol{Z} - \boldsymbol{X}\boldsymbol{\beta}) \quad \text{s.t.} \quad \|\boldsymbol{\beta}\|_2^2 < t \tag{9.18}$$

By matrix calculus, the solution to this problem is immediately seen to be:

$$\widehat{\boldsymbol{\beta}}^{\text{ridge}} = \left(\boldsymbol{X}^\top \boldsymbol{X} + \lambda \boldsymbol{I}_{n \times (p \times n+1)} \right)^{-1} \boldsymbol{X}^\top \boldsymbol{Z} \tag{9.19}$$

The most commonly used way to select a suitable λ is the K–fold cross validation. The training data are first partitioned into K equal sized separate sets. For each $k = 1, 2, \cdots, K$, we fit the model to the training set excluding the kth–fold. The overall cross–validation error through K models is computed. The λ^* which minimizes the cross–validation error is selected.

The lasso

Similar to ridge regression, the lasso coefficients are

$$\widehat{\boldsymbol{\beta}}^{\text{lasso}} = \underset{\boldsymbol{\beta}}{\operatorname{argmin}} \left\{ \|\boldsymbol{Z} - \boldsymbol{X}\boldsymbol{\beta}\|_2^2 + \lambda \|\boldsymbol{\beta}\|_1 \right\} \tag{9.20}$$

or the solutions to the ℓ_1 minimization:

$$\text{minimize} \quad (\boldsymbol{Z} - \boldsymbol{X}\boldsymbol{\beta})^\top (\boldsymbol{Z} - \boldsymbol{X}\boldsymbol{\beta}) \quad \text{s.t.} \quad \|\boldsymbol{\beta}\|_1 < t \tag{9.21}$$

Unlike ridge regression, the lasso shrinks some of the coefficients exactly to zero. This is because of its special geometric implication from the ℓ_1–norm penalty. Thus the lasso can be considered as a parameter selection method, but not ridge regression. However, $\widehat{\boldsymbol{\beta}}^{\text{lasso}}$ has no closed form solution. The problem can be solved using quadratic programming from convex optimization (Tibshirani, 2011).

9.4.2 Proposed shrinkage models

The above models will be used to benchmark the proposed mode along with the persistence model where the forecast is equal to the current observation.

The threshold distance in Singapore has been previously identified to be ≈10 km. Following this guideline, several subnetworks are selected as shown in Fig. 9.8. Each circle has a radius of 10 km; and they jointly cover all the stations. As the proposed shrinkage models are general, they will be applied in both kriging frameworks and VAR frameworks.

9.4.3 Predictive performance

The shrinkage models in an empirical kriging framework are first examined. Fig. 9.5 shows that the maximum σ of lag distribution is 35 minutes, and that the σ at the threshold distance is 20 minutes. If 5 min data are used for forecasting, a maximum temporal lag

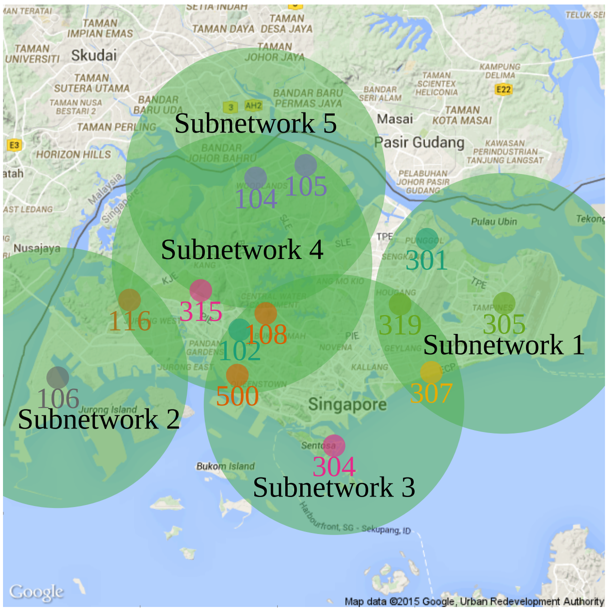

Fig. 9.8 Five subnetworks covering all 13 irradiance monitoring stations, each with a radius of 10 km.

of 7 (35/5 = 7) should be used to fully capture the spatio–temporal dynamics. On the other hand, a temporal lag of 4 corresponds to the threshold distance. Thus $m = 7$ and $m = 4$ in Eqn. 5.25 are set for these two case studies. 5 additional case studies are also performed using a temporal lag of 4 and the subnetworks, which are defined by the threshold distance. The nRMSE shown in Eqn. (1.3) is used as the error metric. Clear sky index is used in the kriging models, the results are converted back to irradiance and the errors are calculated using irradiance I_{glo}. Table 9.1 shows the nRMSEs for various shrinkage schemes in empirical kriging models. The persistence model errors are shown as well.

Similar case studies are made for the VAR models. In addition, the lasso is implemented on top of the VAR(4) model. Ridge regression is not included as it cannot be considered as a parameter selection method. The nRMSEs for various shrinkage schemes in VAR models are shown in Table 9.2.

It is interesting to note that most models that perform better in the empirical kriging framework also perform better in the VAR framework. This indicates that the proposed shrinkage models are general, and can be readily applied to other spatio–temporal predic-

Table 9.1 nRMSEs for various shrinkage schemes in empirical kriging models. Lowest nRMSEs are highlighted in bold.

Station	Pers.	Kriging(m=7)	Kriging(m=4)	Subnet1	Subnet2	Subnet3	Subnet4	Subnet5
S301	26.85	24.54	24.49	**24.45**	—	—	—	—
S500	22.62	21.17	21.10	—	—	**21.09**	21.51	—
S104	27.03	23.88	**23.81**	—	—	—	23.88	23.88
S304	18.77	18.62	18.57	—	—	**18.49**	—	—
S305	24.62	22.88	22.85	**22.81**	—	—	—	—
S307	20.96	20.48	**20.39**	20.54	—	20.53	—	—
S116	25.73	23.16	23.08	—	23.70	—	**23.07**	—
S106	19.87	19.18	**19.12**	—	19.25	—	—	—
S102	25.61	22.97	**22.92**	—	—	22.96	23.03	—
S108	28.40	25.22	25.16	—	—	**25.13**	25.36	—
S105	27.68	24.80	**24.73**	—	—	—	24.81	24.78
S315	25.88	22.97	22.89	—	—	—	**22.87**	23.51
S319	28.34	25.30	**25.19**	25.22	—	25.41	—	—

Table 9.2 nRMSEs for various shrinkage schemes in vector autoregressive (VAR) models. Lowest nRMSEs are highlighted in bold.

Station	Pers.	VAR(p=7)	VAR(p=4)	Lasso	Subnet1	Subnet2	Subnet3	Subnet4	Subnet5
S301	26.85	25.33	25.28	25.33	**25.23**	—	—	—	—
S500	22.62	21.50	21.42	21.51	—	—	**21.40**	21.81	—
S104	27.03	25.01	**24.93**	25.03	—	—	—	24.98	24.99
S304	18.77	18.26	18.19	18.60	—	—	**18.09**	—	—
S305	24.62	23.45	23.40	23.51	**23.36**	—	—	—	—
S307	20.96	20.23	**20.15**	20.61	20.34	—	20.21	—	—
S116	25.73	24.05	23.96	**23.91**	—	24.47	—	23.94	—
S106	19.87	19.12	**19.08**	19.69	—	19.20	—	—	—
S102	25.61	23.60	23.53	23.60	—	—	**23.52**	23.61	—
S108	28.40	25.96	25.90	**25.83**	—	—	25.91	26.14	—
S105	27.68	26.05	**25.97**	26.16	—	—	—	26.03	25.99
S315	25.88	23.95	23.83	24.10	—	—	—	**23.81**	24.52
S319	28.34	26.24	26.12	**26.10**	26.16	—	26.33	—	—

tive frameworks such as vector autoregressive integrated moving average model, space–time Kalman filter, etc. I performed similar forecasts for time horizons beyond 5 minutes, namely, 10 minutes, 15 minutes and 20 minutes; the forecasts perform better than persistence, which is otherwise not achievable via methods such as using a sky camera or using satellite images (Lonij et al., 2013).

9.5 Chapter conclusion

Two novel methods are introduced to quantify the threshold distance in a solar irradiance random field. The results from the two distinct methods agree well with each other and the previous results in the literature. The estimated threshold distance can be considered as an automatic parameter shrinkage and selection tool for spatio–temporal forecasting models. The results are shown to be general. Comparative studies on forecasting are presented and discussed. Although the proposed models only improve the persistence marginally in this chapter, the advantages of the spatio–temporal models shall not be overlooked. I will show in the subsequent chapter that once the spatial resolution of the sensor network is improved, the spatio–temporal models will show significant advantage over all univariate models.

Chapter 10

Summary and future works

10.1 Original contributions of this thesis

Statistical treatments of spatio–temporal data have become important in recent years in many fields. In solar irradiance modeling and forecasting, sky camera and satellite images provide snapshots of the sky; ground point sensors record irradiance as time series; monitoring networks record the time series of spatial processes. The observational nature of such data and the inevitable measurement and modeling errors make statistics, the science of uncertainty, a necessary tool for these studies.

Probability & distribution, likelihood calculation, parameter estimation, regression, hypothesis testing, time series, multivariate models and spatio–temporal models are the main topics of statistics involved in this thesis. Novel applications of statistics in the solar engineering context are the main contributions.

In chapter 3, a novel function form of the clear sky model is proposed. The proposed model is flexible owing to the three shape parameters in Eqn. (3.7). With local data, the parameters can be fitted via non–linear regression thus generate the empirical clear sky model.

In chapter 4, univariate time series forecasting is explored. The univariate approach is well–studied in the literature of solar irradiance forecasting. However, the knowledge based decompositions shown in the chapter have not previously been used. It is shown that by decomposing the GHI time series into DHI and DNI time series, forecast results can be improved. Furthermore, when a cloud cover index time series is present, GHI can be written as a function of the cloud cover index, CC, and the zenith angle, i.e, $I_{\text{glo}} = f(\text{CC}, \theta_z)$, where $f(\cdot)$ represents 11 third–order polynomial functions of the zenith angle, one for each discrete CC value. The application of the seasonal–trend decomposition procedure based on LOESS is also novel.

Chapter 5 describes the spatio–temporal forecast models. There is no literature regarding time–forward kriging in solar irradiance forecasting, apart from a conference publication by Inoue et al. (2012). In that paper, the statistical properties such as stationarity, isotropy, separability and full symmetry are not considered. In chapter 5, the above mentioned statistical properties are carefully examined. A two–step space deformation is used to transform the geographical plane to the dispersion plane so that the spatial stationarity and spatial isotropy are achieved. In the predictive step, i.e., the time–forward kriging, the performance of various covariance models is also compared.

There are very few reports in the literature on inverse transposition; and there is no reference on inverse transposition using only data of a single tilted irradiance component. This makes the proposed algorithm of tilt to horizontal irradiance conversion in chapter 6 novel. Instead of using multiple sets of tilted data, only a tilted reference cell is used to retrieve all the horizontal irradiance components via a decomposition model. The use of the Brent (1973) method, a root search routine, circumvents the need for gradient based optimizations. Last but not the least, the chapter also acts as a regional first report on the performance of 10 transposition models and 5 decomposition models.

Chapter 7 shows an alternative way to transpose the irradiance components on a tilted plane to those on a horizontal plane. In the first half of the chapter, the coefficients of the Perez model are adjusted using tropical data so that the performance of the model is optimized in a least square sense. A complete set of mathematical solutions to the inverse problem is then described, validated and benchmarked in the second half of the chapter. Although the multi–sensor approach to the inverse transposition problem has been around since Faiman et al. (1987), the anisotropic formulation is first proposed here through applying the Perez model. The bidirectional irradiance transposition described in the chapter yields a tolerable error compatible with the measurement uncertainty.

Entropy–based monitoring network expansion is developed in chapter 8. Since neither entropy nor ground–based data have been consider in irradiance network redesign, the materials presented in the chapter are new to solar engineering. Further to the apparent novelty, rigorous statistical methods are employed to make the proposed redesign procedure robust. In fact, the Sampson–Guttorp method adopted in the chapter goes far beyond the field of solar engineering; it is however critically important owing to the almost surely anisotropic nature of the irradiance random field.

Chapter 9 considers the spatio–temporal models using data from an irradiance sensor network. The concept of parameter shrinkage is introduced in solar engineering for the first time. To formulate the shrinkage model, the idea of a geographical threshold distance is proposed. Two distinct methods are used to estimate the threshold distance of an irradiance random field in Singapore. It is shown that the spatio–temporal models perform better under shrinkage.

10.2 Proposed future works

10.2.1 Chapter 4: interval forecast

In chapter 4, three univariate irradiance forecasting models using decomposition were proposed. ARIMA is used in the predictive step. Alternatively, ETS is used to replace ARIMA in (Yang et al., 2015a). The exponential smoothing state space model contains 30 candidate models depending on the choices of the seasonal and error components (Hyndman et al., 2002, 2008). Based on the STL decomposition described in the chapter, the number of candidate models can be reduced to 10. The reduction in the state space formulation gives convenience to likelihood and AIC calculation.

The materials presented in chapter 4 only consider point forecast. However, probabilistic forecasts provide power systems operators with valuable information about the uncertainty associated with the expected generation; it is sometimes more desired than point forecast. As many statistical forecasting models support confidence interval estimations (see Hyndman et al., 2008), it is logical to consider probabilistic forecasts as an extension to the methods developed in chapter 4. However, to combine the probabilistic forecasts with decomposition heuristics, error propagation needs careful consideration.

10.2.2 Chapter 5: computational issues

One of the novelties in chapter 5 is the application of the two–step grid deformation. MDS and TPS mapping are used to transform an anisotropic G plane to an isotropic D plane. However, one of the computational issues is grid folding (see Figure 2 in Meiring et al., 1997a). To solve the folding problem, penalties can be used. In chapter 8, a penalty λ is applied to the thin plate spline mapping. Alternatively, the penalty can be applied during the multidimensional scaling. However, the penalty scale is mostly likely to be different from the one in Eqn. (8.6) (Le and Zidek, 2006). Further research may apply.

Another computational issue is the feasibility of the method with large dataset. The two–step transformation is computationally expensive; therefore when the size of the network scales up, alternative isotropic transformation is needed. One of the possible alternatives is shown by McBratney and Minasny (2013). Spacebender is promising for a purely spatial setup, however, for a spatio–temporal setup such as the one shown in chapter 5, further research is needed.

10.2.3 Chapters 6 and 7: bidirectional transposition at large angles

Both chapters describe the bidirectional irradiance transpositions. However, the largest angle of surface inclination used is 40°. It is known that the performance of transposition models can be compromised at large tilt angles (Gueymard, 2009). With increasing applications of building–integrated PV and vertical bifacial PV (Guo et al., 2013), the accuracies of the bidirectional transposition at large angles need to be evaluated. The coefficient adjustment shown in chapter 7 is useful in this case.

10.2.4 Chapter 9: spatio–temporal statistics, the next frontier

The importance of spatio–temporal formulations for irradiance random processes was emphasized repeatedly throughout the thesis. However, the field of spatio–temporal statistics covers a very wide range of methods, models and techniques. Exploring these further would be of benefit in many areas.

One important concept in spatio–temporal statistics which is not considered in this thesis is the hierarchical model. Hierarchical statistical modeling gives a way to represent uncertainties through well–defined levels of conditional probabilities (Cressie and Wikle, 2011). The data model, the process model and the parameter model form the structure. The hierarchical modeling approach can be considered as a type of analysis–of–variance decomposition, so that the uncertainties associated at each level (data, process and parameter) can be modeled. It is more general than the conventional additive decomposition. Future work on hierarchical modeling may enable inference about the true processes and parameters of an irradiance random field.

Solar irradiance, one of many environmental processes, is the focus of this thesis. Spatio–temporal methods, models and techniques herein developed use solar irradiance data alone. However, the characteristics of the irradiance random process can be jointly described with exogenous parameters such as pressure, temperature and humidity. It is therefore possible to generalize the ideas discussed in this thesis to a multivariate context, and doing so may improve future forecasts.

Future consideration of these issues may show that spatio–temporal statistics is not only the next frontier of solar forecasting, but environmental science in general.

References

Abraham, B. and Ledolter, J. *Statistical methods for forecasting.* John Wiley & Sons, Inc., Hoboken-New Jersey, 1983.

Adnot, J., Bourges, B., Campana, D., and Gicquel, R. Utilisation des courbes de frequence cumulees pour le calcul des installation solaires. In Lestienne, R., editor, *Analise Statistique des Processus Meteorologiques Appliquee al'Energie Solaire*, pages 9 – 40. CNRS, Paris, 1979.

Ahmed, N. and Gokhale, D. Entropy expressions and their estimators for multivariate distributions. *Information Theory, IEEE Transactions on*, 35(3):688 – 692, May 1989. ISSN 0018-9448. doi: 10.1109/18.30996.

Al-Alawi, S. and Al-Hinai, H. An ANN-based approach for predicting global radiation in locations with no direct measurement instrumentation. *Renewable Energy*, 14(1-4):199 – 204, 1998. ISSN 0960-1481. doi: http://dx.doi.org/10.1016/S0960-1481(98)00068-8. URL http://www.sciencedirect.com/science/article/pii/S0960148198000688. 6th Arab International Solar Energy Conference: Bringing Solar Energy into the Daylight.

Al-Sadah, F. H., Ragab, F. M., and Arshad, M. K. Hourly solar radiation over Bahrain. *Energy*, 15(5):395 – 402, 1990. ISSN 0360-5442. doi: http://dx.doi.org/10.1016/0360-5442(90)90036-2. URL http://www.sciencedirect.com/science/article/pii/0360544290900362.

Almonacid, F., Pérez-Higueras, P., Fernández, E. F., and Hontoria, L. A methodology based on dynamic artificial neural network for short-term forecasting of the power output of a PV generator. *Energy Conversion and Management*, 85(0):389 – 398, 2014. ISSN 0196-8904. doi: http://dx.doi.org/10.1016/j.enconman.2014.05.090. URL http://www.sciencedirect.com/science/article/pii/S0196890414005093.

Alsamamra, H., Ruiz-Arias, J. A., Pozo-Vázquez, D., and Tovar-Pescador, J. A comparative study of ordinary and residual kriging techniques for mapping global solar radiation over southern Spain. *Agricultural and Forest Meteorology*, 149(8):1343 – 1357, 2009. ISSN 0168-1923. doi: http://dx.doi.org/10.1016/j.agrformet.2009.03.005. URL http://www.sciencedirect.com/science/article/pii/S0168192309000586.

Ashraf, M., Loftis, J. C., and Hubbard, K. Application of geostatistics to evaluate partial weather station networks. *Agricultural and Forest Meteorology*, 84(3–4):255 – 271, 1997. ISSN 0168-1923. doi: http://dx.doi.org/10.1016/S0168-1923(96)02358-1. URL http://www.sciencedirect.com/science/article/pii/S0168192396023581.

Augustin, N. H., Musio, M., von Wilpert, K., Kublin, E., Wood, S. N., and Schumacher, M. Modeling spatiotemporal forest health monitoring data. *Journal of the American Statistical Association*, 104(487):899 – 911, 2009. doi: 10.1198/jasa.2009.ap07058.

Azadeh, A., Maghsoudi, A., and Sohrabkhani, S. An integrated artificial neural networks approach for predicting global radiation. *Energy Conversion and Management*, 50(6):1497 – 1505, 2009. ISSN 0196-8904. doi: http://dx.doi.org/10.1016/j.enconman.2009.02.019. URL http://www.sciencedirect.com/science/article/pii/S0196890409000685.

Bacher, P., Madsen, H., and Nielsen, H. A. Online short-term solar power forecasting. *Solar Energy*, 83(10):1772 – 1783, 2009. ISSN 0038-092X. doi: http://dx.doi.org/10.1016/j.solener.2009.05.016. URL http://www.sciencedirect.com/science/article/pii/S0038092X09001364.

Badescu, V. 3d isotropic approximation for solar diffuse irradiance on tilted surfaces. *Renewable Energy*, 26(2):221 – 233, 2002. ISSN 0960-1481. doi: http://dx.doi.org/10.1016/S0960-1481(01)00123-9. URL http://www.sciencedirect.com/science/article/pii/S0960148101001239.

Badescu, V. Verification of some very simple clear and cloudy sky models to evaluate global solar irradiance. *Solar Energy*, 61(4):251 – 264, 1998. ISSN 0038-092X. doi: http://dx.doi.org/10.1016/S0038-092X(97)00057-1. URL http://www.sciencedirect.com/science/article/pii/S0038092X97000571.

Baig, A., Akhter, P., and Mufti, A. A novel approach to estimate the clear day global radiation. *Renewable Energy*, 1(1):119 – 123, 1991. ISSN 0960-1481. doi: http://dx.doi.org/10.1016/0960-1481(91)90112-3. URL http://www.sciencedirect.com/science/article/pii/096014819190112З.

Bartlett, M. S. On the theory of statistical regression. *Proc. Royal Soc. Edinburgh*, 53:518 – 534, 1933.

Bechini, L., Ducco, G., Donatelli, M., and Stein, A. Modelling, interpolation and stochastic simulation in space and time of global solar radiation. *Agriculture, Ecosystems & Environment*, 81(1):29 – 42, 2000. ISSN 0167-8809. doi: 10.1016/S0167-8809(00)00170-5. URL http://www.sciencedirect.com/science/article/pii/S0167880900001705.

Bernecker, D., Riess, C., Angelopoulou, E., and Hornegger, J. Continuous short-term irradiance forecasts using sky images. *Solar Energy*, 110(0):303 – 315, 2014. ISSN 0038-092X. doi: http://dx.doi.org/10.1016/j.solener.2014.09.005. URL http://www.sciencedirect.com/science/article/pii/S0038092X14004356.

Beyer, H. G., Martinez, J. P., Suri, M., Torres, J. L., Lorenz, E., Müller, S. C., Hoyer-Klick, C., and Ineichen, P. Report on benchmarking of radiation products. Technical Report 038665, Management and Exploitation of Solar Resource Knowledge, 2009. URL http://www.mesor.org/docs/MESoR_Benchmarking_of_radiation_products.pdf.

Bilonick, R. A. The space-time distribution of sulfate deposition in the northeastern United States. *Atmospheric Environment (1967)*, 19(11):1829 – 1845, 1985. ISSN 0004-6981. doi: http://dx.doi.org/10.1016/0004-6981(85)90009-5. URL http://www.sciencedirect.com/science/article/pii/0004698185900095.

Bjerknes, V. Das problem der wettervorhersage, betrachtet vom standpunkte der mechanik und der physik. *Meteorologische Zeitschrift*, 21:1 – 7, 1904.

Bland, W. and Clayton, M. Spatial structure of solar radiation in Wisconsin. *Agricultural and Forest Meteorology*, 69:75 – 84, 1994. ISSN 0168-1923. doi: 10.1016/0168-1923(94)90082-5. URL http://www.sciencedirect.com/science/article/pii/0168192394900825.

Bookstein, F. Principal warps: Thin-plate splines and the decomposition of deformations. *IEEE Transactions on Pattern Analysis and Machine Intelligence*, 11:567 – 585, 1989. ISSN 0162-8828. doi: http://doi.ieeecomputersociety.org/10.1109/34.24792.

Bookstein, F. *Morphometric Tools for Landmark Data: Geometry and Biology*. Cambridge Univeristy Press, 1997a. ISBN 9780521585989.

Bookstein, F. L. Procrustes distance, bending energy, and the biometrical modeling of shape phenomena. *International Journal of Shape Modeling*, 03(01n02):17 – 38, 1997b.

Bosch, J. and Kleissl, J. Cloud motion vectors from a network of ground sensors in a solar power plant. *Solar Energy*, 95(0):13 – 20, 2013. ISSN 0038-092X. doi: http://dx.doi.org/10.1016/j.solener.2013.05.027. URL http://www.sciencedirect.com/science/article/pii/S0038092X13002193.

Bosch, J., Zheng, Y., and Kleissl, J. Deriving cloud velocity from an array of solar radiation measurements. *Solar Energy*, 87(0):196 – 203, 2013. ISSN 0038-092X. doi: http://dx.doi.org/10.1016/j.solener.2012.10.020. URL http://www.sciencedirect.com/science/article/pii/S0038092X12003854.

Box, G. E. P., Jenkins, G. M., and Reinsel, G. C. *Time Series Analysis: Forecasting and Control*. Prentice Hall, Inc., Englewood Cliffs-New Jersey, 1994.

Boyd, M. Analytical model for solar irradiance near a planar vertical diffuse reflector - formulation, validation, and simulations. *Solar Energy*, 91(0):79 – 92, 2013. ISSN 0038-092X. doi: http://dx.doi.org/10.1016/j.solener.2013.01.015. URL http://www.sciencedirect.com/science/article/pii/S0038092X13000303.

Brent, R. *Algorithms for Minimization without Derivatives*. Prentice Hall, Inc., Englewood Cliffs-New Jersey, 1973.

Brinsfield, R., Yaramanoglu, M., and Wheaton, F. Ground level solar radiation prediction model including cloud cover effects. *Solar Energy*, 33(6):493 – 499, 1984. ISSN 0038-092X. doi: http://dx.doi.org/10.1016/0038-092X(84)90003-3. URL http://www.sciencedirect.com/science/article/pii/0038092X84900033.

Bruno, F., Guttorp, P., Sampson, P., and Cocchi, D. A simple non-separable, non-stationary spatiotemporal model for ozone. *Environmental and Ecological Statistics*, 16(4):515–529, 2009. ISSN 1352-8505. doi: 10.1007/s10651-008-0094-8. URL http://dx.doi.org/10.1007/s10651-008-0094-8.

Bueso, M. C., Angulo, J. M., and Alonso, F. J. A state-space model approach to optimum spatial sampling design based on entropy. *Environmental and Ecological Statistics*, 5(1): 29 – 44, March 1998. ISSN 1352-8505, 1573-3009. doi: 10.1023/A:1009603318668.

Cao, J. and Cao, S. Study of forecasting solar irradiance using neural networks with preprocessing sample data by wavelet analysis. *Energy*, 31(15):3435 – 3445, 2006. ISSN 0360-5442. doi: http://dx.doi.org/10.1016/j.energy.2006.04.001. URL http://www.sciencedirect.com/science/article/pii/S0360544206001009. {ECOS} 2004 - 17th International Conference on Efficiency, Costs, Optimization, Simulation, and Environmental Impact of Energy on Process Systems 17th International Conference on Efficiency, Costs, Optimization, Simulation, and Environmental Impact of Energy on Process Systems.

Cao, J. and Lin, X. Study of hourly and daily solar irradiation forecast using diagonal recurrent wavelet neural networks. *Energy Conversion and Management*, 49(6):1396 – 1406, 2008. ISSN 0196-8904. doi: http://dx.doi.org/10.1016/j.enconman.2007.12.030. URL http://www.sciencedirect.com/science/article/pii/S0196890408000125.

Cao, S. and Cao, J. Forecast of solar irradiance using recurrent neural networks combined with wavelet analysis. *Applied Thermal Engineering*, 25(2-3):161 – 172, 2005. ISSN 1359-4311. doi: http://dx.doi.org/10.1016/j.applthermaleng.2004.06.017. URL http://www.sciencedirect.com/science/article/pii/S1359431104001814.

Capizzi, G., Napoli, C., and Bonanno, F. Innovative second-generation wavelets construction with recurrent neural networks for solar radiation forecasting. *Neural Networks and Learning Systems, IEEE Transactions on*, 23(11):1805–1815, Nov 2012. ISSN 2162-237X. doi: 10.1109/TNNLS.2012.2216546.

Carr, D., ported by Nicholas Lewin-Koh, and Maechler, M. *hexbin: Hexagonal Binning Routines*, 2013. URL http://CRAN.R-project.org/package=hexbin. R package version 1.26.3.

Chapin, D. M., Fuller, C. S., and Pearson, G. L. A new silicon p-n junction photocell for converting solar radiation into electrical power. *Journal of Applied Physics*, 25(5): 676–677, 1954. doi: http://dx.doi.org/10.1063/1.1721711. URL http://scitation.aip.org/content/aip/journal/jap/25/5/10.1063/1.1721711.

Chen, A., Chin, P., Forrest, W., McLean, P., and Grey, C. Solar radiation in Jamaica. *Solar Energy*, 53(5):455 – 460, 1994. ISSN 0038-092X. doi: http://dx.doi.org/10.1016/0038-092X(94)90060-4. URL http://www.sciencedirect.com/science/article/pii/0038092X94900604.

Cheng, H.-Y., Yu, C.-C., and Lin, S.-J. Bi-model short-term solar irradiance prediction using support vector regressors. *Energy*, 70(0):121 – 127, 2014. ISSN 0360-5442. doi: http://dx.doi.org/10.1016/j.energy.2014.03.096. URL http://www.sciencedirect.com/science/article/pii/S0360544214003600.

Chow, C. W., Urquhart, B., Lave, M., Dominguez, A., Kleissl, J., Shields, J., and Washom, B. Intra-hour forecasting with a total sky imager at the UC San Diego solar energy testbed. *Solar Energy*, 85(11):2881 – 2893, 2011. ISSN 0038-092X. doi: http://dx.doi.org/10.1016/j.solener.2011.08.025. URL http://www.sciencedirect.com/science/article/pii/S0038092X11002982.

Chow, S. K., Lee, E. W., and Li, D. H. Short-term prediction of photovoltaic energy generation by intelligent approach. *Energy and Buildings*, 55(0):660 – 667, 2012. ISSN 0378-7788. doi: http://dx.doi.org/10.1016/j.enbuild.2012.08.011. URL http://www.sciencedirect.com/science/article/pii/S037877881200415X. Cool Roofs, Cool Pavements, Cool Cities, and Cool World.

Chu, Y., Pedro, H. T., and Coimbra, C. F. Hybrid intra-hour DNI forecasts with sky image processing enhanced by stochastic learning. *Solar Energy*, 98, Part C(0):592 – 603, 2013. ISSN 0038-092X. doi: http://dx.doi.org/10.1016/j.solener.2013.10.020. URL http://www.sciencedirect.com/science/article/pii/S0038092X13004325.

Chu, Y., Pedro, H. T. C., Nonnenmacher, L., Inman, R. H., Liao, Z., and Coimbra, C. F. M. A smart image-based cloud detection system for intrahour solar irradiance forecasts. *J. Atmos. Oceanic Technol.*, 31(0):1995 – 2007, 2014. doi: http://dx.doi.org/10.1175/JTECH-D-13-00209.1.

Chu, Y., Urquhart, B., Gohari, S. M., Pedro, H. T., Kleissl, J., and Coimbra, C. F. Short-term reforecasting of power output from a 48 MWe solar PV plant. *Solar Energy*, 112 (0):68 – 77, 2015. ISSN 0038-092X. doi: http://dx.doi.org/10.1016/j.solener.2014.11.017. URL http://www.sciencedirect.com/science/article/pii/S0038092X14005611.

Cleveland, R. B., Cleveland, W. S., McRae, J. E., and Terpenning, I. STL: A seasonal-trend decomposition procedure based on loess. *Journal of Official Statistics*, 6(1):3 – 73, 1990.

Cleveland, W. S., Devlin, S. J., and Grosse, E. Regression by local fitting: Methods, properties, and computational algorithms. *Journal of Econometrics*, 37(1):87 – 114, 1988. ISSN 0304-4076. doi: http://dx.doi.org/10.1016/0304-4076(88)90077-2. URL http://www.sciencedirect.com/science/article/pii/0304407688900772.

Cornaro, C., Pierro, M., and Bucci, F. Master optimization process based on neural networks ensemble for 24-h solar irradiance forecast. *Solar Energy*, 111(0):297 – 312, 2015. ISSN 0038-092X. doi: http://dx.doi.org/10.1016/j.solener.2014.10.036. URL http://www.sciencedirect.com/science/article/pii/S0038092X14005234.

Cover, T. M. and Thomas, J. A. *Elements of Information Theory*. John Wiley & Sons, Inc., 2005. ISBN 9780471748823.

Cox, T. F. and Cox, M. A. A. *Multidimensional Scaling*. Chapman & Hall, Boundary Row-London, 2000. ISBN 978-1-58488-094-3.

Cressie, N. and Wikle, C. *Statistics for Spatio-Temporal Data*. Wiley Series in Probability and Statistics. Wiley, 2011. ISBN 9780471692744. URL http://books.google.com.sg/books?id=-kOC6D0DiNYC.

Cressie, N. and Huang, H.-C. Classes of nonseparable, spatio-temporal stationary covariance functions. *Journal of the American Statistical Association*, 94(448):1330 – 1340, 1999. ISSN 01621459. URL http://www.jstor.org/stable/2669946.

Cressie, N. and Majure, J. J. Spatio-temporal statistical modeling of livestock waste in streams. *Journal of Agricultural, Biological, and Environmental Statistics*, 2(1):24 – 47, 1997. ISSN 10857117. URL http://www.jstor.org/stable/1400639.

Cressie, N., Shi, T., and Kang, E. L. Fixed rank filtering for spatio-temporal data. *Journal of Computational and Graphical Statistics*, 19(3):724 – 745, 2010. doi: 10.1198/jcgs.2010.09051.

Cros, S., Liandrat, O., Sebastien, N., and Schmutz, N. Extracting cloud motion vectors from satellite images for solar power forecasting. In *Geoscience and Remote Sensing Symposium (IGARSS), 2014 IEEE International*, pages 4123 – 4126, July 2014. doi: 10.1109/IGARSS.2014.6947394.

Curtright, A. E. and Apt, J. The character of power output from utility-scale photovoltaic systems. *Progress in Photovoltaics: Research and Applications*, 16(3):241 – 247, 2008. ISSN 1099-159X. doi: 10.1002/pip.786. URL http://dx.doi.org/10.1002/pip.786.

Damian, D., Sampson, P. D., and Guttorp, P. Bayesian estimation of semi-parametric non-stationary spatial covariance structures. *Environmetrics*, 12(2):161 – 178, 2001. ISSN 1099-095X. doi: 10.1002/1099-095X(200103)12:2<161::AID-ENV452>3.0.CO;2-G. URL http://dx.doi.org/10.1002/1099-095X(200103)12:2<161::AID-ENV452>3.0.CO;2-G.

Daneshyar, M. Solar radiation statistics for Iran. *Solar Energy*, 21(4):345 – 349, 1978. ISSN 0038-092X. doi: http://dx.doi.org/10.1016/0038-092X(78)90013-0. URL http://www.sciencedirect.com/science/article/pii/0038092X78900130.

David, M., Lauret, P., and Boland, J. Evaluating tilted plane models for solar radiation using comprehensive testing procedures, at a southern hemisphere location. *Renewable Energy*, 51(0):124 – 131, 2013. ISSN 0960-1481. doi: http://dx.doi.org/10.1016/j.renene.2012.08.074. URL http://www.sciencedirect.com/science/article/pii/S0960148112005447.

Davy, R. J. and Troccoli, A. Continental-scale spatial optimisation of a solar irradiance monitoring network. *Solar Energy*, 109(0):36 – 44, 2014. ISSN 0038-092X. doi: http://dx.doi.org/10.1016/j.solener.2014.08.026. URL http://www.sciencedirect.com/science/article/pii/S0038092X14004034.

De Cesare, L., Myers, D. E., and Posa, D. Estimating and modeling space-time correlation structures. *Statistics & Probability Letters*, 51(1):9 – 14, 2001. ISSN 0167-7152. doi: http://dx.doi.org/10.1016/S0167-7152(00)00131-0. URL http://www.sciencedirect.com/science/article/pii/S0167715200001310.

De Iaco, S., Myers, D., and Posa, D. Nonseparable space-time covariance models: Some parametric families. *Mathematical Geology*, 34(1):23 – 42, 2002. ISSN 0882-8121. doi: 10.1023/A:1014075310344.

De Luna, X. and Genton, M. G. Predictive spatio-temporal models for spatially sparse environmental data. <http://www3.stat.sinica.edu.tw/statistica/oldpdf/A15n213.pdf>, 2005. (accessed 09.01.2013).

Deutsch, S. J. and Pfeifer, P. E. Space-time ARMA modeling with contemporaneously correlated innovations. *Technometrics*, 23(4):401 – 409, 1981. ISSN 00401706. URL http://www.jstor.org/stable/1268231.

Diagne, M., David, M., Lauret, P., Boland, J., and Schmutz, N. Review of solar irradiance forecasting methods and a proposition for small-scale insular grids. *Renewable and Sustainable Energy Reviews*, 27(0):65 – 76, 2013. ISSN 1364-0321. doi: http://dx.doi.org/10.1016/j.rser.2013.06.042. URL http://www.sciencedirect.com/science/article/pii/S1364032113004334.

Diagne, M., David, M., Boland, J., Schmutz, N., and Lauret, P. Post-processing of solar irradiance forecasts from WRF model at Reunion Island. *Solar Energy*, 105(0):99 – 108, 2014. ISSN 0038-092X. doi: http://dx.doi.org/10.1016/j.solener.2014.03.016. URL http://www.sciencedirect.com/science/article/pii/S0038092X14001509.

Dong, Z., Yang, D., Reindl, T., and Walsh, W. M. Short-term solar irradiance forecasting using exponential smoothing state space model. *Energy*, 55(0):1104 – 1113, 2013. ISSN 0360-5442. doi: http://dx.doi.org/10.1016/j.energy.2013.04.027. URL http://www.sciencedirect.com/science/article/pii/S0360544213003381.

Dong, Z., Yang, D., Reindl, T., and Walsh, W. M. Satellite image analysis and a hybrid ESSS/ANN model to forecast solar irradiance in the tropics. *Energy Conversion and Management*, 79(0):66 – 73, 2014. ISSN 0196-8904. doi: http://dx.doi.org/10.1016/j.enconman.2013.11.043. URL http://www.sciencedirect.com/science/article/pii/S0196890413007644.

Duffie, J. A. and Beckman, W. A. *Solar Engineering of Thermal Processes*. John Wiley & Sons, Inc., 2006. ISBN 9780471698678. URL http://books.google.com.sg/books?id=tPayQgAACAAJ.

Efron, B., Hastie, T., Johnstone, I., and Tibshirani, R. Least angle regression. *Annals of Statistics*, 32(2):407 – 499, 2004. doi: 10.1214/009053604000000067.

Ehnberg, J. S. and Bollen, M. H. Simulation of global solar radiation based on cloud observations. *Solar Energy*, 78(2):157 – 162, 2005. ISSN 0038-092X. doi: http://dx.doi.org/10.1016/j.solener.2004.08.016. URL http://www.sciencedirect.com/science/article/pii/S0038092X04002373. ISES Solar World Congress 2003.

Elminir, H. K., Ghitas, A. E., El-Hussainy, F., Hamid, R., Beheary, M., and Abdel-Moneim, K. M. Optimum solar flat-plate collector slope: Case study for Helwan, Egypt. *Energy Conversion and Management*, 47(5):624 – 637, 2006. ISSN 0196-8904. doi: http://dx.doi.org/10.1016/j.enconman.2005.05.015. URL http://www.sciencedirect.com/science/article/pii/S0196890405001342.

Erbs, D., Klein, S., and Duffie, J. Estimation of the diffuse radiation fraction for hourly, daily and monthly-average global radiation. *Solar Energy*, 28(4):293 – 302, 1982. ISSN 0038-092X. doi: http://dx.doi.org/10.1016/0038-092X(82)90302-4. URL http://www.sciencedirect.com/science/article/pii/0038092X82903024.

Escobar, R. A., Cortés, C., Pino, A., Pereira, E. B., Martíns, F. R., and Cardemil, J. M. Solar energy resource assessment in Chile: Satellite estimation and ground station measurements. *Renewable Energy*, 71(0):324 – 332, 2014. ISSN 0960-1481. doi: http://dx.doi.org/10.1016/j.renene.2014.05.013. URL http://www.sciencedirect.com/science/article/pii/S096014811400264X.

Espinar, B., Ramírez, L., Drews, A., Beyer, H. G., Zarzalejo, L. F., Polo, J., and Martín, L. Analysis of different comparison parameters applied to solar radiation data from satellite and German radiometric stations. *Solar Energy*, 83(1):118 – 125, 2009. ISSN 0038-092X. doi: http://dx.doi.org/10.1016/j.solener.2008.07.009. URL http://www.sciencedirect.com/science/article/pii/S0038092X08001655.

Evseev, E. G. and Kudish, A. I. The assessment of different models to predict the global solar radiation on a surface tilted to the south. *Solar Energy*, 83(3):377 – 388, 2009. ISSN 0038-092X. doi: http://dx.doi.org/10.1016/j.solener.2008.08.010. URL http://www.sciencedirect.com/science/article/pii/S0038092X08002156.

Faiman, D., Zemel, A., and Zangvil, A. A method for monitoring insolation in remote regions. *Solar Energy*, 38(5):327 – 333, 1987. ISSN 0038-092X. doi: http://dx.doi.org/10.1016/0038-092X(87)90004-1. URL http://www.sciencedirect.com/science/article/pii/0038092X87900041.

Faiman, D., Feuermann, D., and Zemel, A. Site-independent algorithm for obtaining the direct beam insolation from a multipyranometer instrument. *Solar Energy*, 50(1):53 – 57, 1993. doi: 10.1016/0038-092X(93)90007-B. URL http://www.sciencedirect.com/science/article/pii/0038092X9390007B.

Faraway, J. J. Practical regression and anova using R. <http://cran.r-project.org/doc/contrib/Faraway-PRA.pdf>, jul 2002. (accessed 09.11.2011).

Finkenstadt, B., Held, L., and Isham, V. *Statistical Methods for Spatio-Temporal Systems*. Monographs on Statistics and Applied Probability. Chapman & Hall/CRC, 2006. ISBN 9781584885931. URL http://books.google.de/books?id=j-rtW1nVuCoC.

Forsythe, G., Malcolm, M., and Moler, C. Computer methods for mathematical computations. <http://svn.r-project.org/R/trunk/src/appl/zeroin.c>, 2001. (accessed 05.02.2012).

Fu, C.-L. and Cheng, H.-Y. Predicting solar irradiance with all-sky image features via regression. *Solar Energy*, 97(0):537 – 550, 2013. ISSN 0038-092X. doi: http://dx.doi.org/10.1016/j.solener.2013.09.016. URL http://www.sciencedirect.com/science/article/pii/S0038092X13003770.

Gardner, C. L. and Nadeau, C. Estimating south slope irradiance in the Arctic-A comparison of experimental and modeled values. *Solar Energy*, 41(3):227 – 240, 1988. ISSN 0038-092X. doi: http://dx.doi.org/10.1016/0038-092X(88)90140-5. URL http://www.sciencedirect.com/science/article/pii/0038092X88901405.

Gardner, E. S. Exponential smoothing: The state of the art. *Journal of Forecasting*, 4(1): 1 – 28, 1985. ISSN 1099-131X. doi: 10.1002/for.3980040103. URL http://dx.doi.org/10.1002/for.3980040103.

Gardner, E. S. Exponential smoothing: The state of the art - part II. *International Journal of Forecasting*, 22(4):637 – 666, 2006. ISSN 0169-2070. doi: http://dx.doi.org/10.1016/j.ijforecast.2006.03.005. URL http://www.sciencedirect.com/science/article/pii/S0169207006000392.

Garrison, J. A study of the division of global irradiance into direct and diffuse irradiance at thirty-three U.S. sites. *Solar Energy*, 35(4):341 – 351, 1985. ISSN 0038-092X. doi: http://dx.doi.org/10.1016/0038-092X(85)90142-2. URL http://www.sciencedirect.com/science/article/pii/0038092X85901422.

Garrison, J. and Sahami, K. A study of the division of global irradiance into direct beam and diffuse irradiance at seven Canadian sites. *Solar Energy*, 55(6):493 – 504, 1995. ISSN 0038-092X. doi: http://dx.doi.org/10.1016/0038-092X(95)00088-9. URL http://www.sciencedirect.com/science/article/pii/0038092X95000889.

Genton, M. G. Separable approximations of space-time covariance matrices. *Environmetrics*, 18(7):681 – 695, 2007. ISSN 1099-095X. doi: 10.1002/env.854. URL http://dx.doi.org/10.1002/env.854.

Glasbey, C. A. and Allcroft, D. J. A spatiotemporal auto-regressive moving average model for solar radiation. *Journal of the Royal Statistical Society: Series C (Applied Statistics)*, 57(3):343 – 355, 2008. ISSN 1467-9876. doi: 10.1111/j.1467-9876.2007.00617.x. URL http://dx.doi.org/10.1111/j.1467-9876.2007.00617.x.

Glasbey, C., Graham, R., and Hunter, A. Spatio-temporal variability of solar energy across a region: a statistical modelling approach. *Solar Energy*, 70(4):373 – 381, 2001. ISSN 0038-092X. doi: 10.1016/S0038-092X(00)00152-3. URL http://www.sciencedirect.com/science/article/pii/S0038092X00001523.

Gneiting, T. Normal scale mixtures and dual probability densities. *Journal of Statistical Computation and Simulation*, 59(4):375 – 384, 1997. doi: 10.1080/00949659708811867.

Gneiting, T. Nonseparable, stationary covariance functions for space-time data. *Journal of the American Statistical Association*, 97(458):590 – 600, 2002. ISSN 01621459. URL http://www.jstor.org/stable/3085674.

Gneiting, T., Genton, M., and Guttorp, P. Geostatistical space-time models, stationarity, separability, and full symmetry. In Finkenstadt, B., Held, L., and Isham, V., editors, *Statistical Methods for Spatio-Temporal Systems*, chapter 4, pages 151 – 175. Chapman & Hall/CRC, 2006. ISBN 978-1-58488-593-1.

Gneiting, T., Genton, M. G., and Guttorp, P. Geostatistical space-time models, stationarity, separability and full symmetry. Technical Report 475, Department of Statistics, University of Washington, 2007. URL http://www.stat.washington.edu/research/reports/2005/tr475.pdf.

Gu, C., Yang, D., Jirutitijaroen, P., Walsh, W., and Reindl, T. Spatial load forecasting with communication failure using time-forward kriging. *Power Systems, IEEE Transactions on*, 29(6):2875 – 2882, Nov 2014. ISSN 0885-8950. doi: 10.1109/TPWRS.2014.2308537.

Gueymard, C. An anisotropic solar irradiance model for tilted surfaces and its comparison with selected engineering algorithms. *Solar Energy*, 38(5):367 – 386, 1987. ISSN 0038-092X. doi: http://dx.doi.org/10.1016/0038-092X(87)90009-0. URL http://www.sciencedirect.com/science/article/pii/0038092X87900090.

Gueymard, C. A two-band model for the calculation of clear sky solar irradiance, illuminance, and photosynthetically active radiation at the earth's surface. *Solar Energy*, 43(5): 253 – 265, 1989. ISSN 0038-092X. doi: http://dx.doi.org/10.1016/0038-092X(89)90113-8. URL http://www.sciencedirect.com/science/article/pii/0038092X89901138.

Gueymard, C. A. Direct and indirect uncertainties in the prediction of tilted irradiance for solar engineering applications. *Solar Energy*, 83(3):432 – 444, 2009. ISSN 0038-092X. doi: http://dx.doi.org/10.1016/j.solener.2008.11.004. URL http://www.sciencedirect.com/science/article/pii/S0038092X08002983.

Gueymard, C. A. Clear-sky irradiance predictions for solar resource mapping and large-scale applications: Improved validation methodology and detailed performance analysis of 18 broadband radiative models. *Solar Energy*, 86(8):2145 – 2169, 2012. ISSN 0038-092X. doi: 10.1016/j.solener.2011.11.011. URL http://www.sciencedirect.com/science/article/pii/S0038092X11004221.

Gueymard, C. A. and Thevenard, D. Monthly average clear-sky broadband irradiance database for worldwide solar heat gain and building cooling load calculations. *Solar Energy*, 83(11):1998 – 2018, 2009. ISSN 0038-092X. doi: http://dx.doi.org/10.1016/j.solener.2009.07.011. URL http://www.sciencedirect.com/science/article/pii/S0038092X09001790.

Gueymard, C. A. and Wilcox, S. M. Assessment of spatial and temporal variability in the US solar resource from radiometric measurements and predictions from models using ground-based or satellite data. *Solar Energy*, 85(5):1068 – 1084, 2011. ISSN 0038-092X. doi: 10.1016/j.solener.2011.02.030. URL http://www.sciencedirect.com/science/article/pii/S0038092X11000855.

Guo, S., Walsh, T. M., and Peters, M. Vertically mounted bifacial photovoltaic modules: A global analysis. *Energy*, 61(0):447 – 454, 2013. ISSN 0360-5442. doi: http://dx.doi.org/10.1016/j.energy.2013.08.040. URL http://www.sciencedirect.com/science/article/pii/S0360544213007275.

Guttorp, P. and Sampson, P. D. Methods for estimating heterogeneous spatial covariance functions with environmental applications. In Patil, G. and Rao, C., editors, *Environmental Statistics*, volume 12 of *Handbook of Statistics*, pages 661 – 689. Elsevier, 1994.

Guttorp, P., Meiring, W., and Sampson, P. D. A space-time analysis of ground-level ozone data. *Environmetrics*, 5(3):241 – 254, 1994. ISSN 1099-095X. doi: 10.1002/env.3170050305. URL http://dx.doi.org/10.1002/env.3170050305.

Haas, T. C. Local prediction of a spatio-temporal process with an application to wet sulfate deposition. *Journal of the American Statistical Association*, 90(432):1189 – 1199, 1995. ISSN 01621459. URL http://www.jstor.org/stable/2291511.

Haas, T. C. New systems for modeling, estimating, and predicting a multivariate spatio-temporal process. *Environmetrics*, 13(4):311 – 332, 2002. ISSN 1099-095X. doi: 10.1002/env.520. URL http://dx.doi.org/10.1002/env.520.

Hammer, A., Heinemann, D., Lorenz, E., and Lückehe, B. Short-term forecasting of solar radiation: a statistical approach using satellite data. *Solar Energy*, 67(1-3):139 – 150, 1999. ISSN 0038-092X. doi: http://dx.doi.org/10.1016/S0038-092X(00)00038-4. URL http://www.sciencedirect.com/science/article/pii/S0038092X00000384.

Hartfield, M. I. and Gunst, R. F. Identification of model components for a class of continuous spatiotemporal models. *Journal of Agricultural, Biological, and Environmental Statistics*, 8(1):105 – 121, 2003. ISSN 10857117. URL http://www.jstor.org/stable/1400615.

Haslett, J. and Raftery, A. E. Space-time modelling with long-memory dependence: Assessing Ireland's wind power resource. *Journal of the Royal Statistical Society. Series C (Applied Statistics)*, 38(1):1 – 50, 1989. ISSN 00359254. URL http://www.jstor.org/stable/2347679.

Haurwitz, B. Insolation in relation to cloudiness and cloud density. *Journal Meteorology*, 2:154–164, 1945.

Haurwitz, B. Insolation in relation to cloud type. *Journal Meteorology*, 3:123–124, 1946.

Hay, J. E. Calculation of monthly mean solar radiation for horizontal and inclined surfaces. *Solar Energy*, 23(4):301 – 307, 1979. ISSN 0038-092X. doi: http://dx.doi.org/10.1016/0038-092X(79)90123-3. URL http://www.sciencedirect.com/science/article/pii/0038092X79901233.

Haykin, S. *Neural Networks and Learning Machines*. Prentice Hall, November 2008. ISBN 0131471392.

Ho, K.-L., Hsu, Y.-Y., Chen, C.-F., Lee, T.-E., Liang, C.-C., Lai, T.-S., and Chen, K.-K. Short term load forecasting of Taiwan power system using a knowledge-based expert system. *Power Systems, IEEE Transactions on*, 5(4):1214 – 1221, Nov 1990. ISSN 0885-8950. doi: 10.1109/59.99372.

Hoff, T. E. and Perez, R. Quantifying PV power output variability. *Solar Energy*, 84(10): 1782 – 1793, 2010. ISSN 0038-092X. doi: http://dx.doi.org/10.1016/j.solener.2010.07.003. URL http://www.sciencedirect.com/science/article/pii/S0038092X10002380.

Hohm, D. P. and Ropp, M. Comparative study of maximum power point tracking algorithms using an experimental, programmable, maximum power point tracking test bed. In *Photovoltaic Specialists Conference, 2000. Conference Record of the Twenty-Eighth IEEE*, pages 1699 – 1702, 2000. doi: 10.1109/PVSC.2000.916230.

Horvatic, D., Stanley, H. E., and Podobnik, B. Detrended cross-correlation analysis for non-stationary time series with periodic trends. *Europhysics Letters (epl)*, 94, 2011. doi: 10.1209/0295-5075/94/18007.

Huang, C.-M., Huang, Y.-C., and Huang, K.-Y. A hybrid method for one-day ahead hourly forecasting of PV power output. In *Industrial Electronics and Applications (ICIEA), 2014 IEEE 9th Conference on*, pages 526–531, June 2014. doi: 10.1109/ICIEA.2014.6931220.

Huang, H.-C. and Hsu, N.-J. Modeling transport effects on ground-level ozone using a non-stationary space-time model. *Environmetrics*, 15(3):251 – 268, 2004. ISSN 1099-095X. doi: 10.1002/env.639. URL http://dx.doi.org/10.1002/env.639.

Hyndman, R. J., Koehler, A. B., Snyder, R. D., and Grose, S. A state space framework for automatic forecasting using exponential smoothing methods. *International Journal of Forecasting*, 18(3):439 – 454, 2002. ISSN 0169-2070. doi: http://dx.doi.org/10.1016/S0169-2070(01)00110-8. URL http://www.sciencedirect.com/science/article/pii/S0169207001001108.

Hyndman, R. J., Koehler, A. B., Ord, J. K., and Snyder, R. D. *Forecasting with Exponential Smoothing*. Springer, Deblik, Berlin, Germany, 2008.

Hyndman, R. J., Athanasopoulos, G., Razbash, S., Schmidt, D., Zhou, Z., Khan, Y., Bergmeir, C., and Wang, E. *forecast: Forecasting functions for time series and linear models*, 2014. URL http://CRAN.R-project.org/package=forecast. R package version 5.3.

Ianetz, A. and Kudish, A. A method for determining the solar global and defining the diffuse and beam irradiation on a clear day. In Badescu, V., editor, *Modeling Solar Radiation at the Earth's Surface*, pages 93 – 113. Springer, Verlag-Berlin, 2008. ISBN 978-3-540-77454-9.

Ianetz, A., Lyubansky, V., Setter, I., Kriheli, B., Evseev, E. G., and Kudish, A. I. Intercomparison of different models for estimating clear sky solar global radiation for the Negev region of Israel. *Energy Conversion and Management*, 48(1):259 – 268, 2007. ISSN 0196-8904. doi: http://dx.doi.org/10.1016/j.enconman.2006.04.006. URL http://www.sciencedirect.com/science/article/pii/S0196890406001439.

IEA. Solar heating & cooling programme, Task 36, Subtask A: Standard qualification for solar resource products. Technical report, International Energy Agency, 2012. URL http://archive.iea-shc.org/publications/task.aspx?Task=36.

Ineichen, P. Comparison of eight clear sky broadband models against 16 independent data banks. *Solar Energy*, 80(4):468 – 478, 2006. ISSN 0038-092X. doi: http://dx.doi.org/10.1016/j.solener.2005.04.018. URL http://www.sciencedirect.com/science/article/pii/S0038092X05001635. Urban Ventilation.

Ineichen, P. A broadband simplified version of the Solis clear sky model. *Solar Energy*, 82(8): 758 – 762, 2008. ISSN 0038-092X. doi: http://dx.doi.org/10.1016/j.solener.2008.02.009. URL http://www.sciencedirect.com/science/article/pii/S0038092X08000406.

Ineichen, P. and Perez, R. A new airmass independent formulation for the Linke turbidity coefficient. *Solar Energy*, 73(3):151 – 157, 2002. ISSN 0038-092X. doi: http://dx.doi.org/10.1016/S0038-092X(02)00045-2. URL http://www.sciencedirect.com/science/article/pii/S0038092X02000452.

Inman, R. H., Pedro, H. T., and Coimbra, C. F. Solar forecasting methods for renewable energy integration. *Progress in Energy and Combustion Science*, 39(6):535 – 576, 2013. ISSN 0360-1285. doi: http://dx.doi.org/10.1016/j.pecs.2013.06.002. URL http://www.sciencedirect.com/science/article/pii/S0360128513000294.

Inoue, T., Sasaki, T., and Washio, T. Spatio-temporal kriging of solar radiation incorporating direction and speed of cloud movement. In *The 26th Annual Conference of the Japanese Society for Artificial Intelligence*, Yamaguchi city, 2012. <http://kaigi.org/jsai/webprogram/2012/pdf/708.pdf>.

Iovleff, S. and Perrin, O. Estimating a nonstationary spatial structure using simulated annealing. *Journal of Computational and Graphical Statistics*, 13(1):90–105, 2004. doi: 10.1198/1061860043100. URL http://dx.doi.org/10.1198/1061860043100.

Janjai, S., Sricharoen, K., and Pattarapanitchai, S. Semi-empirical models for the estimation of clear sky solar global and direct normal irradiances in the tropics. *Applied Energy*, 88 (12):4749 – 4755, 2011. ISSN 0306-2619. doi: http://dx.doi.org/10.1016/j.apenergy.2011.06.021. URL http://www.sciencedirect.com/science/article/pii/S0306261911004090.

Justus, C., Paris, M., and Tarpley, J. Satellite-measured insolation in the United States, Mexico, and South America. *Remote Sensing of Environment*, 20(1):57 – 83, 1986. ISSN 0034-4257. doi: http://dx.doi.org/10.1016/0034-4257(86)90014-3. URL http://www.sciencedirect.com/science/article/pii/0034425786900143.

Kaplanis, S. New methodologies to estimate the hourly global solar radiation; comparisons with existing models. *Renewable Energy*, 31(6):781 – 790, 2006. ISSN 0960-1481. doi: http://dx.doi.org/10.1016/j.renene.2005.04.011. URL http://www.sciencedirect.com/science/article/pii/S0960148105000959.

Kasten, F. A new table and approximation formula for the relative optial air mass. *Archiv für Meteorologie, Geophysik und Bioklimatologie, Serie B*, 14(2):206 – 223, 1965. ISSN 0066-6424. doi: 10.1007/BF02248840. URL http://dx.doi.org/10.1007/BF02248840.

Kasten, F. and Czeplak, G. Solar and terrestrial radiation dependent on the amount and type of cloud. *Solar Energy*, 24(2):177 – 189, 1980. ISSN 0038-092X. doi: http://dx.doi.org/10.1016/0038-092X(80)90391-6. URL http://www.sciencedirect.com/science/article/pii/0038092X80903916.

Kazantzidis, A., Tzoumanikas, P., Bais, A., Fotopoulos, S., and Economou, G. Cloud detection and classification with the use of whole-sky ground-based images. *Atmospheric Research*, 113(0):80 – 88, 2012. ISSN 0169-8095. doi: http://dx.doi.org/10.1016/j.atmosres.2012.05.005. URL http://www.sciencedirect.com/science/article/pii/S0169809512001342.

Klucher, T. Evaluation of models to predict insolation on tilted surfaces. *Solar Energy*, 23(2): 111 – 114, 1979. ISSN 0038-092X. doi: http://dx.doi.org/10.1016/0038-092X(79)90110-5. URL http://www.sciencedirect.com/science/article/pii/0038092X79901105.

Koronakis, P. S. On the choice of the angle of tilt for south facing solar collectors in the Athens basin area. *Solar Energy*, 36(3):217 – 225, 1986. ISSN 0038-092X. doi: http://dx.doi.org/10.1016/0038-092X(86)90137-4. URL http://www.sciencedirect.com/science/article/pii/0038092X86901374.

Kourentzes, N., Petropoulos, F., and Trapero, J. R. Improving forecasting by estimating time series structural components across multiple frequencies. *International Journal of Forecasting*, 30(2):291 – 302, 2014. ISSN 0169-2070. doi: http://dx.doi.org/10.1016/j.ijforecast.2013.09.006. URL http://www.sciencedirect.com/science/article/pii/S0169207013001477.

Krige, D. A statistical approach to some basic mine valuation problems on the Witwatersrand. *Journal of the Chemical, Metallurgical and Mining Society of South Africa*, 52(6): 119 – 139, 1951. URL http://dx.doi.org/10.2307/3006914.

Kruskal, J. Multidimensional scaling by optimizing goodness of fit to a nonmetric hypothesis. *Psychometrika*, 29(1):1 – 27, March 1964a. ISSN 0033-3123. doi: 10.1007/BF02289565. URL http://dx.doi.org/10.1007/BF02289565.

Kruskal, J. Nonmetric multidimensional scaling: A numerical method. *Psychometrika*, 29(2):115 – 129, June 1964b. ISSN 0033-3123. doi: 10.1007/BF02289694. URL http://dx.doi.org/10.1007/BF02289694.

Kwiatkowski, D., Phillips, P. C. B., and Schmidt, P. Testing the null hypothesis of stationarity against the alternative of a unit root: How sure are we that economic time series have a unit root? *Journal of Econometrics*, 54:159 – 178, 1992.

Kyriakidis, P. C. and Journel, A. G. Geostatistical space-time models: A review. *Mathematical Geology*, 31(6):651–684, 1999. ISSN 0882-8121. doi: 10.1023/A:1007528426688.

Lacis, A. A. and Hansen, J. A parameterization for the absorption of solar radiation in the earth's atmosphere. *Journal of the Atmospheric Sciences*, 31(1):118 – 133, 2014/05/28 1974. doi: 10.1175/1520-0469(1974)031<0118:APFTAO>2.0.CO;2. URL http://dx.doi.org/10.1175/1520-0469(1974)031<0118:APFTAO>2.0.CO;2.

Lave, M. and Kleissl, J. Solar variability of four sites across the state of Colorado. *Renewable Energy*, 35(12):2867 – 2873, 2010. ISSN 0960-1481. doi: http://dx.doi.org/10.1016/j.renene.2010.05.013. URL http://www.sciencedirect.com/science/article/pii/S0960148110002314.

Law, E. W., Prasad, A. A., Kay, M., and Taylor, R. A. Direct normal irradiance forecasting and its application to concentrated solar thermal output forecasting: A review. *Solar Energy*, 108(0):287 – 307, 2014. ISSN 0038-092X. doi: http://dx.doi.

org/10.1016/j.solener.2014.07.008. URL http://www.sciencedirect.com/science/article/pii/S0038092X14003466.

Le, N. D. and Zidek, J. V. *Statistical Analysis of Environmental Space-Time Processes*. Springer, 2006. ISBN 0-387-26209-1.

Lee, Y.-M. and Ellis, J. H. On the equivalence of kriging and maximum entropy estimators. *Mathematical Geology*, 29(1):131 – 152, March 1997. ISSN 0882-8121, 1573-8868. doi: 10.1007/BF02769622.

Lefevre, M., Oumbe, A., Blanc, P., Espinar, B., Gschwind, B., Qu, Z., Wald, L., Schroedter-Homscheidt, M., Hoyer-Klick, C., Arola, A., Benedetti, A., Kaiser, J. W., and Morcrette, J.-J. McClear: a new model estimating downwelling solar radiation at ground level in clear-sky conditions. *Atmospheric Measurement Techniques*, 6(9):2403 – 2418, 2013. doi: 10.5194/amt-6-2403-2013. URL http://www.atmos-meas-tech.net/6/2403/2013/.

Li, R., Zeng, B., and Liou, M. A new three-step search algorithm for block motion estimation. *Circuits and Systems for Video Technology, IEEE Transactions on*, 4(4):438 –442, aug 1994. ISSN 1051-8215. doi: 10.1109/76.313138.

Lipperheide, M., Bosch, J., and Kleissl, J. Embedded nowcasting method using cloud speed persistence for a photovoltaic power plant. *Solar Energy*, 112(0):232 – 238, 2015. ISSN 0038-092X. doi: http://dx.doi.org/10.1016/j.solener.2014.11.013. URL http://www.sciencedirect.com/science/article/pii/S0038092X1400557X.

Liu, B. Y. H. and Jordan, R. C. Daily insolation on surfaces tilted towards the equator. *Trans ASHRAE*, 67:526–541, 1962.

Lonij, V. P., Brooks, A. E., Cronin, A. D., Leuthold, M., and Koch, K. Intra-hour forecasts of solar power production using measurements from a network of irradiance sensors. *Solar Energy*, 97(0):58 – 66, 2013. ISSN 0038-092X. doi: http://dx.doi.org/10.1016/j.solener.2013.08.002. URL http://www.sciencedirect.com/science/article/pii/S0038092X13003125.

Lophaven, S., Carstensen, J., and Rootzén, H. Space-time modeling of environmental monitoring data. *Environmental and Ecological Statistics*, 11(3):237–256, 2004. ISSN 1352-8505. doi: 10.1023/B:EEST.0000038014.91328.58.

Lorenz, E., Hurka, J., Heinemann, D., and Beyer, H. Irradiance forecasting for the power prediction of grid-connected photovoltaic systems. *Selected Topics in Applied Earth Observations and Remote Sensing, IEEE Journal of*, 2(1):2 –10, march 2009. ISSN 1939-1404. doi: 10.1109/JSTARS.2009.2020300.

Lorenz, E., Kühnert, J., and Heinemann, D. Overview of irradiance and photovoltaic power prediction. In Troccoli, A., Dubus, L., and Haupt, S. E., editors, *Weather Matters for Energy*, pages 429–454. Springer New York, 2014. ISBN 978-1-4614-9220-7. doi: 10.1007/978-1-4614-9221-4_21. URL http://dx.doi.org/10.1007/978-1-4614-9221-4_21.

Lorenzo, A., Holmgren, W., Leuthold, M., Kim, C. K., Cronin, A., and Betterton, E. Short-term PV power forecasts based on a real-time irradiance monitoring network. In *Photovoltaic Specialist Conference (PVSC), 2014 IEEE 40th*, pages 75 – 79, June 2014. doi: 10.1109/PVSC.2014.6925212.

Luo, L., Hamilton, D., and Han, B. Estimation of total cloud cover from solar radiation observations at Lake Rotorua, New Zealand. *Solar Energy*, 84(3):501 – 506, 2010. ISSN 0038-092X. doi: http://dx.doi.org/10.1016/j.solener.2010.01.012. URL http://www.sciencedirect.com/science/article/pii/S0038092X10000253.

Ma, C. and Iqbal, M. Statistical comparison of models for estimating solar radiation on inclined surgaces. *Solar Energy*, 31(3):313 – 317, 1983. ISSN 0038-092X. doi: http://dx.doi.org/10.1016/0038-092X(83)90019-1. URL http://www.sciencedirect.com/science/article/pii/0038092X83900191.

Ma, C. Families of spatio-temporal stationary covariance models. *Journal of Statistical Planning and Inference*, 116(2):489 – 501, 2003. ISSN 0378-3758. doi: http://dx.doi.org/10.1016/S0378-3758(02)00353-1. URL http://www.sciencedirect.com/science/article/pii/S0378375802003531.

Ma, C. Linear combinations of space-time covariance functions and variograms. *Signal Processing, IEEE Transactions on*, 53(3):857–864, March 2005. ISSN 1053-587X. doi: 10.1109/TSP.2004.842186.

Mahamadou, A. T., Mamadou, B. C., Brayima, D., and Cristian, N. Ultracapacitors and batteries integration for power fluctuations mitigation in wind-PV-diesel hybrid system. *International Journal of Renewable Energy Research*, 1(2):86 – 95, 2011. ISSN 1309-0127.

Marcos, J., Marroyo, L., Lorenzo, E., and García, M. Smoothing of PV power fluctuations by geographical dispersion. *Progress in Photovoltaics: Research and Applications*, 20(2): 226 – 237, 2012. ISSN 1099-159X. doi: 10.1002/pip.1127. URL http://dx.doi.org/10.1002/pip.1127.

Marquez, R. and Coimbra, C. F. Intra-hour DNI forecasting based on cloud tracking image analysis. *Solar Energy*, 91(0):327 – 336, 2013. ISSN 0038-092X. doi: http://dx.doi.org/10.1016/j.solener.2012.09.018. URL http://www.sciencedirect.com/science/article/pii/S0038092X1200343X.

Marquez, R., Pedro, H. T., and Coimbra, C. F. Hybrid solar forecasting method uses satellite imaging and ground telemetry as inputs to ANNs. *Solar Energy*, 92(0):176 – 188, 2013. ISSN 0038-092X. doi: http://dx.doi.org/10.1016/j.solener.2013.02.023. URL http://www.sciencedirect.com/science/article/pii/S0038092X13000881.

Martin, L., Zarzalejo, L. F., Polo, J., Navarro, A., Marchante, R., and Cony, M. Prediction of global solar irradiance based on time series analysis: Application to solar thermal power plants energy production planning. *Solar Energy*, 84(10):1772 – 1781, 2010. ISSN 0038-092X. doi: http://dx.doi.org/10.1016/j.solener.2010.07.002. URL http://www.sciencedirect.com/science/article/pii/S0038092X10002379.

Martins, F. R. and Pereira, E. B. Estudo comparativo da confiabilidade de estimativas de irradiação solar para o sudeste Brasileiro obtidas a partir de dados de satélite e por interpolação/extrapolação de dados de superfície. *Revista Brasileira de Geofísica*, 29(2): 265 – 276, 2011. ISSN 0102-261X.

Masters, G. M. *Renewable and Efficient Electric Power Systems*. John Wiley & Sons, Inc., Hoboken-New Jersey, 2004.

Matheron, G. Principles of geostatistics. *Economic Geology*, 58(8):1246 – 1266, 1963. doi: 10.2113/gsecongeo.58.8.1246. URL http://economicgeology.org/content/58/8/1246.abstract.

Mathiesen, P. and Kleissl, J. Evaluation of numerical weather prediction for intra-day solar forecasting in the continental united states. *Solar Energy*, 85(5):967 – 977, 2011. ISSN 0038-092X. doi: http://dx.doi.org/10.1016/j.solener.2011.02.013. URL http://www.sciencedirect.com/science/article/pii/S0038092X11000570.

Mathiesen, P., Collier, C., and Kleissl, J. A high-resolution, cloud-assimilating numerical weather prediction model for solar irradiance forecasting. *Solar Energy*, 92(0):47 – 61, 2013. ISSN 0038-092X. doi: http://dx.doi.org/10.1016/j.solener.2013.02.018. URL http://www.sciencedirect.com/science/article/pii/S0038092X13000832.

Maxwell, E. L. Quasi-physical model for converting hourly global horizontal to direct normal insolation. <http://www.nrel.gov/docs/leg-osti/old/3087.pdf>, 1987. (accessed 25.01.2012).

McBratney, A. B. and Minasny, B. Spacebender. *Spatial Statistics*, 4(0):57 – 67, 2013. ISSN 2211-6753. doi: http://dx.doi.org/10.1016/j.spasta.2013.04.001. URL http://idc311-www.sciencedirect.com/science/article/pii/S2211675313000171.

McKenney, D. W., Pelland, S., Poissant, Y., Morris, R., Hutchinson, M., Papadopol, P., Lawrence, K., and Campbell, K. Spatial insolation models for photovoltaic energy in Canada. *Solar Energy*, 82(11):1049 – 1061, 2008. ISSN 0038-092X. doi: http://dx.doi.org/10.1016/j.solener.2008.04.008. URL http://www.sciencedirect.com/science/article/pii/S0038092X08000996.

Meiring, W., Guttorp, P., and Sampson, P. D. Computational issues in fitting spatial deformation models for heterogeneous spatial correlation. In *Proceedings of the 29th Symposium on the Interface: Computing Science and Statistics*. America, Inc, 1997a.

Meiring, W., Monestiez, P., Sampson, P. D., and Guttorp, P. Developments in the modelling of nonstationary spatial covariance structure from space-time monitoring data. In Baafi, E. and Schofield, N., editors, *Geostatistics Wollongong '96*, volume 1, pages 162 – 173. Kluwer Academic Publishers, 1997b. ISBN 0792344944.

Meiring, W., Sampson, P., and Guttorp, P. Space-time estimation of grid-cell hourly ozone levels for assessment of a deterministic model. *Environmental and Ecological Statistics*, 5 (3):197–222, 1998. ISSN 1352-8505. doi: 10.1023/A:1009663518685.

Mellit, A., Eleuch, H., Benghanem, M., Elaoun, C., and Pavan, A. M. An adaptive model for predicting of global, direct and diffuse hourly solar irradiance. *Energy Conversion and Management*, 51(4):771 – 782, 2010. ISSN 0196-8904. doi: http://dx.doi.org/10.1016/j.enconman.2009.10.034. URL http://www.sciencedirect.com/science/article/pii/S0196890409004427.

Mellit, A. and Pavan, A. M. A 24-h forecast of solar irradiance using artificial neural network: Application for performance prediction of a grid-connected PV plant at Trieste, Italy. *Solar Energy*, 84(5):807 – 821, 2010. ISSN 0038-092X. doi: http://dx.doi.org/10.1016/j.solener.2010.02.006. URL http://www.sciencedirect.com/science/article/pii/S0038092X10000782.

Merino, G. G., Jones, D., Stooksbury, D. E., and Hubbard, K. G. Determination of semivariogram models to krige hourly and daily solar irradiance in western Nebraska. *Journal of Applied Meteorology and Climatology*, 40(6):1085 – 1094, 2001. ISSN 0038-092X. doi: http://dx.doi.org/10.1175/1520-0450(2001)040<1085:DOSMTK>2.0.CO;2.

Meydbray, J., Emery, K., and Kurtz, S. Pyranometers, reference cells: What's the difference? Technical report, National Renewable Energy Laboratory, 3 2012a. URL http://www.gl-garradhassan.com/assets/downloads/pyranometers_and_reference_cells_part1.pdf.

Meydbray, J., Riley, E., Dunn, L., Emery, K., and Kurtz, S. Pyranometers, reference cells: Part 2: What makes the most sense for PV power plants. Technical report, National Renewable Energy Laboratory, 10 2012b. URL http://www.gl-garradhassan.com/assets/downloads/pyranometers_and_reference_cells_part2.pdf.

Michalsky, J. J. The astronomical almanac's algorithm for approximate solar position (1950 - 2050). *Solar Energy*, 40(3):227 – 235, 1988. ISSN 0038-092X. doi: 10.1016/0038-092X(88)90045-X. URL http://www.sciencedirect.com/science/article/pii/0038092X8890045X.

Michis, A. A. Time scale evaluation of economic forecasts. *Economics Letters*, 123(3):279 – 281, 2014. ISSN 0165-1765. doi: http://dx.doi.org/10.1016/j.econlet.2014.03.002. URL http://www.sciencedirect.com/science/article/pii/S0165176514000937.

Miller, A. *Subset Selection in Regression*. Monographs on Statistics and Applied Probability. Chapman & Hall/CRC, 2002. ISBN 1-58488-171-2.

Mogheir, Y., Singh, V., and de Lima, J. Spatial assessment and redesign of a groundwater quality monitoring network using entropy theory, Gaza Strip, Palestine. *Hydrogeology Journal*, 14(5):700 – 712, 2006. ISSN 1431-2174. doi: 10.1007/s10040-005-0464-3. URL http://dx.doi.org/10.1007/s10040-005-0464-3.

Monestiez, P. and Switzer, P. Semiparametric estimation of nonstationary spatial covariance models by metric multidimensional scaling. SIMS Tech. Rep. 165, Stanford University, November 1991.

Monestiez, P., Sampson, P. D., and Guttorp, P. Modelling of heterogeneous spatial correlation structure by spatial deformation. *Cahiers de Geostatistique*, 3:35 – 46, 1993.

Moreno, A., Gilabert, M., and Martinez, B. Mapping daily global solar irradiation over Spain: A comparative study of selected approaches. *Solar Energy*, 85(9):2072 – 2084, 2011. ISSN 0038-092X. doi: http://dx.doi.org/10.1016/j.solener.2011.05.017. URL http://www.sciencedirect.com/science/article/pii/S0038092X11001976.

Möser, W. and Raschke, E. Incident solar radiation over Europe estimated from METEOSAT data. *Journal of Climate and Applied Meteorology*, 23(1):166 – 170, 2014/05/28 1984. doi: 10.1175/1520-0450(1984)023<0166:ISROEE>2.0.CO;2. URL http://dx.doi.org/10.1175/1520-0450(1984)023<0166:ISROEE>2.0.CO;2.

Murata, A., Yamaguchi, H., and Otani, K. A method of estimating the output fluctuation of many photovoltaic power generation systems dispersed in a wide area. *Electrical Engineering in Japan*, 166(4):9 – 19, 2009. ISSN 1520-6416. doi: 10.1002/eej.20723. URL http://dx.doi.org/10.1002/eej.20723.

Nonnenmacher, L., Kaur, A., and Coimbra, C. F. Verification of the SUNY direct normal irradiance model with ground measurements. *Solar Energy*, 99(0):246 – 258, 2014. ISSN 0038-092X. doi: http://dx.doi.org/10.1016/j.solener.2013.11.010. URL http://www.sciencedirect.com/science/article/pii/S0038092X13004908.

Noorian, A. M., Moradi, I., and Kamali, G. A. Evaluation of 12 models to estimate hourly diffuse irradiation on inclined surfaces. *Renewable Energy*, 33(6):1406 – 1412, 2008. ISSN 0960-1481. doi: http://dx.doi.org/10.1016/j.renene.2007.06.027. URL http://www.sciencedirect.com/science/article/pii/S0960148107002509.

Ododo, J., Agbakwuru, J., and Ogbu, F. Correlation of solar radiation with cloud cover and relative sunshine duration. *Energy Conversion and Management*, 37(10):1555 – 1559, 1996. ISSN 0196-8904. doi: http://dx.doi.org/10.1016/0196-8904(96)86837-3. URL http://www.sciencedirect.com/science/article/pii/0196890496868373.

Orgill, J. and Hollands, K. Correlation equation for hourly diffuse radiation on a horizontal surface. *Solar Energy*, 19(4):357 – 359, 1977. ISSN 0038-092X. doi: http://dx.doi.org/10.1016/0038-092X(77)90006-8. URL http://www.sciencedirect.com/science/article/pii/0038092X77900068.

Owlia, R., Abrishamchi, A., and Tajrishy, M. Spatial-temporal assessment and redesign of groundwater quality monitoring network: a case study. *Environmental Monitoring and Assessment*, 172(1-4):263 – 273, 2011. ISSN 0167-6369. doi: 10.1007/s10661-010-1332-8. URL http://dx.doi.org/10.1007/s10661-010-1332-8.

Padovan, A. and Col, D. D. Measurement and modeling of solar irradiance components on horizontal and tilted planes. *Solar Energy*, 84(12):2068 – 2084, 2010. ISSN 0038-092X. doi: http://dx.doi.org/10.1016/j.solener.2010.09.009. URL http://www.sciencedirect.com/science/article/pii/S0038092X10003014.

Paltridge, G. and Proctor, D. Monthly mean solar radiation statistics for Australia. *Solar Energy*, 18(3):235 – 243, 1976. ISSN 0038-092X. doi: http://dx.doi.org/10.1016/0038-092X(76)90022-0. URL http://www.sciencedirect.com/science/article/pii/0038092X76900220.

Paoli, C., Voyant, C., Muselli, M., and Nivet, M.-L. Forecasting of preprocessed daily solar radiation time series using neural networks. *Solar Energy*, 84(12):2146 – 2160, 2010. ISSN 0038-092X. doi: http://dx.doi.org/10.1016/j.solener.2010.08.011. URL http://www.sciencedirect.com/science/article/pii/S0038092X10002793.

Pattanasethanon, S., Lertsatitthanakorn, C., Atthajariyakul, S., and Soponronnarit, S. All sky modeling daylight availability and illuminance/irradiance on horizontal plane for Mahasarakham, Thailand. *Energy Conversion and Management*, 48(5):1601 – 1614, 2007. ISSN 0196-8904. doi: 10.1016/j.enconman.2006.11.012. URL http://www.sciencedirect.com/science/article/pii/S0196890406003566.

Pedro, H. T. and Coimbra, C. F. Assessment of forecasting techniques for solar power production with no exogenous inputs. *Solar Energy*, 86(7):2017 – 2028, 2012. ISSN 0038-092X. doi: http://dx.doi.org/10.1016/j.solener.2012.04.004. URL http://www.sciencedirect.com/science/article/pii/S0038092X12001429.

Perez, R., Stewart, R., Arbogast, C., Seals, R., and Scott, J. An anisotropic hourly diffuse radiation model for sloping surfaces: Description, performance validation, site dependency evaluation. *Solar Energy*, 36(6):481 – 497, 1986. ISSN 0038-092X. doi: 10.1016/0038-092X(86)90013-7. URL http://www.sciencedirect.com/science/article/pii/0038092X86900137.

Perez, R., Seals, R., and Michalsky, J. All-weather model for sky luminance distribution, preliminary configuration and validation. *Solar Energy*, 50(3):235 – 245, 1993. ISSN 0038-092X. doi: 10.1016/0038-092X(93)90017-I. URL http://www.sciencedirect.com/science/article/pii/0038092X9390017I.

Perez, R., Seals, R., Ineichen, P., Stewart, R., and Menicucci, D. A new simplified version of the Perez diffuse irradiance model for tilted surfaces. *Solar Energy*, 39(3):221 – 231, 1987. ISSN 0038-092X. doi: 10.1016/S0038-092X(87)80031-2. URL http://www.sciencedirect.com/science/article/pii/S0038092X87800312.

Perez, R., Stewart, R., Seals, R., and Guertin, T. The development and verification of the Perez diffuse radiation model. Technical Report SAND88- 7030, Atmospheric Sciences Research Center, SUNY at Albany, Albany, NY, October 1988.

Perez, R., Ineichen, P., Seals, R., Michalsky, J., and Stewart, R. Modeling daylight availability and irradiance components from direct and global irradiance. *Solar Energy*, 44(5):271 – 289, 1990. ISSN 0038-092X. doi: 10.1016/0038-092X(90)90055-H. URL http://www.sciencedirect.com/science/article/pii/0038092X9090055H.

Perez, R., Ineichen, P., Moore, K., Kmiecik, M., Chain, C., George, R., and Vignola, F. A new operational model for satellite-derived irradiances: description and validation. *Solar Energy*, 73(5):307 – 317, 2002. ISSN 0038-092X. doi: http://dx.doi.org/10.1016/S0038-092X(02)00122-6. URL http://www.sciencedirect.com/science/article/pii/S0038092X02001226.

Perez, R., Ineichen, P., Kmiecik, M., Moore, K., Renne, D., and George, R. Producing satellite-derived irradiances in complex arid terrain. *Solar Energy*, 77(4):367 – 371, 2004. ISSN 0038-092X. doi: http://dx.doi.org/10.1016/j.solener.2003.12.016. URL http://www.sciencedirect.com/science/article/pii/S0038092X03004687. The American Solar Energy Society's Solar 2003 Special Issue.

Perez, R., Moore, K., Wilcox, S., Renne, D., and Zelenka, A. Forecasting solar radiation - preliminary evaluation of an approach based upon the national forecast database. *Solar Energy*, 81(6):809 – 812, 2007. ISSN 0038-092X. doi: http://dx.doi.org/10.1016/j.solener.2006.09.009. URL http://www.sciencedirect.com/science/article/pii/S0038092X06002404.

Perez, R., Kivalov, S., Schlemmer, J., Jr., K. H., Renne, D., and Hoff, T. E. Validation of short and medium term operational solar radiation forecasts in the US. *Solar Energy*, 84(12):2161 – 2172, 2010. ISSN 0038-092X. doi: http://dx.doi.org/10.1016/j.solener.2010.08.014. URL http://www.sciencedirect.com/science/article/pii/S0038092X10002823.

Perez, R., Kivalov, S., Schlemmer, J., Jr., K. H., and Hoff, T. E. Short-term irradiance variability: Preliminary estimation of station pair correlation as a function of distance. *Solar Energy*, 86(8):2170 – 2176, 2012. ISSN 0038-092X. doi: 10.1016/j.solener.2012.02.027. URL http://www.sciencedirect.com/science/article/pii/S0038092X12000928.

Perez, R., Lorenz, E., Pelland, S., Beauharnois, M., Knowe, G. V., Jr., K. H., Heinemann, D., Remund, J., Muller, S. C., Traunmuller, W., Steinmauer, G., Pozo, D., Ruiz-Arias, J. A., Lara-Fanego, V., Ramirez-Santigosa, L., Gaston-Romero, M., and Pomares, L. M. Comparison of numerical weather prediction solar irradiance forecasts in the US, Canada and Europe. *Solar Energy*, 94(0):305 – 326, 2013. ISSN 0038-092X. doi: http://dx.doi.org/10.1016/j.solener.2013.05.005. URL http://www.sciencedirect.com/science/article/pii/S0038092X13001886.

Pfeifer, P. E. and Bodily, S. E. A test of space-time ARMA modelling and forecasting of hotel data. *Journal of Forecasting*, 9(3):255–272, 1990. ISSN 1099-131X. doi: 10.1002/for.3980090305. URL http://dx.doi.org/10.1002/for.3980090305.

Pfeifer, P. E. and Deutsch, S. J. Identification and interpretation of first order space-time ARMA models. *Technometrics*, 22(3):397 – 408, 1980a. ISSN 00401706. URL http://www.jstor.org/stable/1268325.

Pfeifer, P. E. and Deutsch, S. J. A STARIMA model-building procedure with application to description and regional forecasting. *Transactions of the Institute of British Geographers*, 5(3):330 – 349, 1980b. ISSN 00202754. URL http://www.jstor.org/stable/621846.

Pfeifer, P. E. and Deutsch, S. J. A three-stage iterative procedure for space-time modeling. *Technometrics*, 22(1):35 – 47, 1980c. ISSN 00401706. URL http://www.jstor.org/stable/1268381.

Podobnik, B., Jiang, Z.-Q., Zhou, W.-X., and Stanley, H. E. Statistical tests for power-law cross-correlated processes. *Phys. Rev. E*, 84:066118, Dec 2011. doi: 10.1103/PhysRevE.84.066118. URL http://link.aps.org/doi/10.1103/PhysRevE.84.066118.

Polo, J., Antonanzas-Torres, F., Vindel, J., and Ramirez, L. Sensitivity of satellite-based methods for deriving solar radiation to different choice of aerosol input and models. *Renewable Energy*, 68(0):785 – 792, 2014. ISSN 0960-1481. doi: http://dx.doi.org/10.1016/j.renene.2014.03.022. URL http://www.sciencedirect.com/science/article/pii/S0960148114001670.

Porcu, E., Gregori, P., and Mateu, J. Nonseparable stationary anisotropic space-time covariance functions. *Stochastic Environmental Research and Risk Assessment*, 21(2):113 – 122, 2006. ISSN 1436-3240. doi: 10.1007/s00477-006-0048-3. URL http://dx.doi.org/10.1007/s00477-006-0048-3.

Porcu, E., Mateu, J., and Saura, F. New classes of covariance and spectral density functions for spatio-temporal modelling. *Stochastic Environmental Research and Risk Assessment*, 22(1):65 – 79, 2008. ISSN 1436-3240. doi: 10.1007/s00477-007-0160-z. URL http://dx.doi.org/10.1007/s00477-007-0160-z.

Quesada-Ruiz, S., Chu, Y., Tovar-Pescador, J., Pedro, H., and Coimbra, C. Cloud-tracking methodology for intra-hour {DNI} forecasting. *Solar Energy*, 102(0):267 – 275, 2014. ISSN 0038-092X. doi: http://dx.doi.org/10.1016/j.solener.2014.01.030. URL http://www.sciencedirect.com/science/article/pii/S0038092X14000486.

R Core Team. *R: A Language and Environment for Statistical Computing*. R Foundation for Statistical Computing, Vienna, Austria, 2014. URL http://www.R-project.org/.

Rahman, S. and Hazim, O. A generalized knowledge-based short-term load-forecasting technique. *Power Systems, IEEE Transactions on*, 8(2):508 – 514, May 1993. ISSN 0885-8950. doi: 10.1109/59.260833.

Reda, I. and Andreas, A. Solar position algorithm for solar radiation applications. *Solar Energy*, 76(5):577 – 589, 2004. ISSN 0038-092X. doi: http://dx.doi.org/10.1016/j.solener.2003.12.003. URL http://www.sciencedirect.com/science/article/pii/S0038092X0300450X.

Reda, I. and Andreas, A. Solar position algorithm for solar radiation applications. Technical Report TP-560-34302, National Renewable Energy Laboratory, Golden, CO, January 2008.

Rehman, S. and Ghori, S. G. Spatial estimation of global solar radiation using geostatistics. *Renewable Energy*, 21:583 – 605, 2000. ISSN 0960-1481. doi: 10.1016/S0960-1481(00)00078-1. URL http://www.sciencedirect.com/science/article/pii/S0960148100000781.

Reikard, G. Predicting solar radiation at high resolutions: A comparison of time series forecasts. *Solar Energy*, 83(3):342 – 349, 2009. ISSN 0038-092X. doi: http://dx.doi.org/10.1016/j.solener.2008.08.007. URL http://www.sciencedirect.com/science/article/pii/S0038092X08002107.

Reindl, D., Beckman, W., and Duffie, J. Diffuse fraction correlations. *Solar Energy*, 45(1):1 – 7, 1990a. ISSN 0038-092X. doi: http://dx.doi.org/10.1016/0038-092X(90)90060-P. URL http://www.sciencedirect.com/science/article/pii/0038092X9090060P.

Reindl, D., Beckman, W., and Duffie, J. Evaluation of hourly tilted surface radiation models. *Solar Energy*, 45(1):9 – 17, 1990b. ISSN 0038-092X. doi: http://dx.doi.org/10.1016/0038-092X(90)90061-G. URL http://www.sciencedirect.com/science/article/pii/0038092X9090061G.

Ricci, V. R functions for regression analysis. <http://cran.r-project.org/doc/contrib/Ricci-refcard-regression.pdf>, oct 2005. (accessed 29.06.2011).

Ridley, B., Boland, J., and Lauret, P. Modelling of diffuse solar fraction with multiple predictors. *Renewable Energy*, 35(2):478 – 483, 2010. ISSN 0960-1481. doi: http://dx.doi.org/10.1016/j.renene.2009.07.018. URL http://www.sciencedirect.com/science/article/pii/S0960148109003012.

Righini, R., Gallegos, H. G., and Raichijk, C. Approach to drawing new global solar irradiation contour maps for Argentina. *Renewable Energy*, 30(8):1241 – 1255, 2005. ISSN 0960-1481. doi: http://dx.doi.org/10.1016/j.renene.2004.10.010. URL http://www.sciencedirect.com/science/article/pii/S0960148104004057.

Roberts, S. A. A general class of Holt-Winters type forecasting models. *Management Science*, 28(7):808 – 820, 1982. doi: 10.1287/mnsc.28.7.808. URL http://pubsonline.informs.org/doi/abs/10.1287/mnsc.28.7.808.

Robledo, L. and Soler, A. Luminous efficacy of global solar radiation for clear skies. *Energy Conversion and Management*, 41(16):1769 – 1779, 2000. ISSN 0196-8904. doi: http://dx.doi.org/10.1016/S0196-8904(00)00019-4. URL http://www.sciencedirect.com/science/article/pii/S0196890400000194.

Rouhani, S. and Hall, T. Space-time kriging of groundwater data. In Armstrong, M., editor, *Geostatistics*, volume 4 of *Quantitative Geology and Geostatistics*, pages 639 – 650. Springer Netherlands, 1989. ISBN 978-94-015-6846-3. doi: 10.1007/978-94-015-6844-9_50. URL http://dx.doi.org/10.1007/978-94-015-6844-9_50.

Russo, M., Leotta, G., Pugliatti, P., and Gigliucci, G. Genetic programming for photovoltaic plant output forecasting. *Solar Energy*, 105(0):264 – 273, 2014. ISSN 0038-092X. doi: http://dx.doi.org/10.1016/j.solener.2014.02.021. URL http://www.sciencedirect.com/science/article/pii/S0038092X14000991.

Salvador, S. and Chan, P. Learning states and rules for detecting anomalies in time series. *Applied Intelligence*, 23(3):241 – 255, 2005. ISSN 0924-669X. doi: 10.1007/s10489-005-4610-3. URL http://dx.doi.org/10.1007/s10489-005-4610-3.

Sampson, P. D. and Guttorp, P. Nonparametric estimation of nonstationary spatial covariance structure. *Journal of the American Statistical Association*, 87(417):108 – 119, 1992. URL http://www.jstor.org/stable/2290458.

Sayed, M. A fast architecture for exhaustive search block matching algorithm with MPEG-4 applications. In *Electronics, Circuits, and Systems, 2009. ICECS 2009. 16th IEEE International Conference on*, pages 787 – 790, Dec 2009. doi: 10.1109/ICECS.2009.5410777.

Schmidt, A. M. and O'Hagan, A. Bayesian inference for non-stationary spatial covariance structure via spatial deformations. *Journal of the Royal Statistical Society: Series B (Statistical Methodology)*, 65(3):743 – 758, 2003. ISSN 1467-9868. doi: 10.1111/1467-9868.00413. URL http://dx.doi.org/10.1111/1467-9868.00413.

Shahan, Z. World solar power capacity increased 35% in 2013. <http://cleantechnica.com/2014/04/13/world-solar-power-capacity-increased-35-2013-charts/>, Apr 2014. (accessed 30.05.2014).

Shannon, C. E. A mathematical theory of communication. *Bell System Technical Journal*, 27(3):379 – 423, July 1948. ISSN 1538-7305. doi: 10.1002/j.1538-7305.1948.tb01338.x. URL http://onlinelibrary.wiley.com/doi/10.1002/j.1538-7305.1948.tb01338.x/abstract.

Sherman, M. *Spatial Statistics and Spatio-Temporal Data: Covariance Functions and Directional Properties*. John Wiley & Sons, Inc., Hoboken-New Jersey, 2010. ISBN 9780470699584.

Shewry, M. C. and Wynn, H. P. Maximum entropy sampling. *Journal of Applied Statistics*, 14(2):165 – 170, January 1987. ISSN 0266-4763. doi: 10.1080/02664768700000020. URL http://dx.doi.org/10.1080/02664768700000020.

Singh, V. P. *Entropy Theory and its Application in Environmental and Water Engineering*. Wiley-Blackwell, 2013. ISBN 978-1-119-97656-1.

Skartveit, A. and Olseth, J. A. Modelling slope irradiance at high latitudes. *Solar Energy*, 36(4):333 – 344, 1986.

Sozen, A., Arcaklioglu, E., Ozalp, M., and Caglar, N. Forecasting based on neural network approach of solar potential in Turkey. *Renewable Energy*, 30(7):1075 – 1090, 2005. ISSN 0960-1481. doi: http://dx.doi.org/10.1016/j.renene.2004.09.020. URL http://www.sciencedirect.com/science/article/pii/S0960148104003702.

Stein, M. L. Space: Time covariance functions. *Journal of the American Statistical Association*, 100(469):310 – 321, 2005. ISSN 01621459. URL http://www.jstor.org/stable/27590540.

Stroud, J. R., Stein, M. L., Lesht, B. M., Schwab, D. J., and Beletsky, D. An ensemble Kalman filter and smoother for satellite data assimilation. *Journal of the American Statistical Association*, 105(491):978–990, 2010. doi: 10.1198/jasa.2010.ap07636.

Sudheer, G. and Suseelatha, A. Short term load forecasting using wavelet transform combined with Holt-Winters and weighted nearest neighbor models. *International Journal of Electrical Power & Energy Systems*, 64(0):340 – 346, 2015. ISSN 0142-0615. doi: http://dx.doi.org/10.1016/j.ijepes.2014.07.043. URL http://www.sciencedirect.com/science/article/pii/S0142061514004785.

Tarpley, J. D. Estimating incident solar radiation at the surface from geostationary satellite data. *Journal of Applied Meteorology*, 18(9):1172 – 1181, 2014/05/28 1979. doi: 10.1175/1520-0450(1979)018<1172:EISRAT>2.0.CO;2. URL http://dx.doi.org/10.1175/1520-0450(1979)018<1172:EISRAT>2.0.CO;2.

Taylor, J. W. Smooth transition exponential smoothing. *Journal of Forecasting*, 23(6):385 – 404, 2004. ISSN 1099-131X. doi: 10.1002/for.918. URL http://dx.doi.org/10.1002/for.918.

Taylor, J. W. Density forecasting for the efficient balancing of the generation and consumption of electricity. *International Journal of Forecasting*, 22(4):707 – 724, 2006. ISSN 0169-2070. doi: http://dx.doi.org/10.1016/j.ijforecast.2006.02.001. URL http://www.sciencedirect.com/science/article/pii/S0169207006000227.

Taylor, J. W. Forecasting daily supermarket sales using exponentially weighted quantile regression. *European Journal of Operational Research*, 178(1):154 – 167, 2007. ISSN 0377-2217. doi: http://dx.doi.org/10.1016/j.ejor.2006.02.006. URL http://www.sciencedirect.com/science/article/pii/S0377221706000737.

Taylor, J. W. A comparison of univariate time series methods for forecasting intraday arrivals at a call center. *Management Science*, 54(2):253 – 265, 2008. doi: 10.1287/mnsc.1070.0786.

Taylor, J. W. Triple seasonal methods for short-term electricity demand forecasting. *European Journal of Operational Research*, 204(1):139 – 152, 2010. ISSN 0377-2217. doi: http://dx.doi.org/10.1016/j.ejor.2009.10.003. URL http://www.sciencedirect.com/science/article/pii/S037722170900705X.

Taylor, J. W. Short-term load forecasting with exponentially weighted methods. *Power Systems, IEEE Transactions on*, 27(1):458 – 464, Feb 2012a. ISSN 0885-8950. doi: 10.1109/TPWRS.2011.2161780.

Taylor, J. W. Density forecasting of intraday call center arrivals using models based on exponential smoothing. *Management Science*, 58(3):534 – 549, 2012b. doi: 10.1287/mnsc.1110.1434.

Taylor, J. W. and Snyder, R. D. Forecasting intraday time series with multiple seasonal cycles using parsimonious seasonal exponential smoothing. *Omega*, 40(6):748 – 757, 2012. ISSN 0305-0483. doi: http://dx.doi.org/10.1016/j.omega.2010.03.004. URL http://www.

sciencedirect.com/science/article/pii/S0305048310000307. Special Issue on Forecasting in Management Science.

Taylor, J. and McSharry, P. Short-term load forecasting methods: An evaluation based on European data. *Power Systems, IEEE Transactions on*, 22(4):2213 – 2219, Nov 2007. ISSN 0885-8950. doi: 10.1109/TPWRS.2007.907583.

Teleke, S., Baran, M., Bhattacharya, S., and Huang, A. Rule-based control of battery energy storage for dispatching intermittent renewable sources. *Sustainable Energy, IEEE Transactions on*, 1(3):117 – 124, Oct 2010. ISSN 1949-3029. doi: 10.1109/TSTE.2010.2061880.

Temps, R. C. and Coulson, K. Solar radiation incident upon slopes of different orientations. *Solar Energy*, 19(2):179 – 184, 1977. ISSN 0038-092X. doi: http://dx.doi.org/10.1016/0038-092X(77)90056-1. URL http://www.sciencedirect.com/science/article/pii/0038092X77900561.

Thiart, C. and Stein, A. Continental-scale kriging of gold-bearing commodities. *Spatial Statistics*, 6(0):57 – 77, 2013. ISSN 2211-6753. doi: http://dx.doi.org/10.1016/j.spasta.2013.07.004. URL http://www.sciencedirect.com/science/article/pii/S2211675313000432.

Tian, Y., Davies-Colley, R., Gong, P., and Thorrold, B. Estimating solar radiation on slopes of arbitrary aspect. *Agricultural and Forest Meteorology*, 109(1):67 – 74, 2001. ISSN 0168-1923. doi: http://dx.doi.org/10.1016/S0168-1923(01)00245-3. URL http://www.sciencedirect.com/science/article/pii/S0168192301002453.

Tibshirani, R. Regression shrinkage and selection via the Lasso. *Journal of the Royal Statistical Society. Series B (Methodological)*, 58(1):267 – 288, 1996. ISSN 00359246. URL http://www.jstor.org/stable/2346178.

Tibshirani, R. Regression shrinkage and selection via the lasso: a retrospective. *Journal of the Royal Statistical Society: Series B (Statistical Methodology)*, 73(3):273 – 282, 2011. ISSN 1467-9868. doi: 10.1111/j.1467-9868.2011.00771.x. URL http://dx.doi.org/10.1111/j.1467-9868.2011.00771.x.

Topcu, S. and Oney, S. The estimation of hourly total irradiation for cloudy sky in Istanbul. *Renewable Energy*, 4(2):223 – 226, 1994. ISSN 0960-1481. doi: http://dx.doi.org/10.1016/0960-1481(94)90007-8. URL http://www.sciencedirect.com/science/article/pii/0960148194900078.

Venables, B., Hornik, K., and Maechler, M. A collection of functions to implement a class for univariate polynomial manipulations. <http://cran.r-project.org/web/packages/polynom/polynom.pdf>, sep 2009. (accessed 16.04.2011).

Vignola, F., Grover, C., Lemon, N., and McMahan, A. Building a bankable solar radiation dataset. *Solar Energy*, 86(8):2218 – 2229, 2012. ISSN 0038-092X. doi: http://dx.doi.org/10.1016/j.solener.2012.05.013. URL http://www.sciencedirect.com/science/article/pii/S0038092X1200182X. Progress in Solar Energy 3.

Voyant, C., Muselli, M., Paoli, C., and Nivet, M.-L. Optimization of an artificial neural network dedicated to the multivariate forecasting of daily global radiation. *Energy*, 36(1):348 – 359, 2011. ISSN 0360-5442. doi: http://dx.doi.org/10.1016/j.energy.2010.10.032. URL http://www.sciencedirect.com/science/article/pii/S0360544210005955.

Wahba, G. and Wendelberger, J. Some new mathematical methods for variational objective analysis using splines and cross validation. *Monthly Weather Review*, 108(8):1122 – 1143, 1980. doi: 10.1175/1520-0493(1980)108<1122:SNMMFV>2.0.CO;2. URL http://dx.doi.org/10.1175/1520-0493(1980)108<1122:SNMMFV>2.0.CO;2.

Wasserman, L. *All of Statistics: A Concise Course in Statistical Inference (Springer Texts in Statistics)*. Springer, December 2003. ISBN 0387402721. URL http://www.amazon.com/exec/obidos/redirect?tag=citeulike07-20&path=ASIN/0387402721.

Webby, R., O'Connor, M., and Lawrence, M. Judgmental time-series forecasting using domain knowledge. In Armstrong, J., editor, *Principles of Forecasting*, volume 30 of *International Series in Operations Research & Management Science*, pages 389 – 403. Springer US, 2001. ISBN 978-0-7923-7401-5. doi: 10.1007/978-0-306-47630-3_17. URL http://dx.doi.org/10.1007/978-0-306-47630-3_17.

West, S. R., Rowe, D., Sayeef, S., and Berry, A. Short-term irradiance forecasting using skycams: Motivation and development. *Solar Energy*, 110(0):188 – 207, 2014. ISSN 0038-092X. doi: http://dx.doi.org/10.1016/j.solener.2014.08.038. URL http://www.sciencedirect.com/science/article/pii/S0038092X14004150.

Wikle, C. K. and Cressie, N. A dimension-reduced approach to space-time Kalman filtering. *Biometrika*, 86(4):815 – 829, 1999. ISSN 00063444. URL http://www.jstor.org/stable/2673587.

Wilcox, S. and Marion, W. *Users manual for TMY3 data sets*, 2008. URL http://www.nrel.gov/docs/fy08osti/43156.pdf. National Renewable Energy Laboratory.

Wu, J. and Chee, K. C. Prediction of hourly solar radiation using a novel hybrid model of ARMA and TDNN. *Solar Energy*, 85(5):808 – 817, 2011. ISSN 0038-092X. doi: http://dx.doi.org/10.1016/j.solener.2011.01.013. URL http://www.sciencedirect.com/science/article/pii/S0038092X11000259.

Wu, Q. X. A correlation-relaxation-labeling framework for computing optical flow - template matching from a new perspective. *IEEE Trans. Pattern Anal. Mach. Intell.*, 17(9):843 – 853, September 1995. ISSN 0162-8828. doi: 10.1109/34.406650. URL http://dx.doi.org/10.1109/34.406650.

Wu, S. and Zidek, J. V. An entropy-based analysis of data from selected NADP/NTN network sites for 1983-1986. *Atmospheric Environment. Part A. General Topics*, 26(11): 2089 – 2103, 1992. ISSN 0960-1686. doi: 10.1016/0960-1686(92)90093-Z. URL http://www.sciencedirect.com/science/article/pii/096016869290093Z.

Wu, Y.-K., Chen, C.-R., and Abdul-Rahman, H. A novel hybrid model for short-term forecasting in PV power generation. *International Journal of Photoenergy*, 2014(0):1 – 9, 2014. doi: http://dx.doi.org/10.1155/2014/569249. URL http://www.hindawi.com/journals/ijp/2014/569249/cta/.

Xu, Q., Zhang, S. J., and Yan, D. X. A new circular distribution and its application to wind data. *Journal of Mathematics Research*, 2:12 – 17, 2010.

Yadav, A. K. and Chandel, S. Tilt angle optimization to maximize incident solar radiation: A review. *Renewable and Sustainable Energy Reviews*, 23(0):503 – 513, 2013. ISSN 1364-0321. doi: http://dx.doi.org/10.1016/j.rser.2013.02.027. URL http://www.sciencedirect.com/science/article/pii/S1364032113001299.

Yang, D. and Reindl, T. Solar irradiance monitoring network design using the variance quadtree algorithm. *Renewables: Wind, Water, and Solar*, 2(1):1 – 8, 2015. ISSN 2198-994X. doi: 10.1186/s40807-014-0001-x. URL http://www.jrenewables.com/content/2/1/1.

Yang, D., Jirutitijaroen, P., and Walsh, W. M. The estimation of clear sky global horizontal irradiance at the equator. *Energy Procedia*, 25(0):141 – 148, 2012a. ISSN 1876-6102. doi: http://dx.doi.org/10.1016/j.egypro.2012.07.019. URL http://www.sciencedirect.com/science/article/pii/S1876610212011812. PV Asia Pacific Conference 2011.

Yang, D., Jirutitijaroen, P., and Walsh, W. M. Hourly solar irradiance time series forecasting using cloud cover index. *Solar Energy*, 86(12):3531 – 3543, 2012b. ISSN 0038-092X. doi: http://dx.doi.org/10.1016/j.solener.2012.07.029. URL http://www.sciencedirect.com/science/article/pii/S0038092X12003039.

Yang, D., Dong, Z., Nobre, A., Khoo, Y. S., Jirutitijaroen, P., and Walsh, W. M. Evaluation of transposition and decomposition models for converting global solar irradiance from tilted surface to horizontal in tropical regions. *Solar Energy*, 97(0):369 – 387, 2013a. ISSN 0038-092X. doi: http://dx.doi.org/10.1016/j.solener.2013.08.033. URL http://www.sciencedirect.com/science/article/pii/S0038092X13003435.

Yang, D., Gu, C., Dong, Z., Jirutitijaroen, P., Chen, N., and Walsh, W. M. Solar irradiance forecasting using spatial-temporal covariance structures and time-forward kriging. *Renewable Energy*, 60(0):235 – 245, 2013b. ISSN 0960-1481. doi: http://dx.doi.org/10.1016/j.renene.2013.05.030. URL http://www.sciencedirect.com/science/article/pii/S0960148113002759.

Yang, D., Dong, Z., Reindl, T., Jirutitijaroen, P., and Walsh, W. M. Solar irradiance forecasting using spatio-temporal empirical kriging and vector autoregressive models with parameter shrinkage. *Solar Energy*, 103(0):550 – 562, 2014a. ISSN 0038-092X. doi: http://dx.doi.org/10.1016/j.solener.2014.01.024. URL http://www.sciencedirect.com/science/article/pii/S0038092X14000425.

Yang, D., Nobre, A., Baker, R., and Reindl, T. Large-area solar irradiance mapping. *Photovoltaics International*, 24(0):91 – 98, 5 2014b.

Yang, D., Walsh, W. M., and Jirutitijaroen, P. Estimation and applications of clear sky global horizontal irradiance at the equator. *Journal of Solar Energy Engineering*, 136(3), 5 2014c. URL http://dx.doi.org/10.1115/1.4027263.

Yang, D., Ye, Z., Nobre, A. M., Du, H., Walsh, W. M., Lim, L. I., and Reindl, T. Bidirectional irradiance transposition based on the Perez model. *Solar Energy*, 110(0):768 – 780, 2014d. ISSN 0038-092X. doi: http://dx.doi.org/10.1016/j.solener.2014.10.006. URL http://www.sciencedirect.com/science/article/pii/S0038092X14004927.

Yang, D., Sharma, V., Ye, Z., Lim, L. I., Zhao, L., and Aryaputera, A. W. Forecasting of global horizontal irradiance by exponential smoothing, using decompositions. *Energy*, (0):–, 2015a. ISSN 0360-5442. doi: http://dx.doi.org/10.1016/j.energy.2014.11.082. URL http://www.sciencedirect.com/science/article/pii/S0360544214013528.

Yang, D., Ye, Z., Lim, L. I., and Dong, Z. Very short term irradiance forecasting using the lasso. *Solar Energy*, (0):–, 2015b. ISSN 0038-092X. doi: http://dx.doi.org/10.1016/j.solener.2015.01.016.

Yang, H., Kurtz, B., Nguyen, D., Urquhart, B., Chow, C. W., Ghonima, M., and Kleissl, J. Solar irradiance forecasting using a ground-based sky imager developed at UC San Diego. *Solar Energy*, 103(0):502 – 524, 2014e. ISSN 0038-092X. doi: http://dx.doi.org/10.1016/j.solener.2014.02.044. URL http://www.sciencedirect.com/science/article/pii/S0038092X14001327.

Yang, K., Huang, G., and Tamai, N. A hybrid model for estimating global solar radiation. *Solar Energy*, 70(1):13 – 22, 2001. ISSN 0038-092X. doi: http://dx.doi.org/10.1016/S0038-092X(00)00121-3. URL http://www.sciencedirect.com/science/article/pii/S0038092X00001213.

Yap, W. K. and Karri, V. Comparative study in predicting the global solar radiation for Darwin, Australia. *Journal of Solar Energy Engineering*, 134(3):034501–034501, 05 2012. URL http://dx.doi.org/10.1115/1.4006574.

Yaramoglu, M., Brinsfield, R. B., and Jr, R. E. M. Estimation of solar radiation using stochastically generated cloud cover data. *Energy in Agriculture*, 4(0):227 – 242, 1985. ISSN 0167-5826. doi: http://dx.doi.org/10.1016/0167-5826(85)90019-1. URL http://www.sciencedirect.com/science/article/pii/0167582685900191.

Yona, A., Senjyu, T., Saber, A., Funabashi, T., Sekine, H., and Kim, C.-H. Application of neural network to 24-hour-ahead generating power forecasting for pv system. In *Power and Energy Society General Meeting - Conversion and Delivery of Electrical Energy in the 21st Century, 2008 IEEE*, pages 1 – 6, July 2008. doi: 10.1109/PES.2008.4596295.

Yoshida, S., Ueno, S., Kataoka, N., Takakura, H., and Minemoto, T. Estimation of global tilted irradiance and output energy using meteorological data and performance of photovoltaic modules. *Solar Energy*, 93(0):90 – 99, 2013. ISSN 0038-092X. doi: http://dx.doi.org/10.1016/j.solener.2013.04.001. URL http://www.sciencedirect.com/science/article/pii/S0038092X13001321.

Younes, S. and Muneer, T. Improvements in solar radiation models based on cloud data. *Building Services Engineering Research and Technology*, 27(1):41–54, 2006. doi: 10.1191/0143624406bt143oa. URL http://bse.sagepub.com/content/27/1/41.abstract.

Zagouras, A., Kazantzidis, A., Nikitidou, E., and Argiriou, A. Determination of measuring sites for solar irradiance, based on cluster analysis of satellite-derived cloud estimations. *Solar Energy*, 97(0):1 – 11, 2013. ISSN 0038-092X. doi: http://dx.doi.org/10.1016/j.solener.2013.08.005. URL http://www.sciencedirect.com/science/article/pii/S0038092X13003150.

Zagouras, A., Inman, R. H., and Coimbra, C. F. On the determination of coherent solar microclimates for utility planning and operations. *Solar Energy*, 102(0):173 – 188, 2014a. ISSN 0038-092X. doi: http://dx.doi.org/10.1016/j.solener.2014.01.021. URL http://www.sciencedirect.com/science/article/pii/S0038092X14000395.

Zagouras, A., Pedro, H. T., and Coimbra, C. F. Clustering the solar resource for grid management in island mode. *Solar Energy*, 110(0):507 – 518, 2014b. ISSN 0038-092X. doi: http://dx.doi.org/10.1016/j.solener.2014.10.002. URL http://www.sciencedirect.com/science/article/pii/S0038092X14004836.

Zhang, Q. Development of the typical meteorological database for Chinese locations. *Energy and Buildings*, 38(11):1320 – 1326, 2006. ISSN 0378-7788. doi: http://dx.doi.org/10.1016/j.enbuild.2006.04.003. URL http://www.sciencedirect.com/science/article/pii/S0378778806000958. Energy and Environment of Residential Buildings in China.

Zidek, J. V., Sun, W., and Le, N. D. Designing and integrating composite networks for monitoring multivariate gaussian pollution fields. *Journal of the Royal Statistical Society. Series C (Applied Statistics)*, 49(1):63 – 79, January 2000. URL http://www.jstor.org.libproxy1.nus.edu.sg/stable/2680861.

Zimmerman, D. L. Optimal network design for spatial prediction, covariance parameter estimation, and empirical prediction. *Environmetrics*, 17(6):635 – 652, 2006. ISSN 1099-095X. doi: 10.1002/env.769. URL http://dx.doi.org/10.1002/env.769.

Zografos, K. and Nadarajah, S. Expressions for Rényi and Shannon entropies for multivariate distributions. *Statistics & Probability Letters*, 71(1):71 – 84, January 2005. ISSN 0167-7152. doi: 10.1016/j.spl.2004.10.023. URL http://www.sciencedirect.com/science/article/pii/S016771520400286X.

Zou, H. and Hastie, T. Regularization and variable selection via the elastic net. *Journal of the Royal Statistical Society: Series B (Statistical Methodology)*, 67(2):301 – 320, 2005. ISSN 1467-9868. doi: 10.1111/j.1467-9868.2005.00503.x. URL http://dx.doi.org/10.1111/j.1467-9868.2005.00503.x.

Appendix A

Statistical preliminaries

Given a random variable X, a **cumulative distribution function** $F(x)$ is defined as $F(x) = \mathbb{P}(X \leq x)$, where $\mathbb{P}$ denotes probability. We can then have the following:

Definition. *The* ***expectation****, or mean, or first moment of* X *is defined to be*

$$\mathbb{E}(X) = \int x dF(x) = \mu = \mu_X; \tag{A.1}$$

and the ***variance*** *of* X *is defined by*

$$\mathbb{V}(X) = \mathbb{E}(X-\mu)^2 = \int (x-\mu)^2 dF(x) = \sigma^2 = \sigma_X^2; \tag{A.2}$$

If there is another random variable Y *with mean* μ_Y*, the* ***covariance*** *between* X *and* Y *is*

$$\texttt{Cov}(X,Y) = \mathbb{E}\Big((X-\mu_X)(Y-\mu_Y)\Big); \tag{A.3}$$

and their ***correlation*** *is*

$$\texttt{Corr}(X,Y) = \frac{\texttt{Cov}(X,Y)}{\sigma_X \sigma_Y}. \tag{A.4}$$

A.1 Time series preliminaries

Time series is a subset of what we call temporal processes. A (possible multivariate) temporal process can be written as $\{\boldsymbol{z}(r) \ : \ r \in D_t\}$ where $D_t \subset \mathbb{R}^1$ and r indexes the time of the process. A temporal process can be continuous where $D_t = [0, \infty)$ or discrete where $D_t = \{0, 1, 2, \cdots\}$. We represent the a continuous univariate temporal process as $z(t)$ and a discrete univariate temporal process as z_t. Thus $\{z_t \ : \ t = 0, 1, \cdots\}$ or simply $\{z_t\}$ is a time series. Following the above definition, the **mean of a time series** is given by:

$$\mu_t = \mathbb{E}(z_t), \quad t \in D_t \tag{A.5}$$

Beside the mean of a time series, we are also interested in how the time series co-varies across various time lags; this is described by the **autocovariance function**:

$$\mathbb{C}(t, r) = \texttt{Cov}(z_t, z_r) = \mathbb{E}\Big((z_t - \mu_t)(z_r - \mu_r)\Big), \quad t, r \in D_t. \tag{A.6}$$

Furthermore, by defining the variance of $\sigma_t^2 = \mathbb{V}(z_t) = \mathbb{C}(t, t)$, we have the **autocorrelation function**:

$$\rho(t, r) = \frac{\mathbb{C}(t, r)}{\sqrt{\mathbb{C}(t, t)\mathbb{C}(r, r)}} = \frac{\mathbb{C}(t, r)}{\sigma_t \sigma_r}, \quad t, r \in D_t, \tag{A.7}$$

which is a normalized measure of the co–variation, $\rho(t, r) \in [-1, 1]$.

Let us consider a time series $\{z_t\}$. We say the time series is **strictly stationary** if $\{z_{t_1}, \cdots, z_{t_m}\}$, a collection of m random variables from time series $\{z_t\}$, has an identical joint distribution with another collection of m random variables at a time lag τ, i.e., $\{z_{t_1+\tau}, \cdots, z_{t_m+\tau}\}$, $\forall\ \tau \in \{0, \pm 1, \pm 2, \cdots\}$. A time series is **weakly stationary** (or second–order stationary) if (1) $\mathbb{E}(z_t) = \mu, \ \forall\ t \in D_t$ and (2) $\texttt{Cov}(z_t, z_r) = \mathbb{C}(t - r) = \mathbb{C}(\tau), \ \forall\ t, r \in D_t$ and $\tau = \{0, \pm 1, \pm 2, \cdots\}$.

For a multivariate time series $\{\boldsymbol{z}_t\}$, we use $\{z_t^{(i)}\}$ to denote the ith time series. The

cross–covariance function between time series $\{z_t^{(i)}\}$ and $\{z_t^{(j)}\}$ is defined by:

$$\mathbb{C}_{ij}(t,r) = \texttt{Cov}(z_t^{(i)}, z_r^{(j)}), \quad t, r \in D_t. \tag{A.8}$$

Furthermore if the multivariate time series is weakly stationary, then:

$$\mathbb{C}_{ij}(t,r) = \mathbb{C}_{ij}(\tau) = \texttt{Cov}(z_t^{(i)}, z_{t+\tau}^{(j)}) = \mathbb{C}_{ji}(-\tau). \tag{A.9}$$

Lastly, weakly stationary **cross–correlation function** is given by:

$$\rho_{ij}(\tau) = \frac{\mathbb{C}_{ij}(\tau)}{\sqrt{\mathbb{C}_{ii}(0)\mathbb{C}_{jj}(0)}}, \quad \tau = 0, \pm 1, \pm 2, \cdots . \tag{A.10}$$

The above definitions are general. When data are involved, we are interested in the empirical estimates of the statistics. For a weakly stationary time series $\{z_1, \cdots, z_T\}$, the **empirical mean** (or sample mean) $\widehat{\mu} = \frac{1}{T}\sum_{t=1}^{T} z_t$. The **empirical autocovariance function** is:

$$\widehat{\mathbb{C}}(\tau) = \frac{1}{T}\sum_{t=1}^{T-\tau}(z_{t+\tau} - \widehat{\mu})(z_t - \widehat{\mu}), \quad \tau = 0, 1, \cdots, T-1. \tag{A.11}$$

The above is biased; the denominator can be replaced by $T - \tau$ for a unbiased estimation of the autocovariance function. The **empirical autocorrelation function** is:

$$\widehat{\rho}(\tau) = \frac{\widehat{\mathbb{C}}(\tau)}{\widehat{\mathbb{C}}(0)}, \quad \tau = 0, 1, \cdots, T-1. \tag{A.12}$$

Similarly, the **empirical cross–covariance function** is:

$$\widehat{\mathbb{C}}_{ij}(\tau) = \frac{1}{T}\sum_{t=1}^{T-\tau}(z_{t+\tau}^{(i)} - \widehat{\mu}_i)(z_t^{(j)} - \widehat{\mu}_j), \quad \tau = 0, 1, \cdots, T-1; \tag{A.13}$$

and the **empirical cross–correlation function** is:

$$\widehat{\rho}_{ij}(\tau) = \frac{\widehat{\mathbb{C}}_{ij}(\tau)}{\widehat{\mathbb{C}}_{ii}(0)\widehat{\mathbb{C}}_{jj}(0)}, \quad \tau = 0, 1, \cdots, T-1. \tag{A.14}$$

As a numerical example, consider $\{z_t\} = \{6.7, 5.3, 3.3, 6.7, 3.3, 4.7, 4.7, 6.7, 3.3, 6.7\}$ is a weakly stationary time series, with $T = 10$. The empirical mean is calculated to be $\widehat{\mu} = 5.14$. For $\tau = 3$, the autocorrelation is:

$$\widehat{\rho}(3) = \frac{\widehat{\mathbb{C}}(3)}{\widehat{\mathbb{C}}(0)} = \frac{\frac{1}{10}\sum_{t=1}^{7}(z_{t+3} - 5.14)(z_t - 5.14)}{\frac{1}{10}\sum_{t=1}^{10}(z_t - 5.14)^2} = \frac{-0.48}{2} = -0.24.$$

A.2 Geostatistics preliminaries

A spatial process can be written as $\{z(\boldsymbol{s}) \;:\; \boldsymbol{s} \in D_s\}$ where $D_s \subset \mathbb{R}^d$ and $\boldsymbol{s}$ indexes the location of the process. A spatial process is called a geostatistical process if its parameters are defined via mean, variances and covariances. We are interested to establish the spatial dependence in a geostatistical process.

Variogram is the foundation of geostatistics. A **stationary variogram** is defined as:

$$\gamma(\boldsymbol{h}) = \mathbb{V}\Big(z(\boldsymbol{s} + \boldsymbol{h}) - z(\boldsymbol{s})\Big), \quad \forall\ \boldsymbol{s}, \boldsymbol{s} + \boldsymbol{h} \in D_s. \tag{A.15}$$

where $\boldsymbol{h}$ is a d–dimensional translation in space; $\gamma(\boldsymbol{h})$ denotes the variogram. Furthermore, if the variogram can be written as only a function of $\|\boldsymbol{h}\|$, where $\|\cdot\|$ denote the Euclidian distance, it is an **isotropic variogram**. Similar to the variogram, we can define **stationary spatial covariance function**:

$$\mathbb{C}(\boldsymbol{h}) = \texttt{Cov}\Big(z(\boldsymbol{s} + \boldsymbol{h}), z(\boldsymbol{s})\Big), \quad \forall\ \boldsymbol{s}, \boldsymbol{s} + \boldsymbol{h} \in D_s. \tag{A.16}$$

with $\mathbb{E}(z(\boldsymbol{s})) = \mu$, which is constant. The corresponding **stationary spatial correlation function** is:

$$\rho(\boldsymbol{h}) = \frac{\mathbb{C}(\boldsymbol{h})}{\mathbb{C}(\boldsymbol{0})}, \quad \boldsymbol{h} \in \mathbb{R}^d. \tag{A.17}$$

Isotropic spatial covariance/correlation functions are $\mathbb{C}(\|\boldsymbol{h}\|)$ and $\rho(\|\boldsymbol{h}\|)$ respectively, if they exist.

A.3 Space–time covariance functions

In the spatio–temporal case, if we can define covariance function $\mathbb{C}$ such that:

$$\mathbb{C}(\boldsymbol{s}-\boldsymbol{x};t,r) = \texttt{Cov}\{z(\boldsymbol{s};t), z(\boldsymbol{x};r)\}, \quad \boldsymbol{s},\boldsymbol{x} \in D_s,\ t,r \in D_t \tag{A.18}$$

we say that the covariance function is **spatially stationary**. Similarly, **temporal stationarity** of the covariance function is defined as:

$$\mathbb{C}(\boldsymbol{s},\boldsymbol{x};t-r) = \texttt{Cov}\{z(\boldsymbol{s};t), z(\boldsymbol{x};r)\}, \quad \boldsymbol{s},\boldsymbol{x} \in D_s,\ t,r \in D_t \tag{A.19}$$

and **spatio–temporal stationarity** corresponds to:

$$\mathbb{C}(\boldsymbol{s}-\boldsymbol{x};t-r) = \texttt{Cov}\{z(\boldsymbol{s};t), z(\boldsymbol{x};r)\}, \quad \boldsymbol{s},\boldsymbol{x} \in D_s,\ t,r \in D_t \tag{A.20}$$

Similar to spatial stationarity, **spatial isotropy** corresponds to:

$$\mathbb{C}(\|\boldsymbol{s}-\boldsymbol{x}\|;t,r) = \texttt{Cov}\{z(\boldsymbol{s};t), z(\boldsymbol{x};r)\}, \quad \boldsymbol{s},\boldsymbol{x} \in D_s,\ t,r \in D_t \tag{A.21}$$

From Eqn. (A.18), if we define $\boldsymbol{h} = \boldsymbol{s} - \boldsymbol{x}$, and from Eqn. (A.19) we define $\tau = t - r$, spatially and temporally stationary covariance functions can be written as $\mathbb{C}_S(\boldsymbol{h})$ and $\mathbb{C}_T(\tau)$ respectively, where the subscripts S and T are used to denote space and time. A spatio–temporal random process $z(\boldsymbol{s};t)$ is said to have a **separable spatio–temporal covariance function** if:

$$\texttt{Cov}\{z(\boldsymbol{s};t), z(\boldsymbol{x};r)\} = \mathbb{C}_S(\boldsymbol{s},\boldsymbol{x}) \cdot \mathbb{C}_T(t,r), \quad \forall\ \boldsymbol{s},\boldsymbol{x} \in D_s,\ t,r \in D_t \tag{A.22}$$

When $\mathbb{C}_S(\cdot)$ and $\mathbb{C}_T(\cdot)$ are spatially and temporally stationary, Eqn. (A.22) becomes:

$$\mathbb{C}(\boldsymbol{h};\tau) = \mathbb{C}_S(\boldsymbol{h}) \cdot \mathbb{C}_T(\tau), \quad \boldsymbol{h} \in \mathbb{R}^d,\ \tau = 0, \pm 1, \pm 2, \cdots \tag{A.23}$$

However, environmental data sets are not separable due to the complex time and space interactions. Such separable approximation only facilitates analysis. A more general class of spatio–temporal processes are the fully symmetric processes. A random process is said to be **fully symmetric** if:

$$\texttt{Cov}\{z(\boldsymbol{s};t), z(\boldsymbol{x};r)\} = \texttt{Cov}\{z(\boldsymbol{s};r), z(\boldsymbol{x};t)\}, \quad \forall\ \boldsymbol{s}, \boldsymbol{x} \in D_s,\ t, r \in D_t \tag{A.24}$$

Again, given the stationary covariance functions, Eqn. (A.24) becomes:

$$\mathbb{C}(\boldsymbol{h};\tau) = \mathbb{C}(\boldsymbol{h};-\tau), \quad \boldsymbol{h} \in \mathbb{R}^d,\ \tau = 0, \pm 1, \pm 2, \cdots \tag{A.25}$$

which represents a **stationary fully symmetric covariance function**. Separability is a special case of full symmetry. Therefore when the covariance matrix is not fully symmetric, it can not be separable.

As correlation can be considered as a normalized measure of covariance, the above definitions apply to correlation function $\rho(\cdot;\cdot)$. For example, **a spatio–temporal stationary correlation function** can be defined as:

$$\rho(\boldsymbol{h};\tau) = \texttt{Corr}\{z(\boldsymbol{s};t), z(\boldsymbol{x};r)\}, \quad \boldsymbol{s}, \boldsymbol{x} \in D_s,\ t, r \in D_t,\ \boldsymbol{h} \in \mathbb{R}^d,\ \tau = 0, \pm 1, \pm 2, \cdots \tag{A.26}$$

From Eqns. (A.22), (A.23), (A.24) and (A.25) we can infer that stationarity does not imply full symmetry nor separability. Fig. A.1 shows the Venn diagram for the three statistical properties.

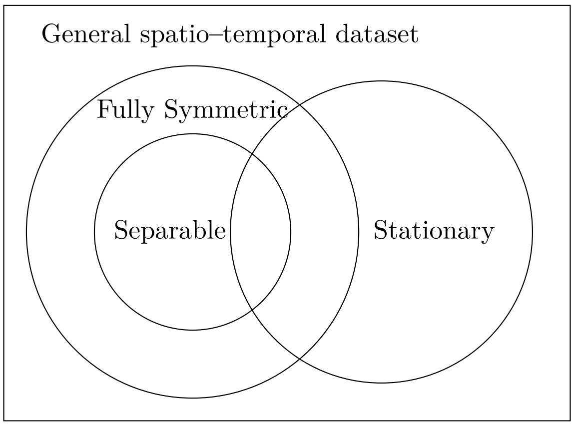

Fig. A.1 Diagram illustration for stationarity, full symmetry and separability.

Appendix B

Selected detrend models

Baig et al. (1991) fit the global horizontal irradiance (GHI) series with a Gaussian function:

$$I_{\text{trend}} = \frac{1}{\sigma\sqrt{2\pi}} e^{-(t-m)^2/2\sigma^2} \tag{B.1}$$

where I_{trend} is the fitted trend, t is time, and σ is the standard deviation of the Gaussian (the regression parameter that should be determined by the data). The parameter m represents the peak hour of a day which corresponds to the expected mean of the Gaussian distribution.

Kaplanis (2006) uses a cosine function to fit the GHI series:

$$I_{\text{trend}} = a_1 + a_2 \cos\left(\frac{2\pi(t-m)}{24}\right) \tag{B.2}$$

where a_1 and a_2 are the regression parameters.

Al-Sadah et al. (1990) find that a high order polynomial model is a good fit:

$$I_{\text{trend}} = b_1 + b_2 t + b_3 t^2 \tag{B.3}$$

where b_1, b_2 and b_3 are the regression parameters.

Appendix C

Multidimensional scaling

Multidimensional scaling (MDS) aims at searching for a low dimensional space (usually Euclidean), in which points in the space represent the objects, in addition, the distance between the set of points in the space, $\{h_{ij}\}$, match as well as possible the original set of dissimilarities $\{d_{ij}\}$ (Cox and Cox, 2000). There are many MDS models, among which the classical scaling and non–metric scaling are used in this thesis.

Multi-dimensional scaling is implemented in many statistical softwares such as R (R Core Team, 2014). Nevertheless, we show the required mathematics for implementing MDS in our context. We use the non–metric MDS developed by Kruskal (1964a,b). Classical MDS is first used to set the initial parameters required by Kruskal's algorithm.

C.1 Classical MDS

Using the definition of dispersion given by Sampson and Guttorp (1992), we can define the proximity (which can be similarity or dissimilarity, in our case the dissimilarity) matrix $\boldsymbol{\Delta}$, which is constructed using the square root of the elements in the dispersion matrix $[d_{ij}^2]$, i.e., $\boldsymbol{\Delta} = [d_{ij}]$ where $i, j \in \{1, 2, \cdots, n\}$ representing n points in space.

The classical MDS algorithm rests on the fact that the coordinate matrix $\boldsymbol{X}$ can be derived by eigenvalue decomposition from the scalar product matrix $\boldsymbol{B} = \boldsymbol{X}\boldsymbol{X}'$. A detailed derivation can be found in chapter 2 of (Cox and Cox, 2000). The following steps describe the solution mathematically.

Given the matrix of squared proximities $\boldsymbol{\Delta}^{(2)} = [d_{ij}^2]$, we perform double centering:

$$\boldsymbol{B} = -\frac{1}{2}\boldsymbol{J}\boldsymbol{\Delta}^{(2)}\boldsymbol{J} \tag{C.1}$$

where $\boldsymbol{J} = \boldsymbol{I} - n^{-1}\mathbf{1}\mathbf{1}^\top$, n is the number of objects. For example, if we have 4 objects,

$$\boldsymbol{J} = \begin{pmatrix} 1 & 0 & 0 & 0 \\ 0 & 1 & 0 & 0 \\ 0 & 0 & 1 & 0 \\ 0 & 0 & 0 & 1 \end{pmatrix} - \frac{1}{4} \times \begin{pmatrix} 1 & 1 & 1 & 1 \\ 1 & 1 & 1 & 1 \\ 1 & 1 & 1 & 1 \\ 1 & 1 & 1 & 1 \end{pmatrix} \tag{C.2}$$

The purpose of the double centering step is to overcome the indeterminacy of the solution due to arbitrary translation. $\boldsymbol{B}$ calculated this way is relative to the origin. We can then use spectral decomposition:

$$\boldsymbol{B} = \boldsymbol{Q}_m\boldsymbol{\Lambda}_m\boldsymbol{Q}_m^{-1} \tag{C.3}$$

$\boldsymbol{\Lambda}_m$ is the diagonal matrix of m eigenvalues and $\boldsymbol{Q_m}$ is the matrix of m eigenvectors. The coordinate matrix can then be obtained by:

$$\boldsymbol{X} = \boldsymbol{B}^{(1/2)} = \boldsymbol{Q}_m\boldsymbol{\Lambda}_m^{(1/2)} \tag{C.4}$$

If the desired MDS results are two dimensional, only the first two columns of $\boldsymbol{X}$ are needed.

C.2 Kruskal's algorithm

In contrast to the classical MDS, non–metric MDS interests only in the ranking of the dissimilarities. Recall the definition earlier, for n objects (points) in space, there are only $n(n-1)/2$ dissimilarities d_{ij} for $i < j$ with $i \in \{1, 2, \cdots, n-1\}$ and $j \in \{2, 3, \cdots, n\}$. In the ideal case, if we arrange the dissimilarities in an ascending order, we can define disparities $\widehat{h}_{ij} = \delta(d_{ij})$, where $\delta(\cdot)$ is a monotonic regression passing through all n points in the exact order. However, this ideal situation is not always present at the initial condition set by classical MDS; further optimization is required. It is achieved by minimizing some stress functions. Unfortunately, even when the stress functions are minimized, the monotonic relationship may not be present due to the degeneracies in the dissimilarity matrix.

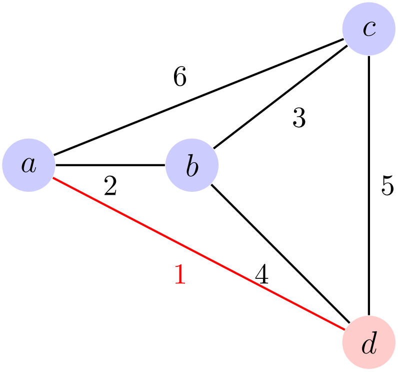

Fig. C.1 A representation for degeneracy in the dissimilarity matrix. a, b, c and d are objects, the numbers indicate their dissimilarities.

Consider the example shown in Fig. C.1. If only objects a, b and c are considered, the dissimilarities (numbers in the figure) are immediately seen to be related with their distances, i.e., the dissimilarity increases monotonically with increasing separation. Now consider that one more object, d, is added into configuration. After examining the inter-object distances, the logical dissimilarity between a and d would be 7 (they are furthest apart). However, the set dispersion is 1; the relationships among the objects become less obvious. In the later case, non–metric MDS would locate d somewhere near a to achieve the minimum stress. In our application of irradiance forecasting, the degeneracies in the dissimilarity matrix is not severe as the dissimilarity is based on the physical guild line of "closer things are more alike". Practical examples shown in chapter 5 and 9 both reflect the physical principle and the applicability of MDS.

With that being said, we consider the stress functions. A raw stress $\mathcal{S}^*$ is defined as:

$$\mathcal{S}^* = \sum_{i<j}(h_{ij} - \widehat{h}_{ij})^2, \quad i \in \{1, 2, \cdots, n-1\},\ j \in \{2, 3, \cdots, n\} \tag{C.5}$$

which is the sum of square error between the desired distances and the disparities. However, this raw stress function lacks certain desirable properties. For instance, it is not invariant under uniform stretching. If the dissimilarities change by a factor of k, then $\mathcal{S}^*$ changes to $k^2\mathcal{S}^*$. To overcome the defect, a normalizing term can be added as a denominator, furthermore, the square root is included, which is analogous to choosing the standard deviation in place of the variance:

$$\mathcal{S} = \sqrt{\frac{\sum\limits_{i<j}(h_{ij} - \widehat{h}_{ij})^2}{\sum\limits_{i<j} h_{ij}^2}} \tag{C.6}$$

The stress function $\mathcal{S}$ can be minimized through an iterative gradient descent method. The steps are given below:

1. Use classical MDS for initial configuration.

2. Normalize the configuration to have its centroid at the origin and unit mean square distance from the origin. Although the classical MDS centers the data, normalization is need for each iteration to prevent the continually expanding in successive iterations.

3. Find set of distance $\{h_{ij}\}$ from the configuration.

4. Fit a monotonic regression line of $\{h_{ij}\}$ on $\{d_{ij}\}$ by least square. Details of this least square method is found in chapter 3 of (Cox and Cox, 2000).

5. Find the gradient $\dfrac{\partial \mathcal{S}}{\partial \boldsymbol{x}}$, where $\boldsymbol{x} = (x_1, y_1, x_2, y_2, \cdots, x_n, y_n)'$ are the coordinates of the N points in space. For higher dimension scalings, $\boldsymbol{x}$ is adjusted accordingly. If the absolute value $\left|\dfrac{\partial \mathcal{S}}{\partial \boldsymbol{x}}\right|$ is smaller than some ϵ, the algorithm converges. Otherwise:

6. Find the step length sl which controls the convergence speed. An ad hoc rule of finding

sl is given in (Kruskal, 1964b). Comprehensively, sl is determined by $g(\mathcal{S}_m, \mathcal{S}_{m-1}, \mathcal{S}_{m-5})$, a function of present stress $\mathcal{S}_m$, the previous stress $\mathcal{S}_{m-1}$ and the stress 5 steps ago, $\mathcal{S}_{m-5}$.

7. Calculate the new configuration using:

$$\boldsymbol{x}_{m+1} = \boldsymbol{x}_m - \frac{\dfrac{\partial \mathcal{S}}{\partial \boldsymbol{x}} \times sl}{\left| \dfrac{\partial \mathcal{S}}{\partial \boldsymbol{x}} \right|} \tag{C.7}$$

   where m is the iteration step.

8. Go back to step 2.

The configuration at convergence will give the non–metric MDS result.

Appendix D

Thin plate spline mapping

Given two sets of coordinates:

$$\mathcal{G} = \begin{pmatrix} x_1 & x_2 & \cdots & x_n \\ y_1 & y_2 & \cdots & y_n \end{pmatrix}^\top, \quad \in \mathbb{R}^{n\times 2} \tag{D.1a}$$

$$\mathcal{D} = \begin{pmatrix} x_1^* & x_2^* & \cdots & x_n^* \\ y_1^* & y_2^* & \cdots & y_n^* \end{pmatrix}^\top, \quad \in \mathbb{R}^{n\times 2} \tag{D.1b}$$

where $\mathcal{G}$ and $\mathcal{D}$ stand for geographical and dispersion planes. For each pair of coordinates in $\mathcal{G}$, we can find the Euclidean distance between them, i.e,:

$$r_{ij} = \|\boldsymbol{s}_i - \boldsymbol{s}_j\| = \sqrt{(x_i - x_j)^2 + (y_i - y_j)^2} \tag{D.2}$$

By defining the thin plate spline $U(r_{ij}) = r_{ij}^2 \log r_{ij}^2$. We can write matrices:

$$\boldsymbol{K} = \begin{pmatrix} 0 & U(r_{12}) & \cdots & U(r_{1n}) \\ U(r_{21}) & 0 & \cdots & U(r_{2n}) \\ \vdots & \vdots & \ddots & \vdots \\ U(r_{n1}) & U(r_{n2}) & \cdots & 0 \end{pmatrix}, \quad \in \mathbb{R}^{n \times n} \tag{D.3a}$$

$$\boldsymbol{P} = \begin{pmatrix} 1 & \\ \vdots & \mathcal{G} \\ 1 & \end{pmatrix} = \begin{pmatrix} 1 & \boldsymbol{s}_1 \\ \vdots & \vdots \\ 1 & \boldsymbol{s}_n \end{pmatrix} = \begin{pmatrix} 1 & x_1 & y_1 \\ \vdots & \vdots & \vdots \\ 1 & x_n & y_n \end{pmatrix}, \quad \in \mathbb{R}^{n \times 3} \tag{D.3b}$$

$$\boldsymbol{L} = \left(\begin{array}{c|c} \boldsymbol{K} & \boldsymbol{P} \\ \hline \boldsymbol{P}^\top & \mathbf{0} \end{array}\right), \quad \in \mathbb{R}^{(n+3) \times (n+3)} \tag{D.3c}$$

where $\mathbf{0}$ is a 3×3 matrix of zeros. We find the inverse of $\boldsymbol{L}$ through spectral decomposition:

$$\boldsymbol{L} = \boldsymbol{Q}\boldsymbol{\Lambda}\boldsymbol{Q}^{-1} \tag{D.4}$$

and

$$\boldsymbol{L}^{-1} = \boldsymbol{Q}\boldsymbol{\Lambda}^{-1}\boldsymbol{Q}^{-1} \tag{D.5}$$

We write:

$$\boldsymbol{L}^{-1} = \left(\begin{array}{c|c} \boldsymbol{L}_n^{-1} & \cdots \\ \boldsymbol{L}_1^{-1} & \vdots \\ \boldsymbol{L}_2^{-1} & \cdots \end{array}\right), \quad \in \mathbb{R}^{(n+3)\times(n+3)} \tag{D.6a}$$

$$\boldsymbol{L}_n^{-1} = \begin{pmatrix} L_{1,1}^{-1} & L_{1,2}^{-1} & \cdots & L_{1,n}^{-1} \\ L_{2,1}^{-1} & L_{2,2}^{-1} & \cdots & L_{2,n}^{-1} \\ \vdots & \vdots & \ddots & \vdots \\ L_{n,1}^{-1} & L_{n,2}^{-1} & \cdots & L_{n,n}^{-1} \end{pmatrix}, \quad \in \mathbb{R}^{n\times n} \tag{D.6b}$$

$$\boldsymbol{L}_1^{-1} = \begin{pmatrix} L_{(n+1),1}^{-1} & L_{(n+1),2}^{-1} & \cdots & L_{(n+1),n}^{-1} \end{pmatrix}, \quad \in \mathbb{R}^{1\times n} \tag{D.6c}$$

$$\boldsymbol{L}_2^{-1} = \begin{pmatrix} L_{(n+2),1}^{-1} & L_{(n+2),2}^{-1} & \cdots & L_{(n+2),n}^{-1} \\ L_{(n+3),1}^{-1} & L_{(n+3),2}^{-1} & \cdots & L_{(n+3),n}^{-1} \end{pmatrix}, \quad \in \mathbb{R}^{2\times n} \tag{D.6d}$$

where $L_{i,j}^{-1}$ denotes the entry of $\boldsymbol{L}^{-1}$ at ith row, jth column.

Consider the n–vector $\boldsymbol{V}_{x^*}$ and the $(n+3)$–vector $\boldsymbol{Y}_{x^*}$:

$$\boldsymbol{V}_{x^*} = \begin{pmatrix} x_1^* & x_2^* & \cdots & x_n^* \end{pmatrix}, \quad \in \mathbb{R}^{1\times n} \tag{D.7}$$

$$\boldsymbol{Y}_{x^*} = \begin{pmatrix} \boldsymbol{V}_{x^*} & 0 & 0 & 0 \end{pmatrix}^\top, \quad \in \mathbb{R}^{(n+3)\times 1} \tag{D.8}$$

We can thus define a function $f_{x^*}(x,y)$ so that an arbitrary G plane point $\boldsymbol{s}_0$ with coordinates (x,y) can be mapped to the x–coordinate in the D plane:

$$f_{x^*}(x,y) = a_1 + a_x x + a_y y + \sum_{i=1}^{n} w_i U(\|\boldsymbol{s}_i - \boldsymbol{s}_0\|) \tag{D.9}$$

where the coefficients a_1, a_x, a_y and w_i are found via:

$$\boldsymbol{L}^{-1}\boldsymbol{Y}_{x^*} = \begin{pmatrix} w_1 & \cdots & w_n & a_1 & a_x & a_y \end{pmatrix}^\top, \quad \in \mathbb{R}^{(n+3)\times 1} \tag{D.10}$$

Similarly the point $\boldsymbol{s}_0$ can be mapped to the y–coordinate in the D plane using $f_{y^*}(x, y)$, which is defined similarly through the vectors $\boldsymbol{V}_{y^*}$ and $\boldsymbol{Y}_{y^*}$. From Eqn. (D.10), it is clear that the role of the last 3 rows of $\boldsymbol{L}$ is to ensure that the sum of the coefficients w_i are zero. Furthermore, the cross products of w_i with the x and y coordinates of $\boldsymbol{s}_i$ are likewise zero. In matrix format, the above procedure can be rewritten by computing:

$$\boldsymbol{W} = \boldsymbol{L}_n^{-1}\mathcal{D}, \quad \in \mathbb{R}^{n\times 2} \tag{D.11a}$$

$$\boldsymbol{T} = \boldsymbol{L}_1^{-1}\mathcal{D}, \quad \in \mathbb{R}^{1\times 2} \tag{D.11b}$$

$$\boldsymbol{B} = \boldsymbol{L}_2^{-1}\mathcal{D}, \quad \in \mathbb{R}^{2\times 2} \tag{D.11c}$$

For an arbitrary point $\boldsymbol{s}_0$ in geographical plane (x, y), its position in the dispersion plane (x^*, y^*) is:

$$\begin{pmatrix} x^* \\ \\ y^* \end{pmatrix} = \boldsymbol{T}^\top + \boldsymbol{B}^\top \begin{pmatrix} x \\ \\ y \end{pmatrix} + \boldsymbol{W}^\top \boldsymbol{S} \tag{D.12}$$

where

$$\boldsymbol{S} = \begin{pmatrix} U\|\boldsymbol{s}_0 - \boldsymbol{s}_1\| \\ \\ U\|\boldsymbol{s}_0 - \boldsymbol{s}_2\| \\ \vdots \\ \\ U\|\boldsymbol{s}_0 - \boldsymbol{s}_n\| \end{pmatrix}, \quad \in \mathbb{R}^{n\times 1} \tag{D.13}$$

We obtain the one–to–one mapping from the geographical plane to dispersion plane.

Appendix E

Transposition models

E.1 Isotropic models

Four isotropic models are accessed in chapter 6. In isotropic approximation, we assume the diffuse radiance were ideally constant over the whole sky hemisphere. Tilt angle s is the only input to these models.

The Badescu (2002) model

$$R_\mathrm{d} = [3 + \cos(2s)]/4 \tag{E.1}$$

The Koronakis (1986) model

$$R_\mathrm{d} = (2 + \cos s)/3 \tag{E.2}$$

The Liu and Jordan (1962) model

$$R_\mathrm{d} = (1 + \cos s)/2 = \cos^2(s/2) \tag{E.3}$$

The Tian et al. (2001) model

$$R_\mathrm{d} = 1 - s/180 \tag{E.4}$$

E.2 Anisotropic Models

In reality, a plane of tilt s facing the sun receives more diffuse radiation than a plane of same tilt in the opposite direction. More parameters are involved in anisotropic models.

The Hay (1979) model

$$R_{\mathrm{d}} = \frac{I_{\mathrm{beam}}}{I_{\mathrm{oh}}} R_{\mathrm{b}} + \left(1 - \frac{I_{\mathrm{beam}}}{I_{\mathrm{oh}}}\right) \left(\frac{1 + \cos s}{2}\right) \tag{E.5}$$

where R_{b} is beam irradiance transposition factor, it is given by $\cos\theta_i / \cos\theta_z$.

The Klucher (1979) model

$$R_{\mathrm{d}} = \cos^2\left(\frac{s}{2}\right) \left[1 + F' \sin^3\left(\frac{s}{2}\right)\right] \left[1 + F' \cos^2\theta_i \sin^3\theta_z\right] \tag{E.6}$$

where F' is Klucher's modulating function defined as $1 - (I_{\mathrm{dif}}/I_{\mathrm{glo}})^2$.

The Perez et al. (1990) model

The sky's clearness ε' is first defined by Perez:

$$\varepsilon' = \left[(I_{\mathrm{dif}} + I_{\mathrm{dir}}) \frac{1}{I_{\mathrm{dif}}} + \kappa \left(\frac{\theta_z \times \pi}{180}\right)^3\right] \div \left[1 + \kappa \left(\frac{\theta_z \times \pi}{180}\right)^3\right] \tag{E.7}$$

where κ is constant 1.041 for θ_z in degrees. The sky's brightness Δ' is give by: $\Delta' = I_{\mathrm{dif}} \times m_r / I_{\mathrm{o}}$.

The circumsolar brightening coefficient F_1 and horizon brightening coefficient F_2 is given by:

$$F_1 = \max\left\{0, F_{11} + F_{12} \times \Delta' + F_{13} \times \left(\frac{\theta_z \times \pi}{180}\right)\right\} \tag{E.8}$$

$$F_2 = F_{21} + F_{22} \times \Delta' + F_{23} \times \left(\frac{\theta_z \times \pi}{180}\right) \tag{E.9}$$

where F_{11}, F_{12}, F_{13}, F_{21}, F_{22} and F_{23} are given according to various ε' bins by table:

ε'	F_{11}	F_{12}	F_{13}	F_{21}	F_{22}	F_{23}
$[1, 1.065)$	-0.0083	0.5877	-0.0621	-0.0596	0.0721	-0.022
$[1.065, 1.23)$	0.1299	0.6826	-0.1514	-0.0189	0.066	-0.0289
$[1.23, 1.5)$	0.3297	0.4869	-0.2211	0.0554	-0.064	-0.0261
$[1.5, 1.95)$	0.5682	0.1875	-0.2951	0.1089	-0.1519	-0.014
$[1.95, 2.8)$	0.873	-0.392	-0.3616	0.2256	-0.462	0.0012
$[2.8, 4.5)$	1.1326	-1.2367	-0.4118	0.2878	-0.823	0.0559
$[4.5, 6.2)$	1.0602	-1.5999	-0.3589	0.2642	-1.1272	0.1311
$[6.2, +\infty)$	0.6777	-0.3273	-0.2504	0.1516	-1.3765	0.2506

Finally the diffuse transposition factor is given by:

$$R_{\mathrm{d}} = (1 - F_1) \times \left(\frac{1 + \cos s}{2}\right) + F_1 \times \frac{a}{b} + F_2 \times \sin s \tag{E.10}$$

where $a = \max(0, \cos\theta_i)$ and $b = \max(0.087, \cos\theta_z)$.

The Reindl et al. (1990b) model

$$R_{\mathrm{d}} = \frac{I_{\mathrm{beam}}}{I_{\mathrm{oh}}} R_{\mathrm{b}} + \left(1 - \frac{I_{\mathrm{beam}}}{I_{\mathrm{oh}}}\right)\left(\frac{1 + \cos s}{2}\right)\left[1 + \sqrt{\frac{I_{\mathrm{beam}}}{I_{\mathrm{glo}}}} \sin^3\left(\frac{s}{2}\right)\right] \tag{E.11}$$

where R_{b} is defined earlier in Hay model.

The Skartveit and Olseth (1986) model

$$R_{\mathrm{d}} = \frac{I_{\mathrm{beam}}}{I_{\mathrm{oh}}} R_{\mathrm{b}} + \Omega \cos s + \left(1 - \frac{I_{\mathrm{beam}}}{I_{\mathrm{oh}}} - \Omega\right)\left(\frac{1 + \cos s}{2}\right) \tag{E.12}$$

where $\Omega = \max\left[0, (0.3 - 2I_{\mathrm{beam}}/I_{\mathrm{oh}})\right]$

The Temps and Coulson (1977) model

$$R_{\mathrm{d}} = \cos^2\left(\frac{s}{2}\right)\left[1 + \sin^3\left(\frac{s}{2}\right)\right]\left[1 + \cos^2\theta_i \sin^3\theta_z\right] \tag{E.13}$$

Appendix F

Decomposition models

The Erbs et al. (1982) model

We define diffuse horizontal transmittance K_{d} as:

$$I_{\mathrm{dif}} = K_{\mathrm{d}} I_{\mathrm{oh}} \tag{F.1}$$

Combine the above equation with Eqns. (6.3) to (6.5), we have:

$$K_{\mathrm{d}} = K_{\mathrm{t}} - K_{\mathrm{n}} \tag{F.2}$$

together with the correlation which Erbs developed:

$$\begin{aligned}
\frac{K_{\mathrm{d}}}{K_{\mathrm{t}}} &= 1.0 - 0.09K_{\mathrm{t}}, \quad \text{for } K_{\mathrm{t}} \leq 0.22 && \text{(F.3)} \\
\frac{K_{\mathrm{d}}}{K_{\mathrm{t}}} &= 0.9511 - 0.1604K_{\mathrm{t}} + 4.388K_{\mathrm{t}}^2 - 16.638K_{\mathrm{t}}^3 \\
&\quad +12.336K_{\mathrm{t}}^4, \quad \text{for } 0.22 < K_{\mathrm{t}} \leq 0.80 && \text{(F.4)} \\
\frac{K_{\mathrm{d}}}{K_{\mathrm{t}}} &= 0.165, \quad \text{for } K_{\mathrm{t}} > 0.80 && \text{(F.5)}
\end{aligned}$$

The Orgill and Hollands (1977) Model

$$\frac{K_\mathrm{d}}{K_\mathrm{t}} = 1.0 - 0.249K_\mathrm{t}, \quad \text{for } K_\mathrm{t} \leq 0.35 \tag{F.6}$$

$$\frac{K_\mathrm{d}}{K_\mathrm{t}} = 1.557 - 1.84K_\mathrm{t}, \quad \text{for } 0.35 < K_\mathrm{t} \leq 0.75 \tag{F.7}$$

$$\frac{K_\mathrm{d}}{K_\mathrm{t}} = 0.177, \quad \text{for } K_\mathrm{t} > 0.75 \tag{F.8}$$

The Maxwell (1987) Model

$$K_\mathrm{n} = K_\mathrm{nc} - \Delta K_\mathrm{n} \tag{F.9}$$

$$K_\mathrm{nc} = 0.866 - 0.122m_r - 0.0121m_r^2 - 0.000653m_r^3 + 0.000014m_r^4 \tag{F.10}$$

$$\Delta K_\mathrm{n} = a + b \times \exp(c \times m_r) \tag{F.11}$$

$$m_r = [\cos\theta_z + 0.15(93.885 - \theta_z)^{-1.253}]^{-1} \tag{F.12}$$

K_nc is clear sky direct normal transmittance, m_r is relative optical air mass as described in (Kasten, 1965). a, b and c are parameters used to calculate the change in direct normal transmittance ΔK_n under various values of K_t. a, b and c are related to K_t by a piecewise function:

For $K_\mathrm{t} \leq 0.6$,

$$a = 0.512 - 1.56K_\mathrm{t} + 2.286K_\mathrm{t}^2 - 2.222K_\mathrm{t}^3 \tag{F.13}$$

$$b = 0.370 + 0.962K_\mathrm{t} \tag{F.14}$$

$$c = -0.280 + 0.932K_\mathrm{t} - 2.048K_\mathrm{t}^2 \tag{F.15}$$

For $K_{\mathrm{t}} > 0.6$,

$$a = -5.743 + 21.77K_{\mathrm{t}} - 27.49K_{\mathrm{t}}^2 + 11.56K_{\mathrm{t}}^3 \tag{F.16}$$

$$b = 41.40 - 118.5K_{\mathrm{t}} - 66.05K_{\mathrm{t}}^2 + 31.90K_{\mathrm{t}}^3 \tag{F.17}$$

$$c = -47.01 + 184.2K_{\mathrm{t}} - 222.0K_{\mathrm{t}}^2 + 73.81K_{\mathrm{t}}^3 \tag{F.18}$$

The Reindl et al. (1990a) Model (Univariate)

$$\frac{K_{\mathrm{d}}}{K_{\mathrm{t}}} = 1.020 - 0.248K_{\mathrm{t}}, \quad \text{for } K_{\mathrm{t}} \leq 0.3 \tag{F.19}$$

$$\frac{K_{\mathrm{d}}}{K_{\mathrm{t}}} = 1.45 - 1.67K_{\mathrm{t}}, \quad \text{for } 0.3 < K_{\mathrm{t}} \leq 0.78 \tag{F.20}$$

$$\frac{K_{\mathrm{d}}}{K_{\mathrm{t}}} = 0.147, \quad \text{for } K_{\mathrm{t}} > 0.78 \tag{F.21}$$

The Reindl et al. (1990a) Model (Bivariate)

$$\frac{K_{\mathrm{d}}}{K_{\mathrm{t}}} = 1.020 - 0.254K_{\mathrm{t}} + 0.0123\sin\alpha, \quad \text{for } K_{\mathrm{t}} \leq 0.3 \tag{F.22}$$

$$\frac{K_{\mathrm{d}}}{K_{\mathrm{t}}} = 1.400 - 1.749K_{\mathrm{t}} + 0.177\sin\alpha,$$
$$\text{for } 0.3 < K_{\mathrm{t}} \leq 0.78, \quad K_{\mathrm{d}}/K_{\mathrm{t}} < 0.97 \quad \text{and} \quad K_{\mathrm{d}}/K_{\mathrm{t}} > 0.1 \tag{F.23}$$

$$\frac{K_{\mathrm{d}}}{K_{\mathrm{t}}} = 0.486K_{\mathrm{t}} - 0.182\sin\alpha, \quad \text{for} \quad K_{\mathrm{t}} > 0.78 \quad \text{and} \quad K_{\mathrm{d}}/K_{\mathrm{t}} > 0.1 \tag{F.24}$$

where α is the solar elevation angle. It is given by $90^\circ - \theta_z$ in degrees.